



UNIVERSITY OF  

---

LIVERPOOL

**Porous Organic Cage Membranes for Versatile Molecular  
Separations**

Ai He

November 2021

Supervisor: Prof. Andrew I. Cooper

Thesis submitted in accordance with the requirements of the  
University of Liverpool for the degree of Doctor of Philosophy

## Abstract

# Porous Organic Cage Membranes for Versatile Molecular Separations

Ai He

Membranes with excellent permeance and high selectivity offer an attractive route to molecular separations because technologies such as distillation and chromatography are energy-intensive. However, it remains challenging to fine-tune the structure and porosity in membranes so that they can effectively separate similar-sized molecules. In this thesis, a series of porous organic cage (POC) based membranes have been fabricated via different approaches to investigate the possibility of making membranes with excellent performance using POC as building blocks.

In Chapter 3, the fabrication of composite membranes that comprise crystalline POC films have been fabricated by a novel interfacial synthesis approach on a polyacrylonitrile support (**CC3**-PAN). These membranes are continuous, crystalline, and exhibited ultrafast solvent permeance (including  $177.3 \text{ L}\cdot\text{m}^{-2}\cdot\text{h}^{-1}\cdot\text{bar}^{-1}$  for acetone,  $147.5 \text{ L}\cdot\text{m}^{-2}\cdot\text{h}^{-1}\cdot\text{bar}^{-1}$  for acetonitrile,  $136.9 \text{ L}\cdot\text{m}^{-2}\cdot\text{h}^{-1}\cdot\text{bar}^{-1}$  for hexane,  $55.9 \text{ L}\cdot\text{m}^{-2}\cdot\text{h}^{-1}\cdot\text{bar}^{-1}$  for toluene, and  $42.9 \text{ L}\cdot\text{m}^{-2}\cdot\text{h}^{-1}\cdot\text{bar}^{-1}$  for water), and high rejection of organic dyes with molecular weights over  $585 \text{ g}\cdot\text{mol}^{-1}$ . Other synthetic strategies were used to prepare the **CC3** membranes, including spin-coating, casting, in-situ synthesis, and sonochemistry, and the obtained membranes showed different crystallinity and separation performance. Unlike the crystalline **CC3** membranes, amorphous **CC3** membranes fabricated via spin-coating have demonstrated the molecular weight cut-off (MWCO) shifts to  $\sim 400 \text{ g}\cdot\text{mol}^{-1}$ .

The crystalline **CC3**-PAN membrane discussed in Chapter 3 is dynamic, and its non-covalent structure could be switched using a solvent. The results presented in Chapter 4 demonstrate that the pore aperture of **CC3**-PAN can be switched in methanol to generate larger pores that provide increased methanol permeance and higher MWCO ( $1400 \text{ g}\cdot\text{mol}^{-1}$ ). By varying the water/methanol ratio, the membrane can be switched between two phases that have different selectivities, such that a single, ‘smart’ crystalline membrane can perform graded molecular sieving. This effect has been exemplified by separating three organic dyes in a single-stage, single-membrane process.

In Chapter 5, a series of thin-film composite membranes comprising a cage nanofilm separating layer have been fabricated at an aqueous–organic interface, using a series of reduced amine functionalised POCs cages named **RCC1**, **RCC2** and **RCC3**. The obtained nanofilms were continuous and robust with an ultrathin thickness. By altering the molecule type during the synthesis, **RCC1**, **RCC2**, and **RCC3** nanofilms exhibited distinctive performance, where **RCC1** and **RCC2** nanofilms had a similar MWCO of  $\sim 250 \text{ g}\cdot\text{mol}^{-1}$ . In comparison, **RCC3** nanofilm showed a shift of its cut-off to  $\sim 600 \text{ g}\cdot\text{mol}^{-1}$ . The **RCC3** nanofilm has been used for post-functionalisation, where the unreacted amines were reacted with formaldehyde to make the POC more rigid. A tunable sieving effect was subsequently found in the FT-**RCC3** nanofilm, and its MWCO shifted to  $\sim 450 \text{ g}\cdot\text{mol}^{-1}$  after being post-synthetically modified.

## **Acknowledgements**

First of all, I would like to thank my supervisor, Professor Andy Cooper, for providing fantastic research environment and advanced facilities, as well as valuable supervision to complete these projects and make my PhD. Thanks must go to Dr Marc Little for your guidance, support, and supervision throughout this work and completion of this thesis. I would never forget the hardest work, the darkest walk, the longest night, the most exciting data, and the most cheerful drinking we had experienced in Diamond Light Source. Thanks also to Dr Michael Briggs and Dr Yue Wu for your valuable supervision and patient guidance. Thank you for all your supervision and support, which has been directed a lot for my future road.

I would also like to thank all those I have collaborated with in this work, especially Professor Andrew Livingston and Dr Zhiwei Jiang at Imperial College London. I would like to thank you for your huge support and guidance throughout my PhD projects from many meetings and tea-time discussions. It was my great pleasure to work with you, and I did have learnt a lot from you, which has a pretty positive impact in my lifetime.

Big thanks to the past and present members in the Cooper group for your kind help and company—Peng, Hongmei, Hui, Haofan, Yang, Xiaoyan, Guohong, Donglin, Qiang, Wei, Weiwei, Zhiwei and Xiaowei, Ben Alston and Burger, Steve, Sam, Becky, Mike, Megan, Rich, Lunjie, Zhongfu, Xiaofeng, Linjiang, Xue, Aiting, Yongjie, Yu and Boyu, Chengxi, Caixin, Ying, Xinxin and Zhudan. Thank Ming for teaching and helping with cage synthesis and project discussions. Thanks to Rob Clowes for training, maintaining and fixing all the instruments. Thanks must also go to Christian, Ammar, Duncan, Cath, Andy M, Rachael, CK and Nicola for the lunchtime chat and the great time on AJ Friday. A special mention to my best friend and lab buddy Craig, for helping in experiments, valuable advice on my work, knowledge exchange, and sharing the PhD life. Thanks to all AIC group members for sharing the wonderful and unforgettable campus time. Also, thanks to Bonnie and Zuzka for your kind assistant in daily basis. Thanks to the MIF team for providing great support for the instruments.

Special thanks to Dr Tom Hasell and Dr Tom Mitra for your valuable advices and encouragement on my struggling of PhD project when things didn't go well in the second year. The comments and suggestions from my first- and second-year viva from my assessor Dr Tom Hasell were proved to be truly helpful, such as improving synthesis skills from group colleagues working on different areas and a three-month study at Andrew Livingston group.



Life got overwhelming for me since 2022. I've suffered from the Covid, and have been sadly burgled at home while I was about to finish my PhD - lost invaluable life-time items, memories and data. It has been such a dark period of time in my life, and has been so tough to get through anyway. Sincere thanks to everyone who had helped, financially or mentally. Andy, Marc, Haofan, Craig, Bonnie, Cath, Zuzka, Xiaofeng, Ni, Kai, Arthur, Ming, Ian, Chunchun, the police, the NHS, all my colleagues and my mental health counsellor Yinka. Without all your support, I may not have survived through this and completed this thesis during the final stage.

Finally, I must thank my friends and family for everything they've done for me during the last four years, especially my family for all the support they have provided to me when I decided to study abroad. I would also like to thank my furry (cat) friends Sian, Pierce, Puff, and Didi, for the intimate company and stress-relief during the painful thesis-writing process.

In particular, huge thanks to my incredible boyfriend, now my husband, Yan, after we had a dream wedding at Selby Abbey, for your continued love, understanding and support, and for your persevering company through half of the earth. I couldn't have done this without you.

Last but not least, thanks to my dad in heaven. Although silent all these years, I could still touch the endless love from you, from the other side of the world, from the other space and the time. Love never fails.

“I wanted to be so perfect you see.”

— Dying in the Sun, the Cranberries

Wish You Were Here.

Ai

Liverpool, 2022

## List of Publications

### “A Smart and Responsive Crystalline Porous Organic Cage Membrane with Switchable Pore Apertures for Graded Molecular Sieving”

Ai He, Zhiwei Jiang, Yue Wu, Hadeel Hussain, Jonathan Rawle, Michael E. Briggs, Marc A. Little, Andrew G. Livingston\*, Andrew I. Cooper\*, *Nature Materials*, 2022, **21**, 463–470.

### “Ultrathin Polyamide Nanofilms Incorporating Porous Organic Cages for Tuneable Molecular Sieving”

Ai He, Zhiwei Jiang, Chen Yang, Ming Liu, Michael E. Briggs, Marc A. Little, Andrew I. Cooper\*, Andrew G. Livingston\*, *Manuscript in preparation*.

### “Covalent Organic Framework Membranes with Tuneable Pore Apertures Fabricated by a Rapid Interfacial Method”

Wei Zhao, Ai He, John W. Ward, Marc A. Little\*, Andrew I. Cooper\*, *Manuscript in preparation*.

### “Nano-assemblies of a soluble conjugated organic polymer and an inorganic semiconductor for sacrificial photocatalytic hydrogen production from water”

Haofan Yang, Houari Amari, Lunjie Liu, Chengxi Zhao, Hui Gao, Ai He, Nigel D. Browning, Marc A. Little, Reiner Sebastian Sprick\*, Andrew I. Cooper\*, *Nanoscale*, 2020, **12**, 24488-24494.

### “Engineered Coatings via the Assembly of Amino-Quinone Networks”

Qizhi Zhong, Joseph J Richardson, Ai He, Tian Zheng, René PM Lafleur, Jianhua Li, Wenzhe Qiu, Denzil Furtado, Shuaijun Pan, Zhikang Xu, Lingshu Wan, Frank Caruso\*, *Angewandte Chemie International Edition*, 2021, **60**, 2346-2354.

(In this work, which was in collaboration with Frank Caruso Nanoengineering group, POC nanocrystals were synthesised on amino-quinone network surfaces by liquid-phase epitaxy.)

## List of Abbreviations

1D	One dimensional
2D	Two dimensional
3D	Three dimensional
AAO	Anodic aluminum oxide
ACF	Acid fuchsin
AFM	Atomic force microscopy
Ag	Silver
Al	Aluminum
Au	Gold
BB	Brilliant blue
BET	Brunauer Emmett Teller
BSE	Backscattered electrons
CC3	Covalent Cage 3
CDCl <sub>3</sub>	Deuterated chloroform
CH <sub>4</sub>	Methane
CHDA	1,2-Cyclohexane diamine
CMPs	Conjugated microporous polymers
CNTs	Carbon nanotubes
CO <sub>2</sub>	Carbon dioxide
COFs	Covalent organic frameworks
CR	Congo red
CSP	Crystal structure prediction
CTFs	Covalent triazine frameworks
DCM	Dichloromethane
DFT	Density functional theory

DMSO	Dimethyl sulfoxide
DR	Direct Red 80
<i>e.g.</i>	<i>exempli gratia</i>
<i>et al.</i>	<i>et alia</i>
FIB	Focused ion beam
FO	Forward osmosis
FT-IR	Fourier-transform infrared spectroscopy
FT-RCC3	Formaldehyde tied reduced CC3
GIXRD	Grazing incidence X-ray diffraction
GO	Graphene oxide
H <sub>2</sub>	Hydrogen
HCPs	Hyper-cross-linked polymers
HOFs	Hydrogen-bonded organic frameworks
HPLC	High-performance liquid chromatography
<i>i.e.</i>	<i>id est</i>
IP	Interfacial polymerization
ISA	Integrally skinned asymmetric
LBL	Layer-by-layer
MC	Macrocycle
MD	Membrane distillation
MeOH	Methanol
MF	Microfiltration
MLG	Multilayered graphene
MMMs	Mixed matrix membranes
MO	Methyl orange
MOFs	Metal-organic frameworks

MPD	<i>m</i> -Phenylenediamine
MWCO	Molecular weight cut off
MWNTs	Multi-walled nanotubes
N <sub>2</sub>	Nitrogen
NaBH <sub>4</sub>	Sodium borohydride
NF	Nanofiltration
NMR	Nuclear magnetic resonance spectroscopy
NP	4-Nitrophenol
NPs	Nanoparticles
NR	Neutral red
OSN	Organic solvent nanofiltration
PA	Polyamide
PAN	Polyacrylonitrile
PEI	Polyethyleneimine
PET	Polyethylene terephthalate
PIMs	Polymers of intrinsic microporosity
POCs	Porous organic cages
POPs	Porous organic polymers
PPIX	Protoporphyrin IX disodium
PXRD	Powder X-ray diffraction
RB	Rose bengal
RCC3	Reduced CC3
rGO	Reduced graphene oxide
RO	Reverse osmosis
RR	Reactive red 120
S <sub>BET</sub>	BET surface area

SD	Standard deviations
SE	Secondary electrons
SEM	Scanning electron microscopy
Si	Silicon
SWNTs	Single-walled nanotubes
SY	Sunset yellow
TFB	1,3,5-Triformylbenzene
TFC	Thin film composite
TGA	Thermogravimetric Analysis
TMC	Trimesoyl chloride
UF	Ultrafiltration
Ultraviolet-visible	UV-vis
UV	Ultraviolet
WCA	Water contact angle
XPS	X-ray photoelectron spectroscopy
XRD	X-ray diffraction
ZIFs	Zeolitic imidazolate frameworks

## Contents

Abstract.....	I
Acknowledgements.....	III
List of Publications .....	V
List of Abbreviations .....	VI
<b>Chapter 1 Introduction and Background .....</b>	<b>1</b>
1.1 Introduction.....	2
1.2 A Brief History of Membrane Separation Technology.....	4
1.3 Molecular Sieving Materials for Membranes .....	6
1.3.1 Graphene and Graphene Oxide membranes .....	7
1.3.2 Carbon Nanotube Membranes .....	10
1.3.3 Membranes with Nanoparticles .....	12
1.3.4 Zeolites and Zeolitic Imidazolate Framework Membranes .....	14
1.3.5 Metal-Organic Framework Membranes.....	17
1.3.6 Covalent Organic Framework Membranes .....	20
1.3.7 Hydrogen-bonded Organic Framework Membranes .....	23
1.3.8 Porous Organic Polymer Membranes .....	25
1.3.9 Limitations and Challenges.....	28
1.4 Porous Organic Cages.....	29
1.4.1 Introduction of Porous Molecular Solids.....	29
1.4.2 Structures and Porosity of Porous Organic Cages .....	31
1.4.3 Synthesis and Topology of Porous Organic Cages.....	34
1.4.4 Porous Organic Cage Membranes .....	38
1.5 Membrane Fabrication Technology.....	40
1.5.1 Membrane Types .....	40
1.5.2 Preparation of membranes .....	42
1.5.3 Interfacial Synthesis of Membranes.....	43
1.6 Project Overview and Aims .....	45
1.6.1 Chapter Summary .....	45
1.6.2 Overall Aims.....	49
1.7 Reference .....	49
<b>Chapter 2 Characterisation Methods and Experiments.....</b>	<b>72</b>
2.1 Membrane Separation Principles .....	73

2.2 Membrane Performance Evaluation .....	74
2.2.1 Membrane Flux and Solvent Permeance .....	74
2.2.2 Molecular Weight Cut Off (MWCO) .....	75
2.3 Morphology Study on Membranes .....	77
2.4 Crystal Structure Study .....	78
2.4.1 Powder X-ray Diffraction (PXRD) .....	78
2.4.2 Grazing Incidence X-ray Diffraction (GIXRD).....	80
2.5 Experiments and Methods.....	82
2.5.1 Materials. ....	82
2.5.2 Synthesis. ....	82
2.5.3 Membrane fabrication.....	83
2.5.4 Characterisation Methods .....	86
2.5.4 Membrane performance evaluation .....	89
2.6 References.....	96
<b>Chapter 3 Porous Organic Cage Membranes and Membrane Performance.....</b>	<b>99</b>
3.1 Background and Introduction .....	100
3.2 Membrane Fabrication .....	102
3.3 Membrane Characterisation for Interfacial Crystallization Membranes .....	104
3.3.1 Chemistry Characterisation.....	104
3.3.2 Morphology Characterisation .....	106
3.3.3 Crystallography Characterisation.....	111
3.3.4 Film Formation Mechanism Study .....	114
3.4 Membrane Performance for Interfacial Crystallization Membranes .....	126
3.4.1 Solvent Permeance.....	128
3.4.2 Molecular Separation .....	133
3.4.3 Effects of Crystallinity .....	136
3.4.4 Effects of Reaction Solvents.....	141
3.4.5 Effects of Membrane Activation.....	142
3.4.6 Longer Duration Studies .....	144
3.5 Studies for Amorphous Cage Membranes .....	146
3.6 Characterisation and Performance for Other Cage Membranes .....	152
3.6.1 Cage Membranes Made with Co-crystals .....	152
3.6.2 Surface Morphology Studies of Cage Coatings Made by Other Methods.....	153



3.6.3 Surface Morphology and Dye Rejection of Cage Membranes Made by Other Methods.....	157
3.6.4 Discussions on Scalability .....	159
3.7 Conclusions.....	161
3.8 Chapter Acknowledgements .....	162
3.9 Reference .....	163
<b>Chapter 4 A Smart, Responsive Crystalline Porous Organic Cage Membrane with Switchable Pore Apertures for Graded Molecular Sieving .....</b>	<b>169</b>
4.1 Background and Introduction .....	170
4.2 Solid-state Structural Transformation Study on Cage Membranes .....	176
4.3 Switchable Pore Aperture with Dye Rejection Study.....	187
4.4 Investigations on Effects of Crystallinity and Solvation .....	201
4.5 Grade Sieving and Other Applications .....	216
4.6 Conclusion and Outlook .....	222
4.7 Chapter Acknowledgments.....	224
4.8 References.....	225
<b>Chapter 5 Ultrathin Crosslinked Porous Organic Cage Nanofilm Composite Membranes for Tuneable Molecular Sieving.....</b>	<b>231</b>
5.1 Background and Introduction .....	232
5.2 Fabrication of Nanofilm Composite Membranes .....	238
5.3 Surface Characterisation and Morphology Study .....	240
5.4 Post-functionalisation of the Nanofilm.....	243
5.5 Structure and Composition Study of the Nanofilm.....	246
5.6 Membrane Performance for Separation .....	247
5.7 Conclusions and Future Work .....	252
5.8 Acknowledgements.....	253
5.9 References.....	254
<b>Chapter 6 Conclusions and Outlook .....</b>	<b>257</b>

# **Chapter 1**

## **Introduction and Background**

## 1.1 Introduction

Extended periods of drought and water pollution have become some of the most pervasive environmental issues in the world, principally caused by population growth, industrial development, water scarcity and resource deterioration<sup>1</sup>. For example, drinking water sources, such as rivers and lakes, contain micropollutants from municipal, industrial and agricultural wastewaters<sup>2</sup>. Micropollutants (**Figure 1.1**), which include hormones, pharmaceuticals, pesticides, personal care products and industrial chemicals, can have detrimental effects even at low concentrations<sup>3</sup>. Furthermore, municipal wastewater effluents in water-stressed regions are often recycled for agriculture and even for indirect potable use, introducing a wide range of micropollutants to freshwater resources<sup>4,5</sup>. Therefore, the development of new technologies that remove micropollutants and other contaminants, as listed in **Table 1.1**, is paramount to ensure a constant supply of clean and safe drinking water continues<sup>6</sup>.

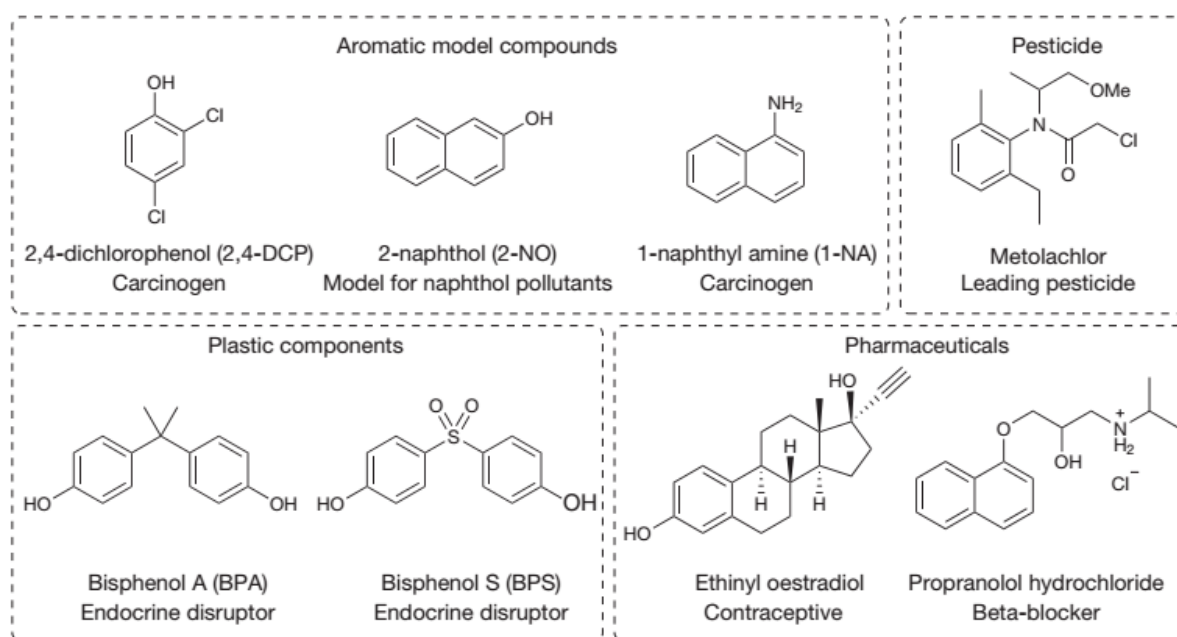


**Figure 1.1** Chemical structures of emerging organic micropollutants<sup>3</sup>. Reprinted from Springer Nature with permission.

The three main processes used for water purification are adsorption, catalysis and separation (**Figure 1.2**)<sup>7,8</sup>, which have different purification mechanisms. Among these current strategies, separation processes are considered the most critical and commonly used for water treatment. Membrane-based separations for water purification and desalination have been increasingly applied to address the global challenges of water scarcity and the pollution of aquatic environments<sup>9</sup>.

**Table 1.1** Contaminants of concern in source waters and membrane technologies that can meet treatment objectives. Reprinted from reference<sup>6</sup> with permission from Springer Nature.

(a) Purification for *Natural waters*

<i>Source water</i>	<i>Key contaminants</i>	<i>Treatment objectives</i>	<i>Membrane technologies</i>	<i>Problems and challenges</i>
Seawater	Boric acid, divalent cations	Reduce salinity	• Pre-treatment: MF, UF • Desalination: RO	Energy of desalination
Brackish groundwater	Divalent cations	Reduce salinity	• Desalination: RO and electrodialysis	Inland discharge of brine
Surface waters	Organic matter	Remove particles, microbial pathogens	MF, UF, NF, RO	High fouling potential
Fresh groundwater	Heavy metals	Reduce ions	MF, UF, NF, RO	Seawater intrusion

(b) Purification for *Wastewaters*

<b>SOURCE WATER</b>	<b>KEY CONTAMINANTS</b>	<b>TREATMENT OBJECTIVES</b>	<b>MEMBRANE TECHNOLOGIES</b>	<b>PROBLEMS AND CHALLENGES</b>
Municipal wastewater	Boric acid, divalent cations	Degrade <b>organic</b> matter	MF, UF, NF, RO	High fouling potential
Shale-gas produced water	Drilling fluid additives, oil and grease	Remove oily compounds and reduce salinity	• Drilling reuse: MF, UF • Desalination: NF, RO, FO, MD	High fouling potential
Coal-fired power flue gas desulfurization	Toxic metals	Remove dissolved toxic metals and reduce salinity	MF, UF, NF, RO, FO, MD	Potential zero liquid discharge requirements

During the last decades, nanofiltration (NF) and reverse osmosis (RO) have rapidly developed and provide tremendous potential for desalination, water softening, wastewater recycling, organic removal and metal removal<sup>10</sup>. Nanofiltration membranes and reverse osmosis membranes are the current state of the art for nanofiltration and reverse osmosis processes for water treatment, with an average pore size between 0.5 – 2 nm<sup>11</sup>. The separation mechanisms

of NF and RO membranes include steric effect, transport effect, Donnan effect and Dielectric exclusion, which describe the separation process by volume exclusion, interaction and surface charges<sup>12</sup>. To obtain favourable performance, high permeability is essential to minimize the membrane area, in combination with good selectivity. Hence, new-generation materials for NF or RO membranes with a high flux and rejection rate simultaneously is dramatically desired for the water treatment applications.

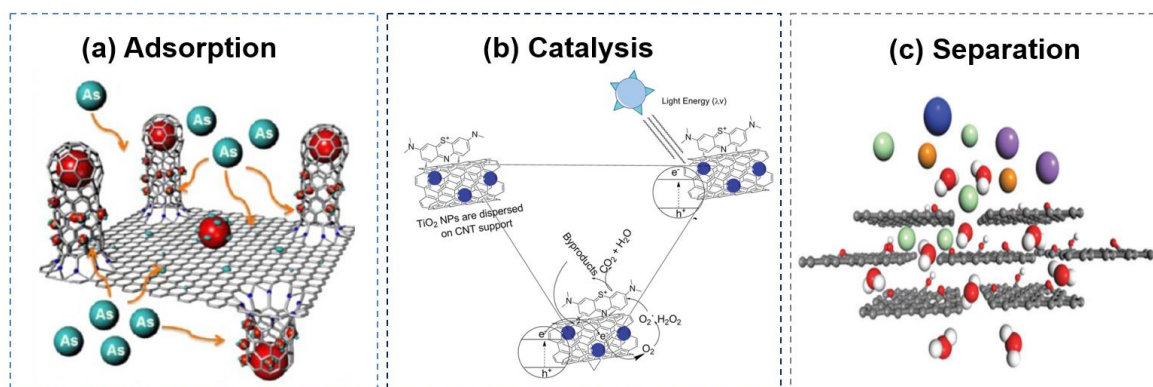


**Figure 1.2** Graphical representation of processes currently used for water purification<sup>7,8</sup>.  
Reprinted from Chemical Society reviews Springer Nature with permission.

## 1.2 A Brief History of Membrane Separation Technology

The record of earliest experiments using membrane technology dates back to the 18th century when Abbé Nolet defined the word ‘osmosis’ as the permeation of water through a membrane (diaphragm) in 1748<sup>13</sup>. This study applied membranes as tools to investigate specific chemicals physicochemical properties rather than as a viable separation technique. However, membrane science in the early stage was not well developed for four main reasons: unreliability, low permeation rate, poor selectivity, and high cost<sup>14</sup>.

After decades of stagnation, the rapid growth of membrane technologies occurred through the development of large scale processing techniques in the 1960’s. For example, the Loeb-Sourirajan process was developed for making defect-free, high-flux, anisotropic reverse osmosis membranes by Loeb and Sourirajan in 1963<sup>15</sup>. These cellulose triacetate membranes were fabricated by asymmetric morphologies, consisting of an upper skin layer bonded to a microporous sublayer. Both the skin layer and porous sublayer have identical chemical composition, and the filtration performance of the membrane depends on the degree of

acetylation. As a result, the flux of the first Loeb-Sourirajan RO membrane was ten times greater than that of other available membranes, making RO a potentially practical approach for desalting water.

The structures of asymmetric membranes casting from dope solutions were first reported by Riley *et al.* in 1965<sup>16</sup>, and showed good RO performance, leading to the first commercial membrane desalination plant in Coalinga. A 16-month trial was performed at the industrial plant, during which time the membrane durability and reliability was tested<sup>17</sup>. During the same period of time, pressure-driven membrane processes began to materialise, with leading journals *Desalination* and *The Journal of Membrane Science* appearing in 1965 and 1976, respectively<sup>18</sup>.

After some promising initial discoveries, membrane technologies started to be used for industrial-scale gas separations where advantages included their overall economics, safety, environmental and technical aspects since the 1980s. The membranes were first used to separate hydrogen from purge streams in ammonia production and for natural gas processing (e.g., CO<sub>2</sub>/CH<sub>4</sub> separation) in the following years of developing<sup>18</sup>.

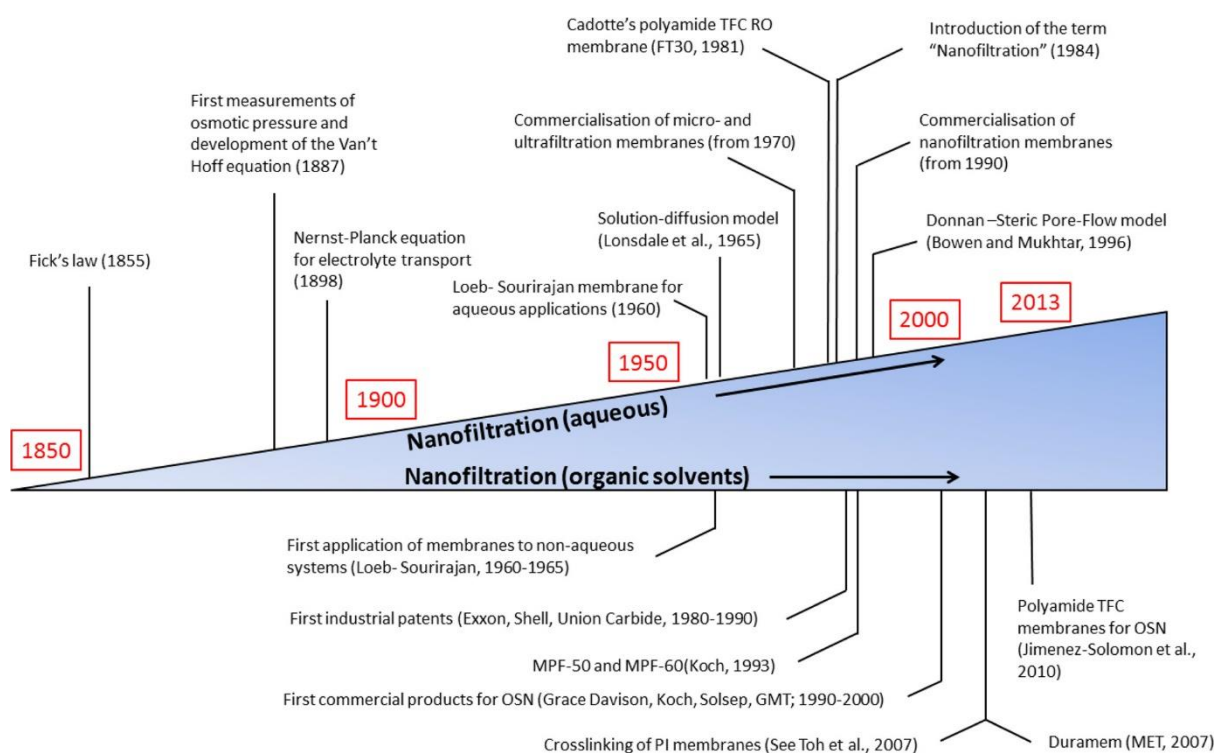


**Figure 1.3** Summary of the most significant events, which have contributed to the development of NF, over time. Reprinted from reference<sup>19</sup> with permission.

Although NF technologies have been mentioned in the literature since the late 1960s<sup>20</sup>, the technology only began to break through into industrial processes in the 21st century. A schematic showing some of the most significant events that have contributed to the development of the field are shown in **Figure 1.3**. The term “Nanofiltration” was defined during a FilmTec meeting in 1984 for the first time<sup>21</sup> to solve the terminology problem for a selective RO process that allows ionic solutes in feed water to permeate through a membrane. Membranes that retain molecules lower than 2 nm in diameter are defined as nanofiltration membranes<sup>22</sup>. NF membranes typically have high retentions of solutes in the 200-1000 g mol<sup>-1</sup> molecular weight range. Commercial membranes prepared for organic solvent nanofiltration (OSN) applications first became available in the late nineties from KOCH Membrane Systems<sup>21</sup>. Since then, several other companies, including Evonik MET and SolSep<sup>21</sup>, have entered the OSN membrane market, endowing the NF fields with increasing interests from both industry and scientific research areas.

Nowadays, membranes are critical components in devices used for applications, such as fuel cells, controlled delivery devices, solar cells,<sup>14,23</sup> separation, and purification systems<sup>24,25</sup>.

Materials research and design is the key point to enable synthetic membranes for large-scale, energy-efficient molecular separations. Materials with rigid, well-engineered pore structures can be favourable for fabricating advanced membranes<sup>26</sup>. In the next section, molecular sieving materials for the next-generation molecularly selective synthetic membranes will be introduced and discussed.

### **1.3 Molecular Sieving Materials for Membranes**

In recent years, porous materials (**Figure 1.4**) have attracted significant attention in NF and RO fields. The types of porous materials investigated include graphene, carbon nanotubes (CNTs), nanoparticles, zeolites, metal-organic frameworks (MOFs), covalent-organic frameworks (COFs), hydrogen-bonded organic frameworks (HOFs), porous organic polymers (POPs) and porous molecular solids<sup>27-30</sup>. With well-defined pore structures and high surface areas, these membranes exhibit high water flux and good salt rejection. Besides, the chemical diversity of these molecular sieving materials also contributes to multi-functional modification.

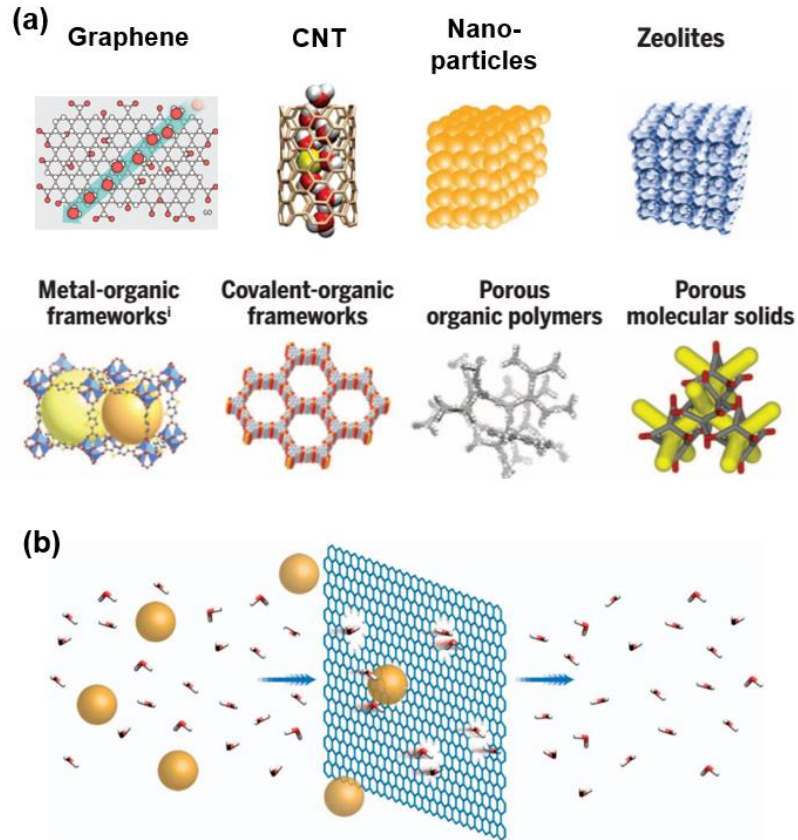


**Figure 1.4** (a) *Molecular sieving materials for versatile separations*<sup>27–30</sup>. (b) *A graphene membrane with subnanometer pores is a promising reverse osmosis membrane*<sup>31</sup>. Reprinted from Springer Nature with permission.

### 1.3.1 Graphene and Graphene Oxide membranes

Ever since their discovery by Prof Andre Geim and Prof Kostya Novoselov at The University of Manchester in 2004<sup>32</sup>, graphene has attracted enormous attention from academia and industry. Including because of its unique electrochemical properties, which include high thermal conductivity, high current, density, chemical inertness, optical transmittance and very high hydrophobicity. Since then, a flurry of studies in 2-D materials led to the generation of the scientific feat that won the Noble Prize in 2010 in Physics, which sparked a global explosion in graphene research. Graphene is a 2-D semimetal with a tiny overlap between valence and conductance bands, which is formed by a thick sheet of carbon atoms bonded by  $sp^2$  hybridization arranged in a hexagonal array<sup>33</sup>. X-ray diffraction revealed the crystal structure of graphene as a closely packed honeycomb-like structure<sup>34</sup>. This material is the simplest form of carbon and is considered the world's thinnest material so far<sup>35</sup>.



The graphene family includes graphene oxide (GO)<sup>36</sup>, reduced graphene oxide (rGO)<sup>37</sup>, graphene sheets and layered graphenes such as few layered graphenes and multilayered graphene (MLG)<sup>38,39</sup>. GO is obtained from a highly oxidized form of graphene molecule by strong oxidizing agents (**Figure 1.5(a)**), showing its unique intrinsic physical and chemical properties<sup>40</sup>. With their large surface area, oxygen-containing functionality, better conductivity and good biocompatibility, the graphene family has been an active candidate in the fields like energy<sup>41</sup> and biomedical<sup>42</sup> applications. Moreover, there was an enormous scope for graphene-based materials to be used as sieving membranes<sup>43–46</sup>, as the 2-D structure and tunable physicochemical properties of these materials are promising for membrane applications.

Nanoporous single-layer graphene has been demonstrated by Mahurin *et al.*<sup>47</sup> as a desalination membrane. Because the only translocation pathways for water and ion molecules were the nanopores, the resulting membranes achieved a salt rejection rate of nearly 100% and rapid water transport. Cohen-Tanugi *et al.*<sup>31,48</sup> showed that nanoporous graphene membranes could successfully desalinate water. They used molecular dynamics simulations to predict that nanoporous graphene membranes can provide water transport of up to 66 L per cm<sup>2</sup> · day · MPa, with >99% salt rejection. By comparison, a typical RO membrane provides water transport of ~0.01–0.05 L per cm<sup>2</sup> · day · MPa, with comparable rejection<sup>31,48</sup>.

GO membranes have been synthesized either by vacuum filtration or by layer-by-layer (LbL) assembly<sup>49</sup>. As is shown in **Figure 1.5(b)**, dry GO membranes prepared by vacuum filtration are tightly packed with a void spacing of ~0.3 nm between GO nanosheets. Thus, only water vapour aligned in a monolayer could permeate through the nanochannel. In contrast, the hydration of GO in an aqueous solution allowed water and small-sized ion molecules (with a hydrated radius less than 0.45 nm) to permeate fast through the interconnected nanochannels formed between GO nanosheets, whilst larger species were blocked<sup>49</sup>. More importantly, the separation capability of the GO membrane can be tuned by adjusting the nanochannel size, thus fitting the demands for desalination (0.3-0.7 nm, **Figure 1.5(c)**), water purification (0.7-2 nm), or biomedical filtration (more than 2 nm).

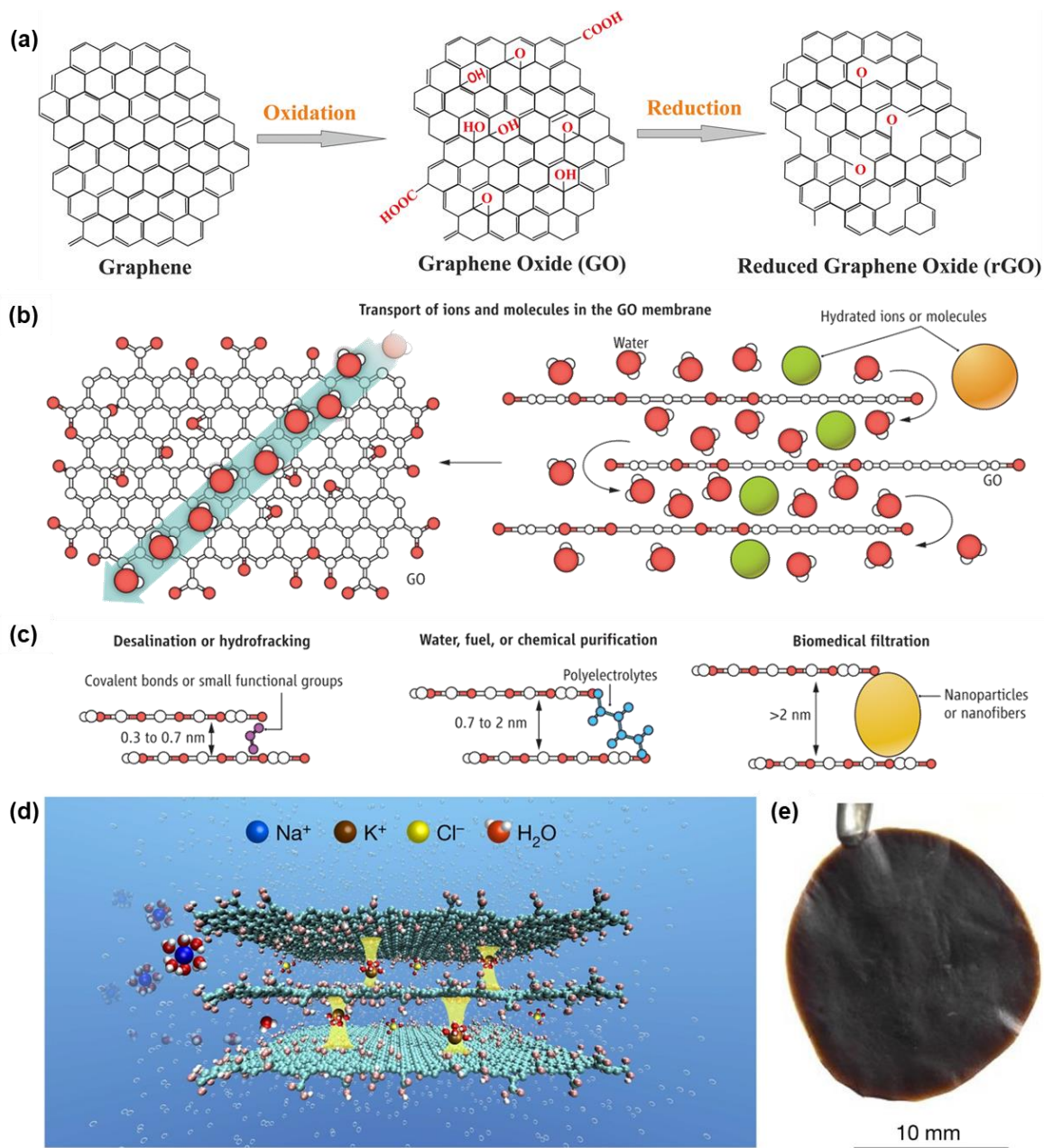


**Figure 1.5** (a) Chemical structure of GO and the conversion of graphene into GO and rGO. Reprinted from reference<sup>40</sup> with permission. (b) Water and small-sized ions and molecules (compared with the void spacing between stacked GO nanosheets) permeate superfast in the GO membrane, but larger species are blocked. (c) The separation capability of the GO membrane is tunable by adjusting the nanochannel size. Reprinted from reference<sup>49</sup> with permission. (d) A schematic of how K<sup>+</sup> ions in a GO membrane determine and fix the interlayer spacing such that other cations are rejected while pure water can penetrate. (e) Photograph of a freestanding GO membrane prepared by drop-casting of a 5 mg ml<sup>-1</sup> GO suspension. (e) Reprinted from reference<sup>50</sup> with permission.

Therefore, GO membranes can be designed and utilised as ultrathin, high-flux, and energy-efficient membranes for precise ionic and molecular sieving in an aqueous solution. For example, Zhou *et al.*<sup>47</sup> fabricated free-standing GO membranes with tunable thickness via facile vacuum filtration process. As the GO was observed to be negatively charged, the GO membrane exhibited a higher rejection rate for electronegative organic dyes and inorganic salts. Wang *et al.*<sup>47</sup> reported a strategy to adjust the interlayer spacing of GO laminates by fullerene grafting, with a fixed interlayer spacing of 1.25 nm achieved. The as-prepared GO membrane obtained a high water flux up to  $10.85 \text{ L h}^{-1} \text{ m}^{-2} \text{ bar}^{-1}$ , and the rejection rate for NaCl reached 89.66%, which showed the potential to purify brackish water into drinkable water. GO membranes have also been reported to be controlled of the interlayer spacing with ångström precision using different ions<sup>50</sup> (**Figure 1.5(d)**).

### 1.3.2 Carbon Nanotube Membranes

Discovered by Sumio Iijima in 1991<sup>51</sup>, carbon nanotubes (CNTs) are nanoscale cylinders of graphene, which can be capped at one or both ends with a half a fullerene molecule. These materials have been called a recipe for strength because of their unprecedented mechanical, electrical, and thermal properties<sup>52</sup>. There are two main types of CNTs: single-walled nanotubes (SWNTs), which comprise a single graphite sheet seamlessly wrapped into a cylindrical tube and have outer diameters in the range of 1–3 nm with inner diameters of 0.4–2.4 nm (**Figure 1.6, A to D**); and multi-walled nanotubes (MWNTs), which consist of an array of these nanotubes that are concentrically nested similar to rings of a tree trunk, with outer diameters ranging from ~2 nm (double walled nanotubes) up to ~100 nm with tens of walls (**Figure 1.6 E**)<sup>53</sup>.

These nanotubes exhibit excellent properties, such as high mechanical strength, large surface area, interconnected open pore structure and tunable chemistry<sup>54</sup>. Combined with their nanoscale dimensions, these properties have led to their study for a wide range of applications, including high-strength conductive composites, field emission displays, hydrogen storage devices, and sensors<sup>55</sup>. Moreover, there has been growing interest in exploring CNTs as the next generation of membrane materials, which exhibit high flux and selectivity, and are resistant to fouling<sup>56</sup>.

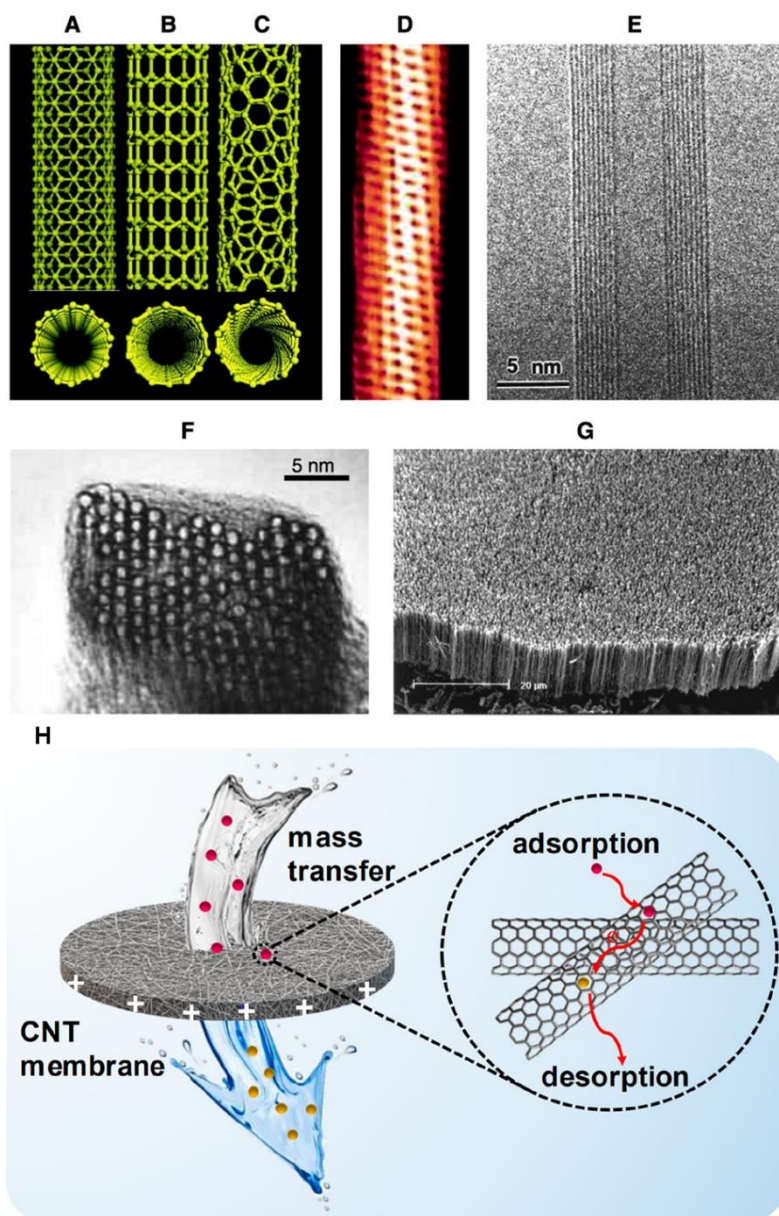


**Figure 1.6** Schematic illustrations of the structures of CNTs: (a) armchair, (b) zigzag, and (c) chiral SWNTs. Projectors normal to the tube axis and perspective views along the tube axis are on the top and bottom, respectively. (d) SPM picture of a 1.3 nm diameter chiral SWNT. (e) TEM image of a MWNT containing a concentrically nested array of nine SWNTs. (f) TEM micrograph (18) showing the lateral packing of 1.4-nm-diameter SWNTs in a bundle. Reprinted from reference<sup>53</sup> with permission. (g) SEM image of an array of MWNTs grown as a nanotube forest. (h) Electrochemical filtration reactive transport mechanism on a CNT membrane. Reprinted from reference<sup>57</sup> with permission.

To exploit these properties for membranes, macroscopic structures must be designed with controlled porosity and pore size. The CNT 1D form allows the assembly of a stable thin-film

fibrous network by various facile techniques. For example, CNT membranes were first fabricated using polymer infiltration by poly(styrene) to achieve a uniform nanoporous structure<sup>58</sup>. Both N<sub>2</sub> and Ru(NH<sub>3</sub>)<sub>6</sub><sup>3+</sup> were transported across the resulting membrane in an aqueous solution, with gas permeance of 2.6 μmol/(m<sup>2</sup> s Pa) and an iron transport flux of 0.07 μmol cm<sup>-2</sup> hour<sup>-1</sup> observed. CNTs and their composites have been demonstrated as electroactive membrane materials<sup>57</sup> by incorporating them into commercial membrane devices (**Figure 1.6 H**). These composite membranes showed fast electrochemical filtration transport and were used to degrade organic compounds and heavy metal ions decontamination. Rasel Das *et al.*<sup>59</sup> reported CNT membranes for water purification with self-cleaning functions. The Tip-functionalized nonpolar interior home of CNTs provides a strong invitation to polar water molecules and rejects salts and pollutants. Chan *et al.*<sup>58</sup> have simulated and fabricated CNT membranes (diameter 1.5 nm) with two zwitter ions at the tip ends, which achieved 98.6% Na<sup>+</sup> ion rejection for water desalination.

### 1.3.3 Membranes with Nanoparticles

Nanoparticles are discrete nanometre scale assemblies of atoms and are a class of material that can exhibit distinct properties compared to their bulk and molecular counterparts<sup>60</sup>. For example, by showing magnetic properties, photocatalytic and/or optical properties, biocompatibility. Therefore, nanoparticles are widely applied in the areas like photocatalysis<sup>61</sup>, biological sensing<sup>62</sup> and drug delivery<sup>63</sup>.

For the past few decades, porous nanoparticles have been found to play an essential role in separation membranes due to their properties such as antimicrobial activity, photoemission, and catalytic activity. In addition, the incorporation of nanoparticles in membranes enhances mechanical properties, hydrophilicity and separation properties<sup>64</sup>, making them ideal additives which lessen the mass transfer resistance for water permeation through membranes. Several metal and metal oxide nanoparticles, *i.e.*, silica (SiO<sub>2</sub>), titanium dioxide (TiO<sub>2</sub>), silver and aluminium nanoparticles, have been incorporated into a polymeric matrix to fabricate nanofiltration membranes to improve the membrane performances. For example, flux and rejection, mechanical and thermal stability, and anti-fouling and/or anti-bacteria properties<sup>65</sup>.



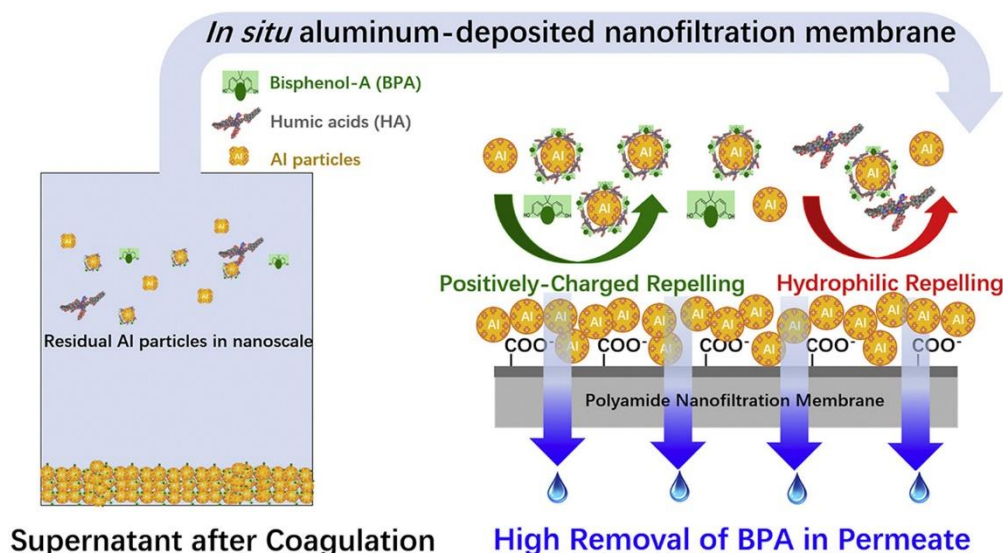


**Figure 1.7** Schematic illustration showing an example of the improvement of nanofiltration performance on micropollutant removal and reduction of membrane fouling by hydrolysed-aluminium nanoparticles. Reprinted from Elsevier with permission.

Babak Rajaeian *et al.*<sup>66</sup> utilised functionalised inorganic nanoparticles to increase the product flux and the separation efficiency. In their study, thin film nanocomposite nanofiltration membranes were prepared via interfacial incorporation of aminosilanised TiO<sub>2</sub> nanoparticles. TiO<sub>2</sub> nanoparticles were incorporated in pure and functionalized forms into trimesoyl chloride organic phase and *m*-phenylenediamine aqueous phase. Zinatizadeh *et al.*<sup>67</sup> prepared a nanofiltration membrane containing carboxymethyl chitosan-coated Fe<sub>3</sub>O<sub>4</sub> nanoparticles, and the retention of Direct Red 16 dye improved from 88% to 99% compared to the nascent membrane. The blended nanoparticle membrane also showed an improved antifouling property with 6.4 times. An in situ hydrolysed-aluminum-deposited membrane, as is shown in **Figure 1.7**, has been demonstrated by Ma *et al.*<sup>68</sup> with improved membrane hydrophilicity, roughness and positively-charging capacity. The percentage removal of the micropollutant, bisphenol-A, was improved to be 88.5%. Moreover, the loosely hydrophilic deposition on the membrane surface successfully alleviated membrane fouling, which was reduced by 2.13 times. Another example was reported by Huang *et al.*<sup>69</sup>, who embedded hollow silica nanoparticles in nanofiltration polyamide membranes by adding them to the interfacial polymerisation reactions. The modified membranes exhibited higher hydrophilicity, along with a great water flux of  $90 \pm 3$  L/m<sup>2</sup> h (6 bar), and the rejection of different salts followed the trend: Na<sub>2</sub>SO<sub>4</sub> (92%) > MgSO<sub>4</sub> (70%) > MgCl<sub>2</sub> (14%) > NaCl (11%).

### 1.3.4 Zeolites and Zeolitic Imidazolate Framework Membranes

Materials with porous frameworks have been developed in the areas of host-guest chemistry, gas storage, separations, and catalysis. Frameworks are well-known and established molecular architectures<sup>70</sup>, and the networks can be 1-dimensional, 2-dimensional or 3-dimensional<sup>70</sup>. The initial discovery of the framework materials can be traced back to zeolites, with the first scientific report of a zeolite by a mineralogist Cronstedt from mineral stilbite (“boiling stones”) in 1756<sup>71</sup>.

Zeolites are hydrated, crystalline tectoaluminosilicates constructed from  $TO_4$  tetrahedra (T = tetrahedral atom, e.g., Si, Al)<sup>72</sup>. Although zeolite materials have been found in nature, they can be synthesized in the laboratory<sup>73</sup>. The typical zeolite framework structures are shown in **Figure 1.8**. The International Zeolite Association monitors verifiable discovery and synthesis of new minerals and materials to associate the new compounds with existing framework types<sup>74</sup>.

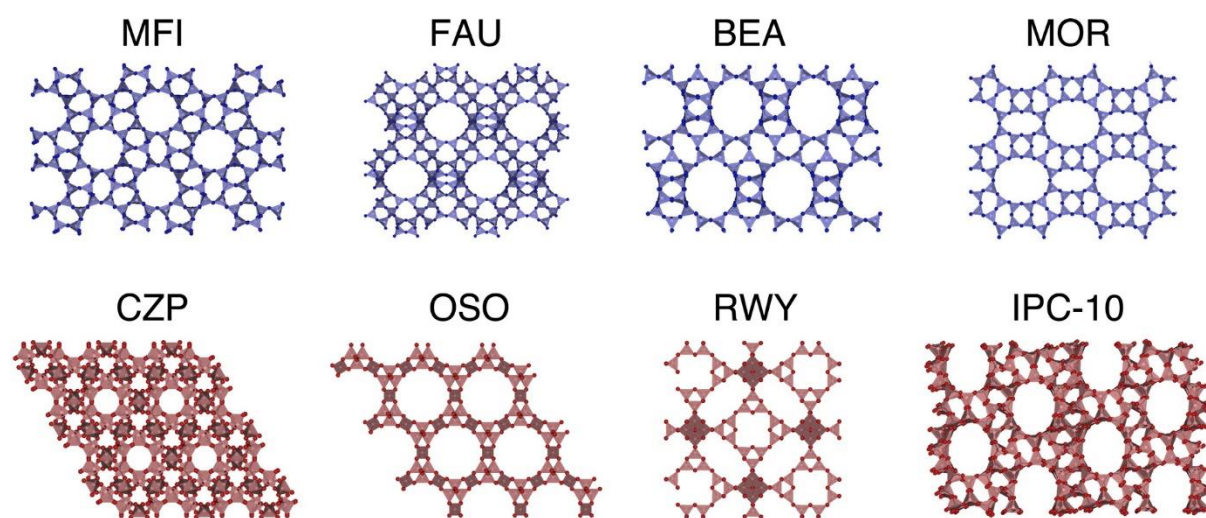


**Figure 1.8** Selected zeolite framework structures. Reprinted from reference<sup>71</sup> with permission.

The close connection between the microscopic structure and the macroscopic properties of these materials allows them to be used as molecular sieves to recognize, discriminate, and organize molecules with precisions that can be less than  $1 \text{ \AA}$ <sup>75</sup>. As a result, Zeolites have attracted widespread applications in diverse fields of molecular recognition phenomena, such as ion exchange, separations, and catalysis<sup>76</sup>. With additional advantages like thermal stability, solvent and chemistry stability, sterilization ability and biocompatibility, there has been an increasing interest in utilising zeolite materials in separation membranes<sup>77</sup>.

Zeolite membranes combine the general advantages of inorganic membranes, such as temperature stability and solvent resistance, with an ideal shape selectivity. Due to their “molecular sieve” function, zeolite membranes can principally discriminate liquid gaseous or mixtures components based on their molecular sizes<sup>78</sup>. For example, zeolite membranes with long-term stability have been considered ideal candidates for desalination<sup>79</sup>. In these membranes, ions have effects on infiltrating the zeolite material and altering its size-selective property<sup>80</sup>.

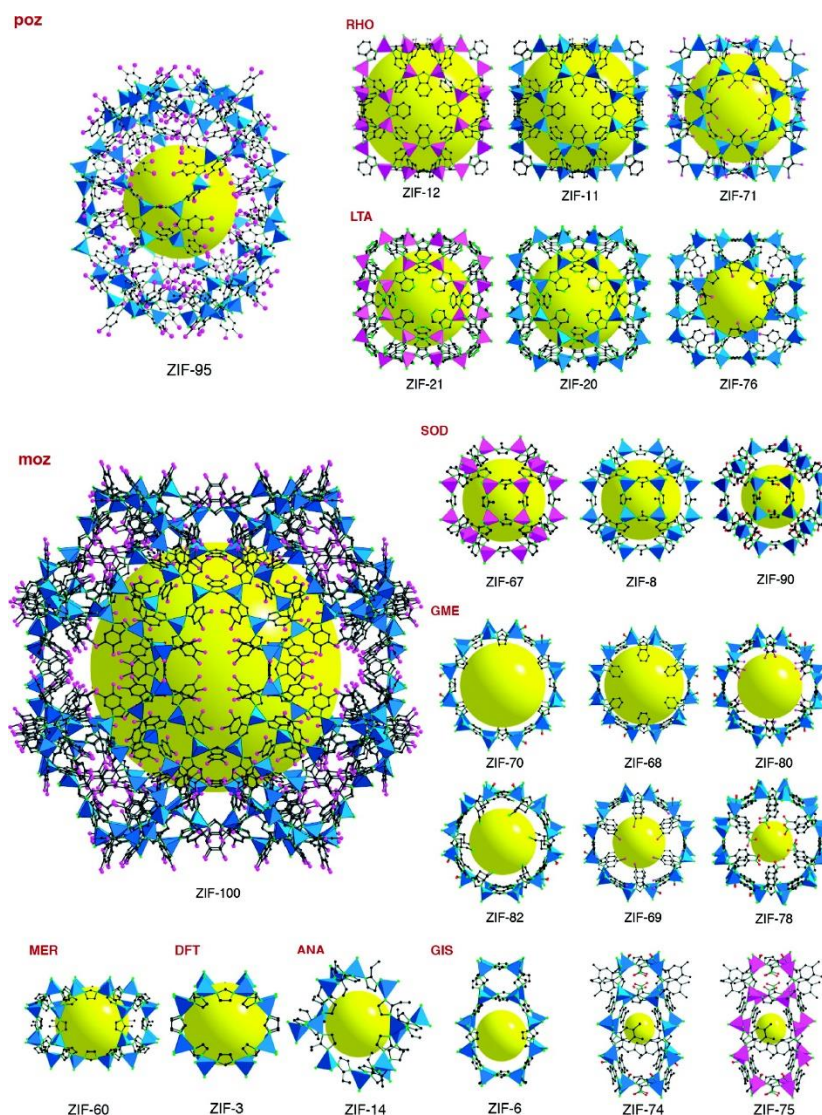


**Figure 1.9** Crystal structures of ZIFs and grouped according to their topology (three-letter symbol). The largest cage in each ZIF is shown with  $ZnN_4$  in blue and  $CoN_4$  in pink polyhedra, and the links in ball-and-stick presentation. The yellow ball indicates space in the cage. H atoms are omitted for clarity (C, black; N, green; O, red; Cl, pink). Reprinted from reference<sup>81</sup> with permission. Copyright 2010 American Chemical Society.



A primary current goal in zeolite chemistry is to create a structure in which metal ions and functionalised organic units can make up an integral part of the framework. Such a structure, by virtue of the flexibility with which metal ions and organic moieties can be varied, has been widely considered as a key to further improving zeolite properties and accessing new applications. Zeolitic imidazolate frameworks (ZIFs) are a class of porous crystals with extended 3-dimensional structures constructed from tetrahedral metal ions (e.g., Zn, Co) bridged by imidazolate. A large number of crystalline ZIFs have been discovered and synthesised by combining metal salts with imidazole in solution and are shown in **Figure 1.9** grouped according to their topology<sup>82</sup>. Remarkably, these ZIF materials exhibit permanent porosity and high thermal and chemical stability, which make them attractive candidates for many applications such as separation and storage of gases<sup>81,83,84</sup>.

Practically, ZIFs have a flexible structure, controllable pore size, and thus adjustable properties, which make them effective materials for membrane separation. ZIF-based membranes have been applied in pervaporation, nanofiltration, reverse osmosis and gas separation processes<sup>85</sup>. The diversity of the size of pores of ZIF within the size range of many vital gases has made the separation of different gases with different pore sizes possible<sup>86,87</sup>.

Incorporating ZIFs into a polymer to fabricate hybrid membranes has experimentally been proven as a practical approach to breaking the trade-off between permeability and selectivity. For example, Zhan Wang *et al.*<sup>84</sup> demonstrates a ZIF hybrid NF membrane with enhanced selectivity for dye removal, fabricated by a combination of self-assembly and interfacial reaction method. Positively charged polyethyleneimine (PEI) molecules and zinc ions were first deposited on the negative charged hydrolyzed polyacrylonitrile substrate by electrostatic attraction (self-assembly), and zeolitic imidazolate framework-8 (ZIF-8) particles were then in-situ formed on the PEI layer via interfacial reaction, thereby forming a thin and uniform ZIF-8/PEI hybrid membrane. This approach was used to prepare a membrane that possessed high permeance of up to  $33.0 \text{ L m}^{-2} \text{ h}^{-1} \text{ bar}^{-1}$ , with a rejection of 99.6% for methyl blue aqueous solutions<sup>84</sup>. Fusheng Pan *et al.*<sup>88</sup> reported a hybrid membrane incorporating multi-functional hollow ZIF-8 has dramatically intensified the diffusion process of water molecules, owing to their well-designed hierarchical structures (**Figure 1.10**). When utilised to separate 90 wt% ethanol aqueous solution at 76 °C, the hybrid membrane displays the highest separation performance with permeation flux of  $2485 \text{ g/m}^2\text{h}$  and separation factor of 1884. A novel nanoconfined composite membrane was invented by Naixin Wang *et al.*<sup>89</sup> to control the size and dispersion of ZIF particles in the polymeric matrix, where the nanopores in the substrate

membrane were used as a template to confine the formation of ZIF particles. A membrane of a thin layer of ZIF-11 on a substrate had a water flux ( $464 \text{ L}\cdot\text{m}^{-2}\cdot\text{h}^{-1}\cdot\text{MPa}^{-1}$ ), which is much higher than most other nanofiltration membranes, and the ZIF-11 membrane showed an excellent rejection (98.4%) to methyl blue dye molecules.

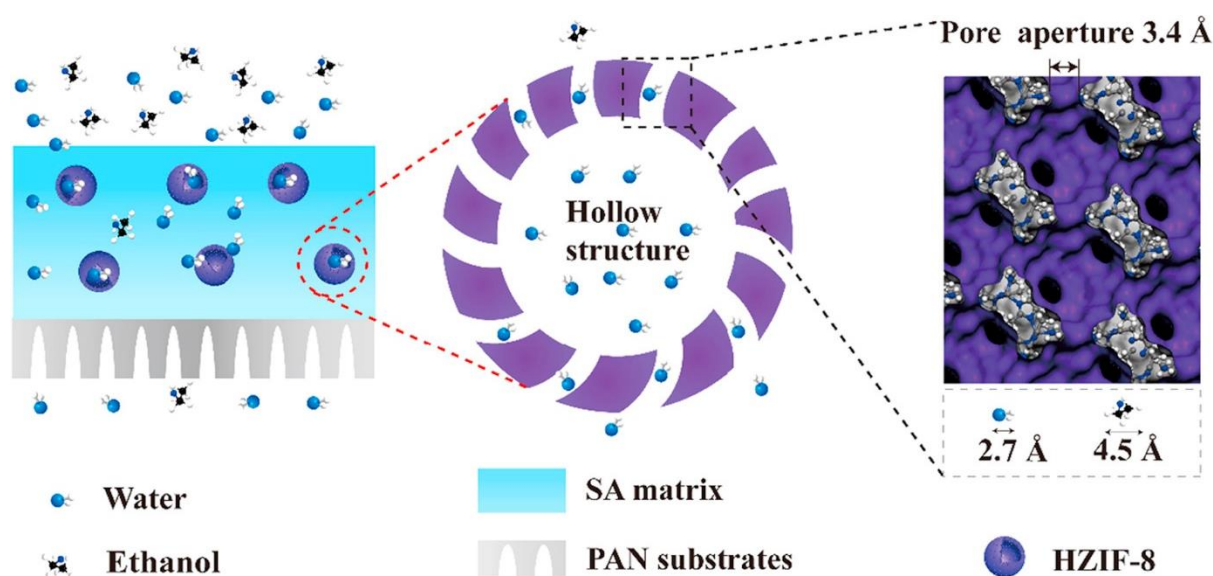


**Figure 1.10** Scheme of the selective for water and ethanol through a hybrid membrane incorporating multi-functional hollow ZIF-8 nanospheres. Reprinted from reference<sup>88</sup> with permission.

### 1.3.5 Metal-Organic Framework Membranes

ZIFs are a sub-class of metal-organic frameworks (MOFs). More generally, MOFs are hybrid materials with crystalline networks, composed of organic ligands co-ordinated to metal clusters (metal "nodes" connected via organic "linkers"), to generate infinite framework materials that remain permanently porous<sup>90</sup>. The first MOFs were reported in 1999 by Williams *et al.* and Yaghi *et al.*, known as HKUST-1<sup>91</sup>, containing copper-based clusters and benzene tricarboxylate linkers, and MOF-5 ( $\text{Zn}_4\text{O}(\text{BDC})_3\cdot(\text{DMF})_8(\text{C}_6\text{H}_5\text{Cl})$ )<sup>92</sup>, containing zinc-based clusters and benzene dicarboxylate linkers.

MOFs are synthesised using bridging organic ligands, which are coordinated to metals, forming infinite framework structures<sup>93,94</sup>. As an important candidate among the porous material family, tens of thousands of different MOFs have been generated<sup>93-99</sup>, with representative MOF examples are shown in **Figure 1.11**.

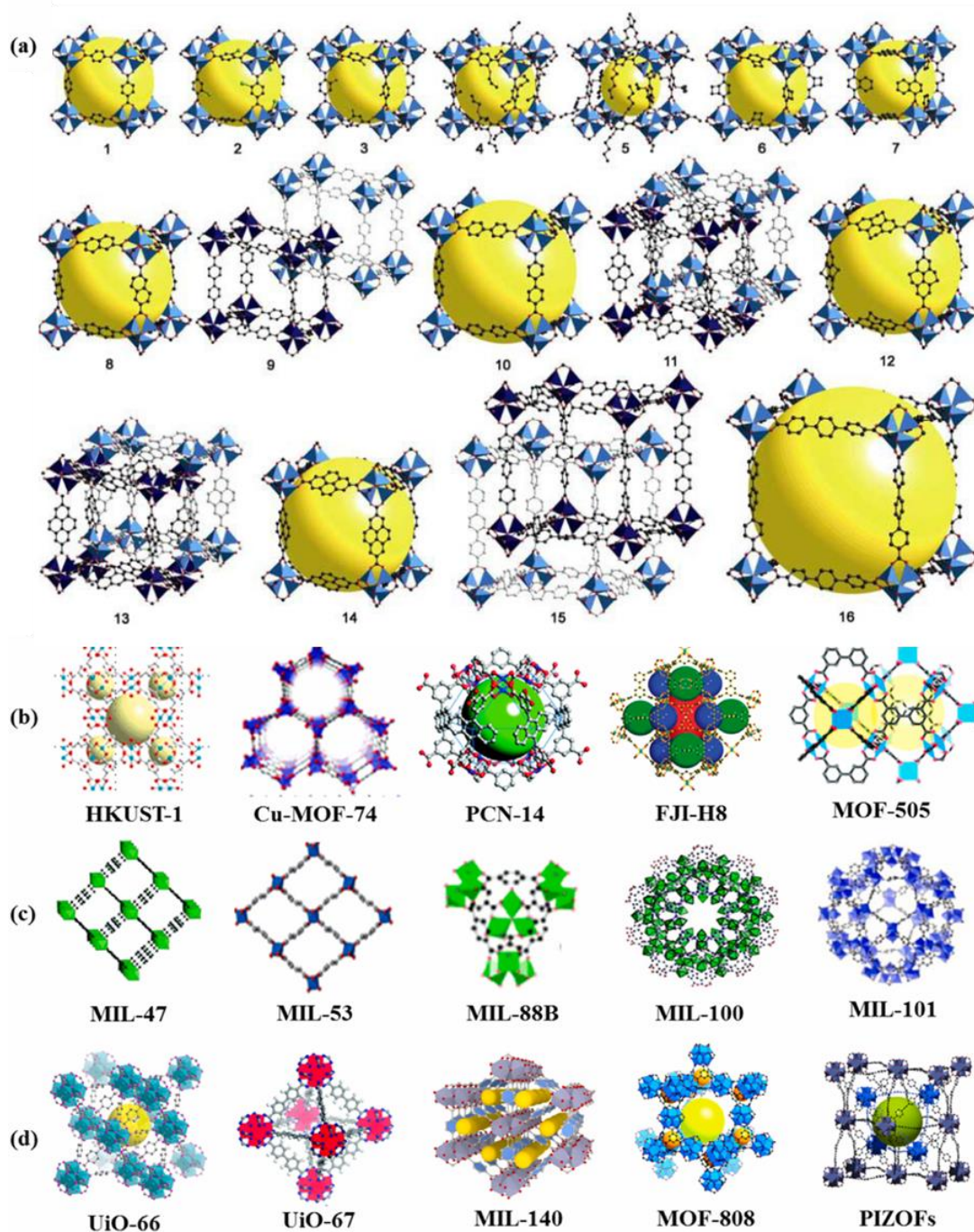


**Figure 1.11** The 3D structures of MOFs with different metal clusters. (a) A series of the isoreticular metal–organic frameworks (IRMOFs) with different functional organic linkers has been produced in which each member shares the same cubic topology. The yellow spheres represent the internal voids. The extended organic linker increases the internal void and it also allows the formation of a catenated structure. Reprinted from reference<sup>97</sup> with permission. (b)–(d) Other representative MOFs. Reprinted from reference<sup>99</sup> with permission.

Unlike zeolites, the channel linings can be chemically functionalized; for example, the aqua ligands can be replaced by pyridines<sup>91</sup>. The size of the pores in MOFs can be determined by the length of the ligand linker used, i.e., the longer the linker, the larger the pore. As a result, adjusting the chemistry and size of the two components helps customise the crystal pores and, thus, tailor the material for a given application. Therefore, MOFs are widely regarded as promising materials for applications in catalysis, separation, gas storage and molecular recognition<sup>100–109</sup>.

MOF-based membranes have shown an excellent gas separation performance in many previous reports<sup>110–113</sup>. More recently, MOFs are emerging as great potential porous nanomaterials for preparing nanofiltration membranes<sup>114–116</sup>. In addition to a high surface area and pore volume, their chemical structure, surface properties and particle size can be easily tuned in order to satisfy the demands of membrane fabrication and specific applications<sup>65</sup>.

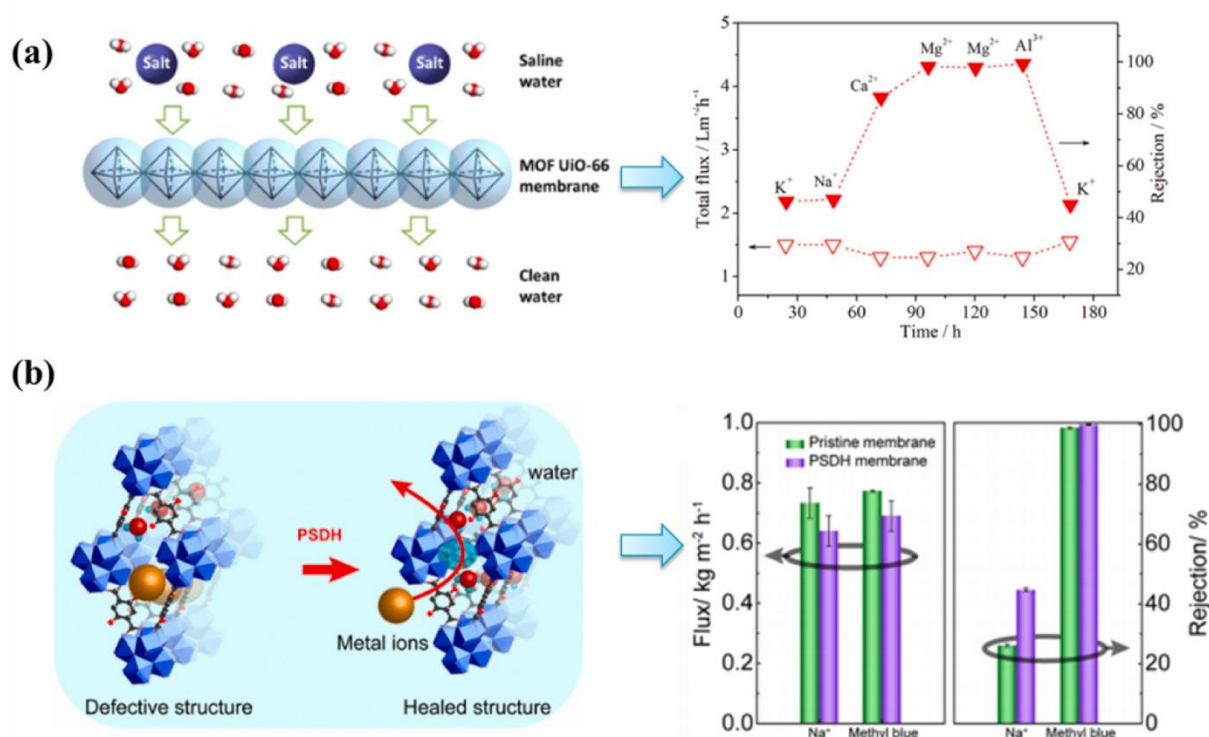


**Figure 1.12** Examples of desalination using MOF membranes. (a) Desalination performance of the UiO-66 membrane. Reprinted from reference<sup>117</sup> with permission. Copyright 2015 American Chemical Society. (b) Scheme of post synthetic defect healing by relinking two adjacent Zr<sub>6</sub>O<sub>4</sub>(OH)<sub>4</sub> clusters (blue polyhedron) by one ligand, and separation performance of the membrane. Reprinted from reference<sup>118</sup> with permission. Copyright 2017 American Chemical Society.



Thin film nanocomposite membranes based on MOFs have been applied for desalination as well as organic solvent nanofiltration with high flux. Livingston *et al.*<sup>119</sup> have fabricated a series of thin film nanocomposite membranes containing a range of 50–150 nm MOFs via in-situ interfacial polymerization on top of the cross-linked polyimide porous supports. It was found that these porous MOFs provided preferential flow paths for the solvents, whilst the polyamide layer surrounding MOFs maintained a high solute rejection. As a result, these membranes exhibited increased solvent permeance compared to the pristine polyamide support membrane without sacrificing rejection. Li *et al.*<sup>117</sup> have synthesized UiO-66 to prepare continuous MOF-based membranes for water softening applications. As is shown in **Figure 1.12(a)**, the membrane showed high rejections for multivalent ions (*e.g.*, 86.3% for Ca<sup>2+</sup>, 98.0% for Mg<sup>2+</sup>, and 99.3% for Al<sup>3+</sup>), moderate water permeation flux (0.14 L m<sup>-2</sup> h<sup>-1</sup> bar<sup>-1</sup>), and competitive permeability (0.28 L m<sup>-2</sup> h<sup>-1</sup> bar<sup>-1</sup> μm). Zhao *et al.*<sup>118</sup> further presented a highly selective water treatment Zr-MOF membrane, which increased the Na<sup>+</sup> rejection of the membrane by 74.9% and resulted in excellent hydrothermal stability in aqueous solutions (>600 h) (**Figure 1.12(b)**).

### 1.3.6 Covalent Organic Framework Membranes

Covalent Organic Frameworks (COFs) are an emerging class of porous organic material, with well-defined, crystalline porous structures composed of lightweight elements (C, O, B, Si and N) linked by robust covalent bonds. COFs are synthesized by the reversible self-condensation of boronic acids or boronic acids and alcohols, producing water as a by-product to produce strong B-O bonds<sup>120</sup>. These boroxine rings can be viewed as the organic analogues of metal clusters that are seen among MOFs. To obtain a crystalline and ordered structure, the building blocks are required to react under the dynamic covalent bond control with appropriate conformation and rigidity to enforce directional-bond formation<sup>121</sup>.

Originally discovered in 2005 by Yaghi *et al.*<sup>122</sup>, the first reported COFs, 2-D COF-1 and COF-5 have been successfully prepared via boroxine and boronate ester bond formation. COF-1 was synthesized by reversible self-condensation of 1,4-benzenediboronic acid, giving a staggered layer framework linked by planar boroxine rings. COF-5 was synthesized by the condensation of the same boronic acid reagent along with hexahydroxy triphenylene, which produced an eclipsed framework structure (see the structures of COF-1 and COF-5 in **Figure 1.13**). The two COFs demonstrated permanent porosities with high thermal stabilities. Since then, a range of

COF materials have been reported using various approaches<sup>123</sup>, with the examples shown in **Figure 1.13**. The variation of building blocks with different geometries and sizes determines the structures and features of a specific COF<sup>124</sup>. A series of COFs with 3-D architectures have been prepared by the self-condensation and co-condensation reactions of the rigid molecular building blocks, tetrahedral and triangular monomers (see the structures of COF-102 and COF-103 in **Figure 1.13**).

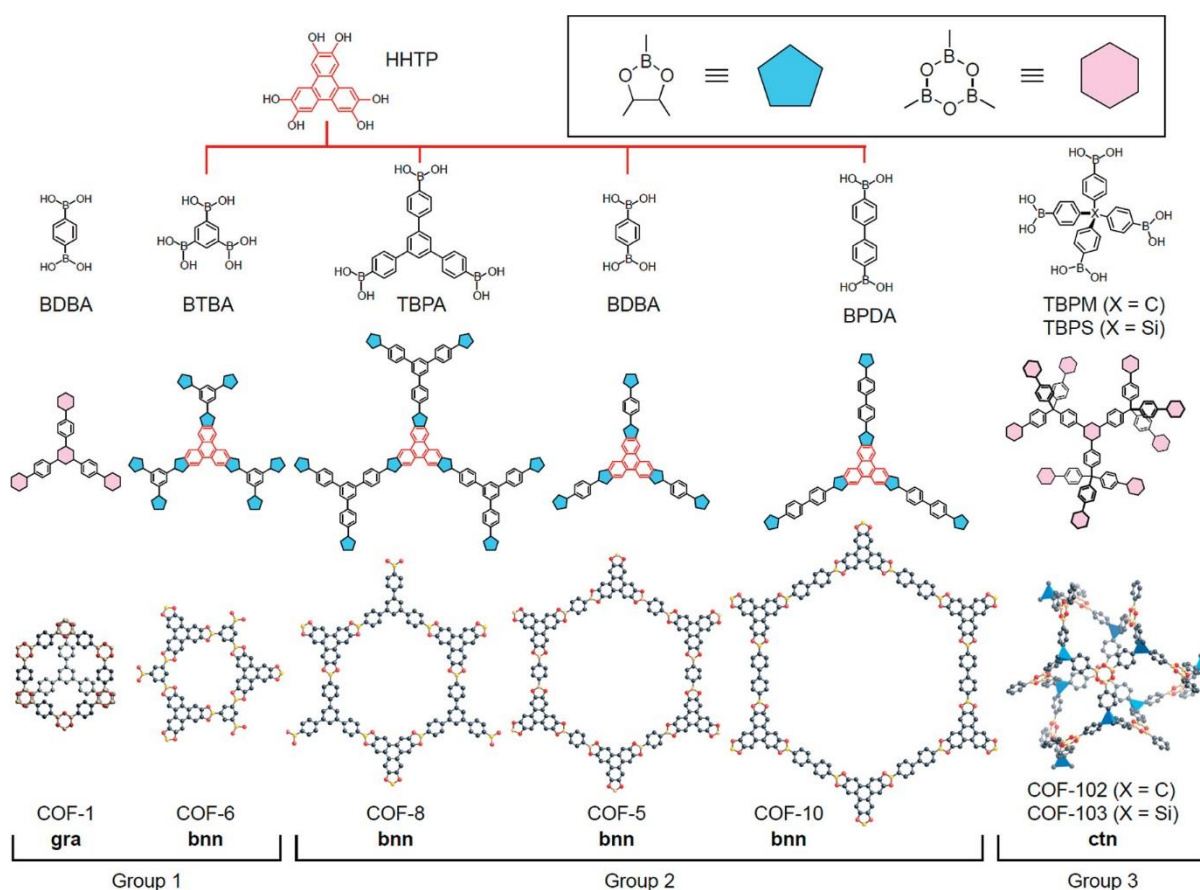


**Figure 1.13** Condensation reactions of boronic acids and 2,3,6,7,10,11-hexahydroxytriphenylene used to produce COFs (top), resulting in fragments of the COFs (middle), and atomic connectivity and structure of crystalline products of 2D and 3D COFs (bottom). Reprinted from reference<sup>123</sup> with permission by 2009 American Chemical Society.

Since these materials are entirely constructed from strong covalent bonds (C-C, C-O, C-B, and B-O), they exhibited high thermal stabilities (400° to 500 °C), high surface areas (3472 and 4210 m<sup>2</sup> g<sup>-1</sup> for COF-102 and COF-103, respectively) and extremely low crystal densities (0.17 cm<sup>3</sup>g<sup>-1</sup>)<sup>125</sup>. With lower densities than MOFs, COFs show higher gas uptakes due to the large pore volumes coupled with low densities. As the unique architectures endow such material with desirable properties, i.e., inherent porosity, large surface area, high stability, versatile

chemical composition, and multi-dimension, COFs, therefore, have been considered as good candidates for energy storage<sup>126</sup>, organic molecules adsorption<sup>127</sup>, catalysis<sup>124</sup>, as well as semi-conducting and photo-conducting materials<sup>128</sup>. Furthermore, 2-dimensional COFs have great promise for separation applications because of their well-defined pore aperture, ordered channel structure, and permanent porosity<sup>129</sup>.

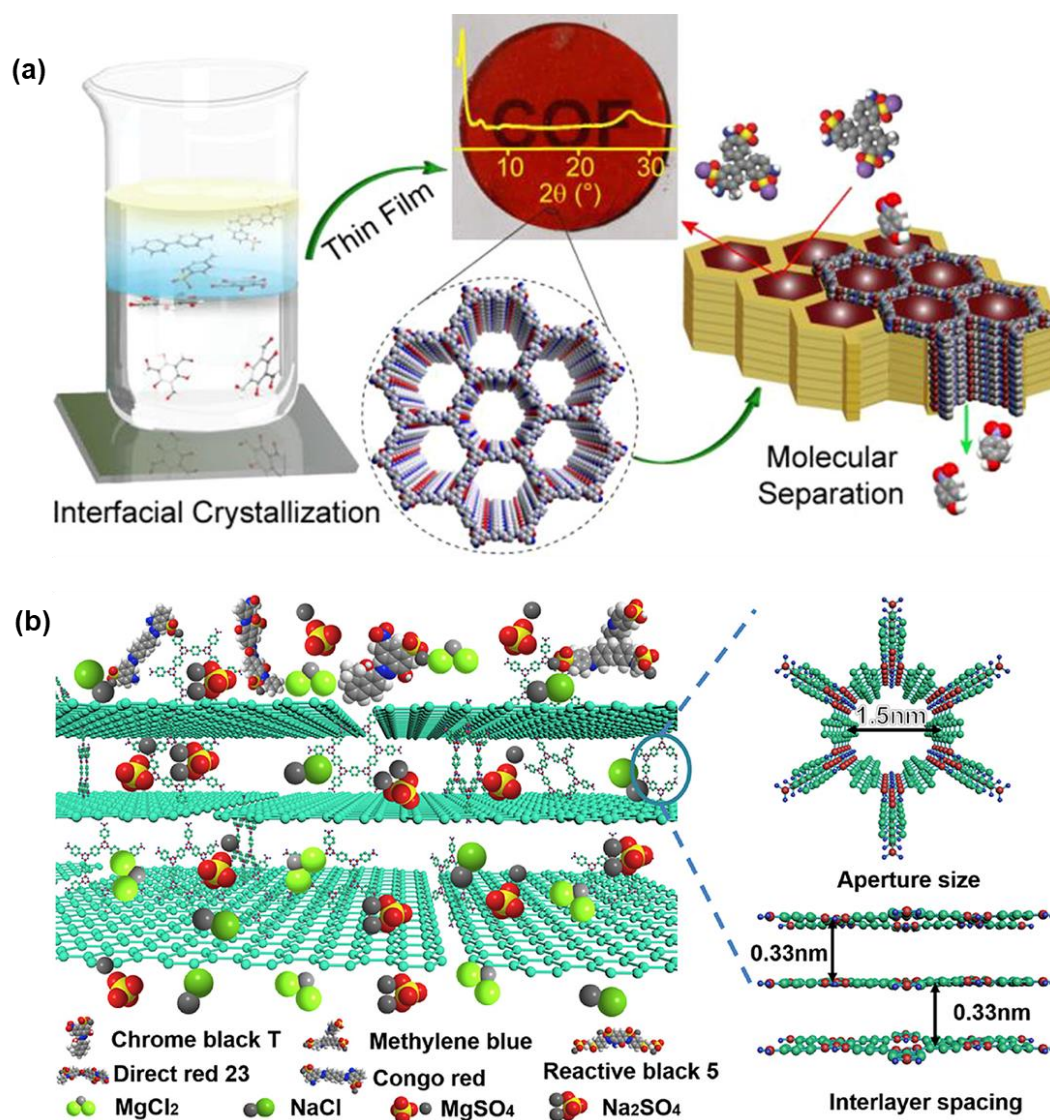


**Figure 1.14** Examples of two COF membranes for molecular separation. (a) Crystalline COF thin films prepared by interfacial synthesis for molecular separation. Reprinted from reference<sup>7</sup> with permission by American Chemical Society. (b) COF-1/GO nanocomposites as the membrane material for dye removal. Reprinted from reference<sup>130</sup> with permission.

In recent years, as they are highly compatible with polymers<sup>131</sup>, COFs have been applied to obtain defect-free membranes with enhanced separation performance, for gas separation<sup>132–135</sup>, organic solvent nanofiltration<sup>136,137</sup>, and water purification<sup>7,130,138,139</sup>. Different from graphene,

COFs with intrinsic nanopores (0.5 to 4.7 nm) can serve as the channels for molecular transport<sup>140</sup>. Therefore, these COF membranes exhibit recyclability and retain their structural integrity in water, organic solvents, and mineral acids<sup>141</sup>.

To separate molecular dyes, Ma *et al.*<sup>138</sup> demonstrated a bottom-up interfacial crystallisation method to synthesize a cationic COF by combining the cationic monomer with the Schiff base reaction, and the continuous COF membrane was further prepared by a facial vacuum filtration with controlled thickness. The prepared membrane obtained a dye rejection of 99.6%, 99.2%, and 98.1% for Rhodamine B, Methylene Blue, and N,N-dimethyl-p-phenylenediamine dihydrochloride, respectively. For neutral dyes, the rejection rates were found to be 22.3%, 74.4%, and 15.7% for Nile Red, Calcein, and p-Nitroaniline, respectively, where the pore size sieving effect played a dominant role rather than the static electric effect in this case. It was shown by Lai *et al.* that the effective molecular size for dyes depends on the smallest projection size<sup>139</sup>. Also, Banerjee *et al.*<sup>7</sup> reported a series of crystalline COF thin films by interfacial synthesis with pore sizes ranging from 14-26 Å, and they showed good performance in nanofiltration dye rejection studies after being deposited between macroporous polyester (**Figure 1.14(a)**). Zhang *et al.*<sup>130</sup> prepared COF-1/GO nanocomposites as the membrane material for dye removal. The obtained membranes achieved high performance with a water permeation of 310 L m<sup>-2</sup> h<sup>-1</sup>MPa<sup>-1</sup> with the dye rejection of 99% (**Figure 1.14(b)**). Dichtel *et al.*<sup>142</sup> fabricated a thin-film COF composite prepared using a 2D COF with 3.4 nm sized hexagonal pore performed, which was used for nanofiltration application.

### 1.3.7 Hydrogen-bonded Organic Framework Membranes

More recently, a novel type of porous crystalline solids, hydrogen-bonded organic frameworks (HOFs), have attracted increasing interest as molecular sieving materials from researchers<sup>143–145</sup>, although they have been known for decades. These porous HOF materials are assembled by organic or metal-organic building blocks through hydrogen-bonding interactions, which interact with one another, forming a supramolecular assembly<sup>146,147</sup>. Desiraju<sup>148</sup> introduced the concept for constructing porous HOF materials using hydrogen-bonding interactions in 1995, by taking advantage of H-bonding tectons for crystal engineering in supramolecular materials. A key milestone of HOF chemistry is the establishment of the microporosity of HOF materials around 2010<sup>149,150</sup>, which significantly expanded the exploration of new HOFs for applications in various fields. In 2012, Mastalerz *et al.*<sup>151</sup> reported a HOF with an ultra-high Brunauer



Emmett Teller Surface Area ( $S_{\text{BET}}$ ) of  $2796 \text{ m}^2\text{g}^{-1}$ . **Figure 1.15** shows the representative examples of the construction of porous HOFs.

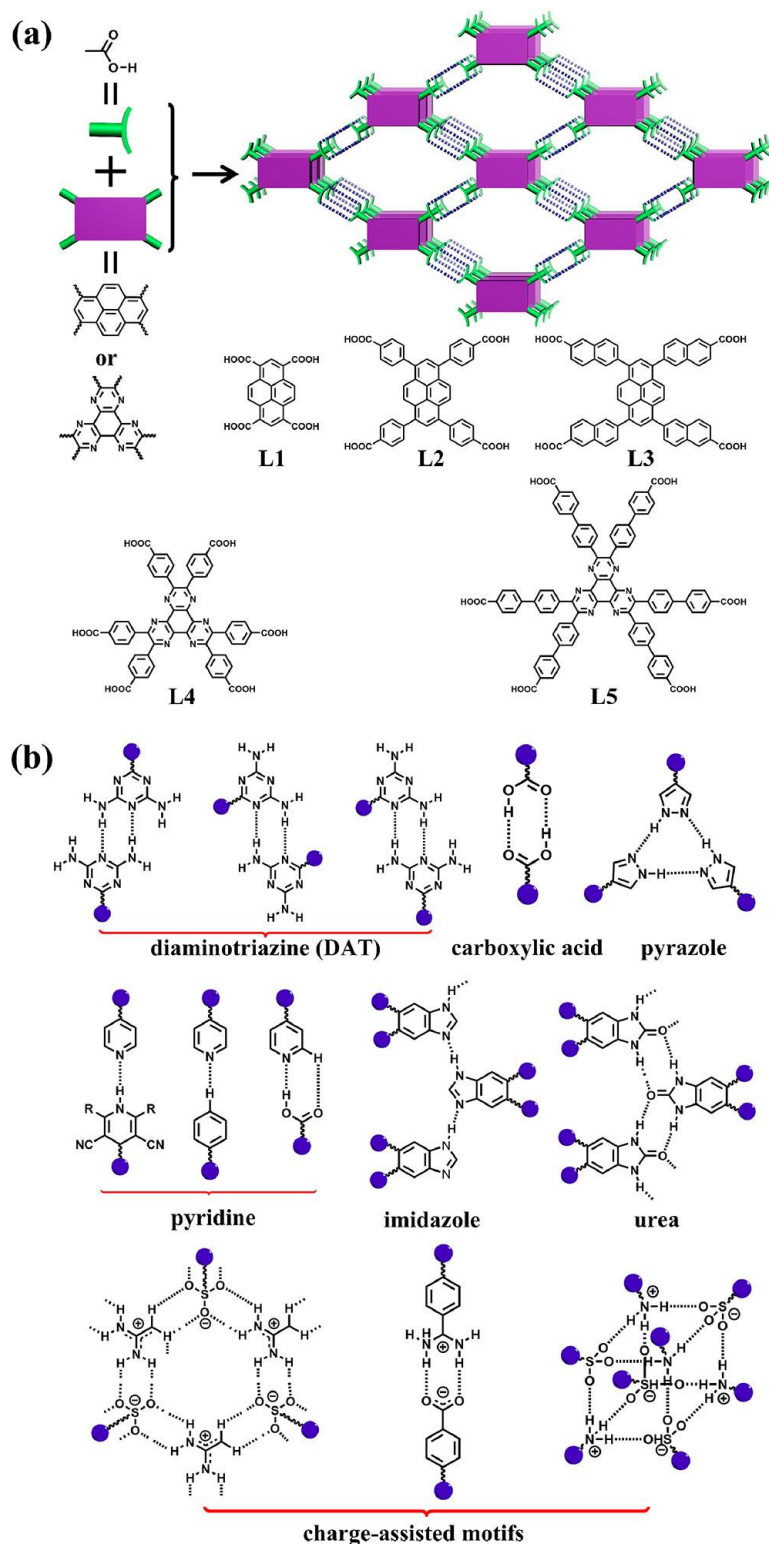


**Figure 1.15** (a) Reticular construction of HOFs. (b) H-bonding motifs used for the construction of porous HOFs. Reprinted from reference<sup>143</sup> with permission by American Chemical Society.

To achieve permanent porosity in HOF materials, stable and robust open frameworks can be constructed by the use of rigid molecular building blocks and hydrogen-bonded units via strong H-bonding interactions. The stability of the HOFs can be further improved by framework interpenetration or other types of weak intermolecular interactions such as  $\pi \cdots \pi$  interactions<sup>152</sup>. As a result, HOFs can be fine-tuned for host-guest chemistry by judicious selection of building blocks of a specific size. The pores can be therefore tailored for a desired guest<sup>153</sup>. In addition, HOFs have improved solubility compared with other organic framework materials, such as COFs. Owing to the reversible and flexible nature of H-bonding connections, HOF materials have shown unique features such as mild synthesis condition, high crystallinity, solution processability, easy healing, and regeneration<sup>143</sup>. They can also be environmentally friendly lightweight porous materials without heavy or transition metal species in the network<sup>152</sup>. These advantages enable HOFs to be considered as multi-functional porous materials for various applications, including gas separation and storage<sup>154–157</sup>, catalysis<sup>158,159</sup>, proton conduction<sup>160,161</sup> as well as membrane-based molecular separations.

Combining the solubility of polymers with the porosity of ordered porous materials, HOFs are promising membrane materials. Sun *et al.*<sup>155</sup> reported the fabrication of a HOF membrane through solution processing, which was used for pressure-regulated H<sub>2</sub>/N<sub>2</sub> separation and possessed a separation factor of 19.5 with good mechanical and thermal stability. However, the applications in liquid-phase molecular separation, such as nanofiltration, haven't been widely explored using HOF membranes. One example, recently reported by Liu *et al.*<sup>162</sup> in 2021, is a HOF membrane fabricated based on a thin-film nanocomposite membrane containing porous HOF nanoparticles. The prepared membranes showed ultra-high water permeability (546.1 L m<sup>-2</sup> h<sup>-1</sup> bar<sup>-1</sup>) with a reasonable rejection of organic dye molecules (95.9% for Congo red, 96.5% for brilliant blue, 97.2% for rhodamine B, and 83.7% for methyl blue).

### 1.3.8 Porous Organic Polymer Membranes

Apart from the crystalline extended porous structures, another classification includes porous organic polymers (POPs), highly cross-linked, amorphous polymers possessing micropores<sup>163–165</sup>. This constitutes a broad area, from covalent triazine frameworks (CTFs)<sup>163,166,167</sup>, hyper-cross-linked polymers (HCPs), to conjugated microporous polymers (CMPs)<sup>163,168–171</sup>, and polymers of intrinsic microporosity (PIMs). One example of a POP was PAF-1 (shown in **Figure 1.16**), synthesised by Ben *et al.*<sup>172</sup> using theoretical simulations to design the structure

of the porous aromatic framework. This extended network, consisting of a diamond-like structure with covalent C-C single bonds replaced with phenyl rings, had shown an insoluble amorphous framework with robust internal cavities. As a result, PAF-1 was thermally stable (up to 520 °C), and its high Brunauer-Emmett-Teller surface area ( $SA_{\text{BET}} = 5600 \text{ m}^2 \text{ g}^{-1}$ ) also contributed to an increased uptake capacity for gases, such as  $\text{H}_2$  (10.7 wt%), and  $\text{CO}_2$  (1300  $\text{mg g}^{-1}$ ).

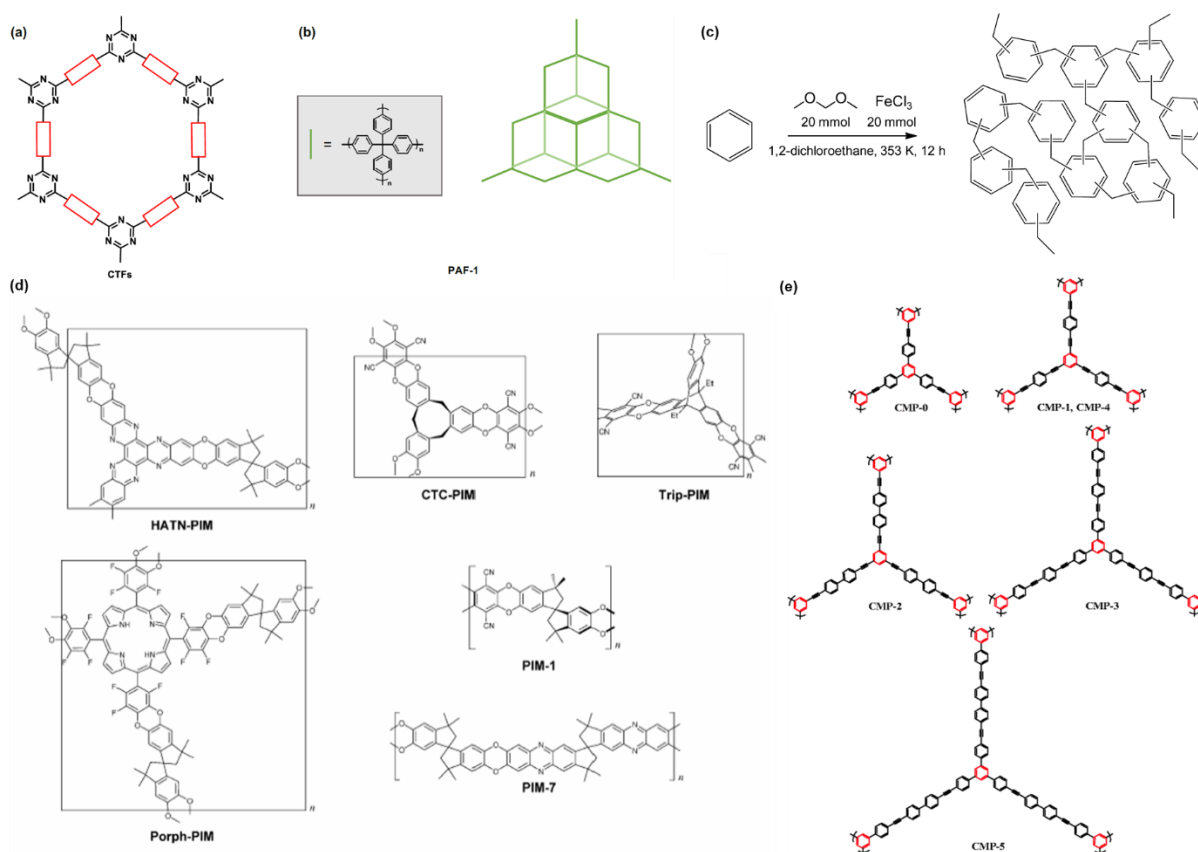


**Figure 1.16** Structure of common porous organic polymers: (a) general structure for CTFs, which can be connected by a variety of linkers<sup>173</sup>, and (b) the extended structure for the porous aromatic framework, PAF-1, with the structure of the linker<sup>172</sup>. Figures cited from PhD thesis repository<sup>174</sup>. (c) Reaction scheme for the synthesis of a microporous “knitted” HCP network. Reprinted from reference<sup>175</sup> with permission. (d) Molecular repeated units for linear and network PIMs: PIM-1 and PIM-7 are linear and soluble; HATN-PIM, CTC-PIM, Trip-PIM, Porph-PIM are insoluble networks; and (e) Molecular repeated units for CMPs (CMP-0 to CMP-5). Reprinted from reference<sup>176</sup> with permission.

One flaw of the irreversible chemistry of POPs is that these microporous materials are amorphous instead of crystalline, but the benefit is that these solids can show significant physical stability. Therefore, POPs have been considered a versatile platform, not only for the

deployment of catalysts<sup>163</sup>, but also promising for the design of high-performing membranes, thanks to their superior surface area, intrinsic mesoporous structures, and good polymer affinity<sup>177</sup>. With some examples using POPs as membrane materials, such as a microporous membrane comprising CMP with rigid backbones showing ultrafast organic-solvent nanofiltration ( $32 \text{ L m}^{-2} \text{ h}^{-1} \text{ bar}^{-1}$  for hexane)<sup>178</sup>, mixed-matrix membranes with size-controlled HCP additives enabling enhanced gas selectivity ( $\text{H}_2/\text{CH}_4 = +690\%$ )<sup>179</sup>, and a CTF membrane used for the robust and precise molecule/ion separation (water permeance  $\sim 140 \text{ L m}^{-2} \text{ h}^{-1}$ ; Methyl orange rejection  $>96\%$ )<sup>180</sup>; the most popular POP materials for membrane fabrication and relevant separation applications are the PIMs.

PIMs are robust, solution-processable, organic nanoporous materials<sup>181</sup>. As reported by McKeown and Budd<sup>182</sup>, these materials have rigid, contorted structures, where a large amount of interconnected free volume is created by inefficiently packing the polymeric chains. Most PIMs are synthesised using a highly efficient dibenzodioxane-forming reaction between a spirobisindane monomer and an o-dihalide monomer, based on a double-aromatic nucleophilic substitution mechanism to form the dibenzodioxin linkage. This polymerisation reaction provides the simultaneous formation of two covalent bonds, providing a linking group composed of fused rings, thus enabling the construction of ladder polymers of high average molecular mass<sup>183</sup>. The first PIM networks were prepared based on porphyrins and phthalocyanines<sup>184,185</sup>, with the structure of Porph-PIM shown in **Figure 1.16**.

PIMs can be synthesised to be insoluble networks or, uniquely, as soluble linear polymers. In contrast to other types of POP, PIMs are not comprised of a network of cross-linked covalent bonds so that they can be dissolved in organic solvents and processed into robust films, coatings or fibres.<sup>186</sup> Combining solution processability and microporosity with structural diversity, PIMs have proven utility for making membranes and sensors, being used for gas and vapour separations, organic nanofiltration, and pervaporation<sup>183</sup>. A series of PIMs-based gas separation membranes have been reported<sup>187-190</sup>. For example, two membranes prepared of PIM-1 and PIM-7 (see structures in **Figure 1.16**) have shown a significant separation performance for commercially important gas pairs, including  $\text{O}_2/\text{N}_2$  and  $\text{CO}_2/\text{CH}_4$ <sup>190</sup>. Offering excellent solvent resistance and stability, PIMs are widely used as high-performance organic solvent nanofiltration membranes<sup>191-194</sup>. Livingston *et al.*<sup>191</sup> have presented a membrane with ultrathin separation layers down to 35 nm in thickness fabricated from PIM-1, which exhibited a fast permeation of *n*-heptane with a rejection for hexaphenylbenzene of about 90%. **Figure 1.17(a)** shows a PIM-1 thin film composite membrane on the PAN support of 80 cm width,

which a 90% retention detected at below 200 g/mol at 30 bar<sup>192</sup>. Chung *et al.*<sup>193</sup> modified PIM-1 into thioamide-containing PIM-1 (TPIM) and prepared a membrane (as shown in **Figure 1.17(b)**) for dye NF separation with ethanol and acetone as the solvents. The rejection rate of obtained TFC membrane to Remazol Brilliant Blue R reached 90%, with the permeability of pure ethanol of 3.4 L·m<sup>-2</sup>·bar<sup>-1</sup>·h<sup>-1</sup>.

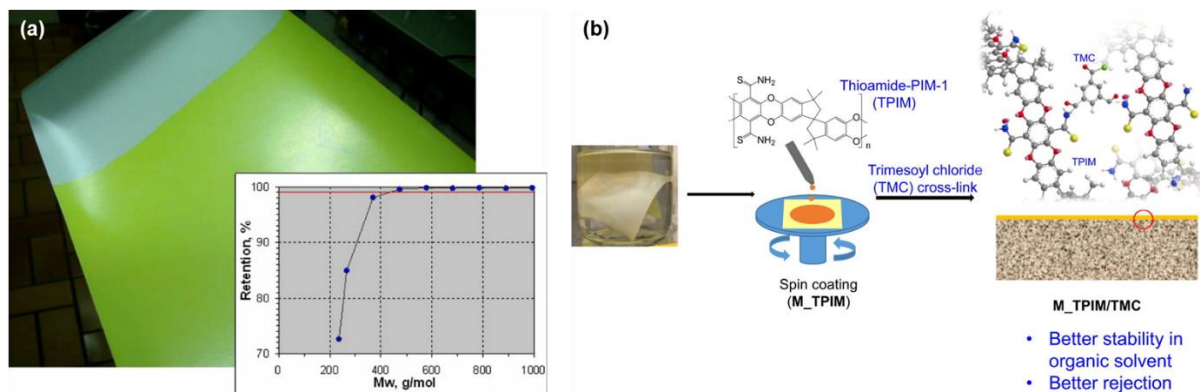


**Figure 1.17** Examples of PIM membranes. (a) A PIM-1 thin film composite membrane (yellow) on PAN support (uncoated, white) of 80 cm width, with its retention curve of in *n*-heptane measured with a polystyrene mixture. Reprinted from reference<sup>192</sup> with permission. (b) The formation of TPIM/TMC membranes and their structure. Reprinted from reference<sup>193</sup> with permission. Copyright 2018 Elsevier B.V.

### 1.3.9 Limitations and Challenges

The porous material field has rapidly developed in the last decade (**Figure 1.18**). However, challenges for these molecular sieving materials, such as fragile and not easily processable property, poor scalability, physical ageing and unknown toxicity for environmental impact, have restricted their comprehensive implementation in membrane fields.

GO usually suffer a poor compatibility with polymer membranes so that they might be easy to be peeled off in a high flow rate during the filtrations. The membranes incorporating nanoparticles or zeolites have been limited by the lower loading content, due to the low solubility of these particles. The growth regularity of MOFs and their stability within membranes are not well controlled to achieve high nanofiltration performance. For example, the inherent defects of UiO-66 due to ligand/cluster deletion affect the molecular sieving performance of UiO-66 membranes<sup>195</sup>. COF membranes contain pores that tend to be robust but are difficult to be scaled up and often have defects, and the processing techniques are

limited by their synthetic conditions. Long-term stability and the operation under high pressure of COF membranes have been rarely reported. HOFs building blocks are soluble, unlike COFs, but their porous low-density crystal packings tend to be metastable and are often unstable in humid environments. The POPs are robust for using as membranes, however the stability and the tuneability of the performance are limited as they don't have well-defined, crystalline structures.

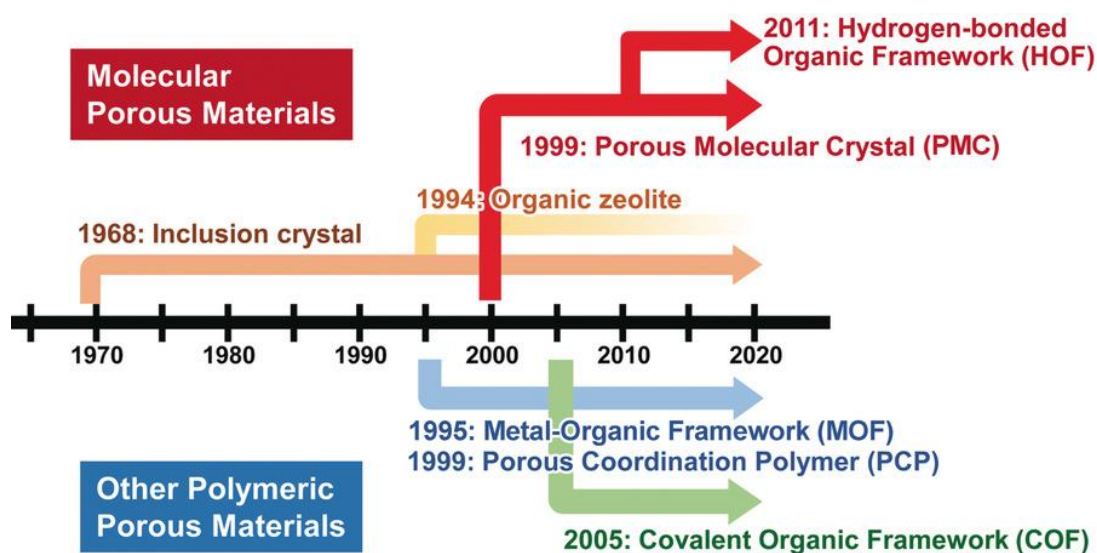


**Figure 1.18** Representative timeline for the development of types of porous molecular materials and related materials. Reprinted from reference<sup>146</sup> with permission.

In addition, these porous materials suffer usually from poor interfacial binding with the polymeric membrane matrix, and this may lead to nonselective molecular transport pathways on membranes. Largely unexplored is the potential of purely organic dispersed phases, comprising only C, H, N, and O atoms, which are expected to show better compatibility with a continuous polymeric matrix. More importantly, novel membrane materials with well-defined structures and tuneable pores would offer scope for tailoring the physical and chemical properties of the membranes through organic synthesis or post-treatment.

## 1.4 Porous Organic Cages (POCs)

### 1.4.1 Introduction of Porous Molecular Solids

Porous organic molecular solids are defined by their modular, molecular structures, and the absence of extended covalent or coordination bonding in the solid-state. Since their extended structures are generally prepared by processing the molecules after synthesis (typically by post synthesis



crystallisation), this distinguishes these materials from extended frameworks, such as MOFs and COFs, where synthesis and crystallization occur in the same step<sup>196</sup>.

Discrete porous organic solids have intrinsic pores, a guest-accessible cavity defined by covalent bonds that is prefabricated during synthesis<sup>197,198</sup>, and these materials have been shown to adsorb guests in their intrinsic cavities in the solid-state. As is shown in **Figure 1.19**, porous organic molecular solids with open, bowl- or ring-shaped, intrinsic cavities, like calix[n]arenes<sup>199,200</sup>, pillar[n]arenes<sup>201</sup>, and cucurbit[n]urils<sup>202</sup>, generally exhibit an open window with the same width as their intrinsic cavity. In this case, the guest accessibility depends on the size and chemistry of the intrinsic cavity, and how these cavities are arranged in their solid-state. Porous organic molecules with cage-like structures (such as porous POCs<sup>203</sup> and cryptophanes<sup>204</sup>), on the other hand, have shown a narrower window size compared to their intrinsic cavity; it is these windows in the molecular structures that control and regulate the guest diffusion into the intrinsic pores.

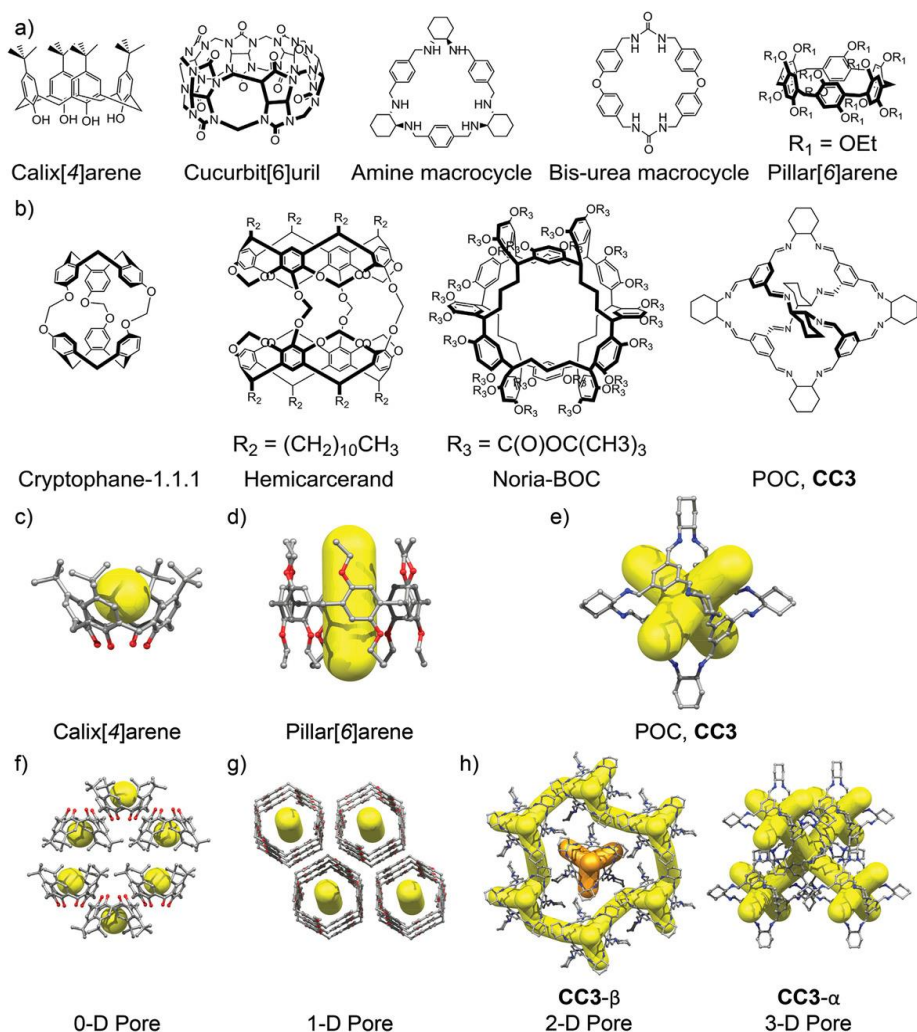


**Figure 1.19** Molecular structures of some organic compounds with a) open, and b) enclosed intrinsic pores. c–e) Different intrinsic pores in organic molecules can be used to modulate the

porosity in organic crystals; including, f) 0D pores for calix[4]arene, g) 1D pores for pillar[6]arene, and h) either 2D or 3D pores for the POC, CC3, depending on the crystallization conditions. Reprinted from reference<sup>196</sup> with permission.

Therefore, with the features of regulated guest accessibility, POCs, known as cage-like macrocyclic organic molecules, have proven to be an exciting new family of molecule sieving materials. These discrete molecular building blocks have intrinsic guest cavities, and the cages can be crystallised to form structures with different pore structures, which can contain additional extrinsic voids located outside of the cage cavity<sup>203</sup>.

#### 1.4.2 Structures and Porosity of Porous Organic Cages

The discovery of organic cages can be dated back to 1960s<sup>205</sup>. However, the measurements for their permanent porosity wasn't investigated in the early years. An important POC, Covalent cage 3 (CC3), synthesized through a reversible imine-forming condensation reaction<sup>206</sup>, was thermodynamically driven to form a [4+6] porous imine cage by Skawronek *et al.*<sup>207</sup> in 2008. This molecule was then systematically studied by Tozawa from Cooper group<sup>203</sup> in 2009, alongside two other analogues (covalently-bonded imine cages, CC1 and CC2), which have been known as the first series of POC molecules.

As is shown in **Figure 1.20**, the reaction of 1,3,5-triformylbenzene (TFB) with three different vicinal diamines successfully yielded [4+6] imine cages where the porosity was pre-fabricated and intrinsic to the cage structures, where the molecules pack together *via* non-covalent interactions to generate extended structures in the solid state. These cages were then isolated as their most thermodynamically stable products and typically adopted a similarly tetrahedral structure with triangular windows. These triangular windows vary in size depending on which diamine was used, showing window sizes of 5.8, 6.1 and 5.8 Å for CC1, CC2 and CC3, respectively. CC1 was found to be non-porous to N<sub>2</sub> (Langmuir surface area of 40 m<sup>2</sup> g<sup>-1</sup>) and packed in a window-to-arene conformation with no extended connection between internal pores. Packing in a similar window-to-arene fashion, CC2 showed a frustrated packing of stacks resulting from these methyl groups from the diamine vertices, where 1D pore channels were therefore created. This was demonstrated by a higher BET surface area of 533 m<sup>2</sup> g<sup>-1</sup>, which results from the extrinsic channels in the more porous CC2. CC3, by contrast, was shown to crystallise in a window-to-window manner that each window in the cage molecule was directly facing a neighbouring cage window, which resulted in an extended 3D diamondoid network of voids with a BET surface area of 624 m<sup>2</sup> g<sup>-1</sup>, and a BET surface area of 409 m<sup>2</sup> g<sup>-1</sup>



in its highly crystalline form<sup>208</sup>. Two pore cavities were found in the 3D pore structure of **CC3**, which include a cage cavity inside the cage molecule itself (shown in dark purple in **Figure 1.20(g)**) and a window cavity between the adjacent cage windows (light purple)<sup>209</sup>.

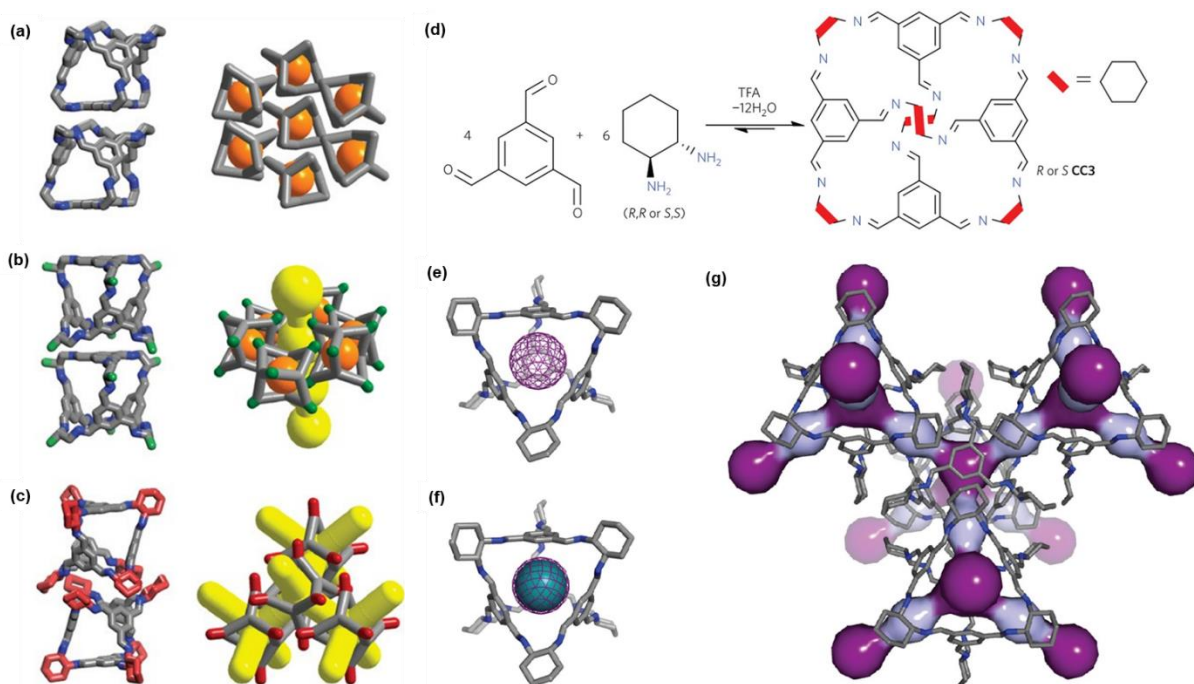


**Figure 1.20** (a)-(c) Schematic representation of cage-cage packing in the crystal structures of **CC1** – **CC3** resulting from a change in the vertex functionality. Reprinted from reference<sup>203</sup> with permission. (d) Reaction scheme for the synthesis of **CC3** by a one-pot [4 + 6] cycloimination reaction involving four trialdehyde and six diamine molecules, catalysed by trifluoroacetic acid (TFA). (e) The largest inclusion sphere inside the cage (dark purple) is the perfect size to accommodate a single xenon atom (cyan sphere, f). (g) Two pore cavities exist in the 3D pore structure: a cage cavity inside the molecule itself (dark purple) and a window cavity between adjacent cage windows (light purple). Reprinted from reference<sup>210</sup> with permission.

Since then, a variety of porous organic cages have been synthesised because of their permanent porosity and crystal assembling. The use of different diamine precursors in conjunction with TFB has led to a collection of POCs from the Cooper group with distinct structures and properties. **Figure 1.21(a)** shows the structures of **CC1-CC10** reported by the Cooper group. For example, **CC4**<sup>211</sup> has a complex pore structure with a close intermolecular interaction, **CC5**<sup>212</sup> exhibits a larger pore volume ( $S_{\text{ABET}}$  of  $1333 \text{ m}^2 \text{ g}^{-1}$ ), and **CC6**<sup>213</sup> possess a [2+3] topology with a narrow 1D channel showing little cage void.

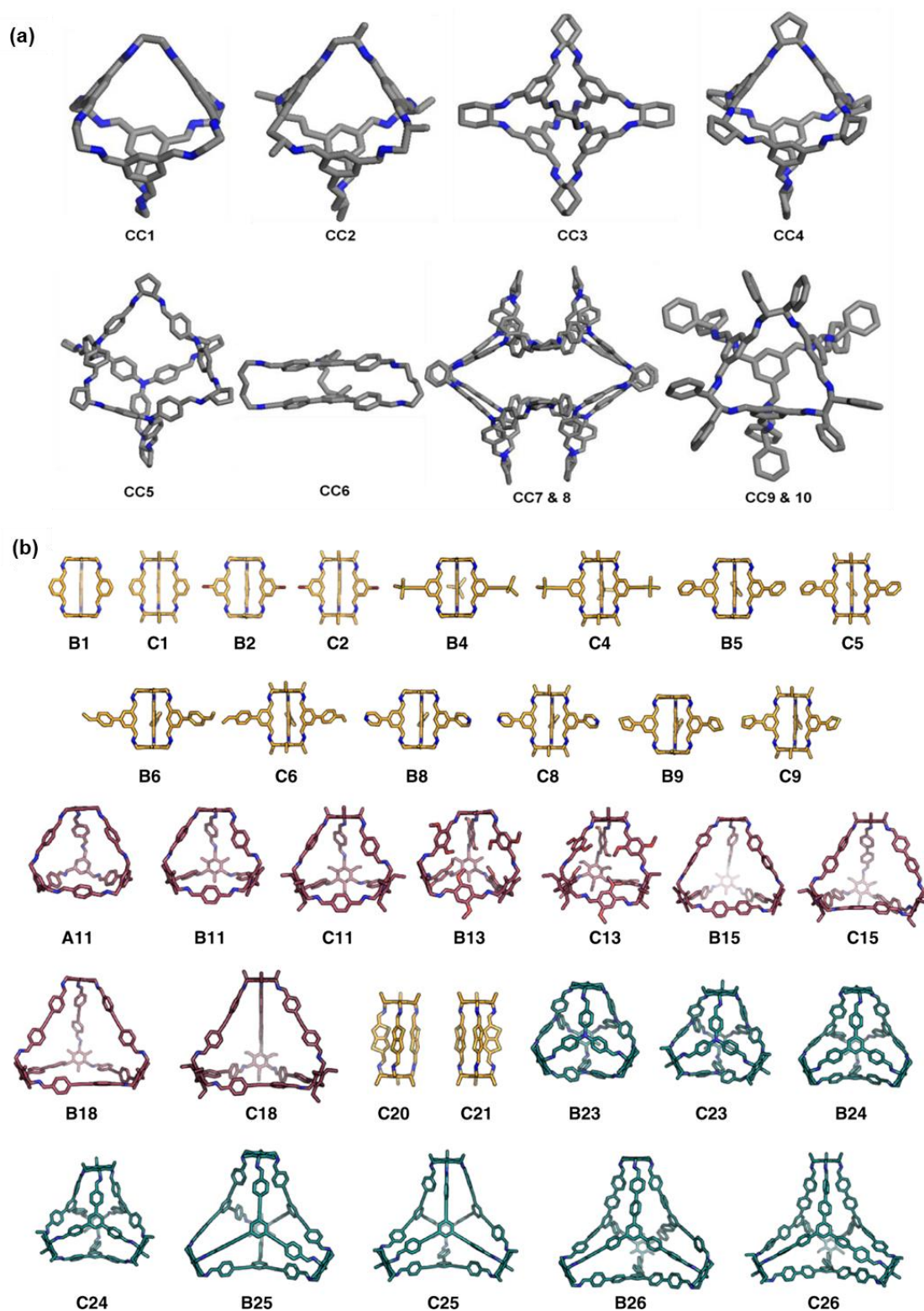


**Figure 1.21** (a) The cage structures synthesized in the Cooper group obtained from single crystal X-ray diffraction. Molecules not all shown on the same scale. Figure taken from the University of Liverpool PhD thesis repository<sup>213</sup>. (b) The 33 cages that formed cleanly in the Cooper group via high-throughput discovery of POCs using computational screening fused with robotic synthesis. Reprinted from reference<sup>214</sup> with permission.

More recently, the Cooper group<sup>214</sup> have reported a new series of shape-persistent organic cage molecules (**Figure 1.21(b)**), which were discovered using a high-throughput synthesis workflow fusing computation with robotic synthesis. A total of 78 precursor combinations were investigated by computation screening and experiment, leading to 33 cages that were formed cleanly in one-pot syntheses. Moreover, a new cage topology—doubly bridged, triply interlocked cage catenanes, have been discovered via this workflow. Such high-throughput studies covering a broad range of conditions, and the discovery of these POCs is beneficial to the current library of new porous materials.

Various organic cages have also been reported by other research groups. Warmuth *et al.*<sup>215,216</sup> have developed a number of molecular nanocages by condensation reactions between tetraformylcavitand and a series of diamines. However, none of these cage molecules were found to be porous, neither nor crystal structures. Mastalerz *et al.*<sup>217</sup> presented examples of porous imine cages synthesized from 1,3,5- triaminobenzene and 1,3,5-triformylbenzene derivatives, and the resulting [4+4] truncated tetrahedral cage showed a shape-persistent structure. The same research group also reported a salicylbisimine cage molecule with a large internal pore volume, and they exhibited an interconnected 3D pore network which is dictated by  $\pi$ - $\pi$  stacking interactions<sup>218</sup>. So far, as a new class of porous materials, POCs have drawn more interests in advanced materials design.

### 1.4.3 Synthesis and Topology of Porous Organic Cages

POCs are synthesised using irreversible bond formation or dynamic covalent reactions. Molecules synthesised with irreversible reactions usually exhibit higher chemical stability but are rarely isolated in high yields because of the kinetic nature of the reactions involved<sup>219</sup>. Therefore, not many examples of irreversible reactions are presented, of which reactions such as amide bond formation and nucleophilic aromatic substitution reaction<sup>220</sup> have been adopted for the synthesis of small capsule-like cage molecules, but larger templates are required to form larger cages.

Cages formed via reversible bond formation are more thermodynamically controlled, and this leads to their most thermodynamically stable products, with higher yields in a single step<sup>197</sup>. A more frequently used approach to the formation of organic cages is based on the dynamic covalent chemistry via the reversible formation of imine bonds. Dynamic covalent chemistry allows self-correction to form discrete cage species. Thus, this is a powerful strategy for

generating molecular cage structures by allowing equilibration to the thermodynamic product, facilitating “one-pot” multicomponent syntheses in high yields. As is shown in **Figure 1.22**, imine and boronate ester chemistry have been used to produce cage molecules of varied topology and cavity size. For example, an imine-bonded cage (**CC1**) with a tetrahedral geometry<sup>203</sup>, an imine-bonded cage with an adamantoid geometry<sup>221</sup>, a cage constructed from C-C bonds with an elongated-dipyramidal geometry<sup>222</sup>, and a boronate-ester based cage with an cuboctahedral geometry<sup>223</sup>.

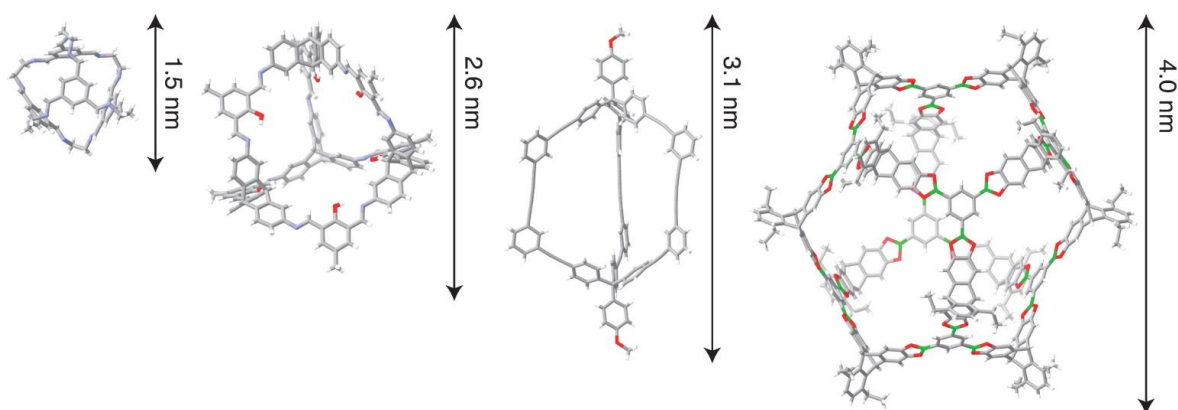


**Figure 1.22** Examples of POC structures with their respective sizes indicated to the right. From left to right: an iminebased cage of tetrahedral geometry<sup>203</sup>, an imine-based cage of adamantoid geometry<sup>221</sup>, a cage constructed from C-C bonds with an elongated-dipyramidal geometry<sup>222</sup>, and a boronate-ester based cage of cuboctahedral geometry<sup>223</sup>. (white: hydrogen, grey: carbon, blue: nitrogen, red: oxygen, green: boron). Reprinted from reference<sup>224</sup> with permission. Copyright 2015, the Chemical Society of Japan.

Varying the functionality on the cage periphery enables the tailoring of a POC’s overall properties for a specific function. In many cases, small changes can result in large effects on both the size and geometry of the resulting cage molecule, and thus the selection of precursors is important. Apart from the imine condensation<sup>203,211,212</sup>, which is the most prevalent reversible route, other approaches, including ester condensation<sup>223,225,226</sup>, boroxine formation<sup>227,228</sup>, and dynamic alkyne metathesis<sup>229–231</sup> have also been utilized for the formation of cage products (**Figure 1.23**). Employing more synthetically challenging building blocks, the Mastalerz group has reported a variety of porous imine-based cages of varied topology and cavity size<sup>221,232,233</sup>. Afterwards, this group also synthesised a shape-persistent, mesoporous cuboctahedral cage by a one-step 48-fold boron ester condensation reaction<sup>223</sup>. These boronate-based cages are

composed of 24 boronate ester bonds and possess a large average internal cavity size of 2.8 nm with BET surface areas approaching 4000 m<sup>2</sup> g<sup>-1</sup>.

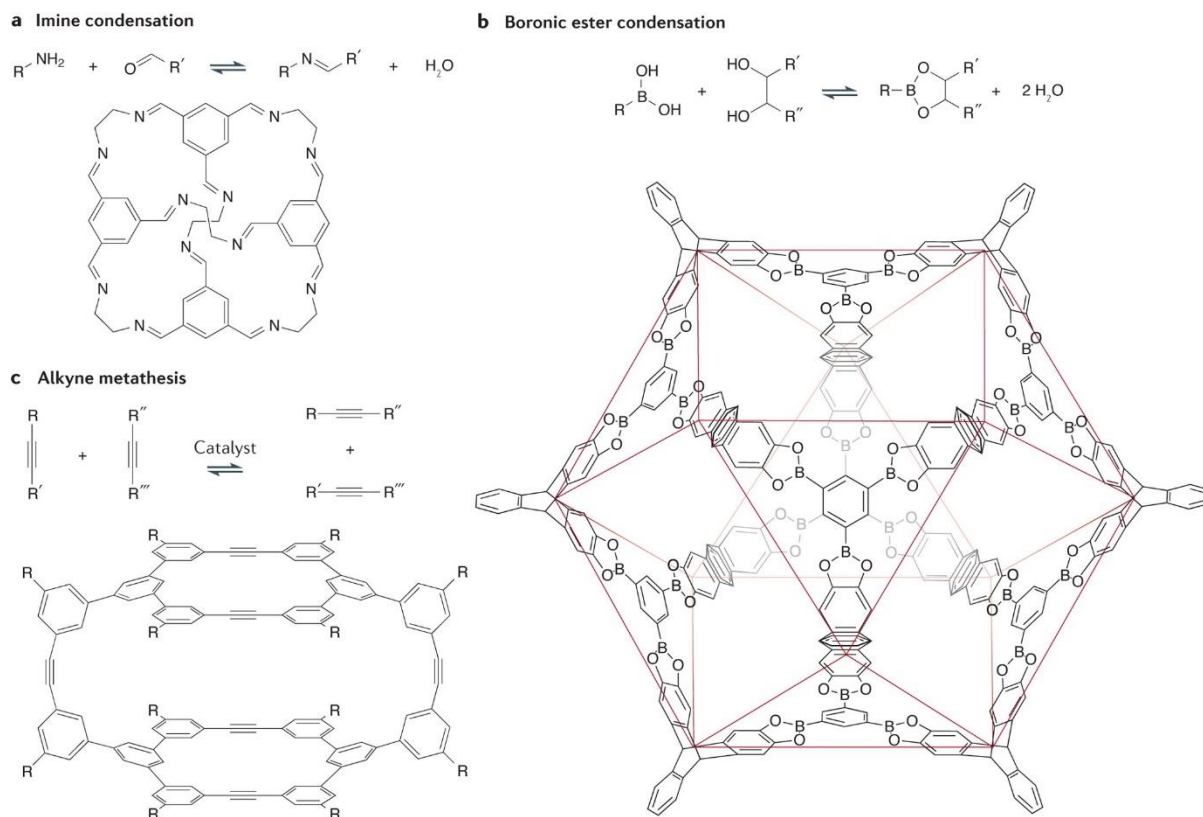


**Figure 1.23** (a) *Imine condensation*<sup>203</sup>. (b) *Boronic ester condensation*<sup>223</sup>. (c) *Alkyne metathesis*<sup>229</sup>. In all three cases, chemical reversibility allows the thermodynamic cage product to form. Reprinted from reference<sup>234</sup> with permission.

Based on the synthesis routes, POCs with various topologies can be designed and discovered. ‘Topology’ is an intrinsic component of every cage and is independent of the geometrical shape the molecule adopts. This is because, mathematically, the topology is the region of space that is preserved upon deformation<sup>235</sup>. The topology plays an important role in how these molecules can be used since the cavities of different shapes and sizes can be designed for specific applications. Since 2009, a variation on the cage topology has been discovered every couple of years (**Figure 1.24(a)**), including [2+3] cages<sup>236</sup>, [8+12] cages<sup>237</sup>, [4+4] cages<sup>238</sup> and [3+6] tubular covalent cages<sup>239</sup>. Other possible cage topologies have been studied by computation modelling and a high-throughput screening process<sup>214</sup>, formed by the reaction of a triamine precursor (2,4,6-trimethylbenzene-1,3,5-triyl)trimethanamine, with three representative aldehyde types: meta and paradi-aldehydes, and trigonal trialdehydes. Since the cages were formed by reversible imine chemistry, the topologies of thermodynamic products with the



lowest relative internal energy were expected to be formed. As a result, seven topologies produced by tritopic + ditopic reactions or tritopic + tritopic reactions have been discovered. The variety of topologies contributed to a larger POC database that we could refer to for the desired material design. Their solubility and the precise control of functionality are important advantages of POC chemistry that enable these novel materials to be used in different fields. For example, where solution processing is required or preferable to other fabrication methods, such as molecular separations<sup>210</sup> and sensing<sup>240</sup>.

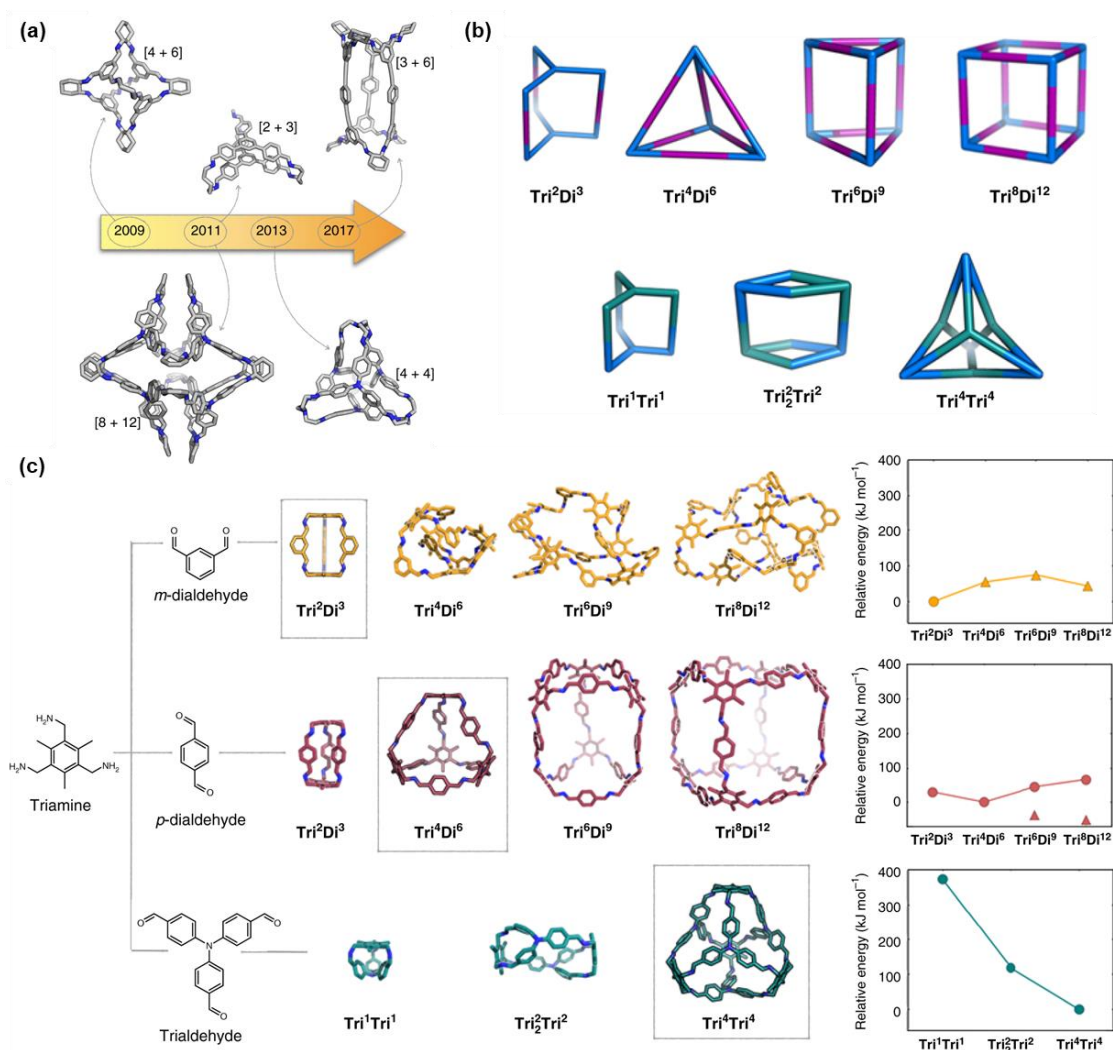


**Figure 1.24** (a) Timeline showing variation in cage topologies. (b) Scheme showing possible cage topologies; (top) candidate topologies for tritopic + ditopic reactions (Tri<sup>x</sup>Di<sup>y</sup>) and (bottom) for tritopic + tritopic reactions (Tri<sup>x</sup>Tri<sup>y</sup>). (c) Reaction schemes and computational modelling for three model covalent organic cages. Reprinted from reference<sup>214</sup> with permission.

#### 1.4.4 Porous Organic Cage Membranes

Porous organic molecules that combine microporosity and solution processability are highly desirable to fabricate the next generation porous membranes. POCs, as opposed to extended crystalline solids, are soluble, and they can be processed into different forms, such as mixed matrix membranes<sup>196</sup>. Therefore, POCs could ameliorate these transport issues by integrating intimately with the polymer matrix. These discrete molecular building blocks can assemble into crystals with both intrinsic cavities and extrinsic voids, thus providing the material with well-defined pore structures and adjustable pore sizes. As a novel class of porous materials with ultrahigh surface areas<sup>210,223</sup> that can exceed  $3000 \text{ m}^2 \text{ g}^{-1}$ , these POCs exhibit good compatibility with the polymer matrix. They can be easily solution-processed, proving a promising strategy to enhance the stability and simultaneously improve the selectivity and permeation of the membranes. Compared with extended porous materials such as zeolites and MOFs, one remarkable feature of POCs is that they are dissolvable in common organic solvents; consequently, POCs are easily processable and can be spin-coated onto porous substrates to form membranes.

Some POC based composite membranes have been fabricated for gas separation applications<sup>241</sup>. POC/PIM-1 composite membranes were demonstrated by Budd *et al.*<sup>242</sup> to enhance the permeabilities of both  $\text{CO}_2$  and  $\text{N}_2$ , while retaining good  $\text{CO}_2/\text{N}_2$  selectivity; in addition, the resistance toward physical ageing was improved. Thin membranes of five POCs were fabricated on various substrates and found to exhibit molecular sieving capability; specifically, high  $\text{H}_2$  permeability and good  $\text{H}_2/\text{N}_2$ ,  $\text{H}_2/\text{CO}_2$  and  $\text{H}_2/\text{CH}_4$  selectivities were observed<sup>243</sup>. But none of the POC membranes were reported for the water purification. In this case, another outstanding feature of POCs is water stability, which is essential for use in a water environment. As a prototype POC, the **CC3** crystal was found to remain stable in boiling water for at least 4 h<sup>244</sup>. Thus their chemical stability and structure persistence make them promising for water applications. Moreover, the POCs could be pre- or post-functionalized, rendering the possibility for versatile water treatment with improved performance.

Based on the above discussed salient features (*e.g.* well-defined pore structures and adjustable pore sizes, easy fabrication into membranes and water stability), it is envisioned that POCs might be intriguing membrane materials for liquid phase separations as well. Consequently, separation properties through 2D membranes using these molecular sieving materials will ultimately depend on which cage is used and how the cage packs in the membrane<sup>210,212,245</sup>.



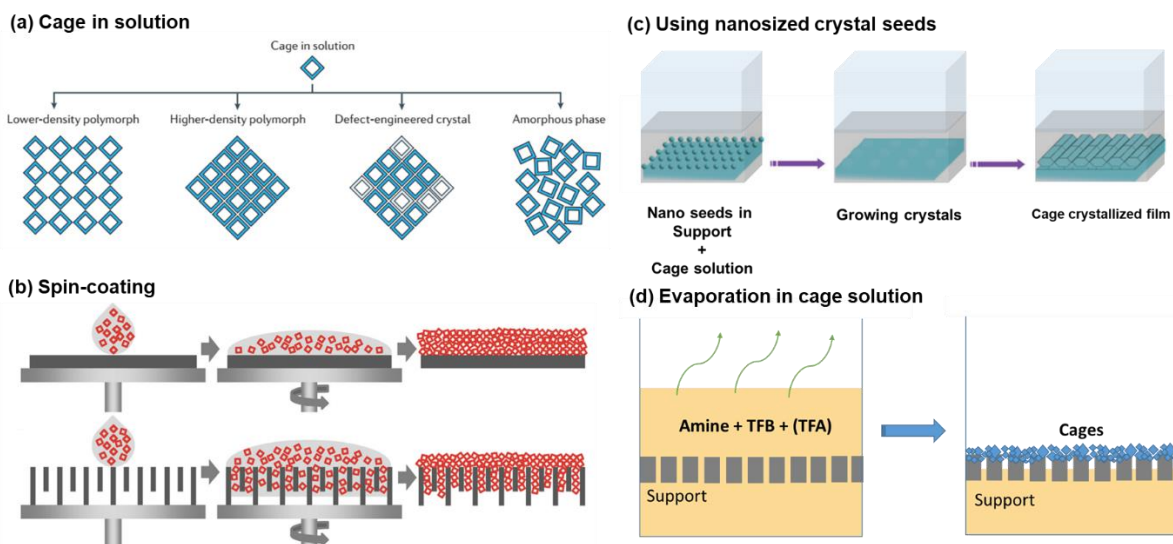


**Figure 1.25** (a) Scheme showing cage molecules in the solution. (b) Spin-coating method for preparing POC coatings. Reprinted from reference<sup>243</sup> with permission. (c) Nanosized crystal seeding method for preparing POC coatings. (d) Solution-casting for preparing POC coatings.

To prepare a proper selective coating using these solution-processable POCs, particularly, several fabrication methods, including spin-coating<sup>243</sup>, nanosized crystal seeding<sup>246</sup>, and solution-casting<sup>247</sup> might be possible, as is shown in **Figure 1.25**. Still, some issues have remained, such as discontinuous surface, physical ageing of the membranes, and a lack of tunable and ordered pore structures as they are commonly fabricated using amorphous polymers. In this case, the development of a simple and scalable fabrication method to organise individual cages into a continuous thin film with the maintained pore structures could be a unique solution to realize the full potential of these materials in advanced technologies like membrane separation. Therefore, to achieve the full merit of the ordered and nanosized pore structures, a technique for the preparation of self-standing thin films, which are exclusively derived from POCs, is highly desirable. Nevertheless, bringing such crystalline materials into a self-standing, defect-free, microporous, and continuous thin film is a monumental challenge, which if accomplished, will create a breakthrough in many niche separation processes of industrial and environmental significance.

## 1.5 Membrane Fabrication Technology

### 1.5.1 Membrane Types

Divided by the membrane materials, there are mainly three types of membranes: polymeric membranes, inorganic membranes and hybrid polymer/inorganic membranes<sup>18,248</sup>. These membranes have been applied to various areas due to their different physical and chemical properties.

Polymeric membranes are favoured for separation processes including NF and RO because they are cheap, robust, and can be manufactured on a large scale<sup>249</sup>. Polymer membranes generally fall into three categories: dense membranes, integrally skinned asymmetric (ISA) membranes, and thin film composite (TFC) membranes.

Dense membranes contain non-porous films in which molecular transport is governed by solution diffusion<sup>250</sup>. These membranes are commonly formed via evaporative phase inversion processes (e.g., casting a dope solution), leading to the formation thick dense homogenous membranes<sup>250</sup>. Thus they are usually used for gas separation processes<sup>251,252</sup>.

ISA polymer membranes (**Figure 1.26**), containing a thin dense selective separation layer on top of a more open support layer of the same material<sup>16</sup>, show advantages include their durability and low manufacturing costs. They have been designed to be flexible so they can be used within membrane modules<sup>253</sup>. The most common preparation methodology for ISA polymer membranes is phase inversion via immersion precipitation<sup>253</sup>.

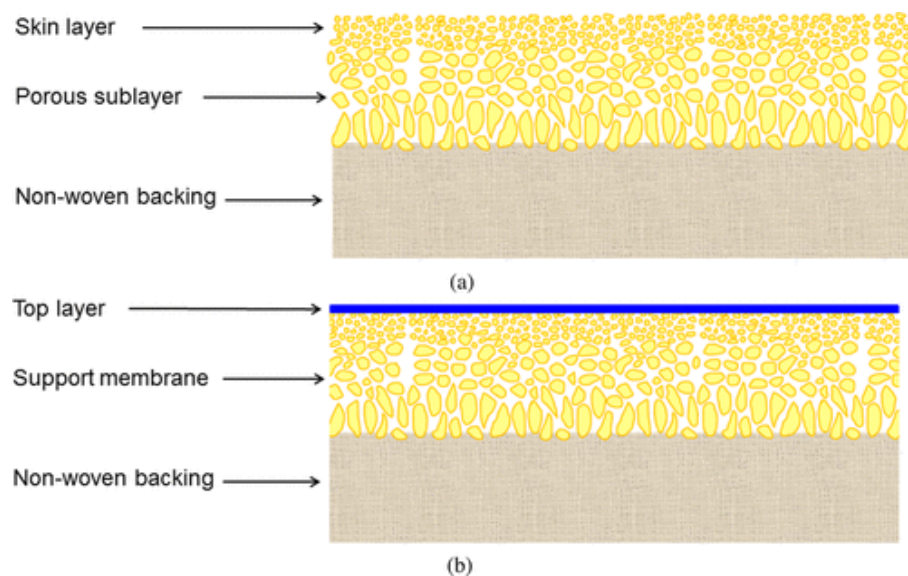


**Figure 1.26** Schematic representation of (a) an integrally skinned asymmetric (ISA) membrane and (b) a thin film composite (TFC) membrane. The main features of these two types

of membranes and the common polymers and synthesis procedures used to make them are described in this section. Reprinted from reference<sup>254</sup> with permission.

TFC membranes consist of a separate thin selective layer on top of a porous support layer made from a different material<sup>23</sup>, as shown in **Figure 1.27**. They exhibit higher fluxes than ISA due to their ultrathin selective layers and the highly porous support layers, while the top layer offers a favourable guest selectivity. Therefore, TFC membranes are used extensively in desalination<sup>255,256</sup> and OSN<sup>257–259</sup> because of their high permeance values and solute retentions. TFC membranes have also been fabricated for OSN applications. Several methods, such as floatation deposition<sup>260</sup>, dip coating and spin-coating, can be used for the preparation of TFC membranes, yet the most commonly-used approach is interfacial synthesis, which will be discussed in the next section.

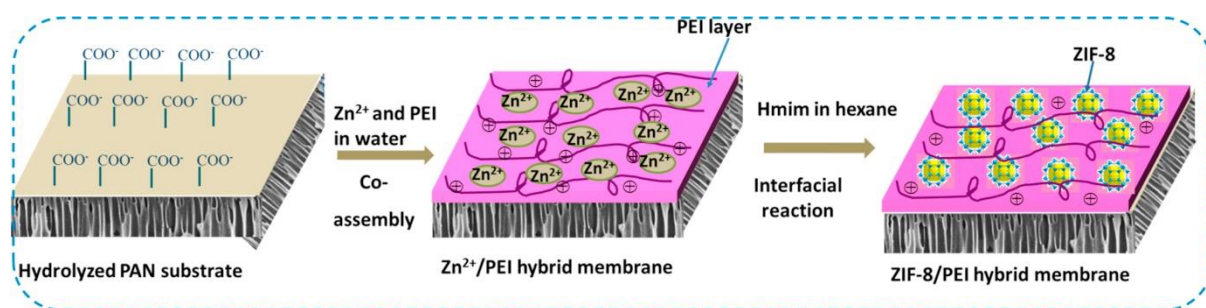


**Figure 1.27** The flowchart of ZIF-8/PEI hybrid membrane preparation process. Reprinted from reference<sup>84</sup> with permission.

Inorganic membranes, such as ceramic membranes or zeolite membranes, have shown permeances up to ten times higher than polymeric membranes<sup>246</sup>. One reason is that the porous structure of some inorganic/crystalline materials can be controlled to produce membranes with regular, repeatable porous structures with a defined pore size, such as those found in MOFs.

Hybrid membranes combine the selective nature of inorganic materials with the flexibility and durability of organic membranes. Among hybrid membranes, most of them fall into a category known as mixed matrix membranes (MMMs). Typically MMMs have a continuous polymer phase in which discrete inorganic materials are dispersed<sup>261,262</sup>. These membranes are designed to improve the selectivity and permeability simultaneously by utilising the best separation properties of both polymer and inorganic materials as a methodology to overcome the Robeson upper bound for gas separations.

## 1.5.2 Preparation of membranes

Industrial membrane technology applies coating-chemical crosslinking method<sup>263</sup>, layer-by-layer (LBL) self-assembly method<sup>264</sup>, graft modification method<sup>265</sup> or interfacial polymerization (IP) method<sup>266</sup> to fabricate target membrane products.

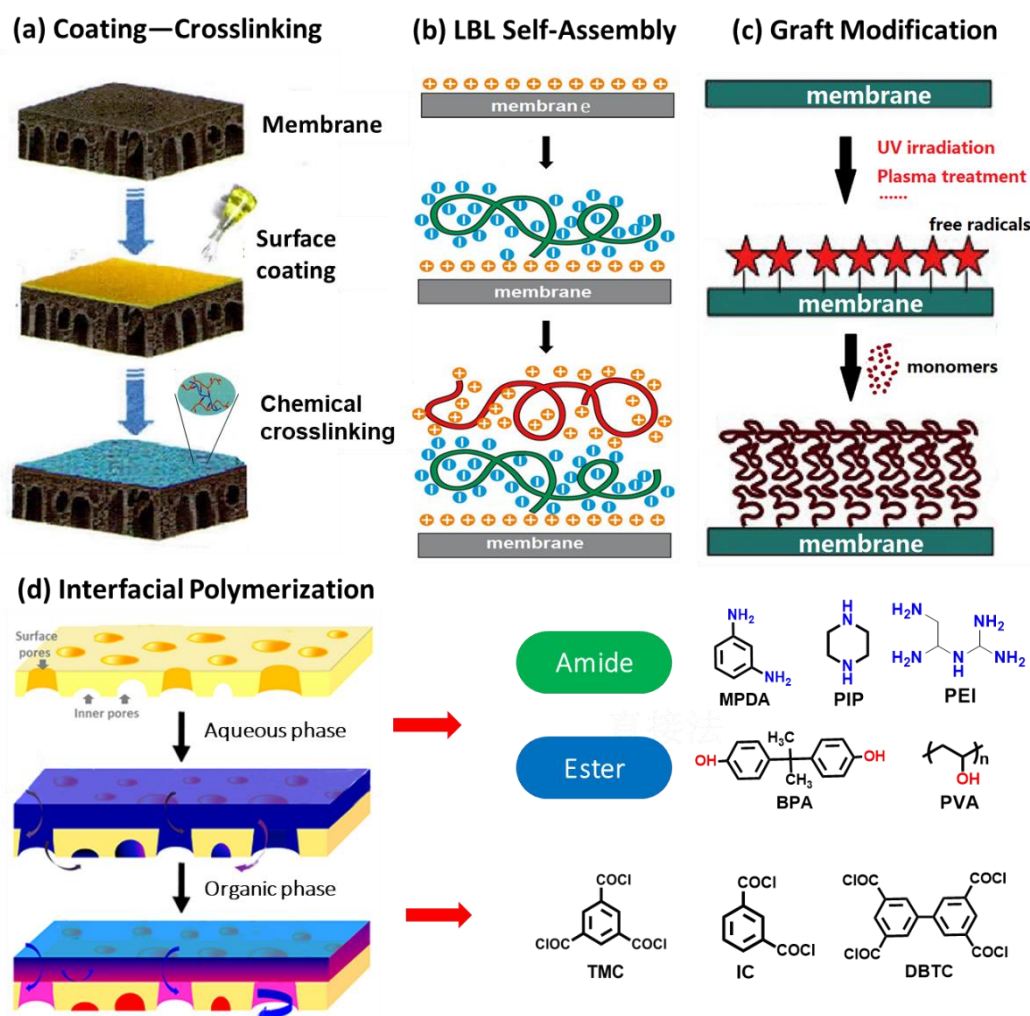


**Figure 1.28** Scheme of industrial membrane technologies including coating-chemical crosslinking method, layer-by-layer (LBL) self-assembly method, graft modification method and interfacial polymerization (IP) method.

The coating-chemical crosslinking method (**Figure 1.28(a)**) usually use polyelectrolytes or charged biological molecules as the polymer, which will be cross-linked with the chemical linker such as glutaraldehyde. This approach is easy and cheap, however lacks controllability. The skin layers are usually very thick and defected, thus lead to low permeability.

The LBL self-assembly (**Figure 1.28(b)**) depends on the drive forces such as electrostatic interaction and covalent bond rather than hydrogen bond. The assembly operation includes alternating deposition assembly, pressure driven assembly, and electric field assembly. The membranes fabricated with this method exhibit high selectivity, with adjustable thickness and charge controlled by the layers. However limited substrates with specific chemical properties can be used, and the process is complex and time-consuming.

The grafting technology ((**Figure 1.28(c)**) applies UV irradiation or plasma to treat the target membrane substrate, so that free radicals are available on the surface. Monomers, including cations, anions, and zwitterions, will be then grafted on the surface, which produces a selective layer on top of the membrane. The process is usually a rapid reaction, and the resulting membranes are usually hydrophilic and antifouling. But this method would damage the substance, also limit the membrane preparation in a large-scale.

### 1.5.3 Interfacial Synthesis of Membranes

Interfacial synthesis<sup>139,267–269</sup> is a well-adapted method for the synthesis of polymer thin films like polyamides and polyesters in the bulk scale<sup>191,270</sup>, where two precursors are dissolved in two immiscible solvents (or air) and react at the two-phase interface. As the chlorides are not stable in water, the aqueous phase usually contains amine or ester monomers with active hydrogen atoms (-OH, -NH, -SH), including *m*-phenylenediamine (MPD), piperazine, polyethylenimine (-NH), and bisphenol-A, polyvinyl alcohol (-OH) (**Figure 1.28(d)**). Acyl chloride such as trimesoyl chloride (TMC) are usually used in the organic phase to react with the monomers in the other phase.

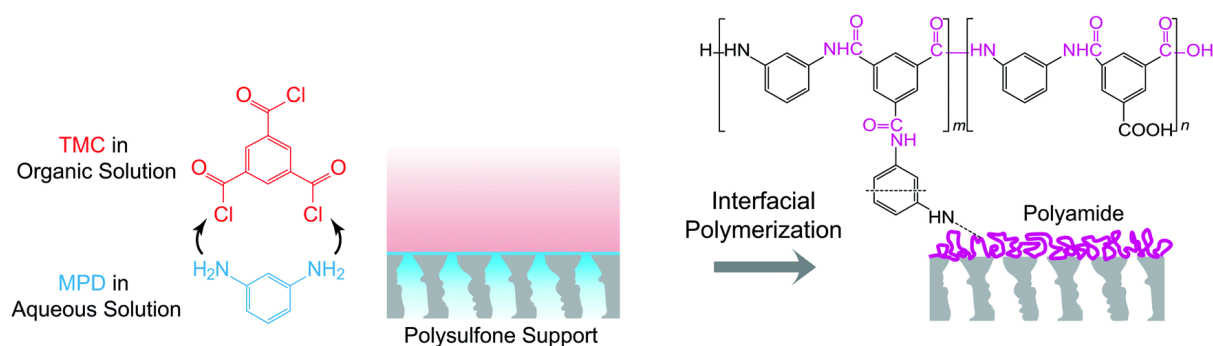


**Figure 1.29** Schematic representation of a typical interfacial polymerization process for making TFC membranes. The reaction between *m*-phenylenediamine (MPD) and trimesoyl chloride (TMC) occurs at the surface of a microporous polysulfone support to form a thin



polyamide layer, whose chemical formula is illustrated. Reprinted from reference<sup>271</sup> with permission from the Royal Society of Chemistry.

A representative procedure for interfacial polymerization (IP) is shown in **Figure 1.29**. A microporous polysulfone membrane support is first immersed in an aqueous diamine solution, with MPD, which allows diamine penetration into the support. After removing the excess diamine on the surface, the impregnated support is brought into contact with an organic phase of TMC. As MPD monomers diffuse to the interface between water-organic phases, they are allowed to react with the TMC, and a thin polyamide layer thus formed on top of the membrane support.<sup>271</sup>

The IP method is a rapid process for the fabrication of TFC membranes. Once the solutions come into contact, polymerization occurs at the interface immediately. At this moment, the polymerization is controlled by chemical kinetics where the monomers contact directly. The rapid polymerization leads to the formation of a thin polymer film as a result of the low solubility. The monomers in the two solutions are gradually separated by the film, and the polymerization becomes slower which is controlled by monomer diffusion through the film. As the thickness of the polymer film further increases in a longer time, the reaction eventually stops due to the diffusion barrier, *i.e.*, the film at the interface<sup>272</sup>. As a result, free-standing thin film is formed at the interface due to its self-restraint.

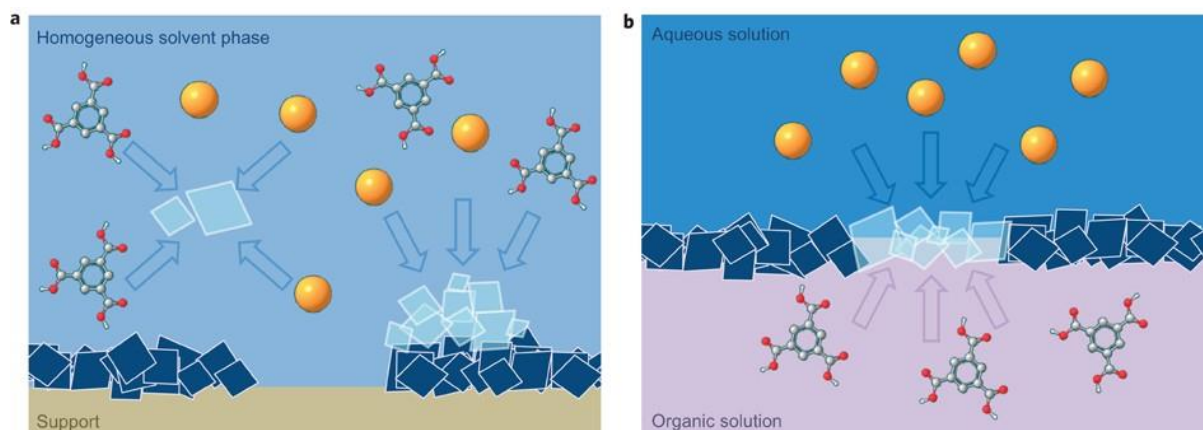


**Figure 1.30** Comparison of MOF layer synthesised from two different approaches. (a) Deposition of a MOF layer on support (brown) in a homogeneous synthesis mixture. Undesired nucleation in solution or growth on top of previously formed crystals can occur. (b) Interfacial preparation of a MOF layer using a biphasic synthesis mixture consisting of an aqueous metal-ion-containing solution (blue) and an organic ligand solution (purple). Reprinted from reference<sup>269</sup> with permission.

The interfacial approach exhibits a strong advantage for the controllable fabrication of thin films, nanofibers, and/or functional materials for use as separation membranes. For example, thin MOF layers have been fabricated using this approach<sup>269</sup>, as is shown in **Figure 1.30**. The difference in solubility characteristics of the organic and inorganic precursors enabled the self-completing interfacial formation of a MOF layer in a biphasic synthesis mixture, as the two precursors encounter each other from opposite sides of the liquid–liquid interface. As layer growth, in this case, does not depend on any specific surface functionalization of support, the approach can be adapted to a wide range of porous support materials.

This method is also promising for soluble POCs. Based on different solubility in the organic and aqueous phases, herein in this work, new types of POCs based membranes via interfacial approaches have been established for versatile molecule separation with improved performance. Furthermore, in-situ crystalline growth and film-formation at the interface has been intelligently designed by a simple interfacial synthesis method under ambient conditions.

## 1.6 Project Overview and Aims

### 1.6.1 Chapter Summary

The project overall studied membranes that have been fabricated using POCs via different methods, and investigated their structures and applications in molecular separations in liquid phase.

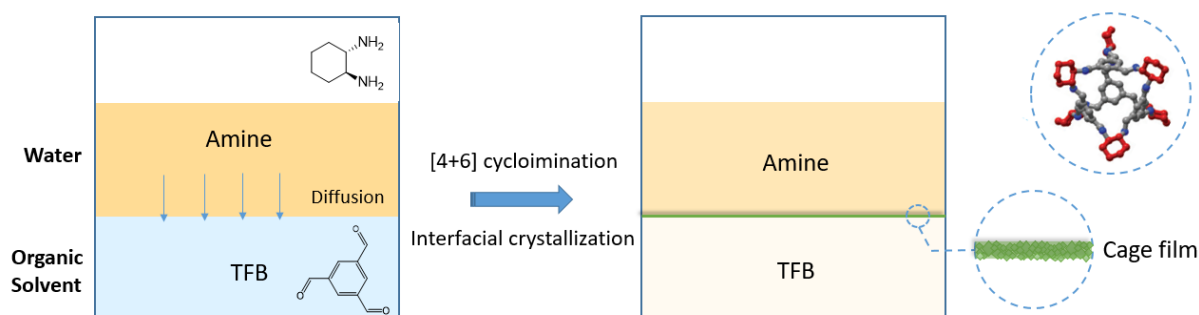


**Figure 1.31** Illustration of interfacial synthesis method to fabricate cage films and the octahedron structure of a CC3 cage molecule.

In **Chapter 3**, the fabrication of pure POC based films via an interfacial reaction and crystallisation method is discussed. The interfacial method was found to allow the two cage precursors to react at the interface of two immiscible solvents. As shown in **Figure 1.31**, triformylbenzene (TFB) and 1,2-cyclohexane diamine (CHDA), as the reagents for the POCs



via [4+6] cycloimination reactions, were added separately into organic solution (dichloromethane) and aqueous solution. The interface was formed, and the two reagents reacted to form the POC when they diffused to the interface. This method was found to provide a direct synthetic route to close-packed defect-free 2D films. The connected porous networks are retained explicitly at the liquid-liquid interface. The resulting POC thin films could be easily transferable onto various substrates, including glass surfaces, silicon wafers, metallic wires, and polymeric membrane supports while retaining their physical cage-shape and crystalline structures.

In **Chapter 4**, it is shown that the crystal packing of the POC in the composite membrane presented in **Chapter 3** can be switched using chemical stimuli. As is shown in **Figure 1.32**, the crystalline POC film is dynamic, and its pore aperture can be switched by exposing the membranes to methanol. This switching process generates larger pores that provide increased methanol permeance and higher molecular weight cut-offs ( $1400 \text{ g}\cdot\text{mol}^{-1}$ ). By varying the water/methanol ratio, the film can be switched between two phases with different selectivities, such that a single, ‘smart’ crystalline membrane can perform graded molecular sieving. We exemplify this by separating three organic dyes in a single-stage, single-membrane process.

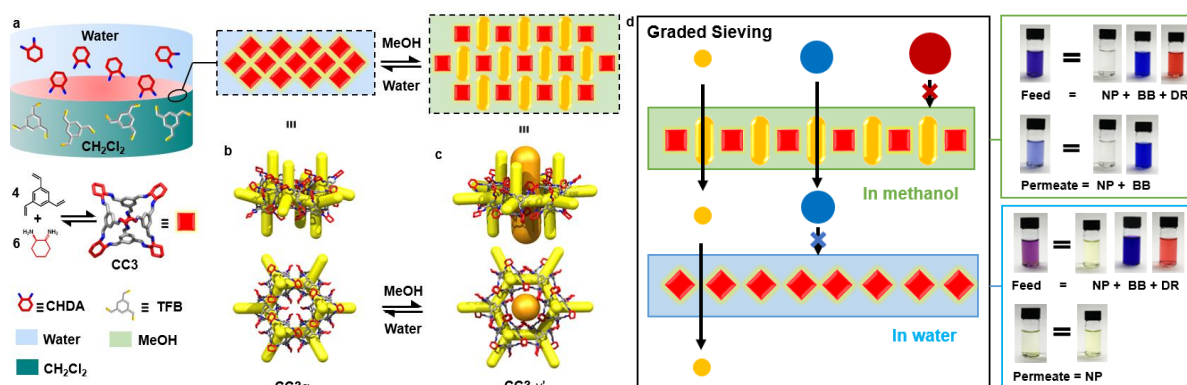


**Figure 1.32** *a*, Interfacial synthesis method used to fabricate *CC3* films associated with its two polymorphic structures in water and methanol. *b*, Structure of the film in its polymorph *CC3 $\alpha$*  with a 3D pore network. *c*, Structure of *CC3* film in its polymorph *CC3- $\gamma'$*  with a 2D honeycomb pore network. *d*, Graded sieving of dyes. DR, Direct Red 80; BB, Brilliant Blue; NP, 4-Nitrophenol, 20 ppm.

At the same time, inspired by the pre- or post-functionalisation properties of POCs, a series of aminic cages, formed by reducing their parent imine cages, were utilised as reactive monomers for cross-linking polymerisation reactions via IP. **Figure 1.33** demonstrates that amines or hydroxyls are possible functional groups in POCs that react with acid chlorides or aldehydes

to form cross-linked, insoluble polymers. Trimesoyl chloride (TMC), as a typical cross-linker in the organic phase for IP reaction with high reactivity, is supposed to enhance the reaction rate and maintain the pore structures of functionalised POCs.

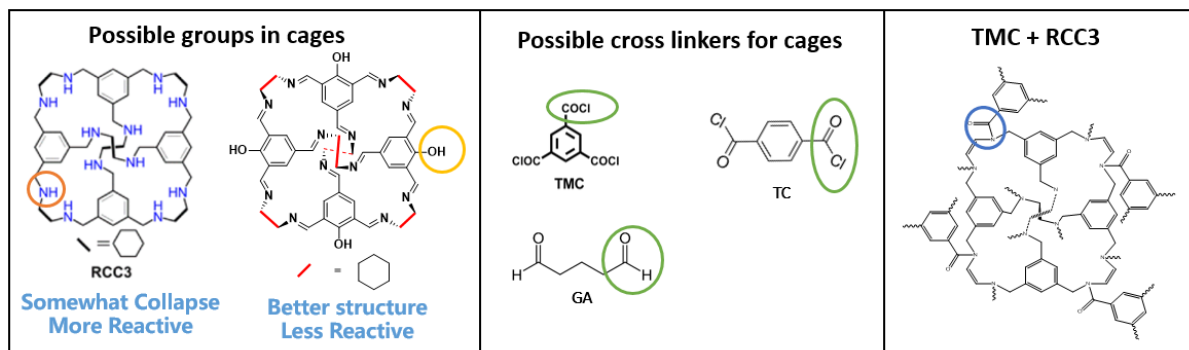


**Figure 1.33** Schematic demonstration of active functional groups in cages and in cross linkers, and possible structure of the cross-linked polymer by interfacial polymerization.

Reduced 1,2-cyclohexane diamine cage (RCC3), 1,2-propylenediamine (RCC2) and ethylenediamine cage (RCC1) have a desirable cage shape in solution and 12 amine groups in each monomer. Since these molecules are easily soluble in water, firstly, the IP process by adding TMC in the organic phase (hexane) and RCC molecules in the aqueous phase was investigated. The associated results are discussed in **Chapter 5 (Figure 1.34)**, which have proved the fabrication possibility with good membrane performance. The continuous thin films formed at the interface in a short time (seconds to minutes) and were continuous, robust with an ultrathin thickness. Supported by a cross linker, the reduced cages are supposed not to collapse in solid state and exhibit excellent pore channels for separation. Containing monomers with different functional groups in each nanofilm, the prepared membranes are expected to show different pore structures, and therefore exhibit a tuneable selectivity for molecules. In addition, it was possible to use RCC3 nanofilm for post-functionalisation where the unreacted amines can be tied up by small molecules, such as formaldehyde. The cavity size in the nanofilm was reduced after the tie-up procedure, and thus endowing the membrane with retention of smaller molecules.

Applying the POCs as membrane materials could substantially enhance the membrane properties, including good selectivity for molecular separation, and better resistance towards physical ageing of the membranes. With well-defined pore structure and channels of specific molecules, these POC based membranes have exhibited narrow size distribution, leading to a sharp molecular weight cut-off (MWCO) with good solvent permeance. By a solvent stimuli,

or pre-/post-synthetic functionalisation procedure, tuneable separation properties have been achieved on these membranes, thus making them attractive candidates in liquid separation for NF and RO applications.

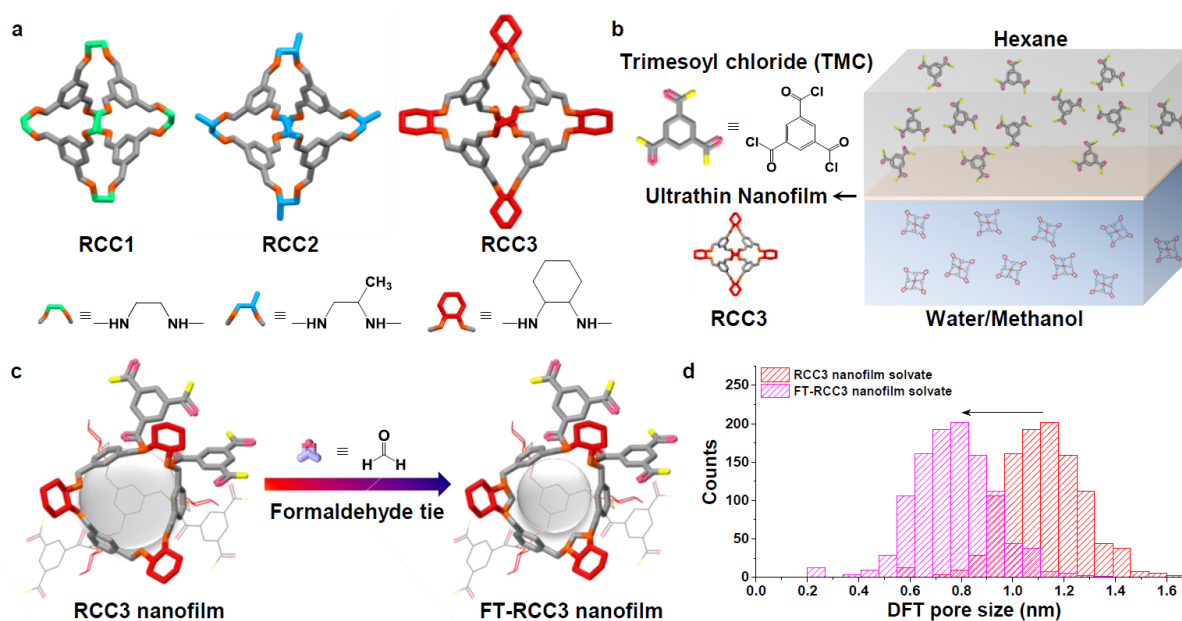


**Figure 1.34** Fabrication of ultrathin polyamide nanofilms incorporating POCs. **a**, Schematic demonstrating the molecular structure of various reduced crystalline cages (RCC) comprising flexible amine bonds and tuneable alkane linkages. **b**, Fabrication of ultrathin polyamide nanofilm at a free interface between a water/methanol solution containing RCC molecules and a hexane solution containing trimesoyl chloride (TMC). **c**, Formation of formaldehyde tied RCC3 (FT-RCC3) nanofilm by soaking RCC3 nanofilm in formaldehyde solution overnight, wherein adjacent unreacted amines of RCC3 nanofilms were tied up to reduce the cavity size. **d**, Proposed DFT pore size distribution simulated from molecular dynamics for FT-RCC3 nanofilm and RCC3 nanofilm solvated in methanol.

## 1.6.2 Overall Aims

The core aim of this project was to utilise new-generation POCs into membrane materials for water purification for versatile molecule separations. There were five primary objectives:

- To fabricate free-standing, continuous films with high retention activities and stabilities using POCs via two different interfacial synthesis strategies.
- Investigate the growth of POCs at the liquid-liquid interface, and study the effects of POC structure on membrane structure, properties, and stability through the related characterisation.
- Utilise POC based membranes for practical wastewater treatment applications such as dye removal, and evaluate the membrane performance.
- Study the unique properties of POCs in composite membranes, such as precisely controlling the POC membranes' performance with tuneable pore sizes and channels, and explore their potential in new applications.
- Narrow the domestic and international development disparities in advanced materials and membrane technology for various practical fields.

## 1.7 Reference

1. Shannon, M. A. *et al.* Science and technology for water purification in the coming decades. *Nature* vol. 452 301–310 (2008).
2. Schwarzenbach, R. P. *et al.* The Challenge of Micropollutants in Aquatic Systems. *Science* **313**, 1072–1077 (2006).
3. Alsaiee, A. *et al.* Rapid removal of organic micropollutants from water by a porous  $\beta$ -cyclodextrin polymer. *Nature* **529**, 190–194 (2015).
4. Kolpin, D. W. *et al.* Pharmaceuticals, Hormones, and Other Organic Wastewater Contaminants in U.S. Streams, 1999–2000: A National Reconnaissance. *Environ. Sci. Technol.* **36**, 1202–1211 (2002).
5. Tang, J. Y. M., Busetti, F., Charrois, J. W. A. & Escher, B. I. Which chemicals drive biological effects in wastewater and recycled water? *Water Res.* **60**, 289–299 (2014).
6. Werber, J. R., Osuji, C. O. & Elimelech, M. Materials for next-generation desalination

- and water purification membranes. *Nat. Rev. Mater.* **1**, 1–15 (2016).
7. Dey, K. *et al.* Selective molecular separation by interfacially crystallized covalent organic framework thin films. *J. Am. Chem. Soc.* **139**, 13083–13091 (2017).
  8. Das, R. *et al.* Recent advances in nanomaterials for water protection and monitoring. *Chem. Soc. Rev.* **46**, 6946–7020 (2017).
  9. Gin, D. L. & Noble, R. D. Designing the Next Generation of Chemical Separation Membranes. *Science* **332**, 674–676 (2011).
  10. Petersen, R. J. Composite reverse osmosis and nanofiltration membranes. *J. Memb. Sci.* **83**, 81–150 (1993).
  11. Luo, J. & Wan, Y. Effects of pH and salt on nanofiltration—a critical review. *J. Memb. Sci.* **438**, 18–28 (2013).
  12. Mohammad, A. W. *et al.* Nanofiltration membranes review: Recent advances and future prospects. *Desalination* **356**, 226–254 (2015).
  13. Nollet, J. A. *Leçons de physique expérimentale*. vol. 5 (Durand, 1784).
  14. Baker, R. W. *Membrane technology and applications*. (John Wiley & Sons, 2012).
  15. Loeb, S. & Sourirajan, S. Saline water conversion-II. *Adv. Chem. Ser.* **38**, 117 (1963).
  16. Riley, R. L., Merten, U. & Gardner, J. O. Replication electron microscopy of cellulose acetate osmotic membranes. *Desalination* **1**, 30–34 (1966).
  17. Loeb, S. & Selover, E. Sixteen months of field experience on the Coalinga pilot plant. *Desalination* **2**, 75–80 (1967).
  18. Glater, J. The early history of reverse osmosis membrane development. *Desalination* **117**, 297–309 (1998).
  19. Marchetti, P., Jimenez Solomon, M. F., Szekeley, G. & Livingston, A. G. Molecular separation with organic solvent nanofiltration: A critical review. *Chemical Reviews* vol. 114 10735–10806 (2014).
  20. Lonsdale, H. K., Merten, U. & Tagami, M. Phenol transport in cellulose acetate membranes. *J. Appl. Polym. Sci.* **11**, 1807–1820 (1967).
  21. Schäfer, A., Fane, A. G. & Waite, T. D. *Nanofiltration: principles and applications*.

- (Elsevier, 2005).
22. Hazer, B. *et al.* Terminology for membranes and membrane processes. (1996).
  23. Li, N. N., Fane, A. G., Ho, W. S. W. & Matsuura, T. *Advanced membrane technology and applications*. (John Wiley & Sons, 2011).
  24. Saxena, A., Tripathi, B. P., Kumar, M. & Shahi, V. K. Membrane-based techniques for the separation and purification of proteins: An overview. *Adv. Colloid Interface Sci.* **145**, 1–22 (2009).
  25. Crespo, J. G. & Bøddeker, K. W. *Membrane processes in separation and purification*. vol. 272 (Springer Science & Business Media, 2013).
  26. Koros, W. J. & Zhang, C. Materials for next-generation molecularly selective synthetic membranes. *Nat. Mater.* **16**, 289–297 (2017).
  27. Kim, H. J. *et al.* A carbonaceous membrane based on a polymer of intrinsic microporosity (PIM-1) for water treatment. *Sci. Rep.* **6**, 36078 (2016).
  28. Harms, S. *et al.* Aging and free volume in a polymer of intrinsic microporosity (PIM-1). *J. Adhes.* **88**, 608–619 (2012).
  29. Homaeigohar, S. & Elbahri, M. Graphene membranes for water desalination. *NPG Asia Mater.* **9**, e427 (2017).
  30. Slater, A. G. & Cooper, A. I. Function-led design of new porous materials. *Science* **348**, aaa8075 (2015).
  31. Wang, E. N. & Karnik, R. Graphene cleans up water. *Nat. Nanotechnol.* 2012 79 **7**, 552–554 (2012).
  32. Joshi, R. K., Yoshimura, M. & Kumar, A. Graphene. *J. Nanomater.* **2010**, (2011).
  33. Chen, J. H., Jang, C., Xiao, S., Ishigami, M. & Fuhrer, M. S. Intrinsic and extrinsic performance limits of graphene devices on SiO<sub>2</sub>. *Nat. Nanotechnol.* 2008 34 **3**, 206–209 (2008).
  34. Allen, M. J., Tung, V. C. & Kaner, R. B. Honeycomb carbon: a review of graphene. *Chem. Rev.* **110**, 132–145 (2010).
  35. Novoselov, K. S. & Geim, A. K. The rise of graphene. *Nat. Mater* **6**, 183–191 (2007).

36. Compton, O. C. & Nguyen, S. T. Graphene oxide, highly reduced graphene oxide, and graphene: versatile building blocks for carbon-based materials. *small* **6**, 711–723 (2010).
37. Li, B. *et al.* All-Carbon Electronic Devices Fabricated by Directly Grown Single-Walled Carbon Nanotubes on Reduced Graphene Oxide Electrodes. *Adv. Mater.* **22**, 3058–3061 (2010).
38. Acik, M. *et al.* The role of intercalated water in multilayered graphene oxide. *ACS Nano* **4**, 5861–5868 (2010).
39. Sanchez, V. C., Jachak, A., Hurt, R. H. & Kane, A. B. Biological interactions of graphene-family nanomaterials: an interdisciplinary review. *Chem. Res. Toxicol.* **25**, 15–34 (2012).
40. Priyadarsini, S., Mohanty, S., Mukherjee, · Sumit, Basu, S. & Mishra, M. Graphene and graphene oxide as nanomaterials for medicine and biology application. *J. Nanostructure Chem.* 2018 82 **8**, 123–137 (2018).
41. Luo, B., Liu, S. & Zhi, L. Chemical Approaches toward Graphene-Based Nanomaterials and their Applications in Energy-Related Areas. *Small* **8**, 630–646 (2012).
42. Liu, Z., Robinson, J. T., Tabakman, S. M., Yang, K. & Dai, H. Carbon materials for drug delivery & cancer therapy. *Mater. Today* **14**, 316–323 (2011).
43. Yang, Q. *et al.* Ultrathin graphene-based membrane with precise molecular sieving and ultrafast solvent permeation. *Nat. Mater.* **16**, 1198–1202 (2017).
44. Mahalingam, D. K. *et al.* Spray-coated graphene oxide hollow fibers for nanofiltration. *J. Memb. Sci.* **606**, 118006 (2020).
45. Chong, J. Y., Aba, N. F. D., Wang, B., Mattevi, C. & Li, K. UV-enhanced sacrificial layer stabilised graphene oxide hollow fibre membranes for nanofiltration. *Sci. Rep.* **5**, 1–11 (2015).
46. Ding, R. *et al.* Graphene oxide-embedded nanocomposite membrane for solvent resistant nanofiltration with enhanced rejection ability. *Chem. Eng. Sci.* **138**, 227–238 (2015).
47. Surwade, S. P. *et al.* Water desalination using nanoporous single-layer graphene. *Nat. Nanotechnol.* 2015 105 **10**, 459–464 (2015).



48. Lee, K. P., Arnot, T. C. & Mattia, D. A review of reverse osmosis membrane materials for desalination—Development to date and future potential. *J. Memb. Sci.* **370**, 1–22 (2011).
49. Mi, B. Graphene oxide membranes for ionic and molecular sieving. *Science* **343**, 740–742 (2014).
50. Chen, L. *et al.* Ion sieving in graphene oxide membranes via cationic control of interlayer spacing. *Nature* **550**, 380–383 (2017).
51. Iijima, S. Helical microtubules of graphitic carbon. *Nat. 1991 3546348* **354**, 56–58 (1991).
52. Calvert, P. A recipe for strength. *Nat. 1999 3996733* **399**, 210–211 (1999).
53. Baughman, R. H., Zakhidov, A. A. & De Heer, W. A. Carbon nanotubes - The route toward applications. *Science* **297**, 787–792 (2002).
54. Sears, K. *et al.* Recent Developments in Carbon Nanotube Membranes for Water Purification and Gas Separation. *Materials (Basel)*. **3**, 127–149 (2010).
55. Rashid, M. H. O. & Ralph, S. F. Carbon Nanotube Membranes: Synthesis, Properties, and Future Filtration Applications. *Nanomater. 2017, Vol. 7, Page 99* **7**, 99 (2017).
56. Kar, S., Bindal, R. C. & Tewari, P. K. Carbon nanotube membranes for desalination and water purification: Challenges and opportunities. *Nano Today* **7**, 385–389 (2012).
57. Liu, Y., Gao, G. & Vecitis, C. D. Prospects of an Electroactive Carbon Nanotube Membrane toward Environmental Applications. *Acc. Chem. Res.* **53**, 2892–2902 (2020).
58. Hinds, B. J. *et al.* Aligned Multiwalled Carbon Nanotube Membranes. *Science* **303**, 62–65 (2004).
59. Das, R., Ali, M. E., Hamid, S. B. A., Ramakrishna, S. & Chowdhury, Z. Z. Carbon nanotube membranes for water purification: A bright future in water desalination. *Desalination* **336**, 97–109 (2014).
60. Biswas, P. & Wu, & C.-Y. Nanoparticles and the Environment. *J. Air Waste Manage. Assoc.* **55**, 708–746 (2012).
61. Beydoun, D., Amal, R., Low, G. & McEvoy, S. Role of Nanoparticles in Photocatalysis. *J. Nanoparticle Res. 1999 14* **1**, 439–458 (1999).

62. De, M., Ghosh, P. S. & Rotello, V. M. Applications of Nanoparticles in Biology. *Adv. Mater.* **20**, 4225–4241 (2008).
63. Mohanraj, V. J. & Chen, Y. Nanoparticles - A review. *Trop. J. Pharm. Res.* **5**, 561–573 (2007).
64. Bandehali, S. *et al.* A planned review on designing of high-performance nanocomposite nanofiltration membranes for pollutants removal from water. *J. Ind. Eng. Chem.* **101**, 78–125 (2021).
65. Ji, Y. *et al.* Recent developments in nanofiltration membranes based on nanomaterials. *Chinese J. Chem. Eng.* **25**, 1639–1652 (2017).
66. Rajaeian, B., Rahimpour, A., Tade, M. O. & Liu, S. Fabrication and characterization of polyamide thin film nanocomposite (TFN) nanofiltration membrane impregnated with TiO<sub>2</sub> nanoparticles. *Desalination* **313**, 176–188 (2013).
67. Zinadini, S. *et al.* Novel high flux antifouling nanofiltration membranes for dye removal containing carboxymethyl chitosan coated Fe<sub>3</sub>O<sub>4</sub> nanoparticles. *Desalination* **349**, 145–154 (2014).
68. Wang, P. *et al.* Strong improvement of nanofiltration performance on micropollutant removal and reduction of membrane fouling by hydrolyzed-aluminum nanoparticles. *Water Res.* **175**, 115649 (2020).
69. Yap Ang, M. B. M. *et al.* Embedding hollow silica nanoparticles of varying shapes and dimensions in nanofiltration membranes for optimal performance. *J. Memb. Sci.* **611**, 118333 (2020).
70. Cheetham, A. K., Rao, C. N. R. & Feller, R. K. Structural diversity and chemical trends in hybrid inorganic–organic framework materials. *Chem. Commun.* **0**, 4780–4795 (2006).
71. Zimmermann, N. E. R. & Haranczyk, M. History and Utility of Zeolite Framework-Type Discovery from a Data-Science Perspective. *Cryst. Growth Des.* **16**, 3043–3048 (2016).
72. Davis, M. E. & Lobo, R. F. Reviews Zeolite and Molecular Sieve Synthesis. *Chem. Mater* **4**, 756–768 (1992).

73. Cundy, C. S. & Cox, P. A. The hydrothermal synthesis of zeolites: Precursors, intermediates and reaction mechanism. *Microporous Mesoporous Mater.* **82**, 1–78 (2005).
74. Baerlocher, C., McCusker, L. & Olson, D. *Atlas of zeolite framework types.* (2007).
75. Flanigen, E., Jansen, J. & Bekkum, H. van. *Introduction to zeolite science and practice.* (1991).
76. Davis, M. E. Zeolites from a Materials Chemistry Perspective. *Chem. Mater.* **26**, 239–245 (2013).
77. Caro, J., Noack, M., Kölsch, P. & Schäfer, R. Zeolite membranes – state of their development and perspective. *Microporous Mesoporous Mater.* **38**, 3–24 (2000).
78. Rangnekar, N., Mittal, N., Elyassi, B., Caro, J. & Tsapatsis, M. Zeolite membranes – a review and comparison with MOFs. *Chem. Soc. Rev.* **44**, 7128–7154 (2015).
79. Duke, M. C. *et al.* Seawater desalination performance of MFI type membranes made by secondary growth. *Sep. Purif. Technol.* **68**, 343–350 (2009).
80. Zhang, Z., Zhang, L., Wang, S., Chen, W. & Lei, Y. A convenient route to polyacrylonitrile/silver nanoparticle composite by simultaneous polymerization–reduction approach. *Polymer (Guildf).* **42**, 8315–8318 (2001).
81. Phan, A. *et al.* Synthesis, structure, and carbon dioxide capture properties of zeolitic imidazolate frameworks. *Acc. Chem. Res.* **43**, 58–67 (2010).
82. O’Keeffe, M., Peskov, M. A., Ramsden, S. J. & Yaghi, O. M. The Reticular Chemistry Structure Resource (RCSR) Database of, and Symbols for, Crystal Nets. *Acc. Chem. Res.* **41**, 1782–1789 (2008).
83. Hao, Q. *et al.* Confined synthesis of two-dimensional covalent organic framework thin films within superspreading water layer. *J. Am. Chem. Soc.* **140**, 12152–12158 (2018).
84. Yang, L., Wang, Z. & Zhang, J. Zeolite imidazolate framework hybrid nanofiltration (NF) membranes with enhanced permselectivity for dye removal. *J. Memb. Sci.* **532**, 76–86 (2017).
85. Mirqasemi, M. S., Homayoonfal, M. & Rezakazemi, M. Zeolitic imidazolate framework membranes for gas and water purification. *Environ. Chem. Lett.* **2019 181** **18**, 1–52

- (2019).
86. Ramu, G., Lee, M. & Jeong, H. K. Effects of zinc salts on the microstructure and performance of zeolitic-imidazolate framework ZIF-8 membranes for propylene/propane separation. *Microporous Mesoporous Mater.* **259**, 155–162 (2018).
  87. Yang, T. & Chung, T. S. High performance ZIF-8/PBI nano-composite membranes for high temperature hydrogen separation consisting of carbon monoxide and water vapor. *Int. J. Hydrogen Energy* **38**, 229–239 (2013).
  88. Cheng, X. *et al.* Water-selective permeation in hybrid membrane incorporating multi-functional hollow ZIF-8 nanospheres. *J. Memb. Sci.* **555**, 146–156 (2018).
  89. Wang, N. *et al.* Nanoconfined Zeolitic Imidazolate Framework Membranes with Composite Layers of Nearly Zero Thickness. *ACS Appl. Mater. Interfaces* **8**, 21979–21983 (2016).
  90. Yaghi, O. M. & Li, H. Hydrothermal Synthesis of a Metal-Organic Framework Containing Large Rectangular Channels. *J. Am. Chem. Soc.* **117**, 10401–10402 (1995).
  91. Chui, S. S. Y., Lo, S. M. F., Charmant, J. P. H., Orpen, A. G. & Williams, I. D. A chemically functionalizable nanoporous material [Cu<sub>3</sub>(TMA)<sub>2</sub>(H<sub>2</sub>O)<sub>3</sub>](n). *Science* **283**, 1148–1150 (1999).
  92. Li, H., Eddaoudi, M., O’Keeffe, M. & Yaghi, O. M. Design and synthesis of an exceptionally stable and highly porous metal-organic framework. *Nat.* 1999 4026759 **402**, 276–279 (1999).
  93. Zhou, H. C. J. & Kitagawa, S. Metal–Organic Frameworks (MOFs). *Chem. Soc. Rev.* **43**, 5415–5418 (2014).
  94. Stock, N. & Biswas, S. Synthesis of Metal-Organic Frameworks (MOFs): Routes to Various MOF Topologies, Morphologies, and Composites. *Chem. Rev.* **112**, 933–969 (2011).
  95. Janiak, C. & Vieth, J. K. MOFs, MILs and more: concepts, properties and applications for porous coordination networks (PCNs). *New J. Chem.* **34**, 2366–2388 (2010).
  96. Lin, Z. J., Lü, J., Hong, M. & Cao, R. Metal–organic frameworks based on flexible ligands (FL-MOFs): structures and applications. *Chem. Soc. Rev.* **43**, 5867–5895 (2014).

97. Rowsell, J. L. C. & Yaghi, O. M. Metal–organic frameworks: a new class of porous materials. *Microporous Mesoporous Mater.* **73**, 3–14 (2004).
98. Wang, S., McGuirk, C. M., d’Aquino, A., Mason, J. A. & Mirkin, C. A. Metal–Organic Framework Nanoparticles. *Adv. Mater.* **30**, 1800202 (2018).
99. Zhao, Y. *et al.* Metal-organic framework based membranes for selective separation of target ions. *J. Memb. Sci.* **634**, 119407 (2021).
100. Boorboor Ajdari, F. *et al.* A review on the field patents and recent developments over the application of metal organic frameworks (MOFs) in supercapacitors. *Coord. Chem. Rev.* **422**, 213441 (2020).
101. Sharanyakanth, P. S. & Radhakrishnan, M. Synthesis of metal-organic frameworks (MOFs) and its application in food packaging: A critical review. *Trends Food Sci. Technol.* **104**, 102–116 (2020).
102. Khan, N. A., Hasan, Z. & Jhung, S. H. Beyond pristine metal-organic frameworks: Preparation and application of nanostructured, nanosized, and analogous MOFs. *Coord. Chem. Rev.* **376**, 20–45 (2018).
103. Jiang, D. *et al.* The application of different typological and structural MOFs-based materials for the dyes adsorption. *Coord. Chem. Rev.* **380**, 471–483 (2019).
104. Falcaro, P. *et al.* Application of metal and metal oxide nanoparticles@MOFs. *Coord. Chem. Rev.* **307**, 237–254 (2016).
105. Abánades Lázaro, I. & Forgan, R. S. Application of zirconium MOFs in drug delivery and biomedicine. *Coord. Chem. Rev.* **380**, 230–259 (2019).
106. Dhaka, S. *et al.* Metal–organic frameworks (MOFs) for the removal of emerging contaminants from aquatic environments. *Coord. Chem. Rev.* **380**, 330–352 (2019).
107. Vaid, T. P., Lobkovsky, E. B. & Wolczanski, P. T. Covalent 3- and 2-dimensional titanium-quinone networks. *J. Am. Chem. Soc.* **119**, 8742–8743 (1997).
108. MacGillivray, L. R., Groeneman, R. H. & Atwood, J. L. Design and self-assembly of cavity-containing rectangular grids [14]. *J. Am. Chem. Soc.* **120**, 2676–2677 (1998).
109. Zaworotko, M. J. Cooperative bonding affords a wholesome story. *Nature* **386**, 220–221 (1997).

110. Seoane, B. *et al.* Metal–organic framework based mixed matrix membranes: a solution for highly efficient CO<sub>2</sub> capture? *Chem. Soc. Rev.* **44**, 2421–2454 (2015).
111. Caro, J. Are MOF membranes better in gas separation than those made of zeolites? *Curr. Opin. Chem. Eng.* **1**, 77–83 (2011).
112. Adatoz, E., Avci, A. K. & Keskin, S. Opportunities and challenges of MOF-based membranes in gas separations. *Sep. Purif. Technol.* **152**, 207–237 (2015).
113. Liu, G. *et al.* Mixed matrix formulations with MOF molecular sieving for key energy-intensive separations. *Nat. Mater.* **17**, 283–289 (2018).
114. Qiu, S., Xue, M. & Zhu, G. Metal–organic framework membranes: from synthesis to separation application. *Chem. Soc. Rev.* **43**, 6116–6140 (2014).
115. Xu, Y. *et al.* Highly stable MIL-101(Cr) doped water permeable thin film nanocomposite membranes for water treatment. *RSC Adv.* **6**, 82669–82675 (2016).
116. Van Goethem, C., Verbeke, R., Hermans, S., Bernstein, R. & Vankelecom, I. F. J. Controlled positioning of MOFs in interfacially polymerized thin-film nanocomposites. *J. Mater. Chem. A* **4**, 16368–16376 (2016).
117. Liu, X., Demir, N. K., Wu, Z. & Li, K. Highly Water-Stable Zirconium Metal-Organic Framework UiO-66 Membranes Supported on Alumina Hollow Fibers for Desalination. *J. Am. Chem. Soc.* **137**, 6999–7002 (2015).
118. Wang, X. *et al.* Improving Water-Treatment Performance of Zirconium Metal-Organic Framework Membranes by Postsynthetic Defect Healing. *ACS Appl. Mater. Interfaces* **9**, 37848–37855 (2017).
119. Sorribas, S., Gorgojo, P., Téllez, C., Coronas, J. & Livingston, A. G. High flux thin film nanocomposite membranes based on metal-organic frameworks for organic solvent nanofiltration. *J. Am. Chem. Soc.* **135**, 15201–15208 (2013).
120. Severin, K. Boronic acids as building blocks for molecular nanostructures and polymeric materials. *Dalt. Trans.* **0**, 5254–5264 (2009).
121. Feng, X., Ding, X. & Jiang, D. Covalent organic frameworks. *Chem. Soc. Rev.* **41**, 6010–6022 (2012).
122. Côté, A. P. *et al.* Chemistry: Porous, crystalline, covalent organic frameworks. *Science*



- 310**, 1166–1170 (2005).
123. Furukawa, H. & Yaghi, O. M. Storage of hydrogen, methane, and carbon dioxide in highly porous covalent organic frameworks for clean energy applications. *J. Am. Chem. Soc.* **131**, 8875–8883 (2009).
  124. Yusran, Y., Li, H., Guan, X., Fang, Q. & Qiu, S. Covalent Organic Frameworks for Catalysis. *EnergyChem* **2**, 100035 (2020).
  125. El-Kaderi, H. M. *et al.* Designed synthesis of 3D covalent organic frameworks. *Science* **316**, 268–272 (2007).
  126. Deblase, C. R., Silberstein, K. E., Truong, T. T., Abruña, H. D. & Dichtel, W. R.  $\beta$ -ketoenamine-linked covalent organic frameworks capable of pseudocapacitive energy storage. *J. Am. Chem. Soc.* **135**, 16821–16824 (2013).
  127. Zhuang, S., Liu, Y. & Wang, J. Covalent organic frameworks as efficient adsorbent for sulfamerazine removal from aqueous solution. *J. Hazard. Mater.* **383**, 121126 (2020).
  128. Ding, X. *et al.* Synthesis of Metallophthalocyanine Covalent Organic Frameworks That Exhibit High Carrier Mobility and Photoconductivity. *Angew. Chemie Int. Ed.* **50**, 1289–1293 (2011).
  129. Wu, M. X. & Yang, Y. W. Applications of covalent organic frameworks (COFs): From gas storage and separation to drug delivery. *Chinese Chem. Lett.* **28**, 1135–1143 (2017).
  130. Zhang, X. *et al.* In-situ grown covalent organic framework nanosheets on graphene for membrane-based dye/salt separation. *J. Memb. Sci.* **581**, 321–330 (2019).
  131. Yuan, S. *et al.* Covalent organic frameworks for membrane separation. *Chem. Soc. Rev.* **48**, 2665–2681 (2019).
  132. Duan, K., Wang, J., Zhang, Y. & Liu, J. Covalent organic frameworks (COFs) functionalized mixed matrix membrane for effective CO<sub>2</sub>/N<sub>2</sub> separation. *J. Memb. Sci.* **572**, 588–595 (2019).
  133. Fan, H. *et al.* Covalent Organic Framework-Covalent Organic Framework Bilayer Membranes for Highly Selective Gas Separation. *J. Am. Chem. Soc.* **140**, 10094–10098 (2018).
  134. Biswal, B. P., Chaudhari, H. D., Banerjee, R. & Kharul, U. K. Chemically Stable

- Covalent Organic Framework (COF)-Polybenzimidazole Hybrid Membranes: Enhanced Gas Separation through Pore Modulation. *Chem. – A Eur. J.* **22**, 4695–4699 (2016).
135. Shan, M. *et al.* Azine-Linked Covalent Organic Framework (COF)-Based Mixed-Matrix Membranes for CO<sub>2</sub>/CH<sub>4</sub> Separation. *Chem. – A Eur. J.* **22**, 14467–14470 (2016).
  136. Shinde, D. B. *et al.* Crystalline 2D covalent organic framework membranes for high-flux organic solvent nanofiltration. doi:10.1021/jacs.8b08788.
  137. Li, C. *et al.* Covalent organic frameworks (COFs)-incorporated thin film nanocomposite (TFN) membranes for high-flux organic solvent nanofiltration (OSN). *J. Memb. Sci.* **572**, 520–531 (2019).
  138. Zhang, W., Zhang, L., Zhao, H., Li, B. & Ma, H. A two-dimensional cationic covalent organic framework membrane for selective molecular sieving. *J. Mater. Chem. A* **6**, 13331–13339 (2018).
  139. Gadwal, I. *et al.* Synthesis of sub-10 nm two-dimensional covalent organic thin film with sharp molecular sieving nanofiltration. *ACS Appl. Mater. Interfaces* **10**, 1 (2018).
  140. Li, J., Zhou, X., Wang, J. & Li, X. Two-Dimensional Covalent Organic Frameworks (COFs) for Membrane Separation: a Mini Review. *Ind. Eng. Chem. Res.* **58**, 15394–15406 (2019).
  141. Kandambeth, S. *et al.* Selective molecular sieving in self-standing porous covalent-organic-framework membranes. *Adv. Mater.* **29**, 1603945 (2017).
  142. Valentino, L., Matsumoto, M., Dichtel, W. R. & Marinas, B. J. Development and performance characterization of a polyimine covalent organic framework thin-film composite nanofiltration membrane. *Environ. Sci. Technol.* **51**, 14352–14359 (2017).
  143. Wang, B., Lin, R. B., Zhang, Z., Xiang, S. & Chen, B. Hydrogen-Bonded Organic Frameworks as a Tunable Platform for Functional Materials. *J. Am. Chem. Soc.* **142**, 14399–14416 (2020).
  144. Yang, J. *et al.* Porous hydrogen-bonded organic frameworks (HOFs): From design to potential applications. *Chem. Eng. J.* **399**, 125873 (2020).
  145. Han, Y. F., Yuan, Y. X. & Wang, H. B. Porous Hydrogen-Bonded Organic Frameworks.

*Mol.* 2017, Vol. 22, Page 266 **22**, 266 (2017).

146. Hisaki, I., Xin, C., Takahashi, K. & Nakamura, T. Designing Hydrogen-Bonded Organic Frameworks (HOFs) with Permanent Porosity. *Angew. Chemie - Int. Ed.* **58**, 11160–11170 (2019).
147. Cooper, A. I. & Cooper, [ A I. Molecular Organic Crystals: From Barely Porous to Really Porous. *Angew. Chemie Int. Ed.* **51**, 7892–7894 (2012).
148. Desiraju, G. R., David, P., Curtin, Y., Lain, P. & Paul, C. Supramolecular Synthons in Crystal Engineering—A New Organic Synthesis. *Angew. Chemie Int. Ed. English* **34**, 2311–2327 (1995).
149. He, Y., Xiang, S. & Chen, B. A microporous hydrogen-bonded organic framework for highly selective C<sub>2</sub>H<sub>2</sub>/C<sub>2</sub>H<sub>4</sub> separation at ambient temperature. *J. Am. Chem. Soc.* **133**, 14570–14573 (2011).
150. Yang, W. *et al.* Exceptional thermal stability in a supramolecular organic framework: Porosity and gas storage. *J. Am. Chem. Soc.* **132**, 14457–14469 (2010).
151. Mastalerz, M. & Oppel, I. M. Rational Construction of an Extrinsic Porous Molecular Crystal with an Extraordinary High Specific Surface Area. *Angew. Chemie Int. Ed.* **51**, 5252–5255 (2012).
152. Lin, R. B. *et al.* Multifunctional porous hydrogen-bonded organic framework materials. *Chem. Soc. Rev.* **48**, 1362–1389 (2019).
153. Beatty, A. M. Open-framework coordination complexes from hydrogen-bonded networks: toward host/guest complexes. *Coord. Chem. Rev.* **246**, 131–143 (2003).
154. Li, P. *et al.* A Rod-Packing Microporous Hydrogen-Bonded Organic Framework for Highly Selective Separation of C<sub>2</sub>H<sub>2</sub>/CO<sub>2</sub> at Room Temperature. *Angew. Chemie Int. Ed.* **54**, 574–577 (2015).
155. Feng, S. *et al.* Fabrication of a Hydrogen-Bonded Organic Framework Membrane through Solution Processing for Pressure-Regulated Gas Separation. *Angew. Chemie* **132**, 3868–3873 (2020).
156. Li, W., Li, Y., Caro, J. & Huang, A. Fabrication of a flexible hydrogen-bonded organic framework based mixed matrix membrane for hydrogen separation. *J. Memb. Sci.* **643**,

- 120021 (2022).
157. Ma, C., Urban, J. J., Ma, C. & Urban, J. J. Hydrogen-Bonded Polyimide/Metal-Organic Framework Hybrid Membranes for Ultrafast Separations of Multiple Gas Pairs. *Adv. Funct. Mater.* **29**, 1903243 (2019).
  158. Gong, W. *et al.* Permanent porous hydrogen-bonded frameworks with two types of Brønsted acid sites for heterogeneous asymmetric catalysis. *Nat. Commun.* **10**, 1–9 (2019).
  159. Kuznetsova, S. A. *et al.* The charge-assisted hydrogen-bonded organic framework (CAHOF) self-assembled from the conjugated acid of tetrakis(4-aminophenyl)methane and 2,6-naphthalenedisulfonate as a new class of recyclable Brønsted acid catalysts. *Beilstein J. Org. Chem.* **16**, 1124–1134 (2020).
  160. Chand, S. *et al.* Metallo Hydrogen-Bonded Organic Frameworks (MHOFs) as New Class of Crystalline Materials for Protonic Conduction. *Chem. – A Eur. J.* **25**, 1691–1695 (2019).
  161. Yang, Q. *et al.* Three Hydrogen-Bonded Organic Frameworks with Water-Induced Single-Crystal-to-Single-Crystal Transformation and High Proton Conductivity. *Cryst. Growth Des.* **20**, 3456–3465 (2020).
  162. Jiang, X. T. *et al.* Porous hydrogen-bonded organic framework membranes for high-performance molecular separation. *Nanoscale Adv.* **3**, 3441–3446 (2021).
  163. Kaur, P., Hupp, J. T. & Nguyen, S. T. Porous Organic Polymers in Catalysis: Opportunities and Challenges. *ACS Catal.* **1**, 819–835 (2011).
  164. Zou, L. *et al.* Porous Organic Polymers for Post-Combustion Carbon Capture. *Adv. Mater.* **29**, 1700229 (2017).
  165. Zhang, Y. & Riduan, S. N. Functional porous organic polymers for heterogeneous catalysis. *Chem. Soc. Rev.* **41**, 2083–2094 (2012).
  166. Bojdys, M. J., Jeromenok, J., Thomas, A. & Antonietti, M. Rational Extension of the Family of Layered, Covalent, Triazine-Based Frameworks with Regular Porosity. *Adv. Mater.* **22**, 2202–2205 (2010).
  167. Liu, M., Guo, L., Jin, S. & Tan, B. Covalent triazine frameworks: synthesis and

- applications. *J. Mater. Chem. A* **7**, 5153–5172 (2019).
168. Xu, Y., Jin, S., Xu, H., Nagai, A. & Jiang, D. Conjugated microporous polymers : design, synthesis and application. *Chem. Soc. Rev.* **42**, 8012–8031 (2013).
  169. Cooper, A. I. Conjugated Microporous Polymers. *Adv. Mater.* **21**, 1291–1295 (2009).
  170. Dawson, R. *et al.* Functionalized conjugated microporous polymers. *Macromolecules* **42**, 8809–8816 (2009).
  171. Xie, Y., Wang, T. T., Liu, X. H., Zou, K. & Deng, W. Q. Capture and conversion of CO<sub>2</sub> at ambient conditions by a conjugated microporous polymer. *Nat. Commun.* **2013** *4*, 1–7 (2013).
  172. Ben, T. *et al.* Targeted Synthesis of a Porous Aromatic Framework with High Stability and Exceptionally High Surface Area. *Angew. Chemie Int. Ed.* **48**, 9457–9460 (2009).
  173. Furukawa, H., Cordova, K. E., O’Keeffe, M. & Yaghi, O. M. The chemistry and applications of metal-organic frameworks. *Science* **341**, (2013).
  174. Kearsley, R. Investigation into [4+6] porous organic cages and their use in porous liquids. *Univ. Liverpool Repos.* PhD Thesis (2020) doi:10.17638/03115599.
  175. Woodward, R. T. *et al.* Swellable, water- and acid-tolerant polymer sponges for chemoselective carbon dioxide capture. *J. Am. Chem. Soc.* **136**, 9028–9035 (2014).
  176. Jiang, J. X. & Cooper, A. I. Microporous Organic Polymers: Design, Synthesis, and Function. *Top. Curr. Chem.* **293**, 1–33 (2009).
  177. Liu, Y. *et al.* Porous organic polymer embedded thin-film nanocomposite membranes for enhanced nanofiltration performance. *J. Memb. Sci.* **602**, 117982 (2020).
  178. Liang, B. *et al.* Microporous membranes comprising conjugated polymers with rigid backbones enable ultrafast organic-solvent nanofiltration. *Nat. Chem.* **2018** *109* **10**, 961–967 (2018).
  179. Hou, R. *et al.* Greatly Enhanced Gas Selectivity in Mixed-Matrix Membranes through Size-Controlled Hyper-cross-linked Polymer Additives. *Ind. Eng. Chem. Res.* **59**, 13773–13782 (2020).
  180. Li, G., Wang, W., Fang, Q. & Liu, F. Covalent triazine frameworks membrane with highly ordered skeleton nanopores for robust and precise molecule/ion separation. *J.*

- Memb. Sci.* **595**, 117525 (2020).
181. Budd, P. M. *et al.* Polymers of intrinsic microporosity (PIMs): robust, solution-processable, organic nanoporous materials. *Chem. Commun.* **0**, 230–231 (2004).
  182. Mc Keown, N. B. & Budd, P. M. Polymers of intrinsic microporosity (PIMs): organic materials for membrane separations, heterogeneous catalysis and hydrogen storage. *Chem. Soc. Rev.* **35**, 675–683 (2006).
  183. Mckeown, N. B., Gan, Y. X. & Jiang, Z. Polymers of Intrinsic Microporosity. *Int. Sch. Res. Netw. ISRN Mater. Sci.* **2012**, 16 (2012).
  184. McKeown, N. B., Hanif, S., Msayib, K., Tattershall, C. E. & Budd, P. M. Porphyrin -based nanoporous network polymers. *Chem. Commun.* **0**, 2782–2783 (2002).
  185. McKeown, N. B., Makhseed, S. & Budd, P. M. Phthalocyanine -based nanoporous network polymers. *Chem. Commun.* **0**, 2780–2781 (2002).
  186. Scherf, U. Ladder-type materials. *J. Mater. Chem.* **9**, 1853–1864 (1999).
  187. Ahmad, M. Z., Castro-Munõz, R. & Budd, P. M. Boosting gas separation performance and suppressing the physical aging of polymers of intrinsic microporosity (PIM-1) by nanomaterial blending. *Nanoscale* **12**, 23333–23370 (2020).
  188. Wang, Y. *et al.* Polymers of intrinsic microporosity for energy-intensive membrane-based gas separations. *Mater. Today Nano* **3**, 69–95 (2018).
  189. Ma, C. Polymers of Intrinsic Microporosity (PIMs) Gas Separation Membranes: A mini Review. (2018) doi:10.11605/j.pnrs.201802002.
  190. Budd, P. M. *et al.* Gas separation membranes from polymers of intrinsic microporosity. *J. Memb. Sci.* **251**, 263–269 (2005).
  191. Gorgojo, P. *et al.* Ultrathin Polymer Films with Intrinsic Microporosity: Anomalous Solvent Permeation and High Flux Membranes. *Adv. Funct. Mater.* **24**, 4729–4737 (2014).
  192. Fritsch, D., Merten, P., Heinrich, K., Lazar, M. & Priske, M. High performance organic solvent nanofiltration membranes: Development and thorough testing of thin film composite membranes made of polymers of intrinsic microporosity (PIMs). *J. Memb. Sci.* **401–402**, 222–231 (2012).

193. Gao, J., Japip, S. & Chung, T. S. Organic solvent resistant membranes made from a cross-linked functionalized polymer with intrinsic microporosity (PIM) containing thioamide groups. *Chem. Eng. J.* **353**, 689–698 (2018).
194. Zhou, S., Zhao, Y., Zheng, J. & Zhang, S. High-performance functionalized polymer of intrinsic microporosity (PIM) composite membranes with thin and stable interconnected layer for organic solvent nanofiltration. *J. Memb. Sci.* **591**, 117347 (2019).
195. Wu, H. *et al.* Unusual and highly tunable missing-linker defects in zirconium metal-organic framework UiO-66 and their important effects on gas adsorption. *J. Am. Chem. Soc.* **135**, 10525–10532 (2013).
196. Little, M. A. & Cooper, A. I. The chemistry of porous organic molecular materials. *Adv. Funct. Mater.* 1909842 (2020) doi:10.1002/adfm.201909842.
197. Zhang, G. & Mastalerz, M. Organic cage compounds – from shape-persistency to function. *Chem. Soc. Rev.* **43**, 1934–1947 (2014).
198. Hasell, T. & Cooper, A. I. Porous organic cages: soluble, modular and molecular pores. *Nat. Rev. Mater.* 2016 19 **1**, 1–14 (2016).
199. Atwood, J. L., Barbour, L. J. & Jerga, A. Storage of methane and freon by interstitial van der Waals confinement. *Science* **296**, 2367–2369 (2002).
200. Atwood, J. L., Barbour, L. J., Jerga, A. & Schottel, B. L. Guest transport in a nonporous organic solid via dynamic van der Waals cooperativity. *Science* **298**, 1000–1002 (2002).
201. Jie, K. *et al.* Near-Ideal Xylene Selectivity in Adaptive Molecular Pillar[ n]arene Crystals. *J. Am. Chem. Soc.* **140**, 6921–6930 (2018).
202. Lim, S. *et al.* Cucurbit[6]uril: Organic Molecular Porous Material with Permanent Porosity, Exceptional Stability, and Acetylene Sorption Properties. *Angew. Chemie* **120**, 3400–3403 (2008).
203. Tozawa, T. *et al.* Porous organic cages. *Nat. Mater.* **8**, 973–978 (2009).
204. Joseph, A. I., Lapidus, S. H., Kane, C. M. & Holman, K. T. Extreme confinement of xenon by cryptophane-111 in the solid state. *Angew. Chemie - Int. Ed.* **54**, 1471–1475 (2015).
205. Hopf, H. & Doering, W. von E. (William V. E. Classics in Hydrocarbon Chemistry:



- Syntheses, Concepts, Perspectives. 547 (2000) doi:10.3/JQUERY-UIJS.
206. Belowich, M. E. & Stoddart, J. F. Dynamic imine chemistry. *Chem. Soc. Rev.* **41**, 2003–2024 (2012).
  207. Skowronek, P. & Gawronski, J. Chiral iminospherand of a tetrahedral symmetry spontaneously assembled in a [6 + 4] cyclocondensation. *Org. Lett.* **10**, 4755–4758 (2008).
  208. Hasell, T., Chong, S. Y., Jelfs, K. E., Adams, D. J. & Cooper, A. I. Porous organic cage nanocrystals by solution mixing. *J. Am. Chem. Soc.* **134**, 588–598 (2012).
  209. Liu, M. *et al.* Barely porous organic cages for hydrogen isotope separation. *Science* **366**, 613–620 (2019).
  210. Chen, L. *et al.* Separation of rare gases and chiral molecules by selective binding in porous organic cages. *Nat. Mater.* **13**, 954–960 (2014).
  211. Mitra, T. *et al.* A Soft Porous Organic Cage Crystal with Complex Gas Sorption Behavior. *Chem. – A Eur. J.* **17**, 10235–10240 (2011).
  212. Jones, J. T. A. *et al.* Modular and predictable assembly of porous organic molecular crystals. *Nature* **474**, 367 (2011).
  213. Jiang, S. Synthesis and simulation of porous organic cages. *Univ. Liverpool Repos.* PhD Thesis (2012).
  214. Greenaway, R. L. *et al.* High-throughput discovery of organic cages and catenanes using computational screening fused with robotic synthesis. *Nat. Commun.* **9**, 2849 (2018).
  215. Liu, X., Liu, Y., Li, G. & Warmuth, R. One-Pot, 18-Component Synthesis of an Octahedral Nanocontainer Molecule. *Angew. Chemie Int. Ed.* **45**, 901–904 (2006).
  216. Liu, X. & Warmuth, R. Solvent effects in thermodynamically controlled multicomponent nanocage syntheses. *J. Am. Chem. Soc.* **128**, 14120–14127 (2006).
  217. Lauer, J. C., Zhang, W. S., Rominger, F., Schröder, R. R. & Mastalerz, M. Shape-Persistent [4+4] Imine Cages with a Truncated Tetrahedral Geometry. *Chem. – A Eur. J.* **24**, 1816–1820 (2018).
  218. Mastalerz, M., Schneider, M. W., Oppel, I. M. & Presly, O. A Salicylbisimine Cage Compound with High Surface Area and Selective CO<sub>2</sub>/CH<sub>4</sub> Adsorption. *Angew.*

- Chemie Int. Ed.* **50**, 1046–1051 (2011).
219. Zhang, G. & Mastalerz, M. Organic cage compounds – from shape-persistency to function. *Chem. Soc. Rev.* **43**, 1934–1947 (2014).
220. Katz, J. L., Selby, K. J. & Conry, R. R. Single-step synthesis of D<sub>3h</sub>-symmetric bicyclooxacalixarenes. *Org. Lett.* **7**, 3505–3507 (2005).
221. Mastalerz, M., Schneider, M. W., Oppel, I. M. & Presly, O. A Salicylbisimine Cage Compound with High Surface Area and Selective CO<sub>2</sub>/CH<sub>4</sub> Adsorption. *Angew. Chemie Int. Ed.* **50**, 1046–1051 (2011).
222. Avellaneda, A. *et al.* Kinetically Controlled Porosity in a Robust Organic Cage Material. *Angew. Chemie Int. Ed.* **52**, 3746–3749 (2013).
223. Zhang, G., Presly, O., White, F., Oppel, I. M. & Mastalerz, M. A Permanent Mesoporous Organic Cage with an Exceptionally High Surface Area. *Angew. Chemie* **126**, 1542–1546 (2014).
224. Evans, J. D., Sumbly, C. J. & Doonan, C. J. Synthesis and Applications of Porous Organic Cages. *Chem. Lett* **44**, 582–588 (2015).
225. Klotzbach, S., Scherpf, T. & Beuerle, F. Dynamic covalent assembly of tribenzotriquinacenes into molecular cubes. *Chem. Commun.* **50**, 12454–12457 (2014).
226. Icli, B. *et al.* Dative boron– nitrogen bonds in structural supramolecular chemistry: multicomponent assembly of prismatic organic cages. *Chem. Sci.* **2**, 1719–1721 (2011).
227. Bull, S. D. *et al.* Exploiting the Reversible Covalent Bonding of Boronic Acids: Recognition, Sensing, and Assembly. *Acc. Chem. Res.* **46**, 312–326 (2012).
228. Ono, K. *et al.* Self-Assembly of Nanometer-Sized Boroxine Cages from Diboronic Acids. *J. Am. Chem. Soc.* **137**, 7015–7018 (2015).
229. Wang, Q. *et al.* Dynamic covalent synthesis of arylenethynylene cages through alkyne metathesis: dimer, tetramer, or interlocked complex? *Chem. Sci.* **7**, 3370–3376 (2016).
230. Wang, Q. *et al.* Solution-Phase Dynamic Assembly of Permanently Interlocked Arylenethynylene Cages through Alkyne Metathesis. *Angew. Chemie* **127**, 7660–7664 (2015).
231. Lee, S., Yang, A., Moneypenny, T. P. & Moore, J. S. Kinetically Trapped Tetrahedral

- Cages via Alkyne Metathesis. *J. Am. Chem. Soc.* **138**, 2182–2185 (2016).
232. Schneider, M. W. *et al.* Exo-Functionalized Shape-Persistent [2+3] Cage Compounds: Influence of Molecular Rigidity on Formation and Permanent Porosity. *Chem. – A Eur. J.* **18**, 4156–4160 (2012).
233. Schneider, M. W. *et al.* Periphery-Substituted [4+6] Salicylbisimine Cage Compounds with Exceptionally High Surface Areas: Influence of the Molecular Structure on Nitrogen Sorption Properties. *Chem. – A Eur. J.* **18**, 836–847 (2012).
234. Hasell, T. & Cooper, A. I. Porous organic cages: soluble, modular and molecular pores. *Nat. Rev. Mater.* **1**, 16053 (2016).
235. Crane, K., Pinkall, U. & Schröder, P. Robust fairing via conformal curvature flow. *ACM Trans. Graph.* **32**, 61 (2013).
236. Jiang, S. *et al.* Selective gas sorption in a [2+3] ‘propeller’ cage crystal. *Chem. Commun.* **47**, 8919 (2011).
237. Jelfs, K. E. *et al.* Large Self-Assembled Chiral Organic Cages: Synthesis, Structure, and Shape Persistence. *Angew. Chemie* **123**, 10841–10844 (2011).
238. Briggs, M. E. *et al.* Shape prediction for supramolecular organic nanostructures: [4 + 4] macrocyclic tetrapods. *Cryst. Growth Des.* **13**, 4993–5000 (2013).
239. Slater, A. G. *et al.* Reticular synthesis of porous molecular 1D nanotubes and 3D networks. *Nat. Chem.* **9**, 17–25 (2016).
240. Brutschy, M., Schneider, M. W., Mastalerz, M. & Waldvogel, S. R. Porous Organic Cage Compounds as Highly Potent Affinity Materials for Sensing by Quartz Crystal Microbalances. *Adv. Mater.* **24**, 6049–6052 (2012).
241. Evans, J. D. *et al.* Feasibility of mixed matrix membrane gas separations employing porous organic cages. *J. Phys. Chem. C* **118**, 1523–1529 (2014).
242. Bushell, A. F. *et al.* Nanoporous organic polymer/cage composite membranes. *Angew. Chemie Int. Ed.* **52**, 1253–1256 (2013).
243. Song, Q. *et al.* Porous organic cage thin films and molecular-sieving membranes. *Adv. Mater.* **28**, 2629–2637 (2016).
244. Hasell, T., Schmidtman, M., Stone, C. A., Smith, M. W. & Cooper, A. I. Reversible

- water uptake by a stable imine-based porous organic cage. *Chem. Commun.* **48**, 4689–4691 (2012).
245. Jones, J. T. A. *et al.* On-off porosity switching in a molecular organic solid. *Angew. Chemie Int. Ed.* **50**, 749–753 (2011).
246. Koros, W. J. & Mahajan, R. Pushing the limits on possibilities for large scale gas separation: which strategies? *J. Memb. Sci.* **175**, 181–196 (2000).
247. Meitl, M. A. *et al.* Solution Casting and Transfer Printing Single-Walled Carbon Nanotube Films. *Nano Lett.* **4**, 1643–1647 (2004).
248. Souza, V. C. & Quadri, M. G. N. Organic-inorganic hybrid membranes in separation processes: a 10-year review. **30**, 683–700.
249. See Toh, Y. H., Lim, F. W. & Livingston, A. G. Polymeric membranes for nanofiltration in polar aprotic solvents. *J. Memb. Sci.* **301**, 3–10 (2007).
250. Zhang, Y., Sunarso, J., Liu, S. & Wang, R. Current status and development of membranes for CO<sub>2</sub>/CH<sub>4</sub> separation: A review. *Int. J. Greenh. Gas Control* **12**, 84–107 (2013).
251. Abedini, R. & Nezhadmoghadam, A. Application of membrane in gas separation processes: its suitability and mechanisms. *Pet. Coal* **52**, 69–80 (2010).
252. Ghadimi, A., Mohammadi, T. & Kasiri, N. A Novel Chemical Surface Modification for the Fabrication of PEBA/SiO<sub>2</sub> Nanocomposite Membranes To Separate CO<sub>2</sub> from Syngas and Natural Gas Streams. *Ind. Eng. Chem. Res.* **53**, 17476–17486 (2014).
253. Vandezande, P., Gevers, L. E. M. & Vankelecom, I. F. J. Solvent resistant nanofiltration: separating on a molecular level. *Chem. Soc. Rev.* **37**, 365–405 (2008).
254. Marchetti, P., Jimenez Solomon, M. F., Szekeley, G. & Livingston, A. G. Molecular separation with organic solvent nanofiltration: a critical review. *Chem. Rev.* **114**, 10735–10806 (2014).
255. Lau, W. J., Ismail, A. F., Misdan, N. & Kassim, M. A. A recent progress in thin film composite membrane: A review. *Desalination* **287**, 190–199 (2012).
256. Riley, P. L., Milstead, C. E., Lloyd, A. L., Seroy, M. W. & Tagami, M. Spiral-wound thin-film composite membrane systems for brackish and seawater desalination by

- reverse osmosis. *Desalination* **23**, 331–355 (1977).
257. Kim, I. C., Jegal, J. & Lee, K. H. Effect of aqueous and organic solutions on the performance of polyamide thin-film-composite nanofiltration membranes. *J. Polym. Sci. Part B Polym. Phys.* **40**, 2151–2163 (2002).
258. Kosaraju, P. B. & Sirkar, K. K. Interfacially polymerized thin film composite membranes on microporous polypropylene supports for solvent-resistant nanofiltration. *J. Memb. Sci.* **321**, 155–161 (2008).
259. Jimenez Solomon, M. F., Bhole, Y. & Livingston, A. G. High flux membranes for organic solvent nanofiltration (OSN)—Interfacial polymerization with solvent activation. *J. Memb. Sci.* **423–424**, 371–382 (2012).
260. Gorgojo, P. *et al.* Ultrathin Polymer Films with Intrinsic Microporosity: Anomalous Solvent Permeation and High Flux Membranes. *Adv. Funct. Mater.* **24**, 4729–4737 (2014).
261. Bernardo, P. & Clarizia, G. 30 Years of Membrane Technology for Gas Separation. *Chem. Eng. Trans.* **32**, 1999–2004 (2013).
262. Dong, G., Li, H. & Chen, V. Challenges and opportunities for mixed-matrix membranes for gas separation. *J. Mater. Chem. A* **1**, 4610–4630 (2013).
263. Kabay, N., Arda, M., Trochimczuk, A. & Streat, M. Removal of chromate by solvent impregnated resins (SIRs) stabilized by coating and chemical crosslinking. I. Batch-mode sorption studies. *React. Funct. Polym.* **59**, 9–14 (2004).
264. Cheng, C. *et al.* One-pot cross-linked copolymerization for the construction of robust antifouling and antibacterial composite membranes. *J. Mater. Chem. B* **3**, 4170–4180 (2015).
265. Ulbricht, M. & Belfort, G. Surface modification of ultrafiltration membranes by low temperature plasma II. Graft polymerization onto polyacrylonitrile and polysulfone. *J. Memb. Sci.* **111**, 193–215 (1996).
266. Zhang, S., Peh, M. H., Thong, Z. & Chung, T.-S. Thin film interfacial cross-linking approach to fabricate a chitosan rejecting layer over poly (ether sulfone) support for heavy metal removal. *Ind. Eng. Chem. Res.* **54**, 472–479 (2014).

267. Sahabudeen, H. *et al.* Wafer-sized multifunctional polyimine-based two-dimensional conjugated polymers with high mechanical stiffness. *Nat. Commun.* **7**, 13461 (2016).
268. Dai, W. *et al.* Synthesis of a two-dimensional covalent organic monolayer through dynamic imine chemistry at the air/water interface. *Angew. Chemie Int. Ed.* **55**, 213–217 (2016).
269. Ameloot, R. *et al.* Interfacial synthesis of hollow metal–organic framework capsules demonstrating selective permeability. *Nat. Chem.* **3**, 382 (2011).
270. Jimenez-Solomon, M. F., Song, Q., Jelfs, K. E., Munoz-Ibanez, M. & Livingston, A. G. Polymer nanofilms with enhanced microporosity by interfacial polymerization. *Nat. Mater.* **15**, 760–767 (2016).
271. Lu, X. & Elimelech, M. Fabrication of desalination membranes by interfacial polymerization: history, current efforts, and future directions. *Chem. Soc. Rev.* **50**, 6290–6307 (2021).
272. Zhang, F., Fan, J. bing & Wang, S. Interfacial Polymerization: From Chemistry to Functional Materials. *Angew. Chemie Int. Ed.* **59**, 21840–21856 (2020).

# **Chapter 2**

## **Characterisation Methods and Experiments**



## 2.1 Membrane Separation Principles

Membranes occupy an important place in the separation field. The basic working principle for a membrane is to form a barrier between two phases (e.g., saltwater vs freshwater), which could restrict the movement of some solute molecules while allowing the rest to get through<sup>1</sup>. The separation is generally driven by a difference in concentration or pressure (or both) across the membrane, while pressurisation is the primary energy provider.

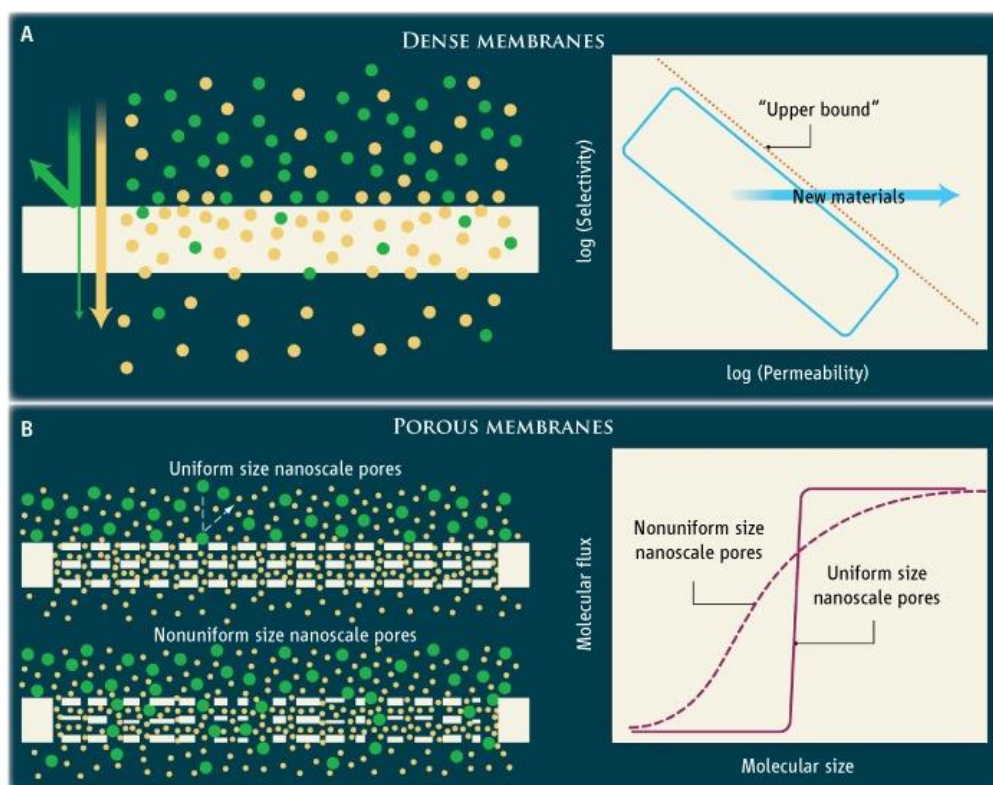


**Figure 2.1** Chemical separation with dense and porous membranes. Reprinted from reference<sup>2</sup> with permission.

Membranes can be densely packed or contain large internal meso- or macro-sized pores, affecting how the molecules move across the barrier<sup>1</sup>. In a dense membrane, molecules usually dissolve into the membrane material and slowly diffuse through it. As is shown in **Figure 2.1**, these orange and green molecules move through the membrane at different rates because their permeabilities—the combination of a molecule's solubility and diffusivity—are different<sup>2</sup>. As a result, most green molecules with a more negligible permeability stayed on the membrane side. The Robeson plot demonstrates that a dense membrane separates molecules mainly depending on their different diffusivity rather than solubilities, and performance is limited by an “upper bound” (known as Robeson upper bound)<sup>3</sup>. That is, a membrane that exhibits a higher

flux and is considered more permeable usually contains more open pore structures, resulting in a lower selectivity of molecules.

On the other hand, porous membranes possess nanopores that are ideally similar to a single molecule, and the molecular separations are based on size differences. During the separation, the nanopores act as a screen or a sieve<sup>1</sup>. The examples shown in **Figure 2.1** are the nanoporous membranes with interconnected 3D networks. For a continuous membrane with uniform nanopores, it can be found that the separation for molecules with different sizes is much more accurate, where the smaller molecules could permeate the membrane whilst most of the larger ones are completely blocked in the membrane side. The sizes of molecules that get through or are rejected by the membrane can be in a short range. Thus, a more complete and effective molecular separation has been achieved. By contrast, both larger and smaller molecules could pass through the membrane for the nonuniform nanoporous membranes, showing an S shape line rather than a sharp drop for the uniform nanopores. In this case, where a pore size distribution can be found in the membrane, the largest membrane pores would act as the “gate” allowing most of the molecules to pass through and thus dictate the guest selectivity<sup>2</sup>. As a result, the selectivity is not satisfying, and the separated products are not pure in each species.

Based on these principles, novel membranes with better performance can be obtained by affording the membrane materials with uniform molecular-size pores. Furthermore, it would also be possible to overcome the membrane upper bound using advanced membrane materials with attractive physical and chemical properties. Therefore, the separation properties (e.g. selectively and permeance) and operational parameters (e.g., stability and longevity) can be finely tuned for the desired applications. Moreover, functional additives such as molecular sieving materials (discussed in **Chapter 1**) can be incorporated into these new classes of membrane materials, providing practical potentials to improve separation performance.

## **2.2 Membrane Performance Evaluation**

### **2.2.1 Membrane Flux and Solvent Permeance**

Membrane flux and solvent permeance are key operating parameters of a membrane<sup>4</sup>, and are affected by a number of different parameters such as the membrane material, hydrophilicity, pore size, and solvent properties<sup>5</sup>.

The flux of a membrane describes the quantity of the permeate passing through the membrane during the separation process, which is defined as the amount of permeate produced per unit of time and per unit area of membrane surface<sup>6</sup>. The flux is measured in volume per square meters per hour.

The solvent permeance is a characteristic of a membrane expressing the ability of a solvent to penetrate and permeate a membrane of a specific thickness. It is an overall coefficient to evaluate the flux of any species (solvents) permeating the membrane as well membrane selectivity. The driving force at the basis of mass transport through the membrane, in most membrane operations such as RO, NF, ultrafiltration, microfiltration, gas separation, membrane distillation, etc., is a difference of feed permeate pressures<sup>7</sup>.

To increase membrane flux and permeance, Mohammad *et al.*<sup>8</sup> showed that the characteristics of a membrane play an important role in the process. For example, a significant improvement in flux could be observed using a looser NF membrane with a higher effective charge density compared to the tightly-packed membranes with a typical charge density.

Studies by Mi *et al.*<sup>9</sup> concluded that permeate flux increases proportionally with an increase in the transmembrane pressure drop and an increase in the operating temperature due to the decrease in solvent (e.g., water) viscosity. Practically, the viscosity decreases significantly with a higher temperature whereas increases with the increasing pressure. The influence of feed pressure on viscosity, generally, is considered insignificant at a pressure less than 4 MPa (~40 bar)<sup>10</sup>. However, it has a great influence on permeate flux. Mendoza-Roca *et al.*<sup>11</sup> have investigated the relationship between the flux and feed pressure of NF-90 and DK-5 membranes, and it was found that the permeate flux changed significantly by increasing the feed pressure from 10 bar to 20 bar.

The detailed experiments for solvent permeance and flux will be presented in the following section.

### **2.2.2 Molecular Weight Cut Off (MWCO)**

To describe a membranes pore size distribution and its selectivity for certain molecules (**Figure 2.1**), molecular weight cut off (MWCO) curves were introduced in the membrane field and are commonly used. This benefits the research in membrane science and industrial manufacturers

since MWCO helps specify membrane performance and thus to select the favourable membranes from the suppliers for certain applications.

MWCO represents the minimum molecular weight of a solute that is 90 % retained by the membrane<sup>12</sup>. As discussed before, a membrane with more uniform nanopores exhibits a more sharp selectivity cut off, meaning the MWCO curve will be sharper, and the membrane may have better practical applications<sup>13</sup>. The MWCO of a membrane is usually obtained by evaluating the retention for the components of different molecular weights<sup>14</sup> as plotted in

**Figure 2.2.**

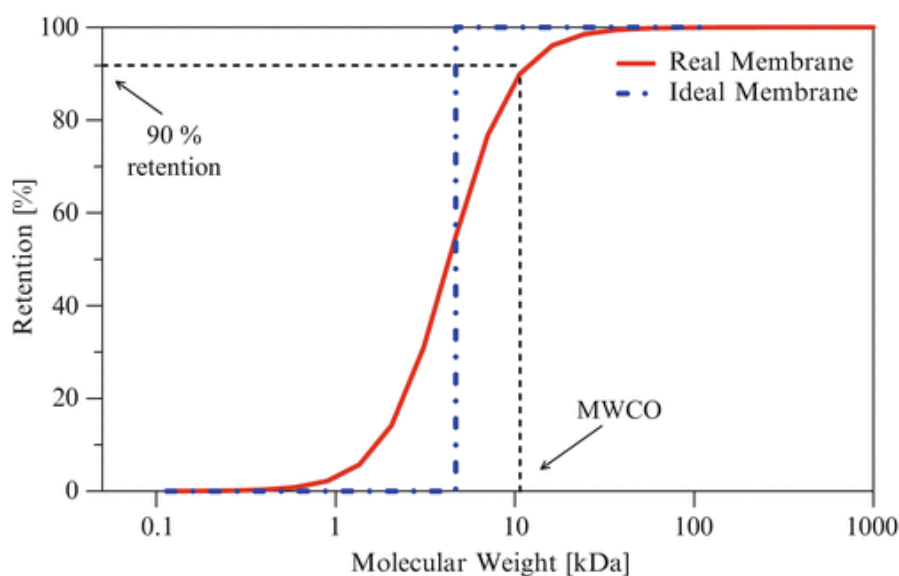


**Figure 2.2** The definition of MWCO and the relationship between retention and molecular weight cutoff of ideal and real membrane. Cited from reference<sup>14</sup>.

However, this method was not ideal for describing the MWCO using different solutes, and inconsistencies could occur between different labs or companies for functionally identical membranes. In 2001, the Livingston group<sup>15</sup> reported that the traditional MWCO values, using positively charged, negatively charged and neutral dyes, seemed to only be valid for aqueous systems instead of the organic solvent-based systems. The role of membrane charge on nanofiltration performance was then investigated, and it was found that separation in nanofiltration membranes primarily occurs due to steric hindrance and membrane solute interactions<sup>16</sup>. As demonstrated by the Livingston group<sup>17</sup> in 2007, the relationship between solute molecular weight and rejection for an OSN membrane has been determined by MWCO curve, using a homologous series of non-charged styrene oligomers spanning the nanofiltration

range (200–1000 g mol<sup>-1</sup>) for the first time. Thus, creating an academia and industry-standard parameter to define the performance of a membrane.

### 2.3 Morphology Study on Membranes

Scanning electron microscopy (SEM) is widely used to observe membrane materials and thin films at a nanometer scale (resolution from 1-20 nm)<sup>18</sup>. The surface of SEM samples needs to be electrically conductive, so non-conductive samples are usually coated with gold, carbon, or chromium etc. Then the sample is mounted on a specimen stage in a high vacuum. An electron beam is generated by an electron gun, then passes through a series of electromagnetic lenses, including one or two condenser lens and an objective lens. The lenses focus the electron beam to 0.4-5 nm in diameter. The beam is deflected by a pair of scanning coils in the x and y axes. Thus, the sample surface can be scanned in a raster pattern<sup>19</sup>. A schematic of an SEM image is shown in **Figure 2.3**.

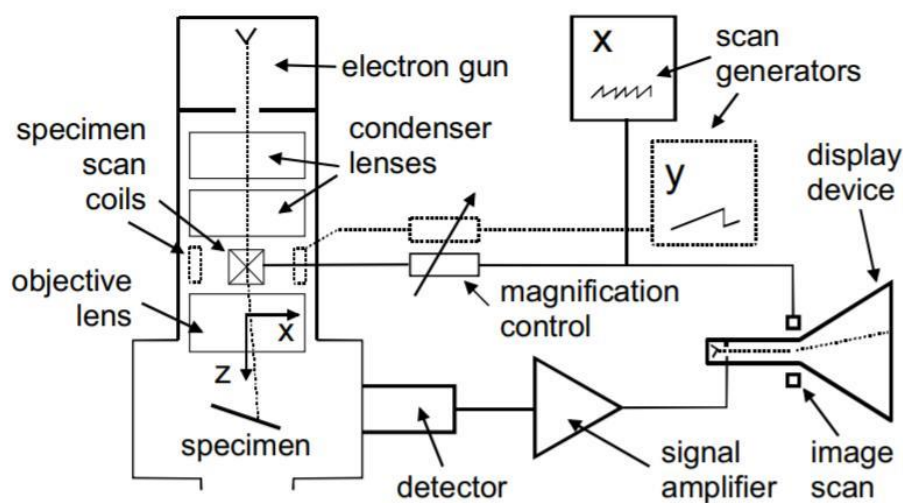


**Figure 2.3** Physical Principles of Electron Microscopy<sup>19</sup>.

When the electron beam hits the sample surface, different kinds of electrons or photons are generated during the interaction, including backscattered electrons (BSE) by elastic scattering, secondary electrons (SE) by inelastic scattering, and electromagnetic radiation such as X-ray. Each of these signals can be detected by certain detectors. Because SEs come from the surface of the sample, while BSEs emerge from deeper regions, SE imaging can show higher resolution than BSE imaging and thus becomes a powerful strategy for surface morphology study of the membrane materials.

In this project, SEM will be used to study the surface morphology of the POC membranes.

## 2.4 Crystal Structure Study

X-ray diffraction (XRD) is a commonly used technique to study the crystalline structure of materials. In this thesis, XRD has been employed to investigate the surface structures of POC thin films.

### 2.4.1 Powder X-ray Diffraction (PXRD)

Unlike single-crystal X-ray diffraction, powder X-ray diffraction (PXRD) obtains diffraction patterns from the powder state of the material<sup>20</sup>. The diffraction pattern can be compared to a reference database to identify any published compounds. Thus PXRD can be used to identify crystal structures easily and more rapidly.

The diffraction pattern from PXRD is decided by the structure of the crystal. Crystals are formed of repeated lattices. The space between adjacent lattice points is called a unit cell, which can be described by a set of vectors<sup>21</sup> with distances between lattice points  $a$ ,  $b$ ,  $c$  and the associated angles  $\alpha$ ,  $\beta$ ,  $\gamma$ .

In three dimension space, based on the relationship of the vectors, there are seven possible lattice systems. According to the locations of the lattice points in the unit cell, there are four centring types:

- Primitive (P): lattice points on the cell corners only,
- Base-centred (S: A, B, or C): a pair of points at the centre of parallel faces,
- Body-centred (I): one point at the centre of the cell,
- Face-centred (F): one point at the centre of each of the faces.

Combining the lattice systems and the centring types, fourteen standard Bravais lattices are available, which are summarised in **Table 2.1**.

**Table 2.1** Parameters of the seven crystal systems and fourteen Bravais lattices. Cited from reference<sup>21</sup>.

Crystal system	Vector relationship	Centring types
Cubic	$a=b=c, \alpha=\beta=\gamma=90^\circ$	P, I, F
Tetragonal	$a=b \neq c, \alpha=\beta=\gamma=90^\circ$	P, I
Hexagonal	$a=b \neq c, \alpha=\beta=90^\circ \gamma=120^\circ$	P, R
Rhombohedral	$a=b=c, \alpha=\beta=\gamma \neq 90^\circ$	R
Orthorhombic	$a \neq b \neq c, \alpha=\beta=\gamma=90^\circ$	P, C, I, F
Monoclinic	$a \neq b \neq c, \alpha=\gamma=90^\circ \beta \neq 90^\circ$	P, C
Triclinic	$a \neq b \neq c, \alpha \neq \beta \neq \gamma \neq 90^\circ$	P

The pattern of X-ray diffracted by a crystal obeys Bragg's law. When the X-rays are incident onto a crystal surface, a part of the X-rays are scattered by the surface of the crystal, and another part passes through the surface, then scattered by the next layer of atoms (**Figure 2.4**). If the spacing between atom layers  $d$  is an integer multiple of the wavelength  $\lambda$ , then the X-ray can interfere constructively in a certain incident angle  $\theta$ . The amplified X-ray peaks will be detected. Otherwise, the destructive interference of X-ray will occur.

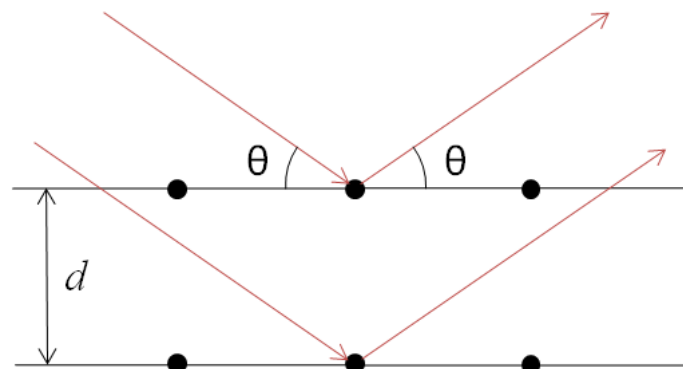


**Figure 2.4** Bragg's law described the relationship of the distance between atom layers  $n$ , the wavelength  $\lambda$ , and the incident angle. Cited from reference<sup>22</sup>.



Braggs law described the relationship of the distance between atom layers  $n$ , the wavelength  $\lambda$ , and the incident angle  $\theta$ , shown in the following equation:

$$n\lambda = 2d\sin\theta \quad (\text{Eq.2.1})$$

In a powder X-ray diffractometer, as is shown in **Figure 2.5**, the X-ray can focus on the sample at a range of incident angle  $\theta$ , which the detector receives the X-ray at the opposite site,  $2\theta$  away from the incident path<sup>22</sup>. The intensity of diffraction is plotted against  $2\theta$ , forming a PXRD pattern. By comparing the PXRD pattern with the reference database or by indexing the patterns, the structure of the synthesised POC film can be identified.

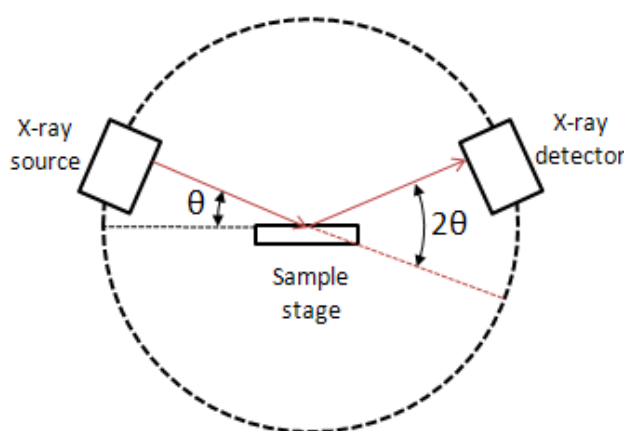


**Figure 2.5** A powder X-ray diffractometer consists of an X-ray source (usually an X-ray tube), a sample stage, a detector and a way to vary angle  $\theta$ . The X-ray is focused on the sample at some angle  $\theta$ , while the detector opposite the source reads the intensity of the X-ray it receives at  $2\theta$  away from the source path. The incident angle is then increased over time while the detector angle always remains  $2\theta$  above the source path. Cited from reference<sup>22</sup>.

#### 2.4.2 Grazing Incidence X-ray Diffraction (GIXRD)

For materials within thin film morphologies, XRD from the material surface often suffers from low peak intensity and poor peak to background ratio for symmetrical XRD measurements such as PXRD techniques. The low diffraction intensity from a thin top layer in a PXRD scan is mainly related to the fact that the path length of the X-rays in the thin film is short. Therefore, most of the radiation instead interacts within the underlying substrate. In addition to lower peak intensity, the thin film reflections may also be superimposed and challenging to distinguish from substrate reflections, which complicate the evaluation of the XRD data<sup>23</sup>.

The POC films discussed in this thesis are only composed of light organic atoms (heaviest atom O), are typically 20 - 200 nm thick, and have low skeleton densities. Therefore, to improve the diffraction intensity for these weakly diffracting thin films (usually 1-1000 nm), low-angle XRD techniques such as grazing incidence X-ray diffraction (GIXRD) have been developed<sup>23</sup>.

GIXRD is a surface-sensitive diffraction technique that utilises a small incident angle X-ray beam to limit penetration into the bulk material and optimise the intensity<sup>24</sup>. One of the ways to avoid intense signals from the substrate and obtain a stronger signal from the film is to perform a  $2\theta$  scan with a fixed grazing angle of incidence. The fixed angle is generally chosen to be slightly above the critical angle for total reflection of the film material.<sup>25</sup> In a symmetric  $\theta/2\theta$  measurement, the scattering vector is perpendicular to the sample surface, and only lattice planes in parallel to the substrate surface contribute to the diffractograms. Furthermore, the angle of the incoming X-rays to the sample surface is changed during the measurement always to be equal to  $\theta$ , that is, half of the scattering angle  $2\theta$ . Thus GIXRD is an asymmetric XRD scan where the path length of the X-rays in a thin film is increased by using a fixed angle of incidence,  $\alpha$ , for the incoming X-rays (**Figure 2.6**).

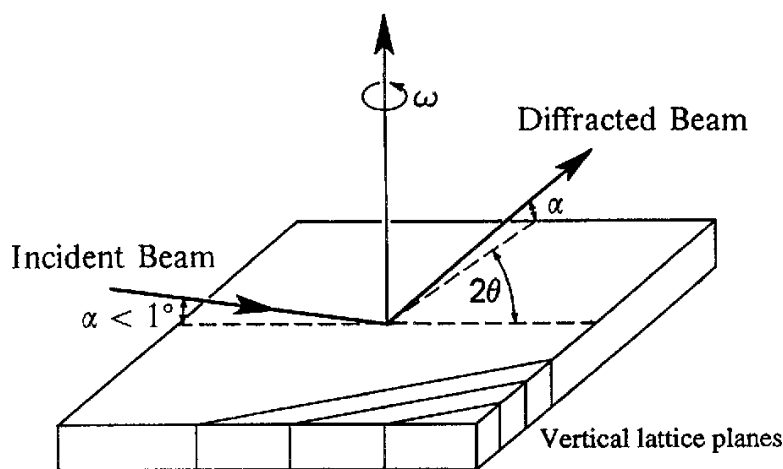


**Figure 2.6** Principle geometry of a GIXRD experiment:  $\alpha$  – incident angle,  $\theta$  – Bragg angle.

*Cited from reference<sup>18</sup>.*

By indexing the obtained diffraction patterns, the crystalline structures of the thin film and the material can be determined. In this way, GIXRD is considered a powerful tool to study the phases and crystallographic changes at the surface of the sample, improve the diffraction signal from thin films, and avoid overlapping peaks from different depths of samples.

## 2.5 Experiments and Methods

### 2.5.1 Materials.

1,3,5-Triformylbenzene (TFB) was purchased from Manchester Organics, UK. (1*R*,2*R*)-1,2-diaminocyclohexane (CHDA), reactive red 120 (RR, 1470 g·mol<sup>-1</sup>), direct red 80 (DR, 1373 g·mol<sup>-1</sup>), rose bengal (RB, 1018 g·mol<sup>-1</sup>), brilliant blue (BB, 826 g·mol<sup>-1</sup>), Congo red (CR, 697 g·mol<sup>-1</sup>), protoporphyrin IX disodium (PPIX, 607 g·mol<sup>-1</sup>), acid fuchsin (ACF, 585 g·mol<sup>-1</sup>), sunset yellow (SY, 452 g·mol<sup>-1</sup>), methyl orange (MO, 327 g·mol<sup>-1</sup>), neutral red (NR, 289 g·mol<sup>-1</sup>), 4-nitrophenol (NP, 139 g·mol<sup>-1</sup>), and all solvents (HPLC grade) were purchased from Sigma-Aldrich. The commercially available membranes, SolSep-NF030306, SolSep-169, and SolSep-NF010206 were supplied by SolSep, Netherland; MPF-50 were supplied by Koch Membrane Systems, US; HITK-T1 was manufactured by Hermsdorfer Institut für Technische Keramik, Germany; and FSTi-128 was manufactured by Flemish Institute for Technological Research, Belgium. All materials were used as received.

### 2.5.2 Synthesis.

A series of porous organic cages (POCs) were prepared via [4+6] cycloimination reactions shown in **Figure 2.7**. Various types of cages can be produced by reactions between 1,3,5-triformyl benzene (TFB) and/or other aldehydes with vicinal diamines. All the cages described in this thesis, which are (1*S*,2*S*)-1,2-cyclohexane diamine cage (**CC3**), ethylenediamine cage (**CC1**), amorphous scrambled porous organic cages (ASPOC), reduced amine cage (**RCC1**, **RCC2**, **RCC3**), and a “tied” cage (FT-**RCC3**) were synthesised using methods reported previously by the Cooper Group<sup>26-28</sup>. **CC3** was synthesised using TFB and (1*S*,2*S*)-1,2-cyclohexanediamine (CHDA) in dichloromethane at room temperature. The crystals were recovered by filtration and washed with 95% ethanol/ 5% dichloromethane, and finally dried under vacuum. **RCC3** was synthesised by reducing **CC3** with NaBH<sub>4</sub> in a mixture of chloroform and methanol. FT-**RCC3** was prepared by reacting the **RCC3** cages with paraformaldehyde in methanol at 70 °C. The reaction was cooled to room temperature and the **FT-RCC3** was obtained after filtration and washing with methanol and further dried under vacuum.

**CC1** and **CC2** were synthesised by the same reaction. For **CC1**, typically, a solution of TFB (3.75 g, 23.13 mmol) in dichloromethane (1.15 L) was added dropwise over 48 h (ca. 0.3

mL=min) via a pressure-equalising dropping funnel to a solution of ethylenediamine (2.08 g, 34.69 mmol) in dichloromethane (0.85 L) in a 2-L, three-necked, round-bottomed flask cooled in an ice bath. The stirring rate used was 260 rpm (0.7 L and 1.05 L reactions) or 400 rpm (2 L reactions). After complete addition, the reaction was allowed to stir for another 24 h at room temperature. The solution was then filtered through filter paper (the loss of solid to filter paper was 0.030 g). The solvent was removed from the filtrate via rotary evaporation (temperature of the water bath maintained below 20 °C), the crude product was redissolved in chloroform (100 mL), and the solution was refiltered. The residue in the filter paper was washed with chloroform (50 mL). The two fractions of the organic filtrate were combined, and the solvent was removed under vacuum on a rotary evaporator (temperature of the water bath was maintained below 20 °C) to afford the product as a beige powder. After this time, sodium borohydride was added, and the reaction stirred for a further 12 hours. Water (5 mL) was then added, and the reaction stirred for a further 12 hours. The solvent was then removed under vacuum. The resulting white solid was extracted with chloroform (2 × 100 mL) and the remaining white solid was removed by filtration. The solvent was then removed with a rotary evaporator (water bath at 30 °C), and crude **RCC1** was obtained as white solid.

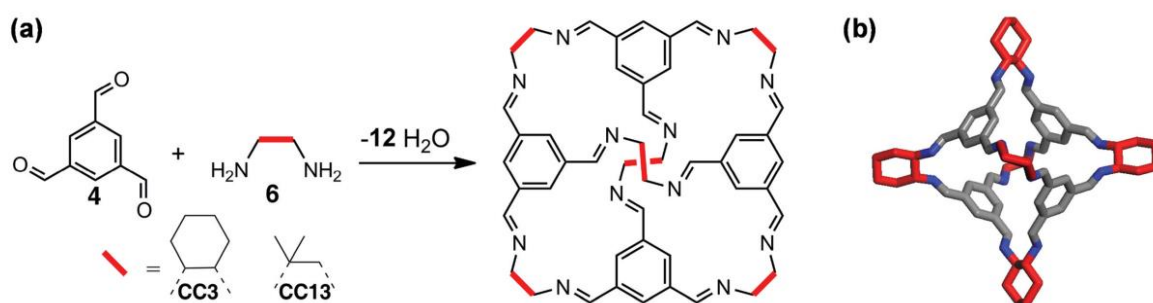


**Figure 2.7** Synthetic pathways and chemical structures of POCs (CC3 and CC13)<sup>26</sup>.

### 2.5.3 Membrane fabrication

**Fabrication of polyacrylonitrile (PAN) supports via phase inversion.** Polyacrylonitrile (PAN) support membranes were cast using a continuous casting machine (Sepratek, South Korea). The dope solution comprised 11 wt.% polyacrylonitrile powder dissolved in a mixture of 44.5 wt.% dimethyl sulfoxide (DMSO) and 44.5 wt.% 1,3-dioxolane and allowed stirring overnight at 75 °C. After cooling down to room temperature and degassing, the PAN membrane was then cast onto a polyethylene terephthalate (PET) non-woven fabric (Hirose RO grade). The casting speed was controlled by the winder tension at 4 rpm with a knife gap 120 μm.

After casting, the support was immediately immersed into a water bath at 60 °C for 3 hours, followed by drying at room temperature.

**Fabrication of crystalline CC3 film.** Continuous crystalline cage films of **CC3** were produced using an interfacial reaction and crystallisation process that occurred at the interface between an immiscible aqueous phase and an organic phase.

An aqueous solution of CHDA (0.26 g, 2.24 mmol, 0.8 wt.%) in water (32 mL) was carefully layered on top of a dichloromethane solution (30 mL) that contained TFB (0.24 g, 1.48 mmol, 0.8 wt.%) and was stored in a glass dish with an inner diameter of 7.4 cm. The interfacial reaction was covered and kept at room temperature (~19-21 °C) for between 4–96 hours (typically, 24 hours).

The continuous crystalline **CC3** film that grew at the dichloromethane-water interface was then isolated as a free-standing film that could then be adhered directly onto different substrates, including glass, carbon tape, steel mesh, silicon wafer, and anodic aluminum oxide for further analysis and to determine crystallinity and surface morphology (**Figure 2.8**).

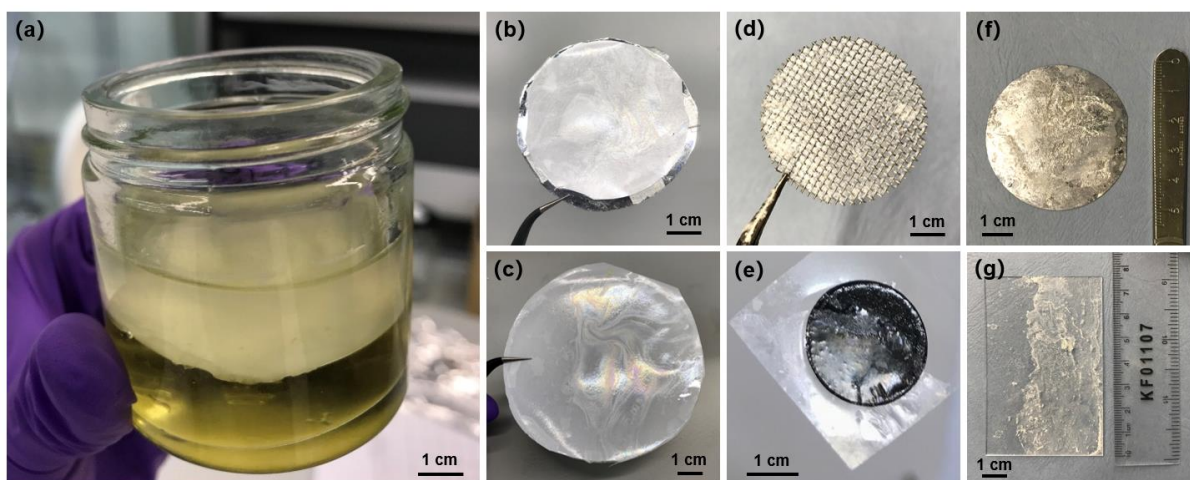


**Figure 2.8** Photographs of as synthesised **CC3** $\alpha$ -PAN-24hr-0.8% film. (a) Free-standing **CC3** film grown in a glass dish at the liquid-liquid interface between water and dichloromethane. (b, c, d, e, f, g) **CC3** films transferred onto different substrates for further analysis: (b) PAN sheet fixed on an aluminum wafer; (c) PAN membrane; (d) stainless mesh; (e) carbon tape used for scanning electron microscopy; (f) silicon wafer; (g) glass slide.

To perform liquid permeation studies, the **CC3** film was transferred onto PAN support to form composite **CC3**-PAN membranes, which were then soaked in pure water for 1 day. The

following procedure was used to produce the continuous crystalline composite **CC3**-PAN membranes for the liquid permeation studies:

A PAN sheet covered a sintered disc at the bottom of an AdvanTec<sup>®</sup> glass filtration funnel with an effective diameter of 7.4 cm. The interfacial reaction was carried out as previously described in the Methods section. After 24 hours, the solvent was removed by filtration (**Figure 2.9**), which enabled the **CC3** film to be transferred directly onto the PAN support. For the membrane thickness analysis measurements performed using AFM, we placed a silicon wafer disc on top of the PAN support and used the same reaction procedure. After removing the solvent by filtration, the **CC3** film was transferred onto a silicon wafer. Note, the diameter of the silicon wafer was <5.0 cm so that the solvent could be removed by filtration.

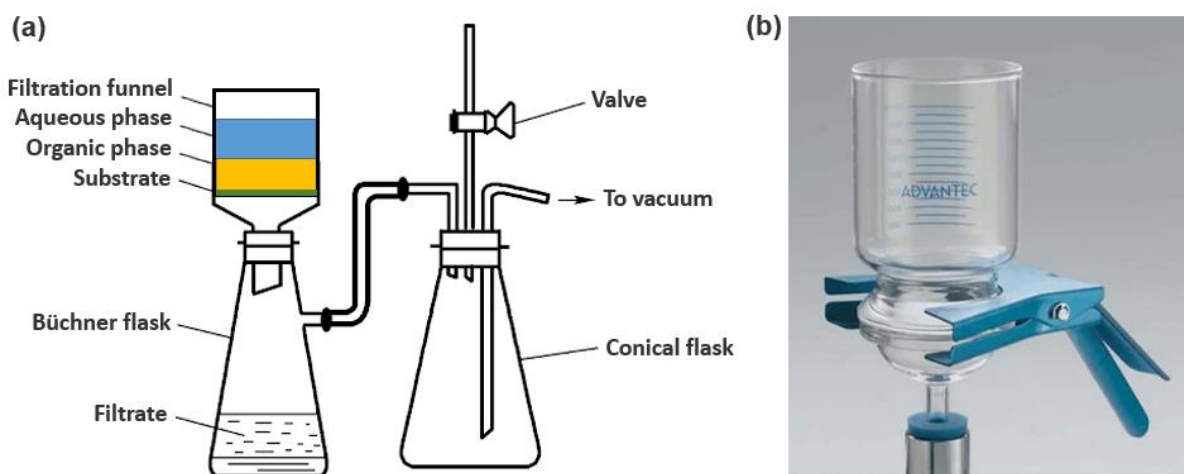


**Figure 2.9** Reactions set-up for the fabrication of **CC3** films. (a) Schematic diagram of filtration funnel system connected to vacuum; (b) Photograph of the AdvanTec<sup>®</sup> glass filtration funnel with a diameter of 7.4 cm. Copyright © 2022, Springer Nature and Ai He, etc.

**Preparation of cage nanofilm composite membranes.** Reduced POC nanofilm membranes were hand-cast on cross-linked polyacrylonitrile (PAN) supports through interfacial polymerisation. First, an aqueous solution of 0.1% (w/v) **RCC1** and a solution of 0.1% (w/v) trimesoyl chloride (TMC, 98%, Sigma-Aldrich) in hexane (HPLC grade, VWR International) were prepared. The support was cut into disks of 60.8 cm<sup>2</sup> and placed in a glass filtration holder for the interfacial polymerisation reaction. For this purpose, 15 mL of the aqueous solution was added, and after 2 min, the excess solution was removed. The resulting membrane was then wiped with tissue paper. Then, 15 mL of the hexane solution was poured, and after 1 min reaction time, the resulting membranes were withdrawn from the hexane solution and rinsed with water.

**Fabrication of amorphous CC3 membrane via a spin-coating method.** The amorphous CC3 membrane was fabricated using a WS-650Mz-23NPP spin-coater (Laurell, USA). A CC3 chloroform solution was prepared by sonicating/stirring CC3 (50 mg) in chloroform (5 g, 3.7 mL) for 10 minutes. The suspension was then filtered using a PTFE syringe filter (0.2  $\mu\text{m}$ ). The edges of a 6 $\times$ 6 cm sized PAN membrane piece was taped to a glass slide that was then attached to the spin-coater by suction. The saturated CC3 chloroform solution (1 mL) was added dropwise onto the membrane. After the addition, the slide was rotated at 500 rpm for 15 seconds and then 1500 rpm for 45 seconds. The amorphous CC3 membrane was cut into 4.7 cm for the filtration experiment. The membrane was subjected to analysis by PXRD.

**Fabrication of CC3 membrane by the in-situ method.** A dichloromethane solution (15 mL) that contained TFB (0.12 g, 0.72 mmol, 0.8 wt.%) was carefully layered on top of a PAN membrane fixed in a glass dish with an inner diameter of 7.4 cm for 8 hours. After this time the dichloromethane solution was moved from the dish, and an aqueous solution of CHDA (0.13 g, 1.12 mmol, 0.8 wt.%) in water (16 mL) was added. The reaction was covered and kept at room temperature ( $\sim$ 19-21  $^{\circ}\text{C}$ ) for another 16 hours.

#### 2.5.4 Characterisation Methods

**Nuclear Magnetic Resonance (NMR).** NMR spectra were recorded on a Bruker 400 NMR spectrometer at 400 MHz ( $^1\text{H}$ ) and referenced against the residual  $^1\text{H}$  signal of the solvent.

**Fourier Transform Infrared Spectroscopy (FT-IR).** FT-IR spectra were recorded on a Bruker Tensor 27 spectrometer. Samples were cut into size and recorded in transmission mode using 16 scans with a resolution of 4  $\text{cm}^{-1}$ .

**Raman Mapping.** Raman spectroscopy was performed using an inVia<sup>TM</sup> Reflex<sup>®</sup> Qontor Confocal Raman Microscope. Images of the CC3 films were captured using the 50x objective and the WiRE spectral acquisition wizard was used for data collections and spectral analysis. Spectral analysis was performed using the following settings: 785 nm laser (power 5%); 1200 l/mm (633/780) grating; Renishaw Centrus 5134M5 detector; 50x L objective; 10 seconds exposure time with 3 accumulations; line focus mode; and spectra were recorded over the range 102  $\text{cm}^{-1}$  to 3202  $\text{cm}^{-1}$ . Cosmic ray deletion was performed using the WiRE software before spectra were analysed. The Raman map was performed by integrating multiple scans over the target, using a step size of 1 $\times$ 1 pixel. For the Raman maps, crystalline CC3- $\alpha$ <sup>26</sup> and amorphous CC3<sup>29</sup> samples were used as references.



**Scanning Electron Microscopy (SEM).** High-resolution images of the **CC3** films were recorded using a Hitachi S-4800 cold field emission scanning electron microscope (FE-SEM). The samples were appended to 15 mm Hitachi M4 aluminium stubs using either silver dag or an adhesive high purity carbon tab. The samples were then coated with a 2 nm layer of gold (Au) or cadmium using an Emitech K550X automated sputter coater. The FE-SEM measurement scale bar was calibrated using a certified SIRA calibration standard. Imaging was conducted at a working distance of 8 mm and a voltage of 3 kV using a mix of upper and lower secondary electron detectors.

**Focused Ion Beam Scanning Electron Microscopy (FIB-SEM).** The cross-sectional structure of the **CC3** films was studied using a Tescan S8000G FIB-SEM. The specimens were attached to aluminum (Al) stubs using carbon tabs, and silver (Ag) dag was applied to aid conductivity. After the dag had dried, the specimens were Au-coated using a Quorum Q150T ES coater (~10 nm). The specimens were studied at a working distance of 6 mm, tilted at 55 degrees from horizontal (so normal to the ion beam), using the ion beam for trenching and polishing (30 kV and 1 nA for trenching, and 30 kV and 250 pA for polishing) and the electron beam for imaging (5 kV, 30 pA, and 10 kV, 60 pA). Surfaces to be sectioned were coated with a protective layer of platinum (Pt), ~18  $\mu\text{m}$  long by ~3  $\mu\text{m}$  wide by ~1  $\mu\text{m}$  thick, before milling (deposited using the ion beam at 30 kV, 150 pA). Micrographs were acquired using ultra-high-resolution mode at various stages of the study using the ET detector (two micrographs were also taken using the LEBSE detector).

**Atomic Force Microscope (AFM).** AFM imaging was used to characterise the morphology of the surface of the **CC3** films with a Multimode 8 (Bruker, CA, USA) model equipped with E - type or J - type pizzo scanner. The samples were attached to a magnetic sample disk and scanned under tapping mode using PointProbe<sup>®</sup> Plus silicon-SPM probes (PPP-NCH, Nanosensors<sup>™</sup>, Switzerland) with a typical tip radius of less than 7 nm and the cantilever resonance frequency was in the range of 204 - 497 kHz with a nominal spring constant of 42  $\text{N}\cdot\text{m}^{-1}$ . Raster scanning was performed at a speed of 0.50 lines per second with a resolution of 512 points per line at a speed of 0.2 – 1.0 Hz. Gwyddion 2.44 SPM data visualisation and analysis software was used to process the AFM images. To measure film thickness, free-standing **CC3** films were transferred to silicon wafers and dried. A scratch was made to expose the wafer surface and allow measurements of the height from the silicon wafer surface to the **CC3** film surface. The thickness was estimated from the height difference between the silicon wafer and the **CC3** film using a one-dimensional statistical function.

**Water Contact Angle (WCA) Measurements.** WCA measurements were performed using a DSA100 expert drop shape analyser with the following measurement conditions, drop phase: water; surrounding phase: air; drop type: sessile drop; drop volume:  $4.15 \pm 0.5 \mu\text{L}$ ; fitting method: Young–Laplace equation. Before recording these measurements, the samples were cut into  $1 \times 4 \text{ cm}$  sized pieces and appended onto glass slides using double-sided tape.

**Grazing incidence X-ray diffraction (GIXRD).** GIXRD measurements were performed using the I07 beamline at Diamond Light Source in the UK ( $\lambda = 0.689 \text{ \AA}$ ), using a vertical (2 + 2)-type diffractometer equipped with a Pilatus 100K area detector<sup>30</sup>. Membrane samples were cut into  $1 \times 2 \text{ cm}^2$  sized pieces and stuck onto glass supports, which were then mounted on a hexapod (PI-Micos) to allow independent alignment with 6 degrees of freedom during the data collections (**Figure 2.10(a)**). The measurements were conducted by moving the detector while maintaining a fixed sample position. The grazing incidence angle is set at  $2^\circ$ . Data collections were performed at room temperature using in-plane (over the  $2\theta$  range  $3\text{--}40^\circ$ ,  $0.50^\circ$  step size) and out-of-plane (over the  $2\theta$  range  $2\text{--}40^\circ$ ,  $0.25^\circ$  step size) measurement geometries and GIXRD scans were processed in DAWN 2<sup>31</sup>. GIXRD patterns were refined by Pawley refinement through TOPAS Academic<sup>32</sup>. High-resolution synchrotron powder X-ray diffraction (PXRD) data were collected using the I11 beamline at Diamond Light Source ( $\lambda = 0.827 \text{ \AA}$ ).

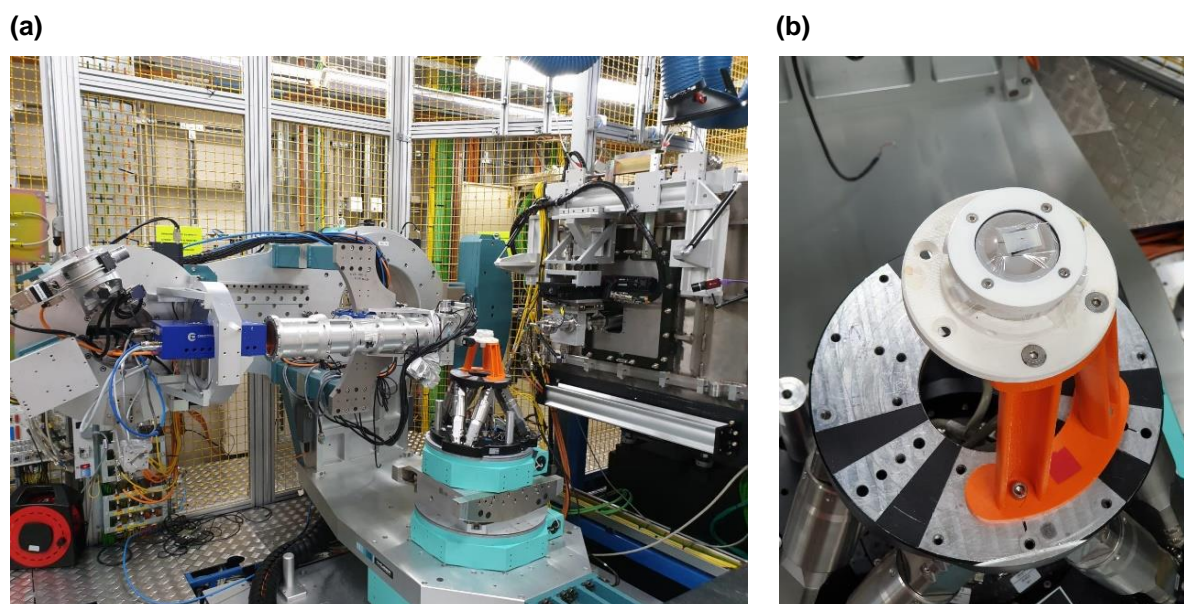


**Figure 2.10** Image showing (a) experimental set-up at beamline I07; (b) a membrane on a glass substrate mounted on the hexapod sample holder and covered with a Mylar film.

For the *in situ* GIXRD measurements performed on solvated samples, pieces of Mylar film were used to cover the membrane surface with a thin layer of solvent (water, MeOH, acetone, and acetonitrile) during the GIXRD scans (**Figure 2.10(b)**). To investigate the reversible transformation between CC3 $\alpha$ -PAN and CC3 $\gamma'$ -PAN, a membrane sample was removed from water without drying and covered with 1.0 mL of MeOH solvent layer before recording the GIXRD data. To more closely mimic the reversible membrane separation experiment where the feedstock was cycled between water and MeOH, a CC3-PAN sample was removed from water without drying, soaked in 100 mL MeOH for 1 minute, and covered with a thin layer of MeOH (1.0 mL) before the GIXRD measurement. The same process was repeated with the identical CC3-PAN sample using water or MeOH. For the *in situ* measurements performed using solvent vapours, nitrogen gas was bubbled through a 2L bottle that contained the organic solvent at a flow rate of 10 L $\cdot$ min<sup>-1</sup>. The 'wet gas' generated during this process was then continually flowed over the membrane sample during the full measurement and Mylar film was used to seal the sample environment.

**Powder X-ray Diffraction (PXRD).** Laboratory PXRD patterns were collected in transmission mode on samples held on thin Mylar film in aluminium well plates on a Panalytical Empyrean diffractometer, equipped with a high throughput screening XYZ stage, X-ray focusing mirror, and PIXcel detector, using Cu-K $\alpha$  ( $\lambda = 1.541 \text{ \AA}$ ) radiation. PXRD patterns were measured over the  $2\theta$  range 4-50 $^\circ$  in 0.013 $^\circ$  steps for 30 minutes. High-resolution synchrotron PXRD patterns were collected using the I11 beamline at Diamond Light Source ( $\lambda = 0.827 \text{ \AA}$ ), which is equipped with a Mythen II position-sensitive detector<sup>33,34</sup>. Samples recorded at Diamond Light Source were loaded in borosilicate glass capillaries that were spun to improve powder averaging during data acquisition. PXRD patterns were refined by Pawley refinement in TOPAS Academic<sup>32</sup>.

#### 2.5.4 Membrane performance evaluation

**Separation Measurements.** Solvent permeance and dye rejection measurements were performed using a Sterlitech<sup>®</sup> HP4750 dead-end membrane filtration system (**Figure 2.11**).

We also used a commercial bench-scale 50 mL transparent Merck Millipore Amicon<sup>®</sup> dead-end stirred cell which is connected to an 800 mL Merck Millipore Amicon<sup>®</sup> RC800 reservoir to visualise the filtration process (**Figure 2.12**).

During these measurements, the feedstocks were kept under a 10 bar nitrogen pressure (3 bar for Merck Millipore Amicon<sup>®</sup> cells) at room temperature, and the feedstock was continually stirred using a stirrer bar rotating at 400 rpm. Hansen solubility parameter ( $\delta$ ) and the physical properties of the organic solvents were used to investigate the relationships between pure solvent permeances and the combined solvent properties.

Flux  $J$  ( $\text{L}\cdot\text{m}^{-2}\cdot\text{h}^{-1}$ ) was calculated according to the following equation:

$$J = \Delta V / (A \times \Delta t) \quad (\text{Eq.2.2})$$

where  $\Delta V$  is the volume of permeate collected in L in a given amount of time,  $A$  is the membrane surface area in  $\text{m}^2$ , and  $\Delta t$  is the time in hours between the start and end of the measurement.



**Figure 2.11** To evaluate the separation performance of the CC3-PAN membranes, the permeance and selectivity measurements were carried out using a commercial bench-scale dead-end stirred-cell filtration unit (Sterlitech<sup>®</sup> HP4750 stirred cell) that was kept under 10 bar upstream nitrogen pressure at room temperature. The agitation speed was kept at 400 rpm during the measurements. The membrane was cut into a coupon with a diameter of 4.7 cm to fix at the bottom of the cell. Copyright © 2022, Springer Nature and Ai He, etc.

Solvent permeance  $P$  ( $\text{L}\cdot\text{m}^{-2}\cdot\text{h}^{-1}\cdot\text{bar}^{-1}$ ) was calculated according to the following equation:

$$P = \Delta V / (A \times \Delta t \times p) \quad (\text{Eq.2.3})$$

where  $\Delta V$  is the volume of permeate collected in L in a given amount of time,  $A$  is the membrane surface area in  $\text{m}^2$ , and  $\Delta t$  is the time in hours between the start and end of the measurement,  $p$  is the transmembrane pressure. To calculate solvent permeance, typically, 0.2 L of pure solvent or dye feedstock (20 ppm dye concentration) was added to the feedstock tank. The cell was then pressurised to 10 bar under nitrogen. The solvent permeate was then calculated based on the amount of time it took  $\sim 0.1$  L of pure solvent or dye feedstock to flow through the membrane. The retentate was collected after each measurement. Error bars ( $SD$ ) were calculated by the  $STDEV.P$  function using data obtained from at least three independent membranes.

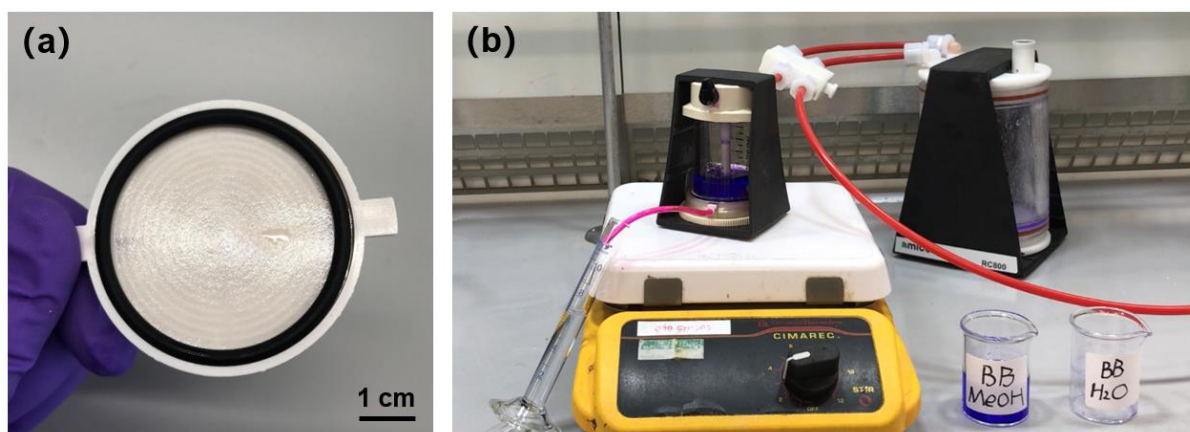


**Figure 2.12** To visualise the filtration process in real-time, a commercial bench-scale 50 mL Merck Millipore Amicon<sup>®</sup> dead-end stirred cell which is connected to a 800 mL Merck Millipore Amicon<sup>®</sup> RC800 reservoir was used. (a) Photograph showing a CC3 $\alpha$ -PAN membrane sample fixed on the support at the base of the cell that was sealed using an O-ring. The membrane was cut into a circle coupon with a diameter of 42 mm to fix at the bottom of the cell. Scale bar: 1cm. (b) Photograph showing the filtration set-up and connections of the dead-end filtration cell that was kept under a 3 bar nitrogen atmosphere. Feed solutions that contained 20 ppm BB in MeOH and 20 ppm BB in water were prepared and used for the filtration experiments. Copyright © 2022, Springer Nature and Ai He, etc.

For the dye rejection measurements, a series of dye feedstocks solutions in different solvents (water, MeOH, acetone, and acetonitrile) were prepared with a dye concentration of 20 ppm using the following dyes: reactive red 120 (RR,  $1470 \text{ g}\cdot\text{mol}^{-1}$ ), direct red 80 (DR,  $1373 \text{ g}\cdot\text{mol}^{-1}$ ), rose bengal (RB,  $1018 \text{ g}\cdot\text{mol}^{-1}$ ), brilliant blue (BB,  $826 \text{ g}\cdot\text{mol}^{-1}$ ), Congo red (CR,  $697 \text{ g}\cdot\text{mol}^{-1}$ ).

<sup>1</sup>), protoporphyrin IX disodium (PPIX, 607 g·mol<sup>-1</sup>), acid fuchsin (ACF, 585 g·mol<sup>-1</sup>), sunset yellow (SY, 452 g·mol<sup>-1</sup>), methyl orange (MO, 327 g·mol<sup>-1</sup>), neutral red (NR, 289 g·mol<sup>-1</sup>), and 4-nitrophenol (NP, 139 g·mol<sup>-1</sup>). Ultraviolet-visible (UV-vis) spectroscopy was used to measure the dye concentration in the permeate to calculate dye rejection performance. Dye rejection,  $R$  (%), of the membranes, was calculated as follows:

$$R = (1 - C_p / C_f) \times 100\% \quad (\text{Eq.2.4})$$

where  $C_p$  and  $C_f$  represent the dye concentrations in the permeate ( $C_p$ ) and feed ( $C_f$ ), respectively. Dye concentrations in permeate and feed were determined using a Cary 5000 UV-Vis-NIR spectrometer with the wavelengths specified in **Chapter 3**. The MWCO was determined by interpolating from the plot of rejection against the molecular weight of the dyes and corresponds to the molecular weight for which rejection is 90%. During these measurements, the volume and the concentration of the permeate and the retentate were measured, and the mass balance of the feed solution could be calculated as follows:

$$C_f \times V_f = C_p \times V_p + C_r \times V_r \quad (\text{Eq.2.5})$$

where  $C_f$ ,  $C_p$ , and  $C_r$  are the dye concentrations in ppm (g·L<sup>-1</sup>) of the feed, permeate, and retentate, respectively;  $V_f$ ,  $V_p$ , and  $V_r$  represent the volume of the feed, permeate, and retentate in L, respectively. Typically, 0.2 L of the feed solution was added into the cell, then 0.1 L permeate was collected, and 0.1 L retentate was left in the cell.

**Reversible filtration test.** For the reversible filtration tests, feedstocks that contained BB dissolved in water and MeOH at a concentration of 20 ppm were used in the six-step procedure decribed below.

- 1) A BB water solution (20 ppm, 0.2 L) was added to the filtration cell, the cell was pressurised to 10 bar under nitrogen, and ~0.1 L of the feedstock was permeated through the **CC3-PAN** membrane.
- 2) The water permeate was collected to determine the dye concentration, and the remaining retentate solution was removed from the filtration cell.
- 3) The filtration cell, including the **CC3-PAN** membrane, was washed with MeOH (0.1 L) and air-dried.
- 4) A BB MeOH solution (20 ppm, 0.2 L) was added to the filtration cell, the cell was pressurised to 10 bar under nitrogen, and ~0.1 L of the feedstock was permeated through the **CC3-PAN** membrane.

- 5) The MeOH permeate was collected to determine the dye concentration, and the remaining retentate solution was removed from the filtration cell.
- 6) The filtration cell, including the **CC3**-PAN membrane, was washed with MeOH (0.1 L) and air-dried.

Here, we define the steps described above as "one cycle", and multiple cycles were performed using the same procedure.

To visualise the filtration process in real-time, we used a commercial bench-scale 50 mL transparent Merck Millipore Amicon® dead-end stirred cell which is connected to an 800 mL Merck Millipore Amicon® RC800 reservoir with a modified procedure: As shown in **Figure 2.12**, a **CC3 $\alpha$** -PAN membrane sample with a diameter of 42 mm was fixed onto the support at the base of the cell. The cell was then sealed using an O-ring and pressurised to 3 bar under nitrogen. To perform the filtration measurements, 50 mL of BB water feedstock (20 ppm dye concentration) was added to the feedstock tank. The solvent permeance was then calculated based on the amount of time it took a certain amount of dye feedstock to flow through the membrane, and the rejection was calculated using the dye concentration in feed and permeate. When the 50 mL feed permeated the membrane, another 50 mL of BB MeOH feedstock (20 ppm dye concentration) was added into the tank without further washing of the filtration system. The permeate was then collected, and the permeance and rejection of the membrane were calculated using the same equation. Multiple cycles were performed with the same procedure. A continual agitation speed of 400 rpm was used during the filtration experiments.

**Membrane absorption test.** Mass balance calculations were used to confirm that dye rejections were due to separation processes instead of dye adsorption by the **CC3**-PAN membrane. Membrane samples of **CC3**-PAN with a diameter of 4.7 cm were also immersed in 100 mL of a 20 ppm BB dye solution for one week and the dye concentration in the solution was monitored by UV-vis absorption to confirm that the dyes were not absorbed by the membrane. 100 mg powder crystals of **CC3 $\alpha$**  were also immersed into aqueous solutions containing 20 ppm dyes (100 mL) for one week to check whether the bulk powders absorb the dyes.

**Long-term operation.** Long-term evaluation of the **CC3**-PAN membrane performance was tested in a 50 mL Merck Millipore Amicon® dead-end stirred cell which is connected to an 800



mL Merck Millipore Amicon<sup>®</sup> RC800 reservoir. ~1 L rose bengal aqueous solution (20 ppm) was added into both cells, and a **CC3** $\alpha$ -PAN membrane sample with a diameter of 42 mm was fixed on the support at the base of the cell, and sealed using an O-ring. To enable to operate the dye filtration process in a longer time (*e.g.*, 20 hours), the feedstocks were kept under lower pressure (1 bar) at room temperature, and the feedstock was continually stirred using a stirrer bar rotating at 400 rpm.

**Membrane stability test.** Freshly prepared water feedstock solutions that contained 20 ppm of BB were used to determine the membrane continuity and stability after measuring its organic solvent permeance. By measuring rejection performance before and after the solvent permeances, we could determine that the membrane remained intact during the organic solvent permeance measurements.

**Membrane rearrangement experiments.** We have activated the membranes to investigate the rearrangement of the membranes. Firstly, the as prepared membranes were directly soaked in water (without drying process) at room temperature for 1 day, 3 days and 7 days, referred to hereafter as **CC3**-PAN, **CC3**-PAN-3, **CC3**-PAN-7, respectively.

**Water and MeOH feedstock mixture separation measurements.** Separations performed with varying water:MeOH volumetric ratios (9:1, 8:2, 7:3, 6:4, 5:5, 4:6, 3:7, 2:8, 1:9) that contained 20 ppm of BB were used to determine the dynamic behaviour of the **CC3**-PAN membrane. Separately, 0.2 L of each feedstock was charged into the dead-end stirred cell, and the cell was pressurised to 10 bar. 0.1 L of permeate was collected, and its UV-vis absorption spectrum was recorded to calculate the dye rejection % using *Eq. 2.6*. Between each measurement, the surface of the **CC3**-PAN membrane was washed with pure water:MeOH mixtures that matched the solvent ratio used during the subsequent measurement. The dye rejection % *versus* water content in MeOH is calculated. By programming in R language, the S-shaped curve (sigmoid curve) was found to fit the logistic function:

$$y = \frac{1}{1 + e^{-k \cdot (x - x_0)}} \quad (\text{Eq. 2.6})$$

where  $k$  is the logistic growth rate (steepness of the curve), and  $x_0$  is the  $x$  value of the sigmoid midpoint. The parameters  $k$  and  $x_0$  were calculated using Nonlinear Least Squares (NLS) function in R language<sup>35</sup>.

**Graded sieving experiments.** Three-component graded sieving dye separations were carried out using DR, BB, and NP dyes in MeOH and the following experimental procedure:

- 1) 100 mL of a MeOH feedstock that contained 20 ppm of the dyes DR, BB, and NP was added to the dead-end stirred cell. The cell was pressurised to 10 bar under nitrogen, and 50 mL of permeate was collected.
- 2) DR, BB, and NP have different UV absorption wavelengths (DR: 528 nm, BB: 586 nm, NP: 312 nm, in MeOH), enabling the rejection of each dye to be calculated using *Eq. 2.4* and the UV-absorption spectra of the permeate. The remaining MeOH feedstock was removed for the dead-end stirred cell and discarded.
- 3) To 10 mL of the MeOH permeate, 90 mL of water was added to generate a 10/90 vol/vol MeOH/water feedstock, which was subsequently added into the dead-end stirred cell. The cell was pressurised to 10 bar under nitrogen, and 50 mL of permeate was collected.
- 4) Due to the dilution of MeOH feedstock after adding 90% by volume of water, we concentrated the 50 mL of MeOH/water permeate to 5 mL before recording its UV-absorption spectra. UV-absorption data for the as-collected dilute and concentrated permeate was recorded, and the rejection of each dye was then calculated using *Eq. 2.4*.

**Ternary separation experiment.** Three-component dye separations were carried out using DR, BB, and NP dyes in water and the experimental procedure listed below. The experiment was performed using a commercial bench-scale 50 mL transparent Merck Millipore Amicon<sup>®</sup> dead-end stirred cell connected to an 800 mL Merck Millipore Amicon<sup>®</sup> RC800 reservoir. No intermediate handling of the membrane or feedstock was undertaken during the molecular separation.

- 1) 100 mL of a water feedstock that contained 20 ppm of the dyes, DR, BB, and NP was added to the transparent dead-end stirred cell. The cell was pressurised to 3 bar under nitrogen, and 90 mL of permeate was collected.
- 2) DR, BB, and NP have different UV absorption wavelengths (DR: 528 nm, BB: 551 nm, NP: 317 nm, in water), enabling the rejection of each dye to be calculated using *Eq. 2.4* and the UV-absorption spectra of the permeate.

- 3) 10 mL of feedstock was kept in the cell. To wash out the remaining NP from the retentate, 90 mL of water was added into the cell, and another 90 mL of permeate was collected. Step 3 was repeated until the NP concentration in the retentate was < 1%, as determined by UV-vis absorption.
- 4) 90 mL of MeOH was then added into the 10 mL of water retentate to form a new feedstock that contained 90 vol.% of MeOH. The cell was pressurised to 3 bar under nitrogen and 90 mL of the permeate was collected.
- 5) The rejection of each dye was calculated using Eq. 2.4 and the UV absorption spectra of the permeate.
- 6) 10 mL of the water/MeOH feedstock was kept in the cell. To wash out the remaining BB from the retentate, 90 mL of MeOH was added into the cell, and another 90 mL of permeate was collected. Step 3 was repeated with MeOH until the BB concentration in the retentate was < 1%, as determined by UV-vis absorption.

## 2.6 References

1. Koros W. J. Membranes: Learning a lesson from nature. *Chem. Eng. Prog.* **91**, 10 (1995).
2. Gin, D. L. & Noble, R. D. Designing the next generation of chemical separation membranes. *Science* **332**, 674–676 (2011).
3. Robeson, L. M. The upper bound revisited. *J. Memb. Sci.* **320**, 390–400 (2008).
4. Lau, W. J. & Ismail, A. F. Polymeric nanofiltration membranes for textile dye wastewater treatment: Preparation, performance evaluation, transport modelling, and fouling control — a review. *Desalination* **245**, 321–348 (2009).
5. Visvanathan, C., Ben Aim, R. & Parameshwaran, K. Membrane Separation Bioreactors for Wastewater Treatment. *Crit. Rev. Environ. Sci. Technol.* **30**, 1–48 (2010).
6. Al-Obaidi, M. A., Kara-Zaitri, C. & Mujtaba, I. M. Simultaneous Removal of Organic Compounds from Wastewater Using Reverse Osmosis Process: Modelling, Simulation, and Optimisation. *Comput. Aided Chem. Eng.* **44**, 1867–1872 (2018).
7. Barbieri, G. Permeance. in *Encyclopedia of Membranes* (eds. Drioli, E. & Giorno, L.) 1484–1485 (Springer Berlin Heidelberg, 2016). doi:10.1007/978-3-662-44324-8\_445.
8. Bowen, W. R. & Mohammad, A. W. A theoretical basis for specifying nanofiltration membranes—dye/salt/water streams. *Desalination* **117**, 257–264 (1998).

9. Chen, G., Chai, X., Po-Lock, Y. & Mi, Y. Treatment of textile desizing wastewater by pilot scale nanofiltration membrane separation. *J. Memb. Sci.* **127**, 93–99 (1997).
10. McCabe, W. L., Smith, J. C. & Harriott, P. *Unit operations of chemical engineering*. vol. 5 (McGraw-hill New York, 1993).
11. Bes-Piá, A. *et al.* Comparison between nanofiltration and ozonation of biologically treated textile wastewater for its reuse in the industry. *Desalination* **157**, 81–86 (2003).
12. Drioli, E. & Giorno, L. *Comprehensive membrane science and engineering*. vol. 1 (Newnes, 2010).
13. Strathmann, H., Giorno, L. & Drioli, E. *Introduction to membrane science and technology*. vol. 544 (Wiley-VCH Weinheim, Germany:, 2011).
14. Cheryan, M. *Ultrafiltration and microfiltration handbook*. (CRC press, 1998).
15. Yang, X. J., Livingston, A. G. & Freitas Dos Santos, L. Experimental observations of nanofiltration with organic solvents. *J. Memb. Sci.* **190**, 45–55 (2001).
16. Teixeira, M. R., Rosa, M. J. & Nyström, M. The role of membrane charge on nanofiltration performance. *J. Memb. Sci.* **265**, 160–166 (2005).
17. See Toh, Y. H., Loh, X. X., Li, K., Bismarck, A. & Livingston, A. G. In search of a standard method for the characterisation of organic solvent nanofiltration membranes. *J. Memb. Sci.* **291**, 120–125 (2007).
18. Huang, T. C. & Predecki, P. Grazing-incidence x-ray technique for surface, interface, and thin-film analysis. *Denver X-ray Conf. Appl. X-ray Anal.* (1997).
19. Egerton, R. F. Physical principles of electron microscopy: An introduction to TEM, SEM, and AEM, second edition. *Phys. Princ. Electron Microsc. An Introd. to TEM, SEM, AEM, Second Ed.* 1–196 (2016) doi:10.1007/978-3-319-39877-8.
20. Holder, C. F. & Schaak, R. E. Tutorial on Powder X-ray Diffraction for Characterizing Nanoscale Materials. *ACS Nano* **13**, 7359–7365 (2019).
21. Speakman, S. A. Basics of X-Ray Powder Diffraction. <http://prism.mit.edu/xray/>.
22. Grebenkemper, J. Powder X-ray Diffraction. <https://chem.libretexts.org/@go/page/314>.
23. Admin. Grazing Incidence X-Ray Diffraction (GIXRD). *Everything about solar energy* Advanced Characterization Techniques for Thin Film

- <http://energyprofessionalsymposium.com/?p=18499> (2015).
24. Simeone, D., Baldinozzi, G., Gosset, D., Le Caer, S. & Bézar, J. F. Grazing incidence X-ray diffraction for the study of polycrystalline layers. *Thin Solid Films* **530**, 9–13 (2013).
  25. Segmüller, A. Characterization of epitaxial films by grazing-incidence X-ray diffraction. *Thin Solid Films* **154**, 33–42 (1987).
  26. Tozawa, T. *et al.* Porous organic cages. *Nat. Mater.* **8**, 973–978 (2009).
  27. Briggs, M. E. & Cooper, A. I. A perspective on the synthesis, purification, and characterization of porous organic cages. *Chemistry of Materials* vol. 29 149–157 (2017).
  28. Liu, M. *et al.* Acid- and base-stable porous organic cages: Shape persistence and pH stability via post-synthetic ‘tying’ of a flexible amine cage. *J. Am. Chem. Soc.* **136**, 7583–7586 (2014).
  29. Jiang, S. *et al.* Molecular dynamics simulations of gas selectivity in amorphous porous molecular solids. *J. Am. Chem. Soc.* **135**, 17818–17830 (2013).
  30. Nicklin, C., Arnold, T., Rawle, J. & Warne, A. Diamond beamline I07: A beamline for surface and interface diffraction. *J. Synchrotron Radiat.* **23**, 1245–1253 (2016).
  31. Basham, M. *et al.* Data Analysis Workbench (DAWN). **22**, 853–858 (2015).
  32. TOPAS Academic version 4.1. *Coelho Software, Brisbane, Australia* (2007).
  33. Thompson, S. P. *et al.* Fast X-ray powder diffraction on I11 at Diamond. *J. Synchrotron Radiat.* **18**, 637–648 (2011).
  34. Parker, J. E., Potter, J., Thompson, S. P., Lennie, A. R., Tang, C. C. In situ gas supply system on the powder diffraction beamline I11 at Diamond Light Source. *Mater. Sci. Forum* (2012).
  35. R Core Team. R: A language and environment for statistical computing. (2020).

# Chapter 3

## Porous Organic Cage Membranes and Membrane Performance

Some of the contents in this chapter are taken from the paper:

“A Smart and Responsive Crystalline Porous Organic Cage Membrane with Switchable Pore Apertures for Graded Molecular Sieving”, *Nature Materials* **21**, 463–470 (2022)

Ai He, Zhiwei Jiang, Yue Wu, Hadeel Hussain, Jonathan Rawle, Michael E. Briggs, Marc A. Little, Andrew G. Livingston\*, Andrew I. Cooper\*

### 3.1 Background and Introduction

Porous organic cages (POCs)<sup>1-4</sup> are discrete molecules with shape persistent intrinsic cavities that have been utilised to create porosity in different materials, including molecular crystals<sup>1</sup>, amorphous solids<sup>5</sup>, and porous liquids<sup>6</sup>. As a result of their shape-persistence nature, the adsorption properties of POCs can sometimes be predicted *in silico*, up to a point, from knowledge of their isolated molecular structures alone<sup>7,8</sup>. The functionalities of POC based materials are affected by the dimensions and topology of the organic cage molecules and their arrangement in different material forms<sup>2,3,9</sup>. For example, POC crystals with well-defined internal pore structures have been shown to selectively adsorb gasses and small organic molecules in kinetic controlled molecular separations that are affected by the size and shape of the POC and their extended crystal packing<sup>2,3,9</sup>. This important combination between POC size, shape and the crystal packing in POC crystals is essential for applications in rare gas capture<sup>10</sup>, xylene separations<sup>11</sup>, and SF<sub>6</sub> capture<sup>12</sup>, amongst others<sup>2,3,9</sup>. This combination of intrinsic and extrinsic porosity determines the functionality of POC-based materials in selective adsorption processes. Furthermore, the porosity characteristics of POC molecules can be fine-tuned. For example, a recent study found that the pore limiting diameter in POC crystals could be tuned over the size range 1.95 to 3.5 Å to optimise their separation performance in kinetically controlled quantum sieving applications<sup>13</sup>. Hence, POC crystals can be designed to have tunable porosity, leading to practical advantages in molecular separations.

Most separation studies involving POCs have focussed on using molecular crystals<sup>2,3,9</sup>, which can exhibit slow adsorption kinetics that might prohibit their larger-scale utilisation. Moreover, many approaches that use POC crystals rely on selective adsorption governed by thermodynamics rather than kinetics, limiting their broader use in size and shape-selective membrane filters. Given their solution processability, however, there is scope to develop crystalline POC-based membranes that operate by selectively removing guests that are either too large or have the wrong shape to diffuse through the POC pore structure.

There is growing interest in emerging membrane technologies that perform industrial and environmentally relevant separations, including energy-expensive distillations<sup>14-17</sup> and inefficient wastewater treatments<sup>16,18,19</sup>. Membranes are of particular relevance for molecular separations where two or more solutes need to be separated from one another, as for distillation or chromatography, as opposed to separations where a whole series of solutes are concentrated, such as during the evaporation or seawater reverse osmosis<sup>14-16,20,21</sup>. A key objective is to make

molecular separations more sustainable and more efficient. A major advantage of membranes is that they can perform separations in the liquid phase, which is often more practical than vapours and eliminates the need for phase changes. However, all membranes exhibit a crucial trade-off between flux and selectivity, where increasing the pore aperture enhances the flux but leads to lower selectivity in size-based separations<sup>22</sup>. There is also a vital link between pore aperture and membrane thickness, which collectively regulate flux and selectivity, but it remains challenging to control both of these variables in practice<sup>23</sup>. Thus, the production of membranes with tunable porosity and optimised thicknesses are essential for new transformative separation technologies.

Membranes for liquid separations are typically produced using phase inversion, which can be followed by coating<sup>24</sup> or interfacial polymerization<sup>25</sup>. A limitation of these synthetic processes is that they produce amorphous polymer networks, limiting the degree of pore tunability in the membranes. Consequently, there is a strong demand to develop membranes with more tunable and modular pore structures. Various porous solids, including zeolites<sup>26</sup>, POCs<sup>1-4</sup>, organic polymers<sup>27</sup>, metal-organic frameworks (MOFs)<sup>28</sup>, covalent organic frameworks (COFs)<sup>29</sup>, and hydrogen-bonded organic frameworks (HOFs)<sup>30</sup> have been explored as candidates to modify membrane separation behaviour. Banerjee *et al.* reported the interfacial synthesis of a series of crystalline COF films with pore sizes ranging from 1.4 to 2.6 nm that showed good performance in dye rejection after being deposited on polyester supports<sup>31</sup>. Dichtel *et al.* reported COF films with 3.4 nm pores and tunable thicknesses over the range of 100  $\mu\text{m}$  to 2.5 nm that rejected up to 91% of an organic dye, Rhodamine WT, from water<sup>32</sup>. The same group also reduced the effective pore size of their COF membrane to 3.3 and 3.2 nm using reticular chemistry<sup>33</sup>. In addition to COFs<sup>34,35</sup>, MOFs and their composites have been used to produce membranes<sup>34,36</sup>. However, the discovery of processing techniques that control porous structure formation and the generation of membranes with optimised thicknesses and crystallinity have proven difficult to discover. Consequently, polymer nanomembranes still dominate much of the research efforts. Despite these recent advances in porous solids, it is still challenging to produce continuous nanofiltration membranes with extended porous frameworks that perform exclusively as size-based molecular sieves rather than selective adsorbents<sup>37</sup>.

POCs have two distinct advantages over the majority of other classes of porous crystalline solids: they are solution-processable in their as-synthesised intrinsically porous form, and their solid-state structures are defined by non-covalent intermolecular interactions. Consequently,



POC structures can be controlled using a range of post-synthesis crystal design strategies<sup>9</sup>. They can also be cast onto different substrates<sup>38–40</sup> or added as 'fillers' to polymers, including mixed matrix membranes<sup>41</sup> and molecularly mixed composite membranes<sup>42</sup> to produce composites with enhanced porous properties. As such, POCs are intriguing but relatively unexplored candidates for new types of membrane materials<sup>43</sup>; indeed, many selectively porous POCs have been reported<sup>44–47</sup>.

In this chapter, different approaches to fabricate the POC films are discussed, including interfacial synthesis, spin coating, casting, and ultra-sonic methods. These resulting POC films were then coated on polyacrylonitrile (PAN) supports and the resulting composites were utilised as continuous membranes in molecular separations. The morphology, crystallinity, solvent permeance and dye rejection have been studied, and the formation mechanism was further investigated. We have compared the membrane performance (i.e., permeance and rejection) on the **CC3** membranes made by different methods and how crystallinity affects their performance.

## 3.2 Membrane Fabrication

Cage membranes have been fabricated by different methods, including interfacial crystallisation, spin-coating, casting, in-situ synthesis, sonochemistry, etc. (see Chapter 2 for full experiment details). The advantages and disadvantages of these methods are discussed later by comparing the surface morphology and membrane performance.

Among these approaches, 2D crystalline porous organic cage films were produced using a combined interfacial condensation reaction and crystallisation process at a water-organic interface. This interfacial technology simultaneously allows the self-assembly of **CC3**, which was synthesised via a [4+6] cycloimination reaction using 1,3,5-triformylbenzene (TFB) and (1*R*,2*R*)-1,2-diaminecyclohexane (CHDA), while directing the formation of crystalline 2D films of the **CC3** product at the liquid-liquid interface. As schematically depicted in **Figure 3.1**, two layers of immiscible solvents were employed in a glass filtration funnel dish with an inner diameter of 7.4 cm (see **Chapter 2** for experimental details). Typically, a bottom layer (0.8 wt.%) was prepared by adding solid TFB (0.24 g, 1.48 mmol, 0.8 wt.%) into dichloromethane (30 mL) until it dissolved, followed by a 32 mL aqueous solution (0.8 wt.%) of CHDA (0.26 g, 2.24 mmol) that was layered slowly on top of the aldehyde solution. The

reaction was kept at room temperature in undisturbed conditions for a period of time (4-96 hr, although a reaction time of 24 hr was typically used).

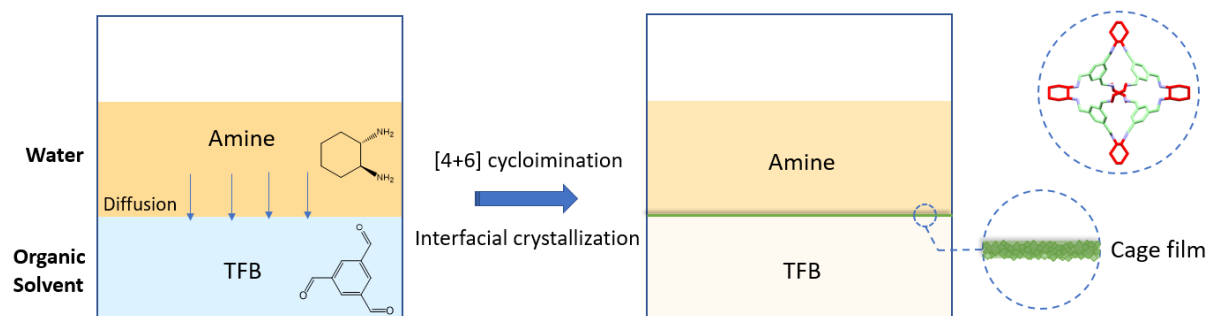


**Figure 3.1** Illustration of interfacial synthesis method used to fabricate cage films and the octahedron structure of a **CC3** cage molecule.

From the reactions, free-standing and continuous films with highly crystalline domains of **CC3** were formed at the liquid–liquid interface. The porous networks were specifically retained at the interface. The **CC3** films were obtained by removing the solvents with water and methanol washing procedure and could easily be transferred from the liquid-liquid interface onto various substrates (*e.g.*, glass, steel mesh, carbon tape, and silicon wafers, as shown in **Figure 3.2**) for further analysis of the crystallinity and surface morphology.

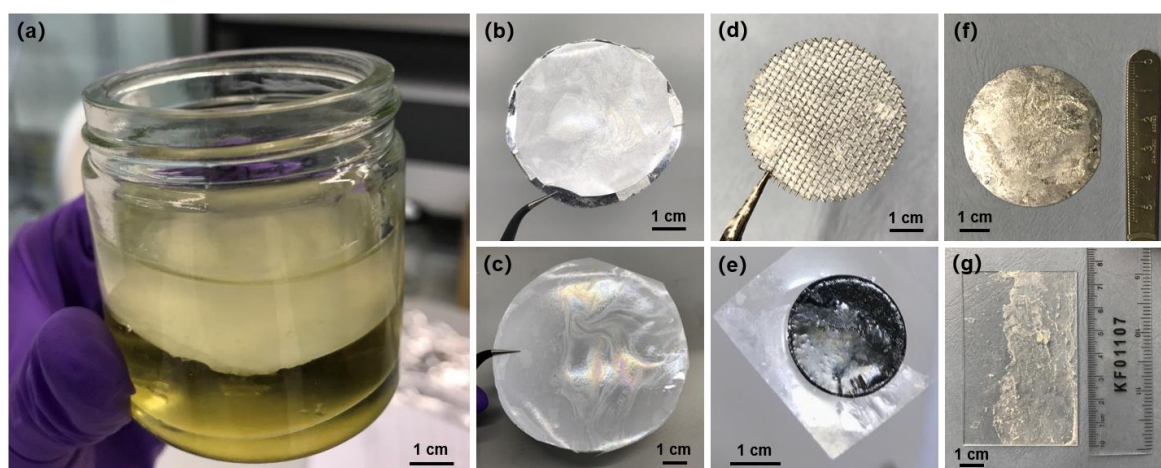


**Figure 3.2** Photographs of as synthesised **CC3-PAN-24H-0.8%** film. (a) Free-standing **CC3** film grown in a glass dish at the liquid-liquid interface between water and dichloromethane. (b, c, d, e, f, g) **CC3** films transferred onto different substrates for further analysis: (b) PAN sheet fixed on an aluminum wafer; (c) PAN membrane; (d) stainless mesh; (e) carbon tape used for scanning electron microscopy; (f) silicon wafer; (g) glass slide.

To perform permeance and dye rejection studies, the **CC3** film was coated onto a polyacrylonitrile (PAN) membrane support by filtration to form the composite membrane, which could easily be manipulated and cut to size. As shown in **Figure 3.3**, the resulting membrane, referred to hereafter as **CC3-PAN**, was free of macroscopic defects up to at least 7.4 cm in diameter using this preparation process (**Figure 3.3**, see **Chapter 2** for experimental details), with no evidence of delamination after cutting the membrane into smaller pieces.

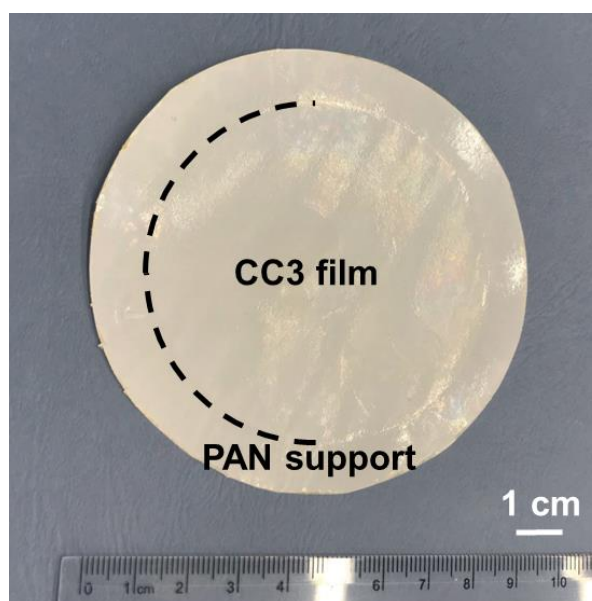


**Figure 3.3** Photograph of a composite membrane **CC3-PAN** with a diameter of 7.4 cm, which could be cut into specific sizes for membrane filtration tests in a dead-end filtration cell.

### 3.3 Membrane Characterisation for Interfacial Crystallization Membranes

The **CC3** film was characterised by Fourier transform infrared (FT-IR), Raman spectroscopy, nuclear magnetic resonance (NMR) spectroscopy, scanning electron microscopy (SEM), focused ion beam SEM (FIB-SEM), X-ray diffraction, and atomic force microscopy (AFM). For spectroscopic measurements, a crystalline **CC3 $\alpha$**  sample was used as a reference<sup>1</sup>. **CC3 $\alpha$**  has a 3D diamondoid pore structure, and it is the thermodynamically most stable polymorph **CC3**<sup>1</sup>.

#### 3.3.1 Chemistry Characterisation

The chemical functional groups for cage films have been detected by Fourier transform infrared (FT-IR). As shown in **Figure 3.4**, the thin film shows characteristic stretching bands at 2924  $\text{cm}^{-1}$  (aliphatic C–H), 2852  $\text{cm}^{-1}$  (aldehydic C–H), 1640  $\text{cm}^{-1}$  (–C=N), 1604–1623  $\text{cm}^{-1}$  (–C=O),

1565–1576  $\text{cm}^{-1}$  ( $-\text{C}=\text{C}$ ), and 1267–1298  $\text{cm}^{-1}$  ( $-\text{C}-\text{N}$ ), matching well with the crystalline **CC3** reference.<sup>1</sup> This indicates the absence of the cage reactants or small oligomers in the formed films.

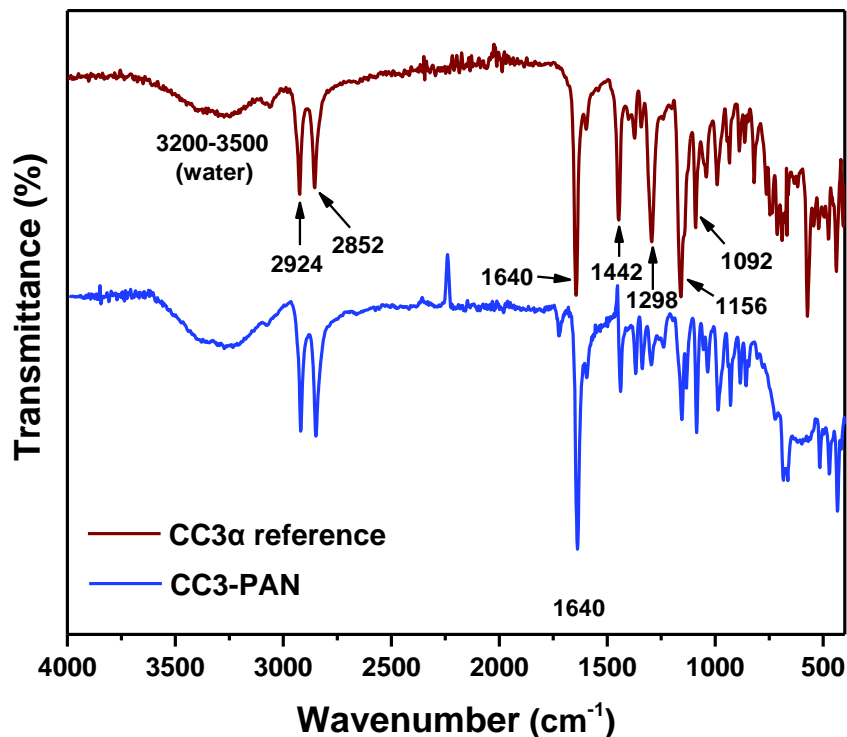


**Figure 3.4** FT-IR spectra of **CC3-PAN-24H-0.8%** and crystalline **CC3 $\alpha^1$**  reference. The signal of blank PAN support was subtracted during the background measurement. Main peaks are labelled with the wavenumber values. Film synthesis conditions, reagent concentration: TFB 0.8 wt.% in DCM (30 mL), CHDA 0.8 wt.% in water (32 mL); reaction conditions: 24 hours at room temperature; dish diameter: 7.4 cm. Copyright © 2022, Springer Nature and Ai He, etc.

$^1\text{H}$  spectroscopy was carried out in deuterated chloroform ( $\text{CDCl}_3$ ) to further investigate the chemical composition of the cage films. These NMR samples were measured within 5 min of collecting the membrane materials to avoid self-sorting of misaligned cage fragments in the NMR solvent – as reported before, cages could be easily formed in the same solvent.<sup>1</sup> It should be noted that all of the **CC3** film on the glass substrate dissolved fully in the  $\text{CDCl}_3$  solvent, indicating no insoluble polymers had formed in the film. This confirmed the formation of **CC3**, where the NMR spectra (**Figure 3.5**) exhibits the same chemical shift as **CC3** solid powder sample ( $\delta$  8.15 (s,  $\text{CH}=\text{N}$ , 12H), 7.89 (s,  $\text{ArH}$ , 12H), 3.33 (m,  $\text{CHN}$ , 12H), 1.9 – 1.4 (m,  $\text{CH}_2$ , 48H) ppm), with a small amount (<2%) of unreacted aldehydes at 10 ppm.

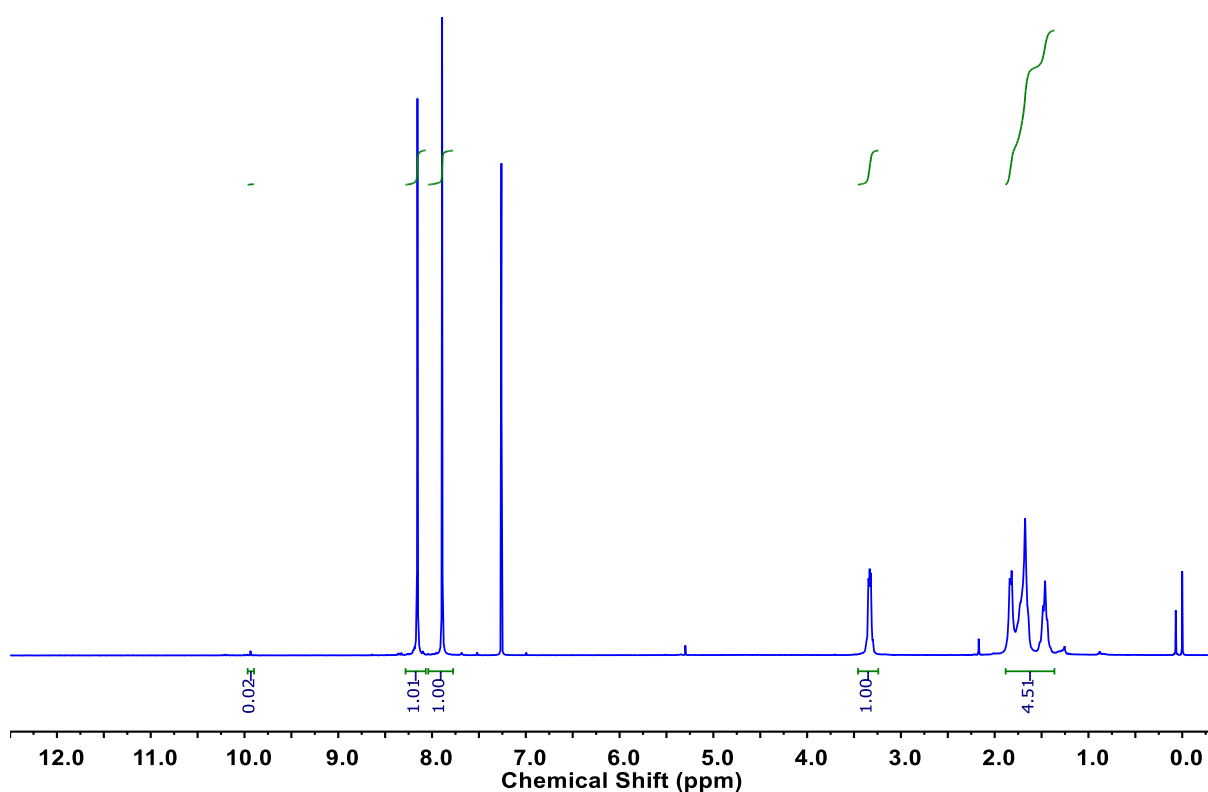


**Figure 3.5**  $^1\text{H}$  NMR (400 MHz,  $\text{CDCl}_3$ ) spectrum for a solid sample of CC3 film that had been deposited on glass and scraped off before being fully dissolved in  $\text{CDCl}_3$ :  $\delta = 8.15$  (s,  $\text{CH}=\text{N}$ , 12H), 7.89 (s, ArH, 12H), 3.33 (m, CHN, 12H), 1.9 – 1.4 (m, cyclohexyl CH and  $\text{CH}_2$ , 48H). Although the  $^1\text{H}$  NMR spectrum was measured within 5 mins of dissolving the CC3 film in  $\text{CDCl}_3$ , self-sorting of misaligned cage fragments can still occur on this timescale and can, therefore, not be ruled out. Film synthesis conditions, reagent concentration: TFB 0.8 wt.% in DCM (30 mL), CHDA 0.8 wt.% in water (32 mL); reaction conditions: 24 hours at room temperature; dish diameter: 7.4 cm. Copyright © 2022, Springer Nature and Ai He, etc.

### 3.3.2 Morphology Characterisation

Magnified optical images of the CC3 film on a glass substrate (50x magnification objective) suggested that the film was homogenous and continuous with a glossy surface (**Figure 3.6**). Surface morphology in higher resolution of the CC3 film was visually investigated by scanning electron microscope (SEM) and focused ion beam scanning electron microscopy (FIB-SEM).



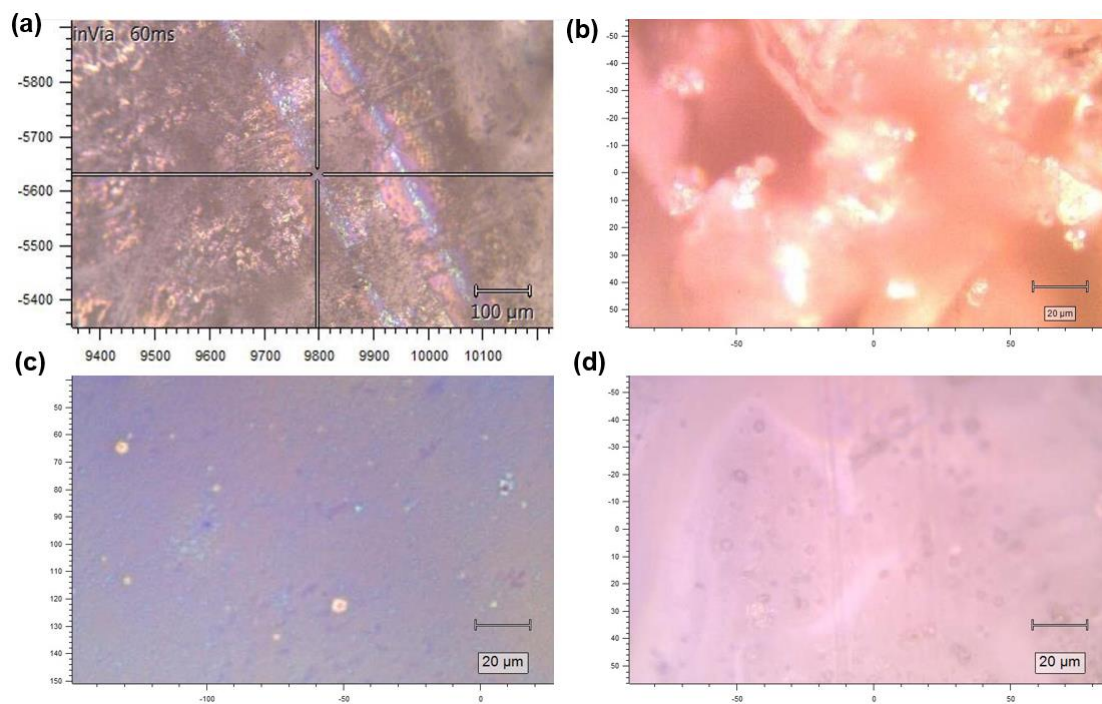


**Figure 3.6** Microscopic images of CC3 film deposited on a glass slide (50x objective), which indicate a homogenous surface morphology. Film synthesis conditions, reagent concentration: TFB 0.8 wt.% in DCM (30 mL), CHDA 0.8 wt.% in water (32 mL); reaction conditions: 24 hours at room temperature; dish diameter: 7.4 cm.

SEM images showed a continuous, integrated and defect-free film in the CC3-PAN composite (**Figure 3.7 (a)**), with a scale of a few micrometres. As is shown in **Figure 3.7 (b)**, the thickness of the CC3-PAN is ~80 nm measured on a free-standing film, where the film was deliberately buckled to show its thickness.

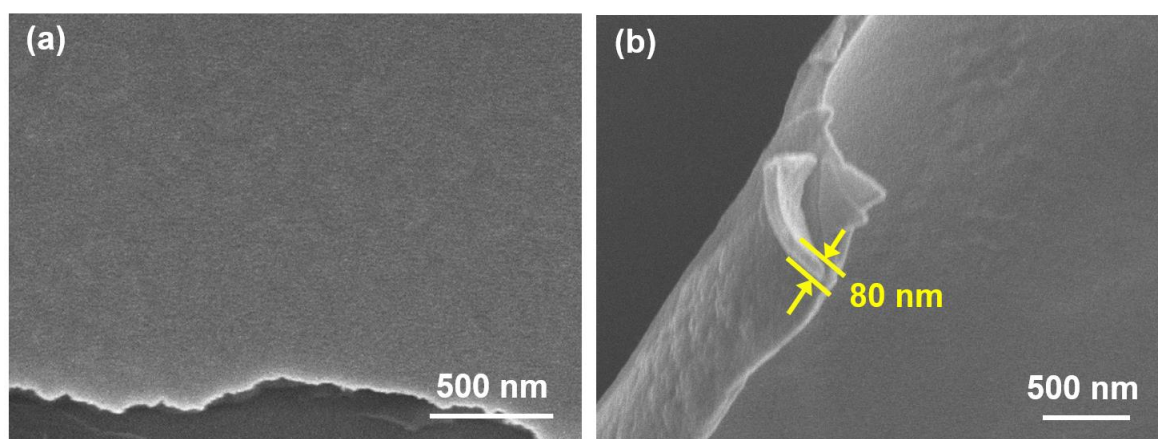


**Figure 3.7** SEM images of (a) CC3-PAN CC3 film on PAN support showing its surface morphology of the CC3 film (CC3-PAN-24H); (b) a free-standing CC3 film, where the film was deliberately buckled to show its thickness.

Notably, it was observed, for the first time, from SEM images for **CC3** film deposited on silicon wafers in **Figure 3.8** that the continuous thin film contained embedded, octahedral **CC3** crystals. These triangles, hexagons or octahedrons vary in sizes from around 50 nm to 600 nm, with an average crystal size of 200 nm.

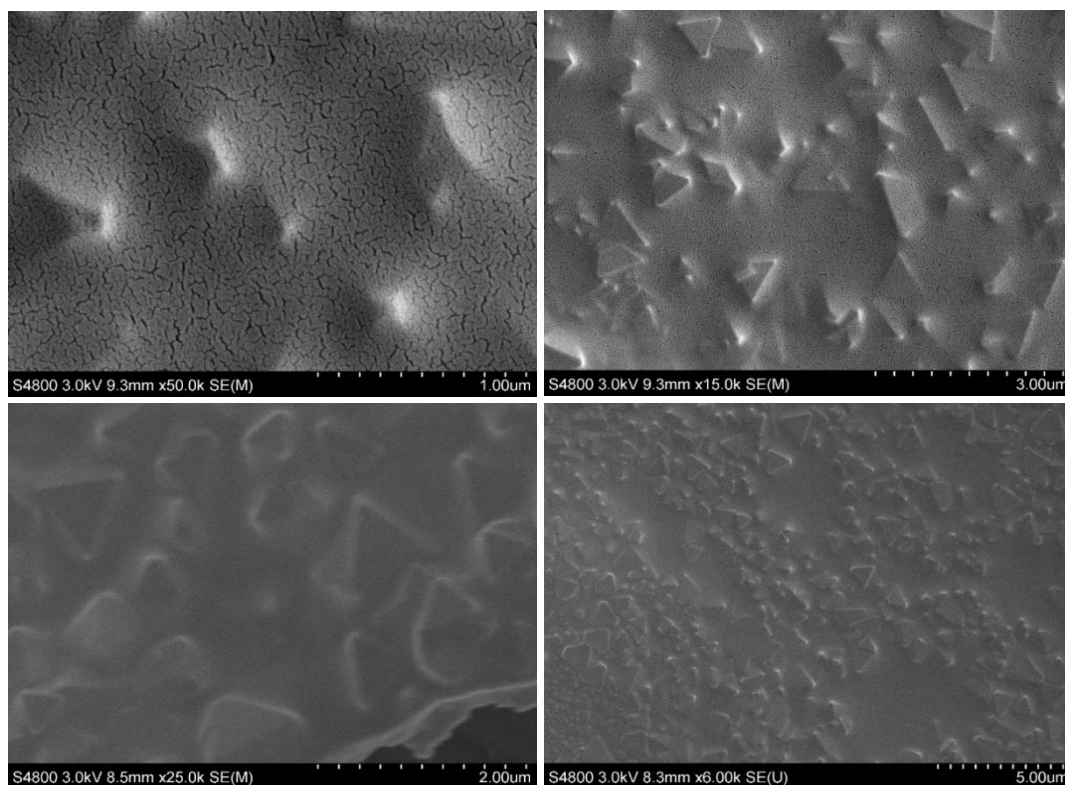


**Figure 3.8** SEM images of continuous **CC3** film deposited on silicon wafers recorded at different resolutions. Octahedron-shaped crystals in the **CC3** film share the same crystal habit as the parent cage in its thermodynamically most stable crystalline form,  $\text{CC3}\alpha^{48}$ . Film synthesis conditions, reagent concentration: TFB 0.8 wt.% in DCM (30 mL), CHDA 0.8 wt.% in water (32 mL); reaction conditions: 24 hours at room temperature; dish diameter: 7.4 cm.

Cross-sectional SEM images were obtained by being cut in a liquid nitrogen cold trap or after step-by-step FIB trenching and polishing of both **CC3**-PAN and a **CC3** film coated on a silicon wafer. As shown in **Figure 3.9**, the **CC3** film can be seen on top of the supporting substrates, and they showed a similar thickness (~85 nm and ~94 nm).

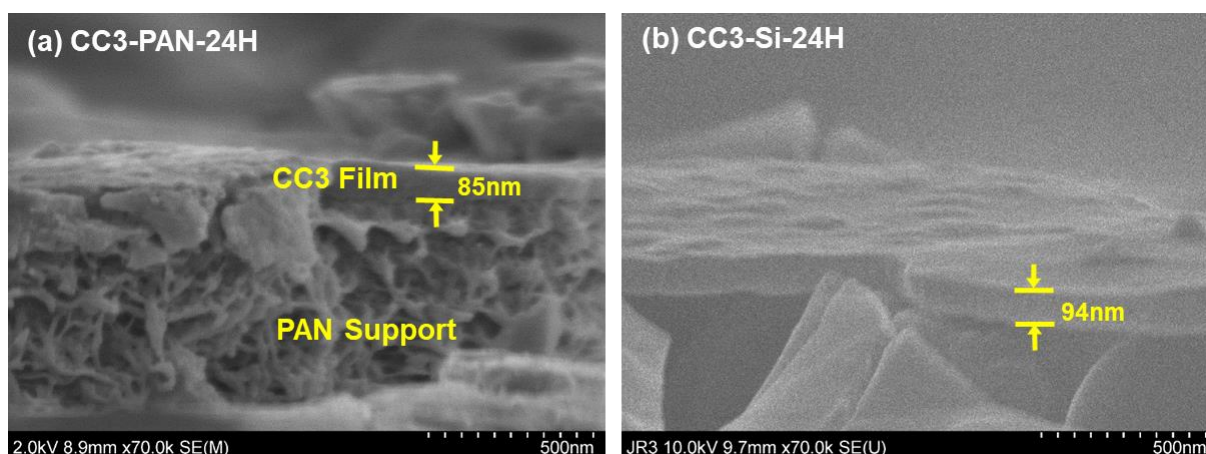


**Figure 3.9** SEM images of continuous CC3 film deposited on (a) PAN support (CC3-PAN-24H) and (b) silicon wafer (CC3-Si-24H). The thicknesses of the CC3 films have been included in the images. Copyright © 2022, Springer Nature and Ai He, etc.

The FIB-SEM images show there is a clear boundary between the CC3 film that is layered on top of the porous PAN support (Figure 3.10) and a silicon wafer (Figure 3.11), where small octahedral crystals can be observed embedded in the CC3 film layer. The thickness data was measured in multiple positions on the cross-sections, which exhibited a constant value (70~90 nm) over a 10  $\mu\text{m}$  distance on the film. A few polishing steps were applied to the membrane samples to investigate the continuity in the film, which are shown in Figure 3.11.

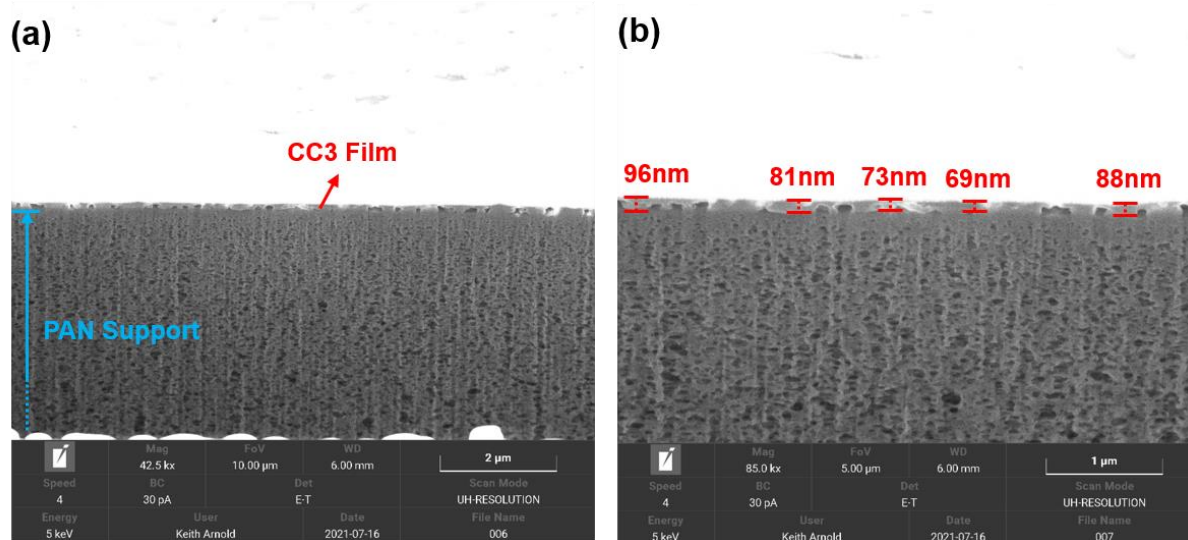


**Figure 3.10** FIB-SEM images for CC3-PAN-24H showing its cross-sectional structures at different resolutions (a) 42.5 k and (b) 85.0 k, and the thickness data measured at different positions. Film synthesis conditions, reagent concentration: TFB 0.8 wt.% in DCM (30 mL), CHDA 0.8 wt.% in water (32 mL); reaction conditions: 24 hours at room temperature; dish diameter: 7.4 cm. Copyright © 2022, Springer Nature and Ai He, etc.



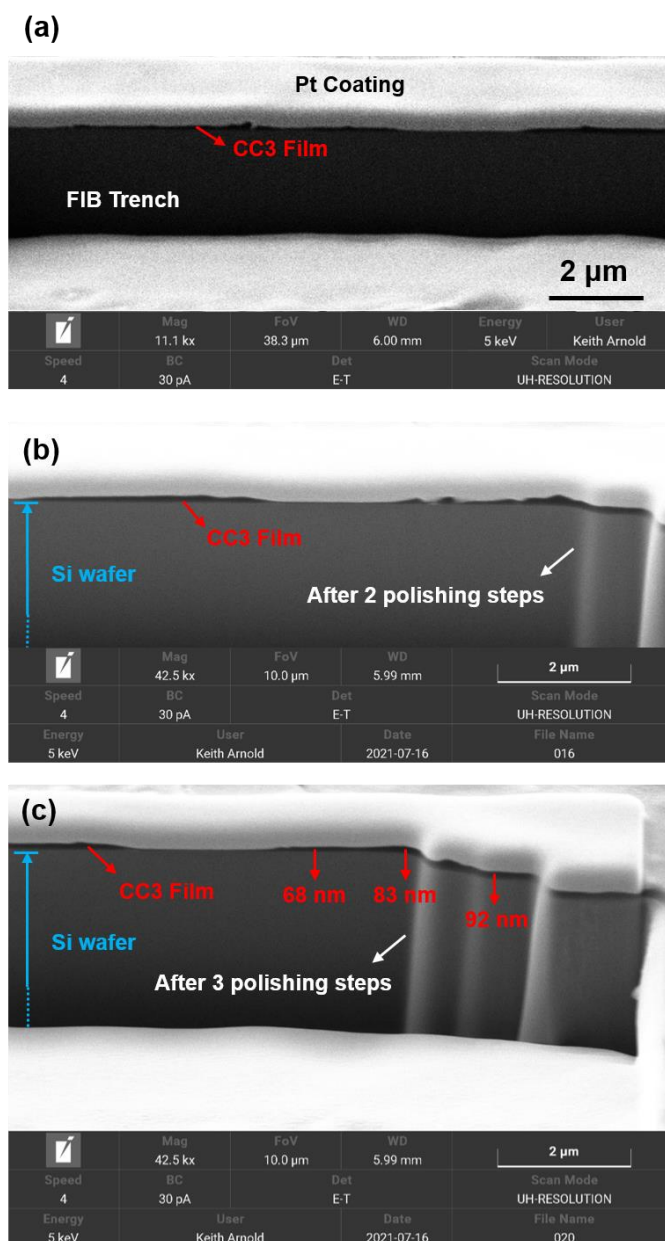


**Figure 3.11** FIB-SEM images for CC3-Si-24H showing its cross-sectional structures: (a) a FIB trench; (b) after 2 polishing steps; (c) after 3 polishing steps at different resolutions, and the thickness data measured at different positions. The ion beam was used for trenching and polishing (30kV and 1nA for trenching, and 30kV and 250pA for polishing), and the electron beam was used for imaging (5kV, 30pA, and 10kV, 60pA). Film synthesis conditions, reagent concentration: TFB 0.8 wt.% in DCM (30 mL), CHDA 0.8 wt.% in water (32 mL); reaction conditions: 24 hours at room temperature. Copyright © 2022, Springer Nature and Ai He, etc.

To further investigate the film thickness in a more accurate way, we performed AFM measurements after transferring the as-synthesised CC3 film onto a silicon wafer and collected AFM height image and its height profile data, as is shown in **Figure 3.12**. Again, this

measurement confirmed that the CC3 film was continuous with a constant thickness of ~80 nm.

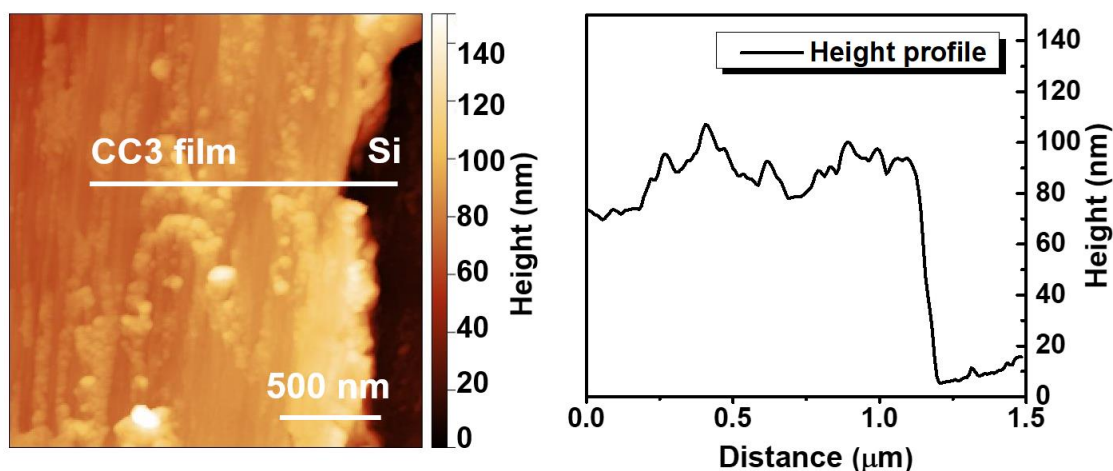


**Figure 3.12** AFM height image (left) and the height profile (right) of CC3 film transferred onto a silicon (Si) wafer (CC3-Si-24H). Copyright © 2022, Springer Nature and Ai He, etc.

### 3.3.3 Crystallography Characterisation

One distinct property of the membrane fabrication process is that the crystals of the CC3 product can be grown and kept at the interface. Therefore, it is of importance to characterise the crystallography properties of the obtained CC3 films.

A distinct environment of the functional groups in different polymorphs, according to X-ray analysis, can also be detected by Raman spectroscopy.<sup>49,50</sup> The sensitivity of Raman spectroscopy to crystal symmetry can be applied to the problem of destabilization and heterogeneous surfaces.<sup>51</sup> Therefore, Raman spectroscopy was used to map the solid-state structure of this CC3 thin film using a 785 nm laser. For the Raman map, we used crystalline CC3 $\alpha^1$  and amorphous CC3<sup>5</sup> samples as references. In the Raman spectra of the crystalline CC3 $\alpha$  reference, strong and sharp characteristic signals at 1600 and 1646 cm<sup>-1</sup> were assigned to imine bonds of CC3 (**Figure 3.13**).

The Raman map was performed on 80 × 80 μm grid sized CC3 film deposited on glass, which is shown in **Figure 3.14**, and this Raman map indicated that the CC3 thin film comprised crystalline domains and that the crystalline regions had the same solid-state structure as the CC3 $\alpha$  polymorph.

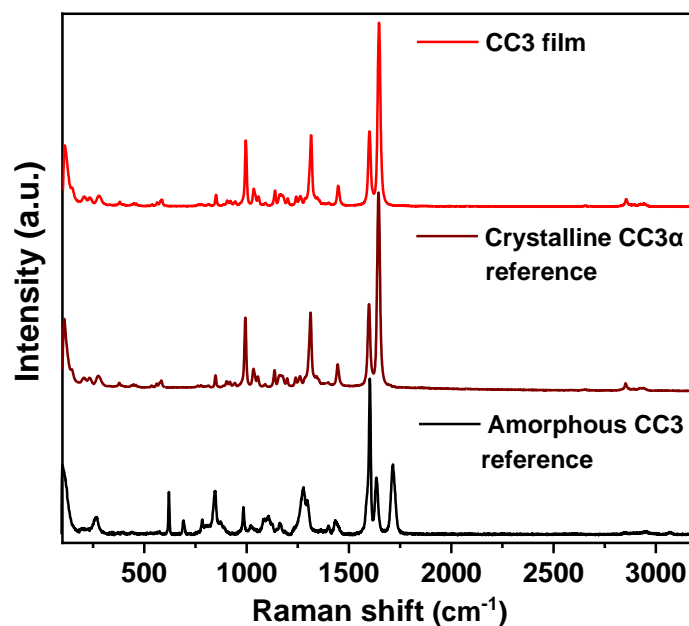


**Figure 3.13** Raman spectra of CC3 film deposited on glass, crystalline CC3 $\alpha$  reference, and amorphous CC3<sup>5</sup>. Spectral analysis settings: 785 nm laser (power 5%); 1200 1/mm (633/780) grating; Renishaw Centrus 5134M5 detector; 50x L objective; 10 seconds exposure time with 3 accumulations; line focus mode; and spectra were recorded over the range 102 cm<sup>-1</sup> to 3202 cm<sup>-1</sup>. Copyright © 2022, Springer Nature and Ai He, etc.

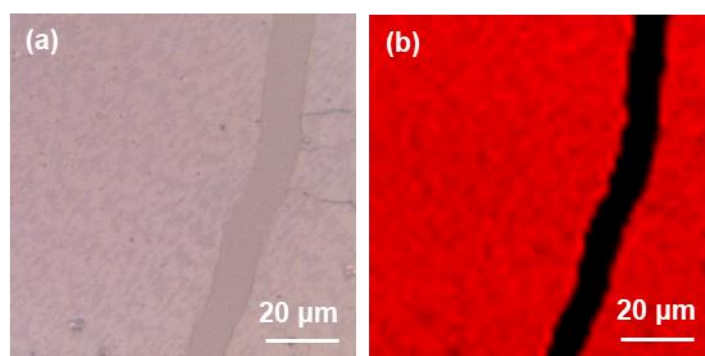


**Figure 3.14** (a) Raman microscope image and (b) Raman map of a of a (100×100) μm<sup>2</sup> area on the cage film. CC3 film on a glass support, where we purposefully scratched the film before the measurement to expose the glass support (black stripe in (b)). The red regions on a CC3 film had comparable Raman spectra to a powdered crystalline CC3 $\alpha$  reference<sup>1</sup>.

To further confirm the crystalline structure of the **CC3** thin film, we performed a series of powder X-ray diffraction (PXRD) and grazing incidence X-ray diffraction (GIXRD) measurements on bulk samples or that were deposited on PAN and measured in their as-prepared forms. These thin-film materials were weakly diffracting due to their light atom composition and low skeleton densities. Therefore, PXRD data was initially obtained by collecting the free-standing films. As is shown in **Figure 3.15**, sharp peaks of the **CC3** films could be observed in the PXRD pattern, indicating that the **CC3** thin film was crystalline and that it had the same polymorphic structure as **CC3 $\alpha$** .

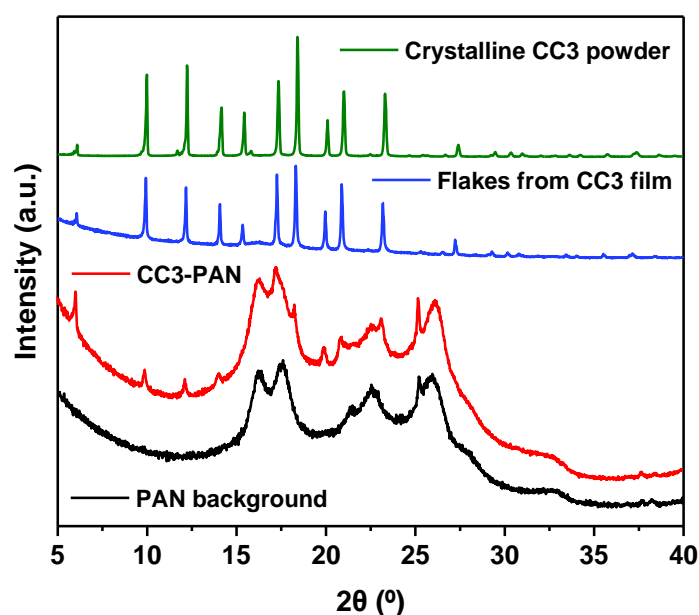


**Figure 3.15** PXRD pattern of blank PAN membrane (black), **CC3-PAN-24H-0.8%** (red), flakes collected from a free-standing **CC3** film that had been deposited on a glass substrate (blue), and crystalline **CC3 $\alpha$**  reference (green). PXRD patterns were collected in transmission mode with *Cu-K $\alpha$*  radiation over the  $2\theta$  range of  $5\text{-}40^\circ$  using a step size of  $0.013^\circ$ . Data collection times, crystalline **CC3 $\alpha$**  reference: 15 minutes; flakes from **CC3** film deposited on glass: 60 minutes; blank PAN and **CC3-PAN-24H-0.8%**: 300 minutes.

GIXRD measurements were performed for the **CC3-PAN** using both out-of-plane and in-plane measurement geometries, as is shown in **Figure 3.16**. With a background signal from the PAN substrate corresponding to the polyacrylonitrile material, distinct reflection positions were obtained in line with the simulated **CC3 $\alpha$**  sample. In both in-plane and out-of-plane diffraction exhibited the same reflection positions, and these spectra revealed that the **CC3** crystals were randomly orientated in **CC3-PAN** membrane.

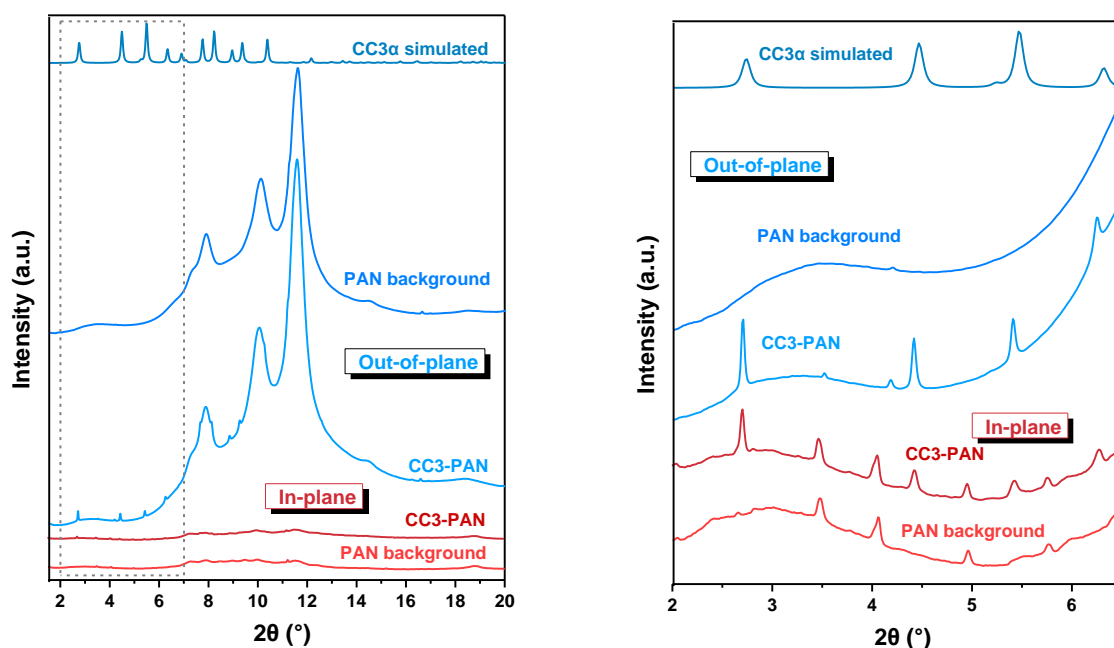


**Figure 3.16** *In-plane and out-of-plane GIXRD patterns of CC3-PAN-24H-0.8% membrane are shown below the simulated PXRD pattern for CC3 $\alpha$  (left). A larger insert over the  $2\theta$  range 2 – 7° is shown in the right figure. Copyright © 2022, Springer Nature and Ai He, etc.*

### 3.3.4 Film Formation Mechanism Study

A key advantage of the interfacial synthesis technology is that it could create continuous films of the product<sup>25,31</sup>. Here, this approach was used to direct the solution-processable **CC3** molecules and their crystals to assemble into continuous and densely packed films at the liquid-liquid solvent interface. The reaction conditions were also modified to optimise the thickness, continuity, and crystallinity of the **CC3** film. This allowed **CC3** films to be created from the interfacial reaction that were four times thinner than the **CC3** film created by spin coating<sup>40</sup>, which potentially allows for faster diffusion of liquids through the membrane.

To further investigate the crystallisation process of **CC3** films at the dichloromethane-water interface, we varied the reaction time from 4 to 96 hours and manipulated the reagent concentrations from 0.2 to 2.5 wt.%. The nomenclature **CC3-PAN-Xh-Y%** is used to refer to the membranes made with X hours of reaction time and Y weight percent of the reagents. The products were analysed by NMR spectroscopy, Raman microscope images and maps, SEM

and FIB-SEM, AFM, and X-ray diffraction so that we were able to study their chemistry, morphologies, structures, and find the effects of the reaction time and concentrations.

As is shown in **Figure 3.17**, CC3-PAN membranes exhibit stronger CC3 NMR signals with the increasing reaction time, and the reaction appears to be near completion after around 16 hours. The NMR spectra then remain very similar after longer reaction times (48 – 96 hours).

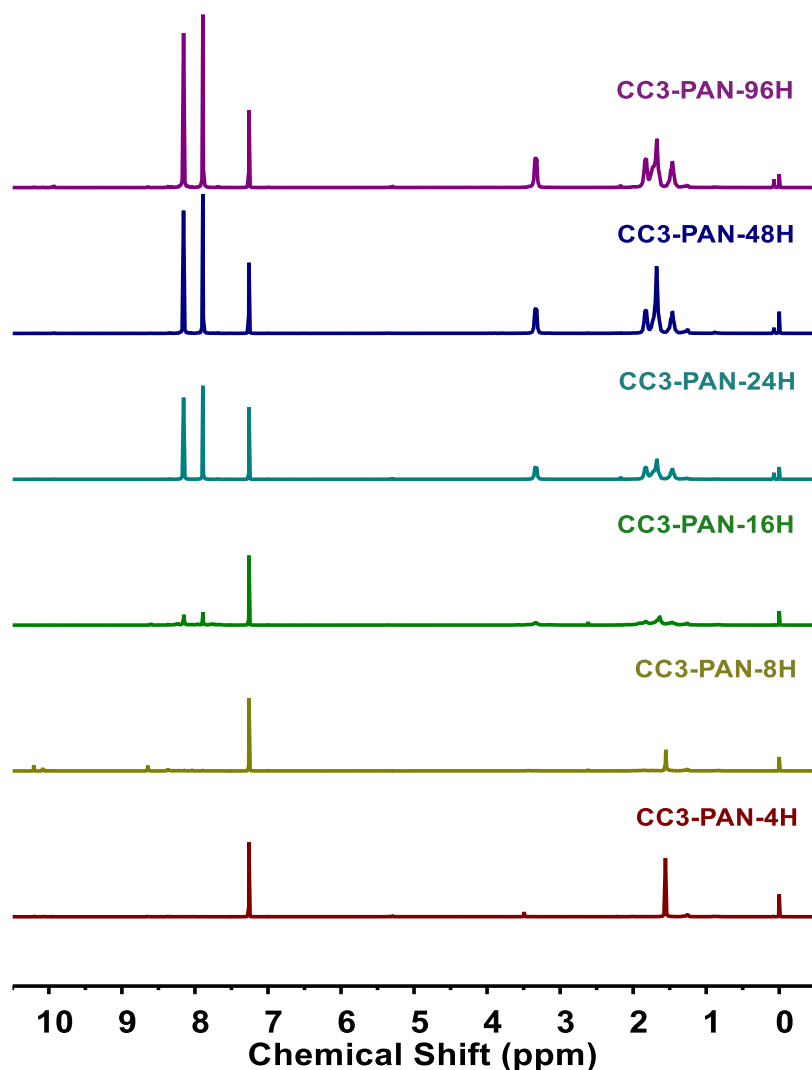


**Figure 3.17**  $^1\text{H}$  NMR ( $\text{CDCl}_3$ , 400 MHz) spectra for CC3-PAN-XH-0.8% membranes fabricated using reaction times that ranged between 4–96 hours. Generic film synthesis conditions, reagent concentration: TFB 0.8 wt.% in DCM (30 mL), CHDA 0.8 wt.% in water (32 mL); reaction conditions: room temperature; dish diameter: 7.4 cm.

Raman microscope images and maps are shown in **Figure 3.18**, where the Raman spectra of CC3 $\alpha$  and amorphous CC3 are used as references, and the red regions represent matches with



the Raman spectrum of **CC3 $\alpha$** . These data reveal a denser surface with larger crystals as the reaction time increased.

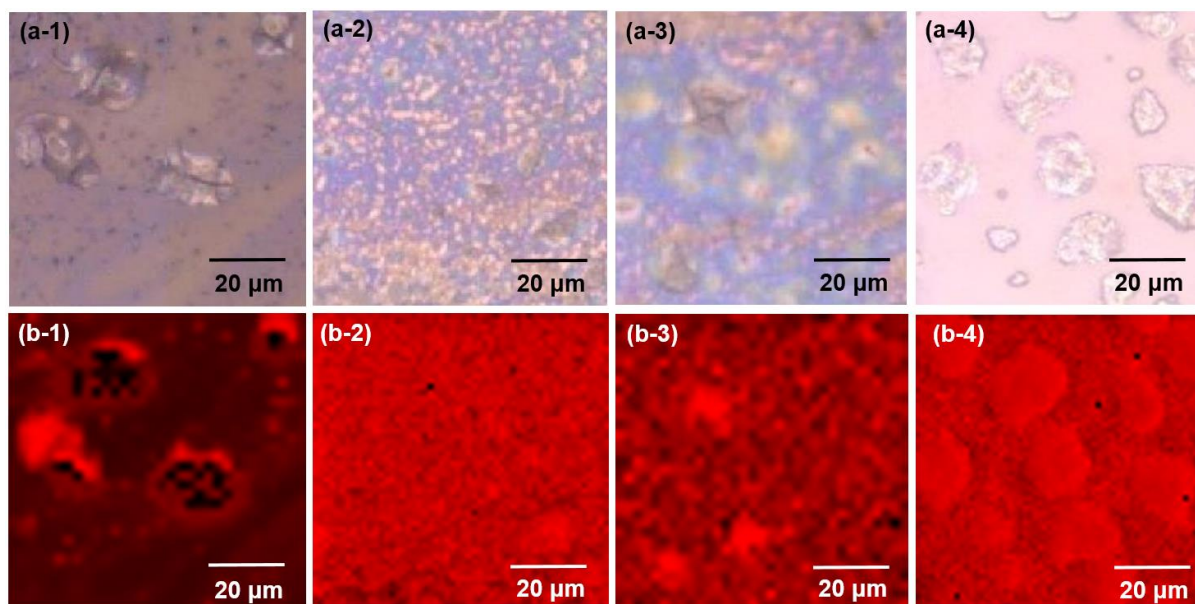


**Figure 3.18** Raman microscope images (a) and maps (b) generated using an  $80 \times 80 \mu\text{m}^2$  sized grid of **CC3-PAN-XH-0.8%** that were fabricated over different reaction times, (1) 8 hours; (2) 16 hours; (3) 48 hours; (4) 96 hours, and deposited on glass substrates. The Raman spectra of **CC3 $\alpha$**  and amorphous **CC3** were used as references, and the red regions represent matches with the Raman spectrum of **CC3 $\alpha$** . Generic film synthesis conditions, reagent concentration: TFB 0.8 wt.% in DCM (30 mL), CHDA 0.8 wt.% in water (32 mL); reaction conditions: room temperature; dish diameter: 7.4 cm. Scar bar: 20  $\mu\text{m}$ . The Raman maps for **CC3-PAN-24H-0.8%** are shown in **Figure 3.14**. Copyright © 2022, Springer Nature and Ai He, etc.

By contrast, using a reagent concentration of 0.2% resulted in poorly formed **CC3** products, with the NMR spectra of films fabricated from different concentrations over 24 hours shown in **Figure 3.19**. The products of **CC3-PAN-0.2%** were impure, indicating that oligomers and small fragments and the reagents such as aldehyde. While the concentration increased to 0.8%, pure **CC3** molecules were obtained in the membrane product; a small amount of aldehyde could be seen in the NMR spectra with the concentration higher than 1.0%, which is due to the higher concentration and some unreacted reagent remained in the **CC3** products.

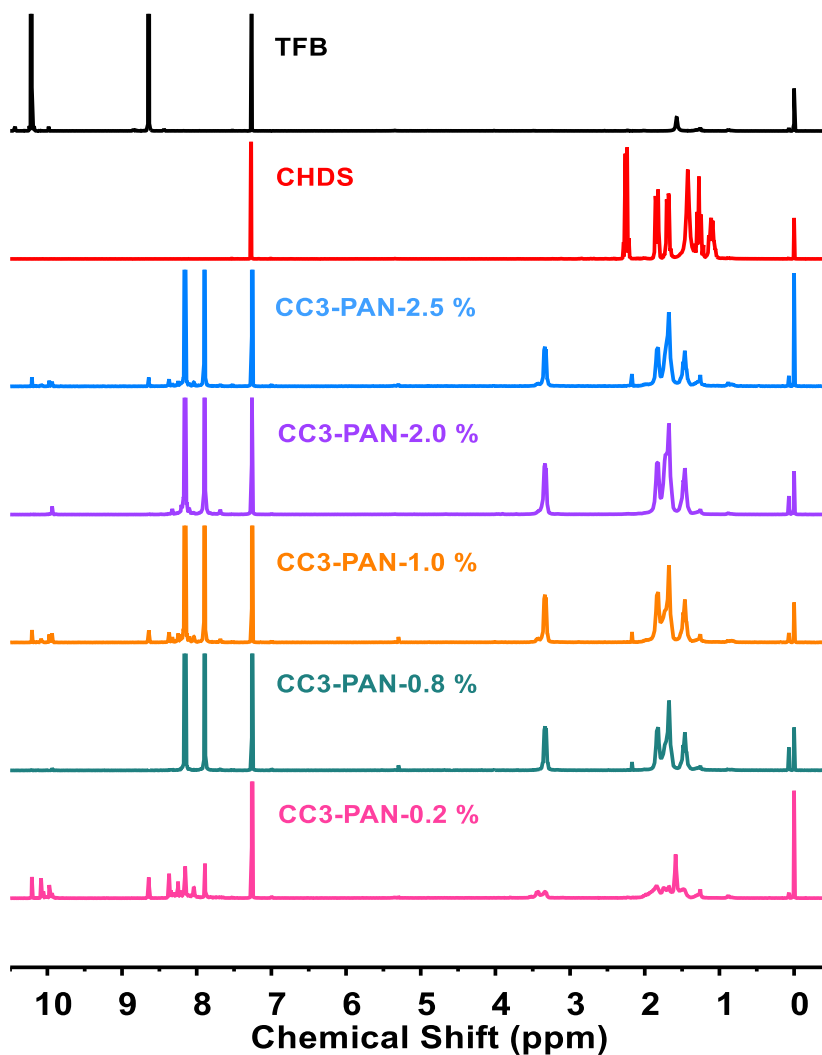


**Figure 3.19**  $^1\text{H}$  NMR ( $\text{CDCl}_3$ , 400 MHz) spectra for TFB, CHDA, and CC3-PAN-24H-Y% membranes fabricated using reagent concentrations that ranged between 0.2 wt.% to 2.5 wt.%. Generic film synthesis conditions, reagent concentration: TFB 0.2 wt.% to 2.5 wt.% in DCM (30 mL), CHDA 0.2 wt.% to 2.5 wt.% in water (32 mL); reaction conditions: 24 hours at room temperature; dish diameter: 7.4 cm. Copyright © 2022, Springer Nature and Ai He, etc.

**Figure 3.20** shows the cross-sectional SEM images of the CC3 films on silicon wafers synthesised using different reaction times. The thickness of the CC3 films increased in line with longer reaction times: 39, 123, 167, 221, 332, 600 nm for 16, 32, 36, 40, 48, 60 hour reactions, respectively. Octahedral crystals started to grow from the film at 72 hours reaction time and accumulate on the substrate, with a diameter of 1.2-1.5  $\mu\text{m}$ . After 96 hours, the film disappeared, and a large amount of CC3 crystals were discretely distributed on the silicon wafers, showing a larger size with a diameter of around 10-20  $\mu\text{m}$ .



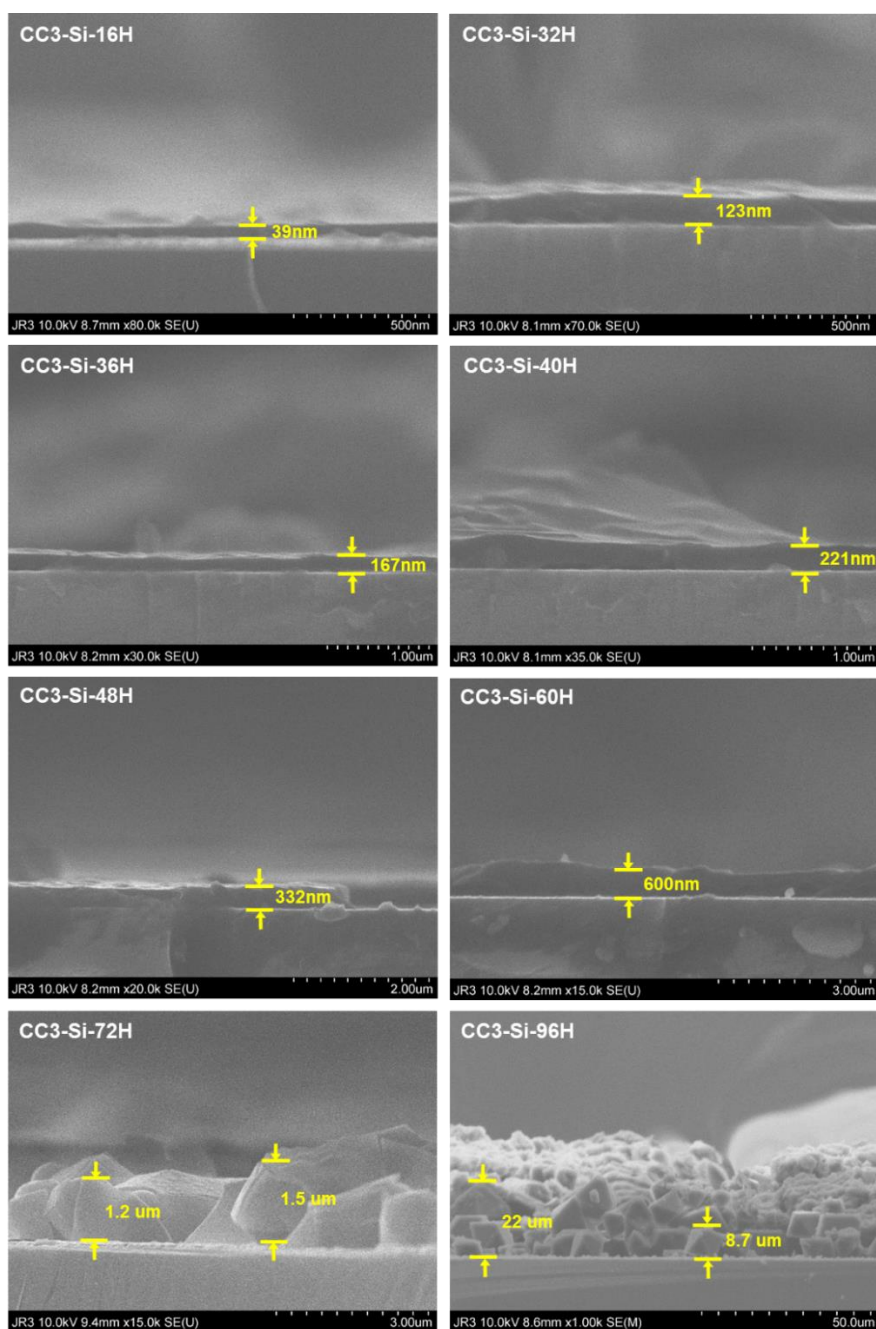


**Figure 3.20** SEM images of CC3 films prepared at different reaction times (CC3-Si-0.8%-XH, where X = 16-96 hr) and then deposited on silicon wafers. The CC3 film thickness is shown in the images. Generic film synthesis conditions, reagent concentration: TFB 0.8 wt.% in DCM (30 mL), CHDA 0.8 wt.% in water (32 mL); reaction conditions: room temperature. Note, the CC3-Si-0.8%-4H was too thin to be observed under the SEM; instead, AFM was used to determine the film thickness. Copyright © 2022, Springer Nature and Ai He, etc.

Since the CC3-Si-0.8%-4H was too thin to be observed under the SEM, instead, AFM height image was obtained to show the thickness. Moreover, AFM images and the corresponding height profile could demonstrate more accurate thickness data, which are shown in **Figure 3.21**.

The thickness of the **CC3** film was 30 nm from the 4 hour reaction and 40 nm from the 16 hour reaction, which matched the SEM data for the 16 hour reaction (39 nm). The **CC3-Si-0.8%** from the 48 and 96 hours reactions were too fragile/loose for AFM measurements, and this conformed to the SEM images that crystal particles started to form on the surface, and the film became less continuous.

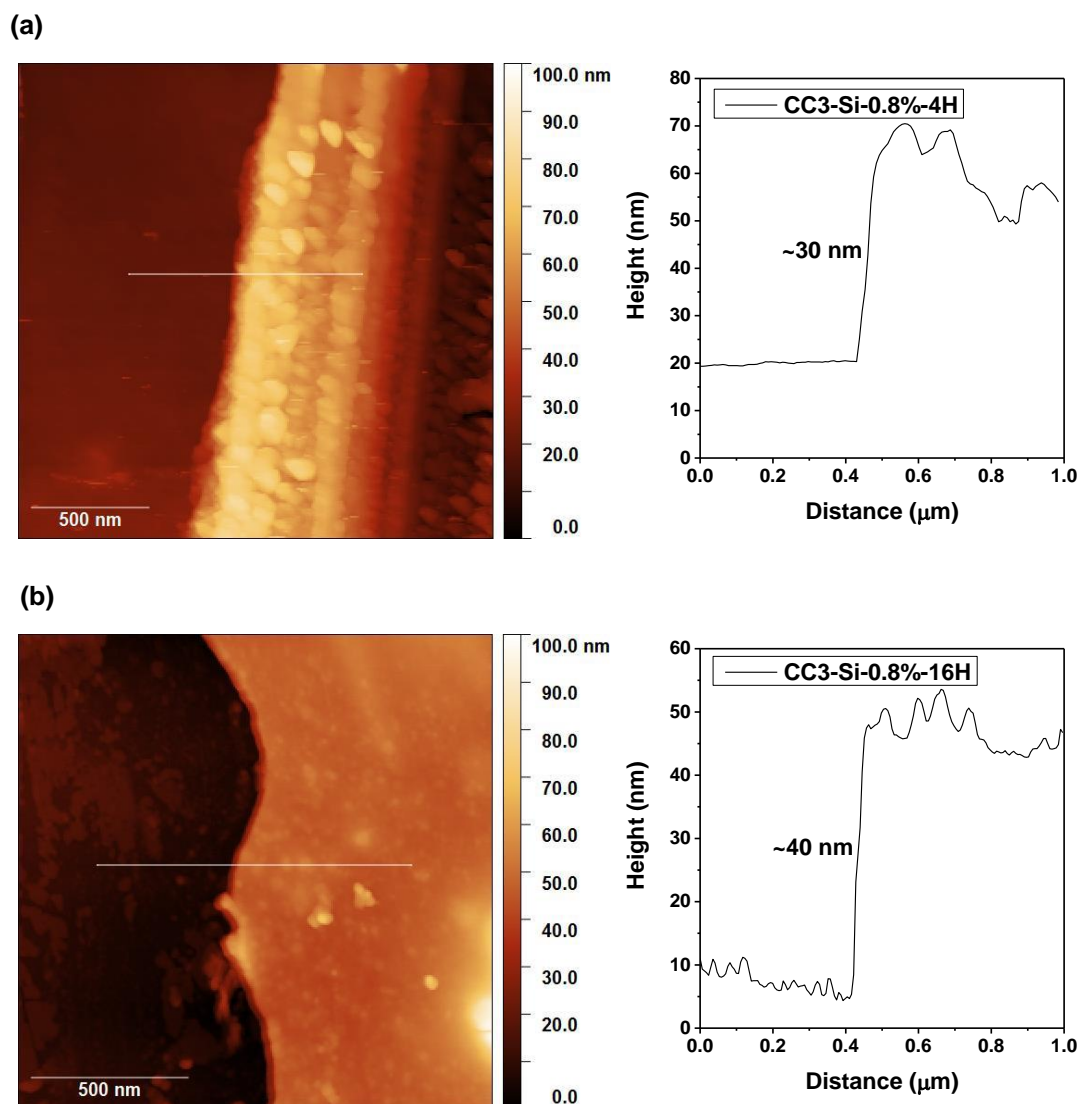


**Figure 3.21** AFM height image and the height profile of **CC3** films prepared under different conditions transferred onto a silicon (Si) wafer. **CC3-Si-0.8%-XH** samples were fabricated using reaction times: (a) 4 hours; (b) 16 hours. Generic film synthesis conditions and reagent concentrations were as follows: TFB 0.8 wt.% in DCM (30 mL), CHDA 0.8 wt.% in water (32 mL); reaction conditions: room temperature. Note that the **CC3-Si-0.8%** after 48 hours and 96 hours reaction were too fragile/loose for AFM measurements. Instead, cross-sectional SEM images were recorded to determine the **CC3** film thickness.

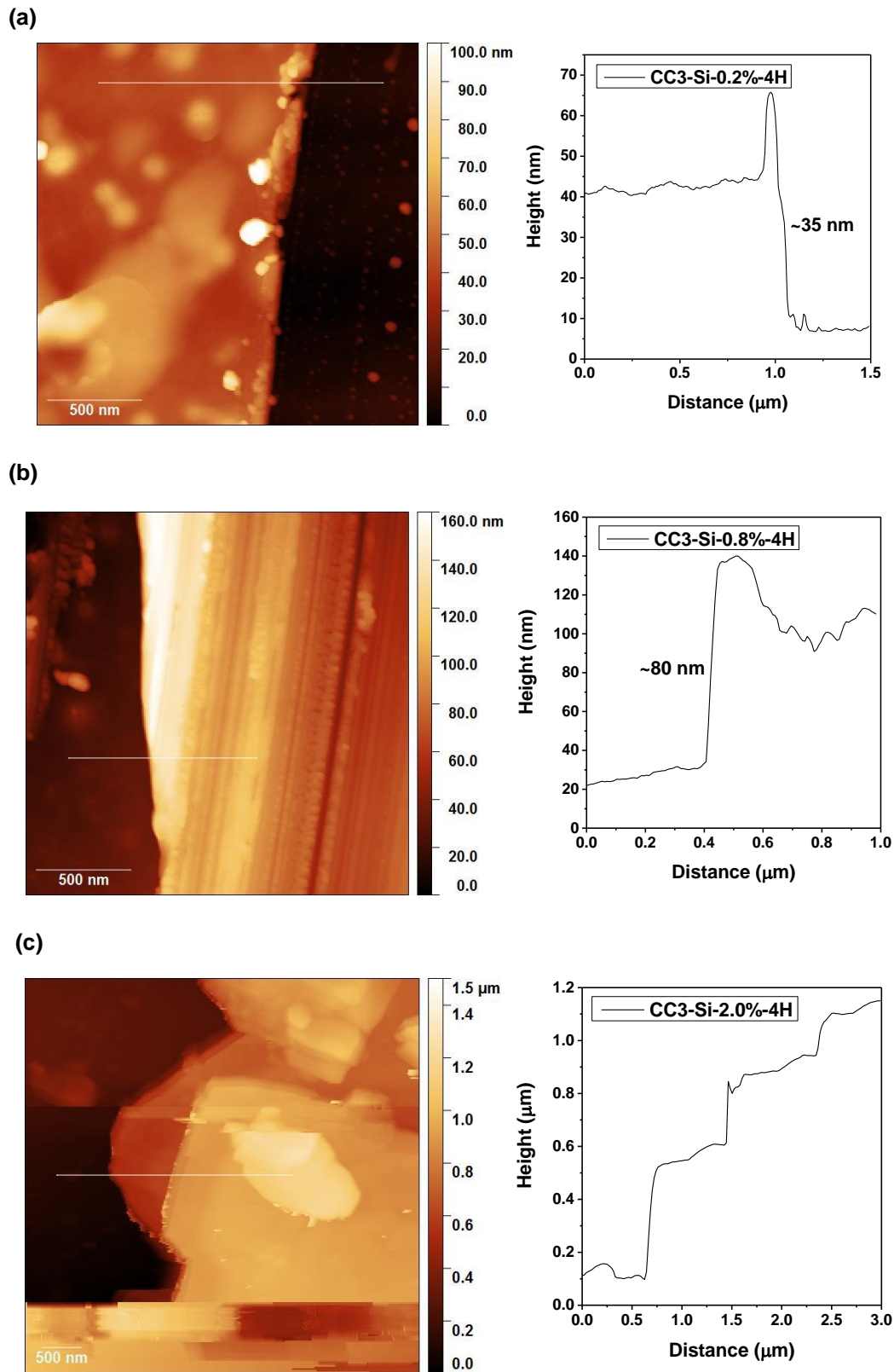


**Figure 3.22** AFM height image and the height profile of CC3 films prepared under different conditions transferred onto a silicon (Si) wafer. CC3-Si-X%-4H samples were fabricated using reaction concentrations: (a) 0.2 wt.%; (b) 0.8 wt.%; (c) 2.0 wt.%. Reaction conditions: 4 hours at room temperature. Copyright © 2022, Springer Nature and Ai He, etc.

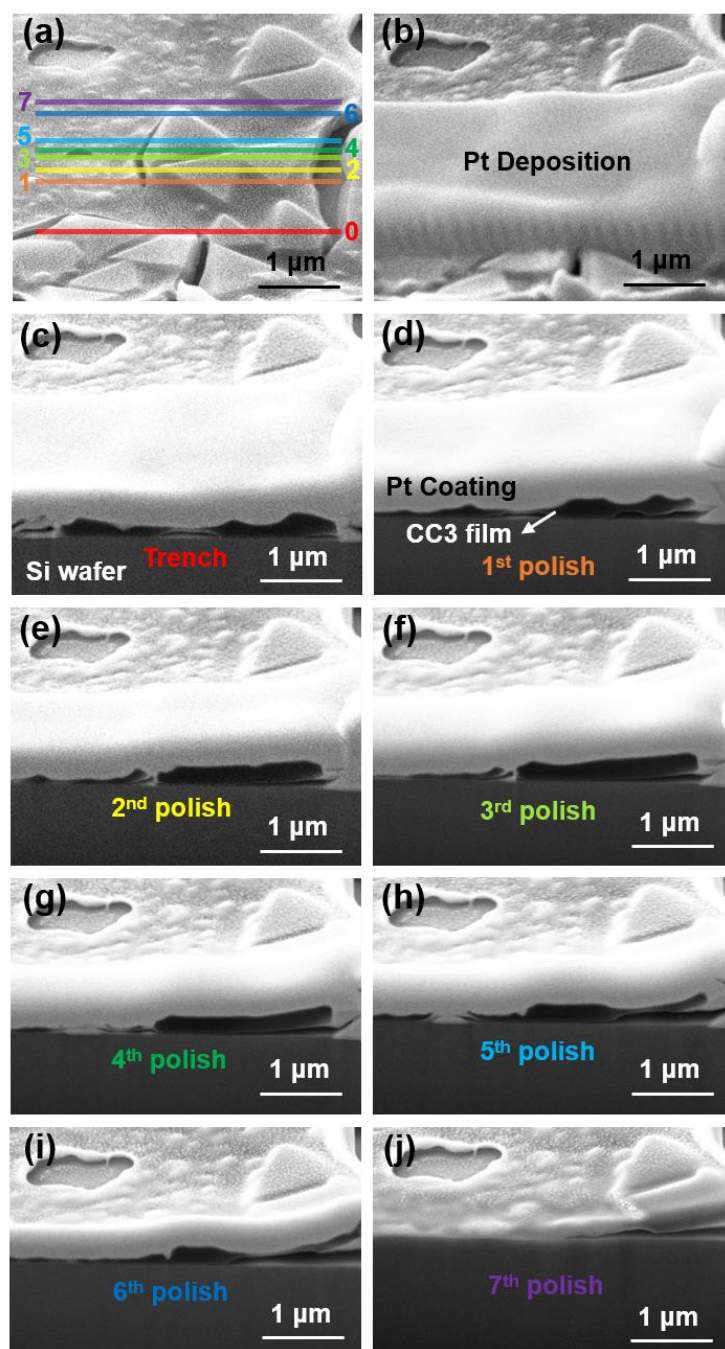


**Figure 3.23** FIB-SEM images of CC3-Si-32H showing its cross-sectional structure during step-by-step trenching and polishing: (a) Surface marked with 0-7 polishing step tracks; (b) Pt-coated surface area; cross-section after FIB treatment: (c) after trenching (0 polishing step); (d) after 1 polishing step; (e) after 2 polishing steps; (f) after 3 polishing steps; (g) after 4 polishing steps; (h) after 5 polishing steps; (i) after 6 polishing steps; (j) after 7 polishing steps. The FIB was used for trenching and polishing (30 kV and 1 nA for trenching, and 30 kV and 250 pA for polishing), and the electron beam was used for imaging (5 kV, 30 pA, and 10 kV, 60 pA). Film synthesis conditions, reagent concentration: TFB 0.8 wt.% in DCM (30 mL), CHDA 0.8 wt.% in water (32 mL); reaction conditions: 32 hours at room temperature.

AFM height images and the height profiles of **CC3** films prepared under different conditions transferred onto a silicon wafer are shown in **Figure 3.22**. The thickness is 35 nm for 0.2% and 80 nm for 0.8%. Unlike those films showing a continuous single **CC3** layer, multiple-layered films were stacked on the surface when a reagent concentration of 2.0% was used.

FIB-SEM images of **CC3-Si-32H** was used to image the cross-sectional structure during step-by-step trenching and polishing (**Figure 3.23**). In the FIB-SEM image, the surface is marked with 0-7 polishing step tracks in **Figure 3.23** (a), which was then coated with platinum. The shape of the **CC3** crystals could be seen as the polishing steps went on. These FIB-SEM images revealed clear triangle/octahedral shaped crystals embedded in the **CC3** films.

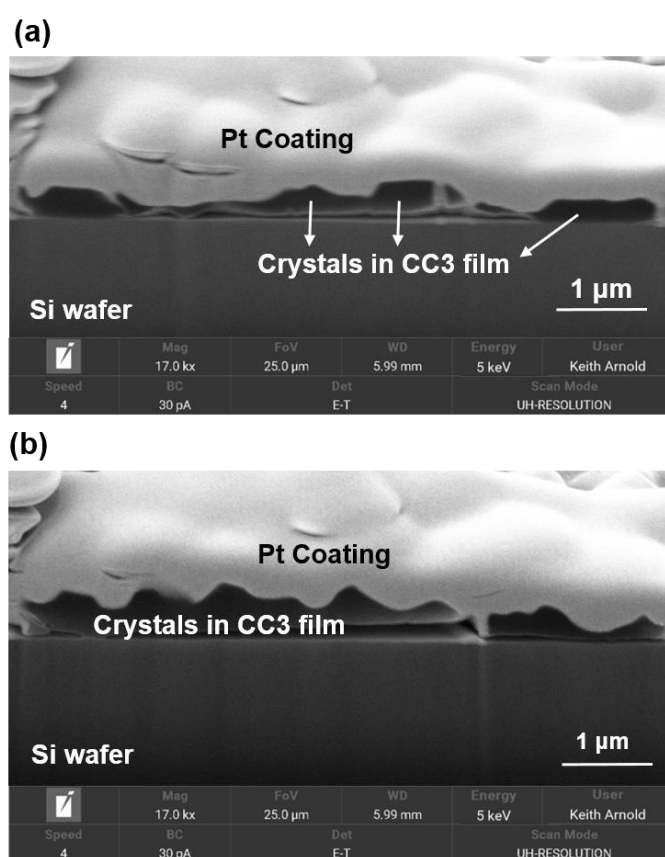


**Figure 3.24** FIB-SEM images of **CC3-Si-48H** (a) showing its cross-sectional structure after FIB trenching, and (b) after polishing. The FIB was used for trenching and polishing (30 kV and 1 nA for trenching, and 30 kV and 250 pA for polishing), and the electron beam was used for imaging (5 kV, 30 pA, and 10 kV, 60 pA). Film synthesis conditions, reagent concentration: TFB 0.8 wt.% in DCM (30 mL), CHDA 0.8 wt.% in water (32 mL); reaction conditions: 48 hours at room temperature. Copyright © 2022, Springer Nature and Ai He, etc.



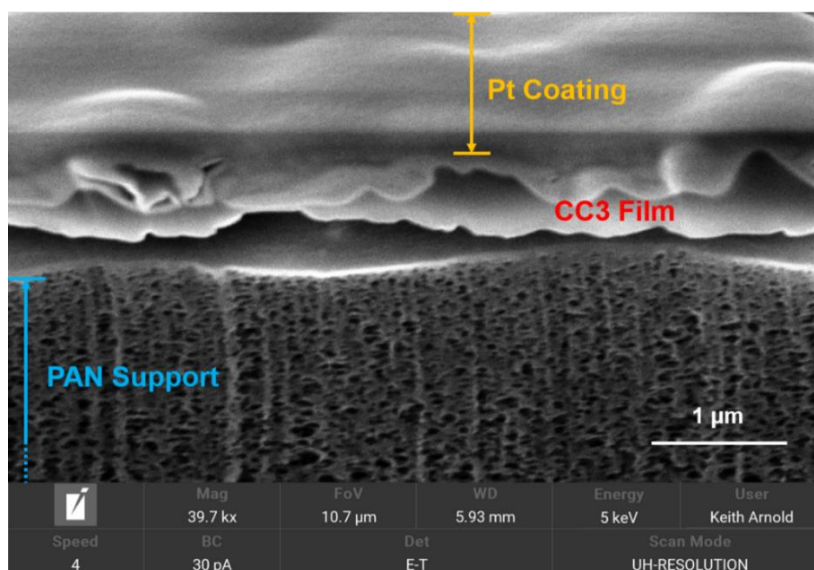


**Figure 3.25** FIB-SEM images of CC3-PAN-48H showing its cross-sectional structure, using the FIB for trenching and polishing (30 kV and 1 nA for trenching, and 30 kV and 250 pA for polishing) and the electron beam for imaging (5 kV, 30 pA, and 10 kV, 60 pA). Film synthesis conditions, reagent concentration: TFB 0.8 wt.% in DCM (30 mL), CHDA 0.8 wt.% in water (32 mL); reaction conditions: 48 hours at room temperature; dish diameter: 7.4 cm.

The cross-sectional FIB-SEM images of CC3-Si-48H are shown in **Figure 3.24**, after FIB trenching and polishing. In the FIB-SEM of CC3-Si-48H, crystals in CC3 film could be observed clearly from the side view and are relatively larger than those made from 32 hour reaction.

FIB-SEM images were also obtained for the CC3 film coated on PAN (CC3-PAN-48H) as is shown in **Figure 3.25**, which represents the real membrane during the liquid separation. The boundary between CC3 film, platinum coating and porous PAN support is less clear, but the CC3 film with the shape of crystals can be observed on top of the support.

GIXRD measurements that were performed on CC3 films deposited on PAN of different reaction times along with their SEM images, as shown in **Figure 3.26**. Both the surface morphologies and the diffraction data indicated that increasing the reaction time from 4 to 48 hours correlated with an increase in the crystalline domains in the CC3 films.

Overall, SEM, FIB-SEM, AFM, Raman microscope images and maps, and GIXRD data revealed that thicker films with larger crystals were produced as the reaction time and reagent concentrations were increased.

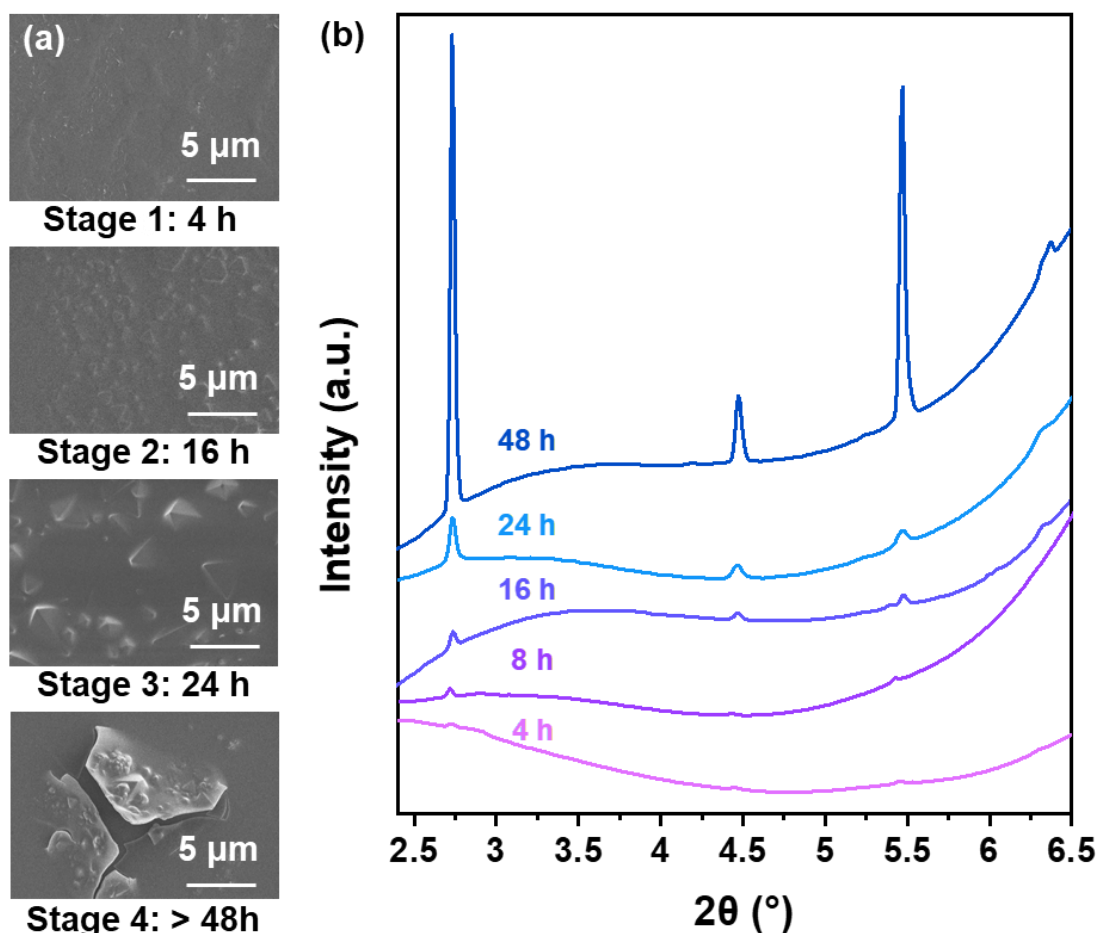


**Figure 3.26** (a) SEM images of CC3-PAN-XH-0.8% membranes formed at different reaction times, showing four stages of CC3 film formation. (b) Out-of-plane GIXRD patterns of CC3-PAN-XH-0.8% membranes were fabricated using reaction times of between 4–48 hours.

Based on these characterisations, it appears that the interfacial synthesis occurs in four stages (**Figure 3.27**): **Stage 1** (0–4 hours), interfacial polymerization of a continuous oligomeric film at the dichloromethane-water interface with no observation of CC3 $\alpha$  crystals; **Stage 2** (4–16 hours), self-sorting of the reactants and oligomers into the CC3 $\alpha$  product to reach a more stable status with lower energy<sup>1</sup>, and the formation of a partially-reacted, semi-cage film; **Stage 3** (24–48 hours), crystallisation of CC3 $\alpha$  and the formation of octahedral crystals in the film; **Stage 4** (48–96 hours), formation of defects in the film which becomes more fragile, caused by larger octahedral crystals creating cracks and imperfections. We, therefore, focused attention on the properties of CC3-PAN-24H-0.8%, referred to hereafter as CC3-PAN. This four-stage mechanism explains the differences that we observed in the permeance and selectivity of CC3-PAN membranes produced using different reaction times and reagent concentrations, as discussed below.

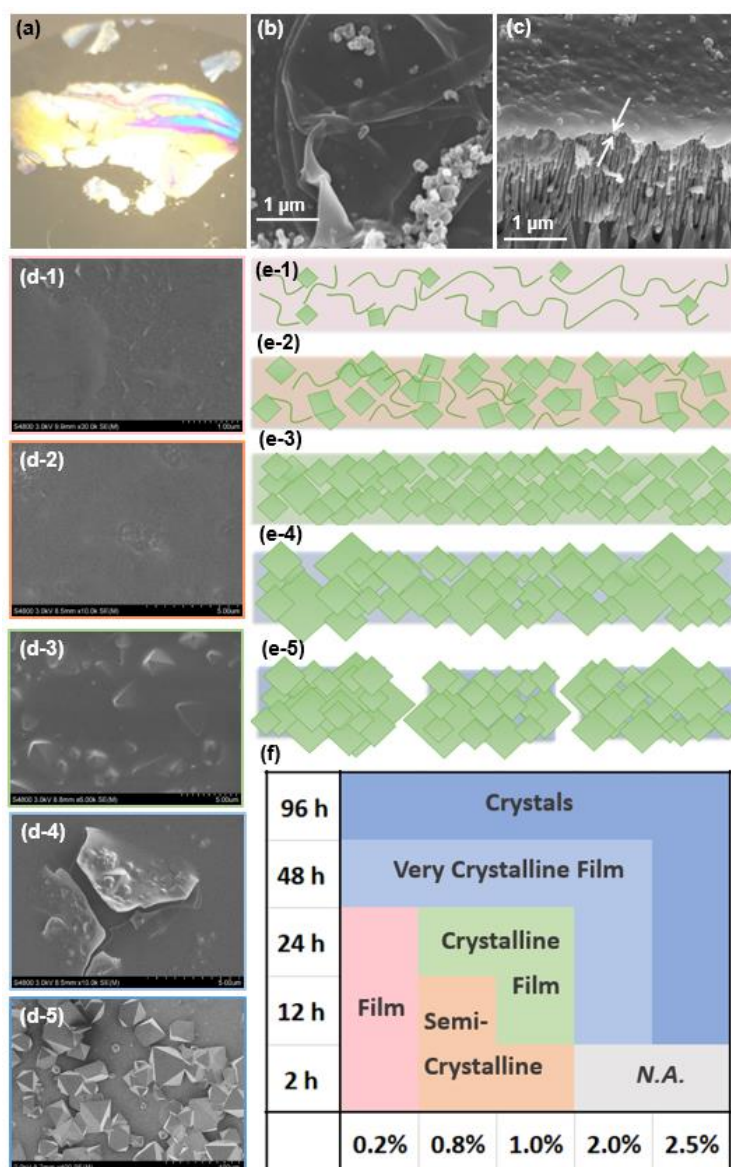


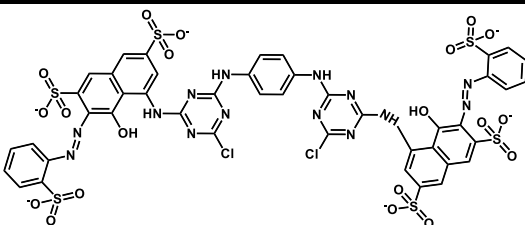
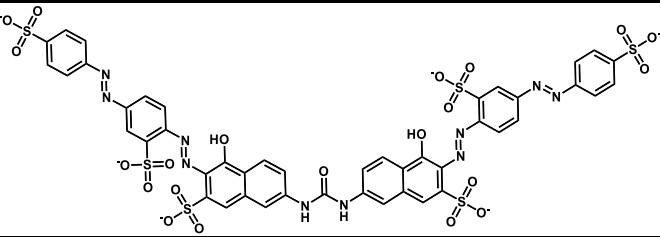
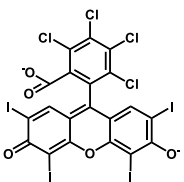
**Figure 3.27** Morphology and proposed mechanism of CC3 film formation. (a) Photography of a CC3 film deposited on an anodic aluminium oxide support, which was synthesised at a concentration of 0.2 wt.% for 24 hours at room temperature. (b, c) SEM images for this CC3 film on an anodic aluminium oxide support showing its surface morphology and cross-sectional view. (d) SEM images of the CC3 films that were synthesised using different reagent concentration and reaction times at room temperature and deposited on silicon wafers: (d-1) 0.2 wt.%, 4 hours (shown in pink in (f)); (d-2) 0.8 wt.%, 8 hours (orange in (f)); (d-3) 1.0 wt.%, 24 hours (green in (f)); (d-4) 2.0 wt.%, 48 hours (cyan in (f)); (d-5) 2.5 wt.%, 96 hours (blue in (f)). (e1-e5) Graphical representation of proposed mechanism, where green squares and lines represent CC3 crystals and non-crystalline components, respectively. (f) Summary of crystalline CC3 film formation using different reaction conditions, which is based on a combination of NMR, XRD, Raman, and SEM data. The pink region represents continuous amorphous film; the orange region represents film with low crystallinity (semi-crystalline); the green region represents the optimal synthesis conditions; cyan and blue regions represent highly crystalline and less continuous (more fragile) samples.

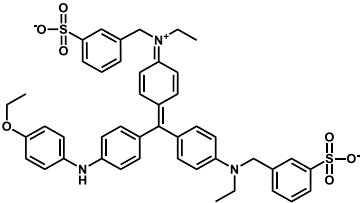
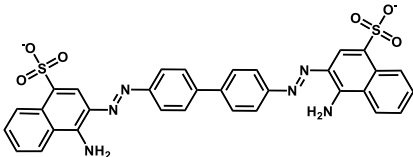
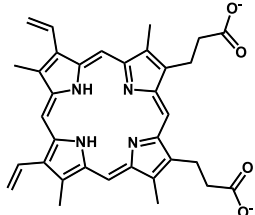
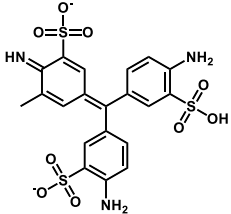
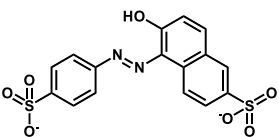
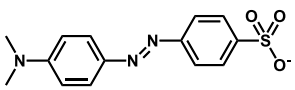
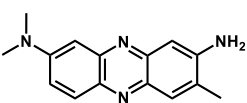
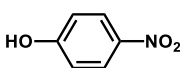


### 3.4 Membrane Performance for Interfacial Crystallization Membranes

Wastewater from the textile and dye-manufacturing industries often contains a low concentration (usually 10-50 mg/L as reported<sup>52,53</sup>) of carcinogenic and mutagenic organic pollutants<sup>54</sup>, such as the nitro-aminoazobenzenes dyes CI Disperse Blue 373, CI Disperse Violet 93, Disperse Orange 37<sup>55</sup>, and benzidine dyes<sup>56</sup>. Often dye molecules are difficult to remove from wastewater because they are resistant to heat, light, and aerobic digestion<sup>57</sup>. Hence, new membranes with excellent permeance and highly selective sieving potential could lead to new technologies in environmental wastewater treatment. To determine the permeance and dye rejection performance of CC3-PAN membrane, and to establish whether the crystalline POC, CC3 $\alpha$ , regulates the diffusion of molecules through the membrane structure, we performed a series of filtration experiments in dead-end cells using solvents and dyes with different sizes and chemical functionalities (shown in **Table 3.1**): reactive red 120 (RR, 1470 g·mol<sup>-1</sup>), direct red 80 (DR, 1373 g·mol<sup>-1</sup>), rose bengal (RB, 1018 g·mol<sup>-1</sup>), brilliant blue (BB, 826 g·mol<sup>-1</sup>), Congo red (CR, 697 g·mol<sup>-1</sup>), protoporphyrin IX disodium (PPIX, 607 g·mol<sup>-1</sup>), acid fuchsin (ACF, 585 g·mol<sup>-1</sup>), sunset yellow (SY, 452 g·mol<sup>-1</sup>), methyl orange (MO, 327 g·mol<sup>-1</sup>), neutral red (NR, 289 g·mol<sup>-1</sup>), and 4-nitrophenol (NP, 139 g·mol<sup>-1</sup>), which were dissolved in separate water solution at a concentration of 20 ppm.

**Table 3.1** Organic dye molecules used in the membrane performance experiments.

Organic Dyes	Molecular Weight (g·mol <sup>-1</sup> )	Molecular Structure	Absorbance Wavelength (nm) <sup>[a]</sup>
Reactive Red 120 (RR)	1470		540
Direct Red 80 (DR)	1373		528
Rose Bengal (RB)	1018		549

<b>Brilliant Blue (BB)</b>	826		551
<b>Congo Red (CR)</b>	697		498
<b>Protoporphyrin IX Disodium (PP IX)</b>	607		366
<b>Acid Fuchsin (ACF)</b>	585		546
<b>Sunset Yellow (SY)</b>	452		482
<b>Methyl Orange (MO)</b>	327		465
<b>Neutral Red (NR)</b>	289		520
<b>4-Nitrophenol (NP)</b>	139		317

<sup>[a]</sup>wavelength of maximum absorbance in water.

The filtrations were performed using a Sterlitech<sup>®</sup> dead-end stirred cell that was kept under 10 bar upstream pressure of nitrogen at room temperature. During the filtrations, the feedstock

was continually stirred using a magnetic stirrer bar oscillating at 400 rpm. Ultraviolet (UV) vis spectroscopy was used throughout these studies to measure the dye concentration in the permeate and calculate dye rejection performance (see **Chapter 2** for full experiment details).

### 3.4.1 Solvent Permeance

**Table 3.2** *Solvent permeance data for CC3-PAN.*

Solvent	Time (min)	Permeated Volume (mL)	Permeance (L.m <sup>-2</sup> .h <sup>-1</sup> .bar <sup>-1</sup> )	Ref. Figure
Water	2	30.0	43.0 ± 4.20	Figure 3.29 [2]
	6	72.5		
	10	112.0		
	28	281.5		
	40	359.5		
Ethanol	2	15.0	30.1 ± 5.25	Figure 3.29 [1]
	6	43.5		
	12	84.0		
	25	162.5		
	40	252.0		
Acetonitrile	2	67.5	147.5 ± 9.57	Figure 3.29 [6]
	5	158.0		
	10	312.5		
	15	465.0		
	20	617.5		
Acetone	1	39.5	177.4 ± 10.23	Figure 3.29 [7]
	3	114.0		
	6	226.0		
	10	374.0		
	15	556.9		

Hexane	1	32.0	$136.86 \pm 10.89$	Figure 3.29 [5]
	5	151.5		
	10	294.0		
	14	406.0		
	20	573.0		
Heptane	2	48.0	$96.02 \pm 8.45$	Figure 3.29 [4]
	5	107.5		
	10	208.5		
	18	369.0		
	25	502.5		
Toluene	3	40.5	$55.89 \pm 6.03$	Figure 3.29 [3]
	5	65.5		
	11	137.5		
	20	242.0		
	30	351.0		

Based on measurement data in **Table 3.2**, CC3-PAN membrane exhibited excellent permeance of water ( $42.9 \text{ L}\cdot\text{m}^{-2}\cdot\text{h}^{-1}\cdot\text{bar}^{-1}$ ) and a range of polar and non-polar organic solvents, including ethanol ( $30.1 \text{ L}\cdot\text{m}^{-2}\cdot\text{h}^{-1}\cdot\text{bar}^{-1}$ ), acetonitrile ( $147.5 \text{ L}\cdot\text{m}^{-2}\cdot\text{h}^{-1}\cdot\text{bar}^{-1}$ ), acetone ( $177.4 \text{ L}\cdot\text{m}^{-2}\cdot\text{h}^{-1}\cdot\text{bar}^{-1}$ ); hexane ( $136.9 \text{ L}\cdot\text{m}^{-2}\cdot\text{h}^{-1}\cdot\text{bar}^{-1}$ ), heptane ( $96.0 \text{ L}\cdot\text{m}^{-2}\cdot\text{h}^{-1}\cdot\text{bar}^{-1}$ ), and toluene ( $55.9 \text{ L}\cdot\text{m}^{-2}\cdot\text{h}^{-1}\cdot\text{bar}^{-1}$ ).

Water contact angle measurements that were performed on CC3-PAN are shown in **Figure 3.28** and indicate that the membrane surface is hydrophobic, with an initial water contact angle of  $94^\circ$ . The contact angle values became smaller the longer the water drop was on the membrane surface and permeated inside the porous structure of the membrane. By comparison, the blank PAN membrane has a water contact angle of  $55^\circ$ , showing it has a relatively more hydrophilic surface.

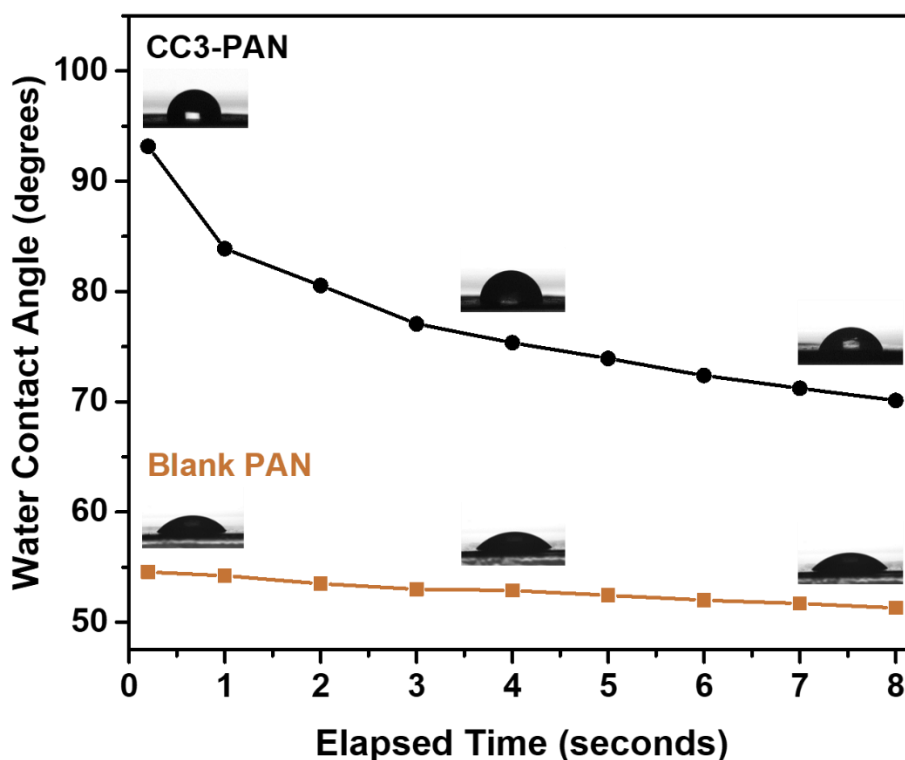


**Figure 3.28** Water contact angles for CC3-PAN membrane. Drop phase: water; surrounding phase: air; drop type: sessile drop; drop volume:  $4.15 \pm 0.5 \mu\text{L}$ ; fitting method: Young–Laplace equation.

The water contact angle data correlates with the general trend that non-polar solvents had better permeance rates, although the size and viscosity of the solvent also had an effect. Hansen solubility parameter ( $\delta$ ) and the physical properties of the organic solvents that were used to determine solvent permeance for CC3-PAN are listed in **Table 3.3**. Pure solvent permeances were plotted versus their combined solvent properties (viscosity  $\eta$ , molar diameter  $d_m$ , and solubility parameter  $\delta_d$ ) for CC3-PAN (**Figure 3.29**), where  $R^2$  is the coefficient of determination for the function. The value is 0.9829, indicating that the pure solvent permeances are in line well with their combined properties.

An important consideration, however, is that CC3 is soluble in organic solvents. Therefore, to confirm that the CC3-PAN remained continuous during the organic solvent permeance measurements, we performed a subsequent series of dye rejection studies with a 20 ppm BB in water feedstock. As is shown in **Figure 3.30**, analysis of the resulting filtrates revealed that CC3-PAN continued to reject BB with the same rejection performance (99.9%) after

measuring permeance rates for ethanol, acetonitrile, acetone, hexane, heptane, and toluene, proving that these solvents do not dissolve **CC3**, and this led to ultrafast solvent permeances.

**Table 3.3** Hansen solubility parameter ( $\delta$ ) and the physical properties of the organic solvents that were used to determine solvent permeance for **CC3-PAN**.

Solvents	Molecular weight ( $\text{g}\cdot\text{mol}^{-1}$ )*	†Hansen solubility parameter ( $\text{MPa}^{1/2}$ )			Molar volume ( $V_m$ )‡ ( $\text{cm}^3 \text{mol}^{-1}$ )	$d_m$ § (nm)	Viscosity at 30 °C ( $\times 10^{-3}$ Pa·S)
		$\delta_d$	$\delta_p$	$\delta_h$			
Water	18.02	15.5	16.0	42.3	18.0	0.39	0.80 <sup>A</sup>
MeOH	32.04	14.7	12.3	22.3	40.7	0.51	0.49 <sup>B</sup>
Ethanol	46.07	15.8	8.8	19.4	58.7	0.57	1.17 <sup>Γ</sup>
Acetonitrile	41.05	15.3	18.0	6.1	52.9	0.55	0.32 <sup>B</sup>
Acetone	58.08	15.5	10.4	7.0	73.9	0.62	0.29 <sup>Γ</sup>
Hexane	86.18	14.9	0	0	131.4	0.75	0.28 <sup>Δ</sup>
Heptane	100.21	15.3	0	0	147.5	0.78	0.33 <sup>Γ</sup>
Toluene	92.13	18	1.4	2	106.9	0.70	0.52 <sup>Γ</sup>

\* Molecular weight taken from CRC Handbook of Chemistry and Physics, see reference<sup>58</sup>.

† Hansen solubility parameter,  $\delta_d$  = solubility parameter due to dispersion forces,  $\delta_p$  = solubility parameter due to dipole forces, and  $\delta_h$  = solubility parameter due to hydrogen bonding (or in general due to donor-acceptor interactions). See reference<sup>59</sup>.

‡ See reference<sup>60,61</sup>.

§ Molar diameter ( $d_m$ ) was calculated from reference<sup>62</sup> using molar volume ( $V_m$ ) of the solvent molecule:  $d_m = 2 \times (3V_m/4\pi N_A)^{1/3}$ ; where  $N_A$  is the Avogadro constant.

<sup>A</sup> See reference<sup>63</sup>.

<sup>B</sup> Calculated from the Lewis and Squires chart<sup>61,64</sup>.

<sup>Γ</sup> Calculated from the experimental values given in reference<sup>61</sup>.

<sup>Δ</sup> See reference<sup>65</sup>.

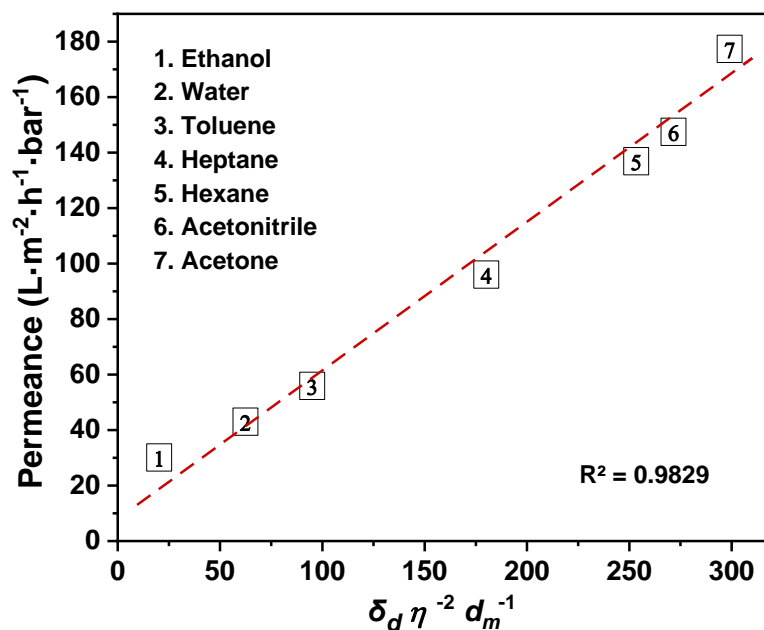


**Figure 3.29** Plot showing pure solvent permeances versus their combined solvent properties (viscosity  $\eta$ , molar diameter  $d_m$ , and solubility parameter  $\delta_d$ ) for CC3-PAN, where  $R^2$  is the coefficient of determination for the function. Hansen solubility parameter ( $\delta$ ) and the physical properties of each organic solvent are listed in **Table 3.3**.

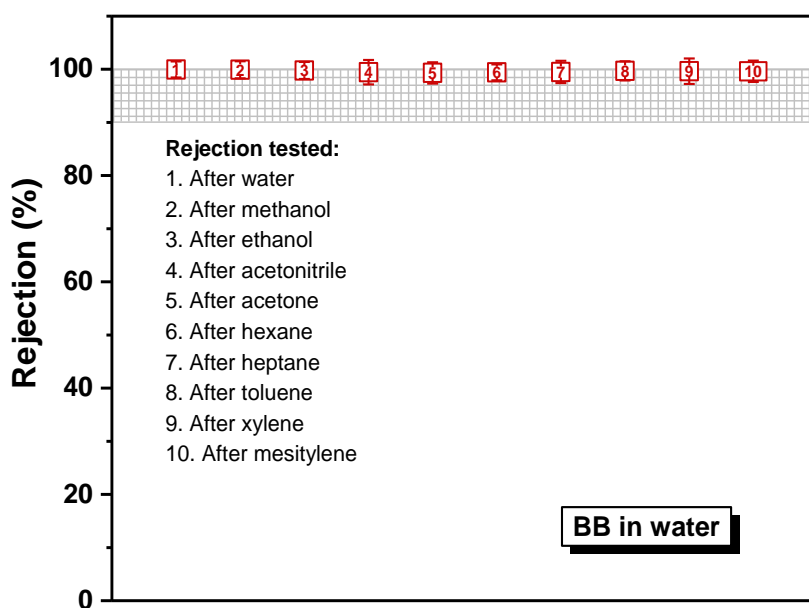


**Figure 3.30** Dye rejection performance of CC3-PAN, determined after measuring the permeance rates of organic solvents. A 20 ppm BB water feedstock was used to check the membrane stability of CC3-PAN after being permeated 100 mL of different organic solvents. The upstream nitrogen pressure was kept at 10 bar during the measurement, and the stirrer agitation speed was 400 rpm. All the error bars depict the standard deviations of the data from at least three independent membranes.

### 3.4.2 Molecular Separation

**Table 3.4** Dye rejection measurement data for CC3-PAN determined using water feedstocks.

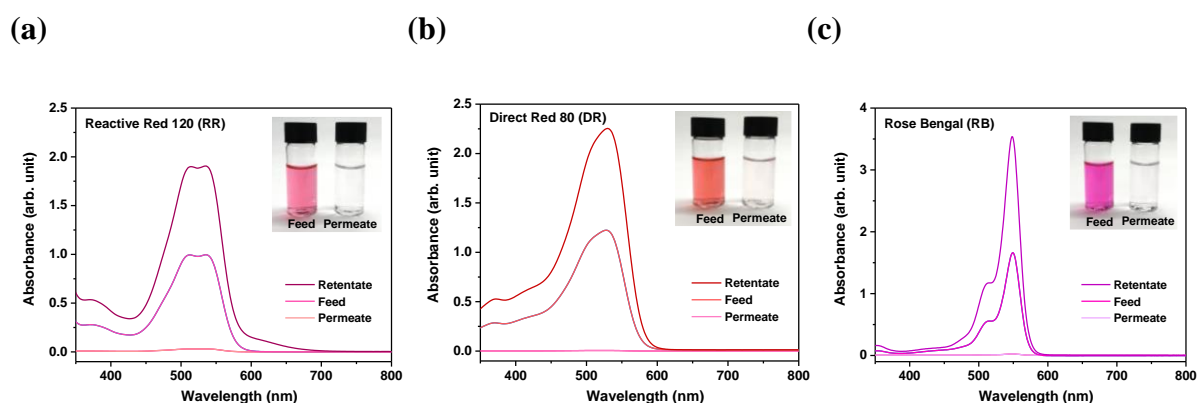
Solvent	Dye	Sample Collected	Volume (mL)	Wavelength <sup>[a]</sup> (nm)	Absorption	Rejection (%)	Ref. Figure
Water	RR	Feed	100	536	1.00	96.10 ± 2.80	Figure 3.31 (a)
		Permeate	50	538	0.05		
		Retentate	50	538	1.91		
Water	DR	Feed	120	528	1.28	98.21 ± 1.52	Figure 3.31 (b)
		Permeate	59	528	0.03		
		Retentate	61	530	2.47		
Water	RB	Feed	100	549	1.66	97.11 ± 0.56	Figure 3.31 (c)
		Permeate	54	551	0.03		
		Retentate	46	550	3.53		
Water	BB	Feed	120	551	1.42	99.89 ± 0.05	Figure 3.31 (d)
		Permeate	57	551	0.02		
		Retentate	63	551	2.67		
Water	CR	Feed	100	498	1.24	99.73 ± 0.12	Figure 3.38
		Permeate	52	498	0.02		
		Retentate	48	498	2.53		
Water	PPIX	Feed	120	366	1.13	99.96 ± 0.03	Figure 3.31 (e)
		Permeate	66	366	0.01		
		Retentate	54	368	2.47		
Water	ACF	Feed	100	546	1.69	62.42 ± 3.40	Figure 3.31 (f)
		Permeate	54	546	0.64		
		Retentate	46	548	2.68		
Water	SY	Feed	100	482	1.59	51.14 ± 3.12	Figure 3.31 (g)
		Permeate	54	482	0.72		
		Retentate	46	482	2.00		
Water	MO	Feed	100	465	2.12	33.07 ± 2.66	



		Permeate	49	464	1.56		Figure 3.31 (h)
		Retentate	51	464	2.37		
		Feed	100	520	2.11		Figure 3.31 (i)
Water	NR	Permeate <sup>[b]</sup>	52	520	0.63	22.43 ± 3.82	
				455	0.44		
		Retentate	48	520	2.79		
		Feed	100	317	2.07		Figure 3.31 (j)
Water	NP	Permeate	45	318	1.70	14.17 ± 2.05	
		Retentate	55	318	2.19		

<sup>[a]</sup> Wavelength of maximum absorbance. <sup>[b]</sup> Wavelength of maximum absorbance of the peak at the red colour absorbance (520 nm) and orange colour absorbance (455 nm). As NR is a pH indicator changing from red to yellow between pH 6.8 and 8.0, the dye concentration was calculated using the absorbance of both yellow and red peaks.

From the rejection measurements for **CC3-PAN** shown in **Table 3.4** and **Figure 3.31**, we found that guests with larger molecular weights than protoporphyrin IX disodium (607 g/mol) were too large to diffuse through the membrane. The permeates are colourless, and the **CC3-PAN** membrane showed a good rejection rate for PPIX (99.96 %), CR (99.96 %), BB (99.89 %), RB (97.11 %), DR (98.21 %) and RR (96.10 %). The molecular weight cut-off (MWCO) curve of the membrane is shown in **Figure 3.32** along with the data of blank PAN membrane, showing **CC3-PAN** has a MWCO of around ~600 Da. The good dye rejection of **CC3-PAN** composite membrane confirmed the cage film has been successfully fabricated on the PAN and is continuous and defect-free.



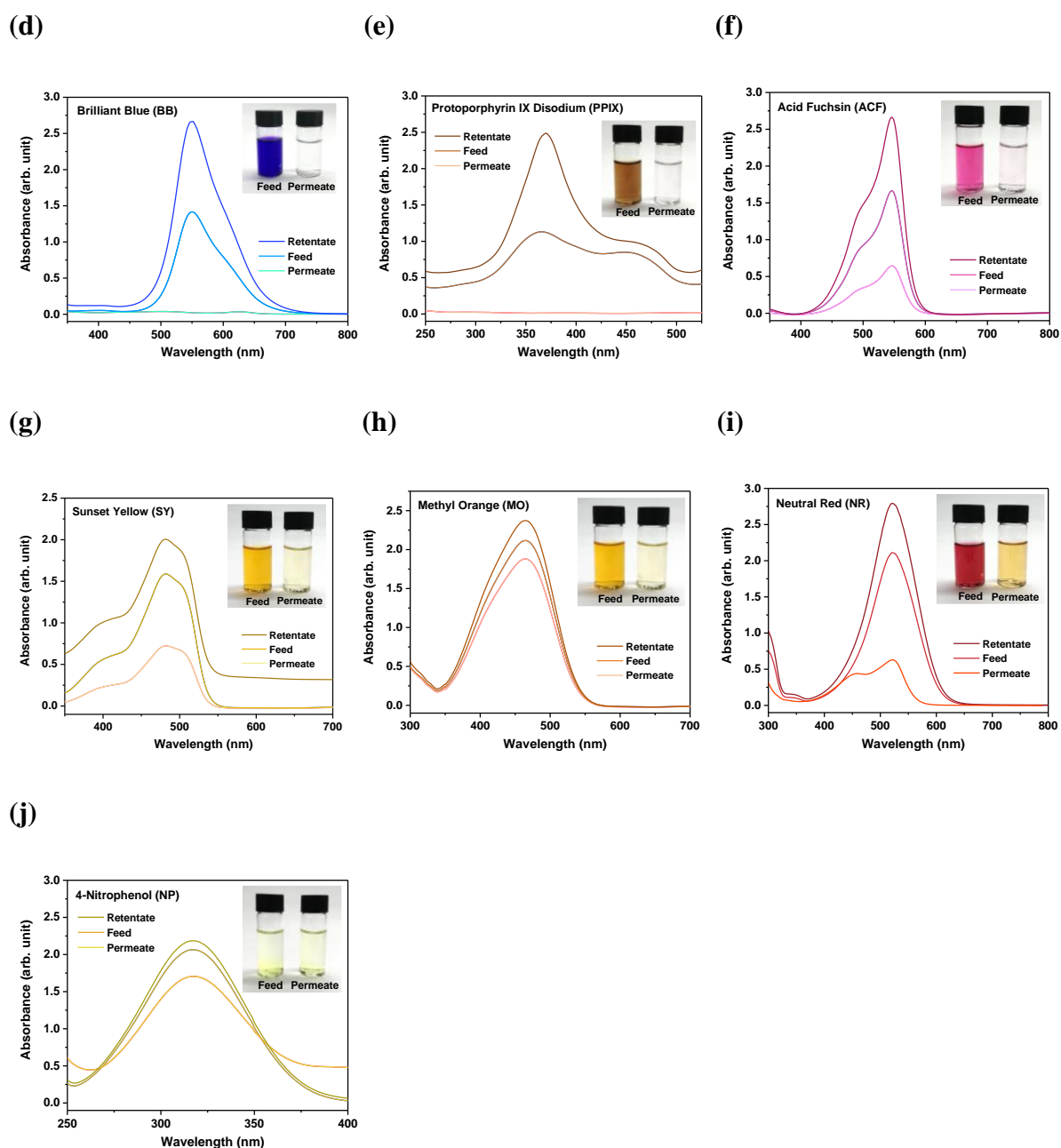


**Figure 3.31** UV absorption spectra of dyes in water before and after selectivity tests performed with CC3-PAN. Inserts show photographs of the feed and the permeate. Dye rejection was calculated using the intensity of the maximum absorption peak in the permeate and the feed and Eq. 2.4 in the Methods section of Chapter 2. Mass balance was calculated using the maximum absorption peaks in the values of the feed, permeate, and retentate Eq. 2.4 in the Methods section of Chapter 2. Note, NR is a pH indicator, changing from red to yellow between pH 6.8 and 8.0; as the NR permeate was orange in colour the dye concentration was calculated using both yellow and red peaks in the UV absorption spectrum. The absorption spectra of CR are presented separately in **Figure 3.38** to demonstrate the mass balance calculations.

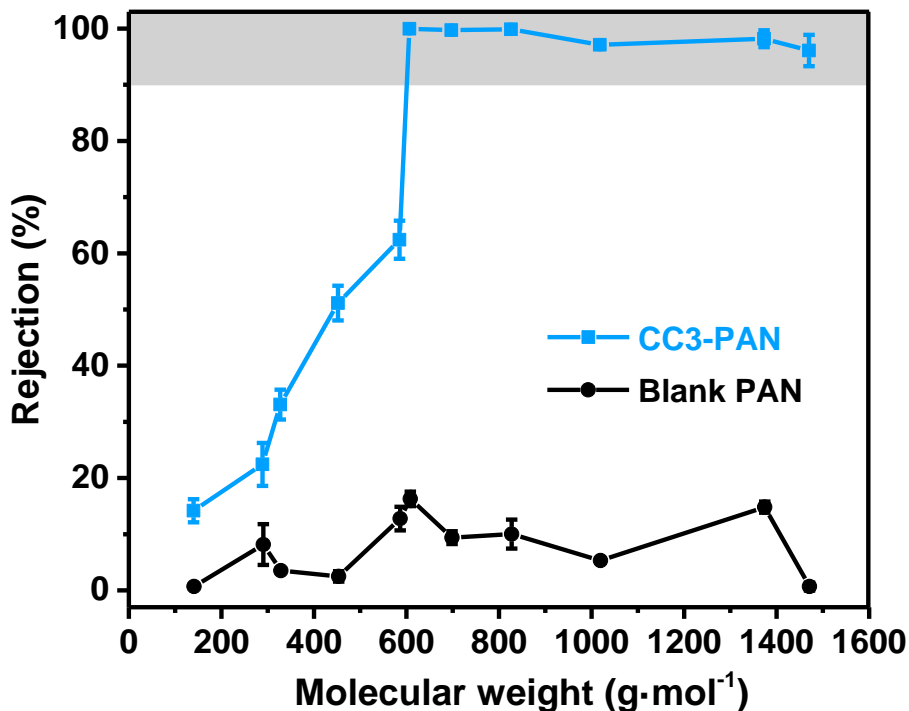


**Figure 3.32** Dye rejection versus molecular weight cut-off curve for CC3-PAN and blank PAN membrane in water containing 20 ppm dye solutes. The upstream nitrogen pressure was kept at 10 bar during the measurement, and the stirrer agitation speed was 400 rpm. The error bars denote the standard deviations for measurements from at least three independent membranes.

### 3.4.3 Effects of Crystallinity

The crystalline CC3-PAN provides sufficient robustness to support the interconnected channels under high applied pressures. To further confirm the importance of crystallinity, CC3 membranes with different crystallinity levels were fabricated at each of the four reaction stages simply by controlling the reaction time. As is shown in **Figure 3.33**, a partially crystalline membrane (CC3-PAN-8H-0.8%) at **Stage 2** exhibited a water permeance of  $3.0 \text{ L} \cdot \text{m}^{-2} \cdot \text{h}^{-1} \cdot \text{bar}^{-1}$ ; that is, an order of magnitude lower than the fully crystalline **Stage 3** membrane ( $49.5 \text{ L} \cdot \text{m}^{-2} \cdot \text{h}^{-1} \cdot \text{bar}^{-1}$  for CC3-PAN-48H-0.8%) prepared with prolonged reaction times. This observation contrasts the behaviour of most nanofiltration membranes that tend to exhibit lower permeance as their thicknesses are increased. For CC3-PAN, the high permeance rates from the longer reaction times is attributed to the improved crystallinity, which creates more diffusion pathways for the solvents to diffuse through the membrane.

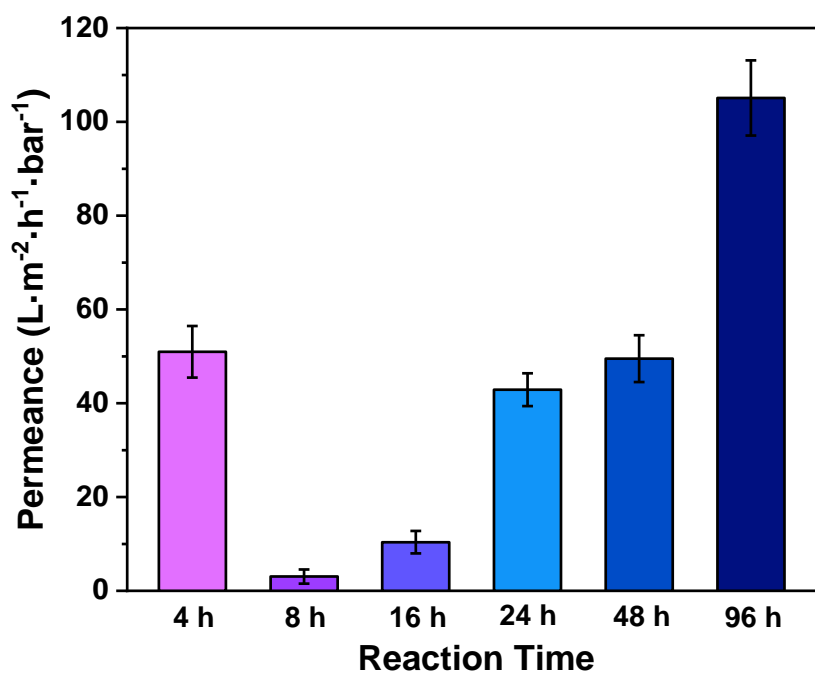


**Figure 3.33** Water permeance for CC3-PAN-XH-0.8% membranes fabricated using reaction times that ranged between 4–96 hours. All error bars depict the standard deviations (SD) of the data points obtained from at least three independent membranes.

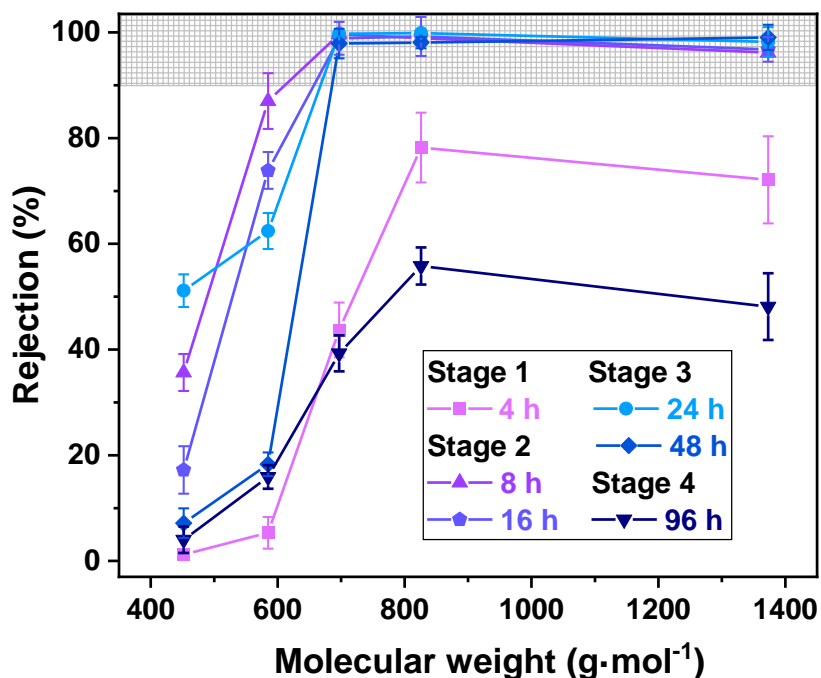


**Figure 3.34** Dye rejection measurements for CC3-PAN-XH-0.8% membranes in water. All error bars depict the standard deviations (SD) of the data points obtained from at least three independent membranes.

Both **CC3-PAN-8H-0.8%** and **CC3-PAN-48H-0.8%** exhibited the same molecular weight cut-off (MWCO), as determined by filtering a range of dyes through the membranes (**Figure 3.34**). By comparison, amorphous oligomeric membranes produced in **Stage 1** (**CC3-PAN-4H-0.8%**), and also cracked highly crystalline membranes produced in **Stage 4** (**CC3-PAN-96H-0.8%**), exhibited unexpectedly higher water permeances but failed to achieve comparable separation performances, indicating that they contained physical defects.

Two limitations of membranes produced from other crystalline porous materials, such as COFs, are poor stability at high pressures<sup>31</sup> and the interference of adsorption processes<sup>37</sup>. To explore these issues using the **CC3** membrane, **CC3-PAN** was tested under a range of applied pressures, up to a maximum of 35 bar, due to instrumentation constraints. As shown in **Figure 3.35**, the pure water flux of the **CC3-PAN** membrane increased linearly with the increasing applied pressure: 106, 202, 429, 790, 1336  $\text{L}\cdot\text{m}^{-2}\cdot\text{h}^{-1}$  for 2, 5, 10, 20, 30 bar, respectively.

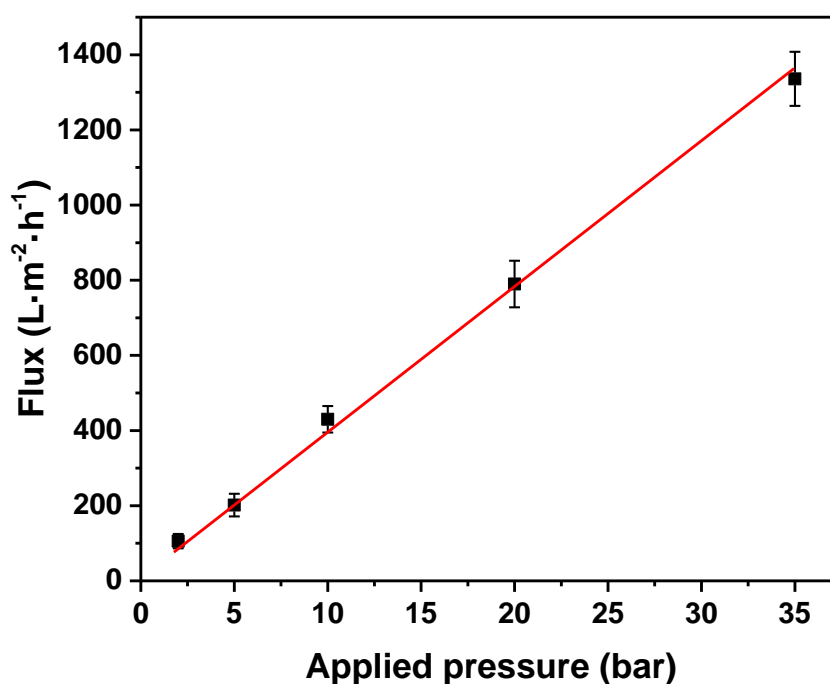


**Figure 3.35** Water flux of a **CC3-PAN** membrane under a range of applied pressures. All error bars depict the standard deviations (SD) of the data points obtained from at least three independent membranes.

The dye filtration measurements were carried out at different pressures for **CC3-PAN** membrane, and the rejection date is shown in **Figure 3.36**. The membrane could reject the dyes larger than PPIX and CR, showing a WMCO of  $\sim 600$  Da in all the applied pressures. This indicated that the flux increased with pressure without affecting rejection performance. The

applied pressure of 35 bar is an order of magnitude higher than used for liquid filtration through COF membranes<sup>31</sup>, which suggests that these CC3-PAN membranes might be more competitive for separations that require higher pressures.

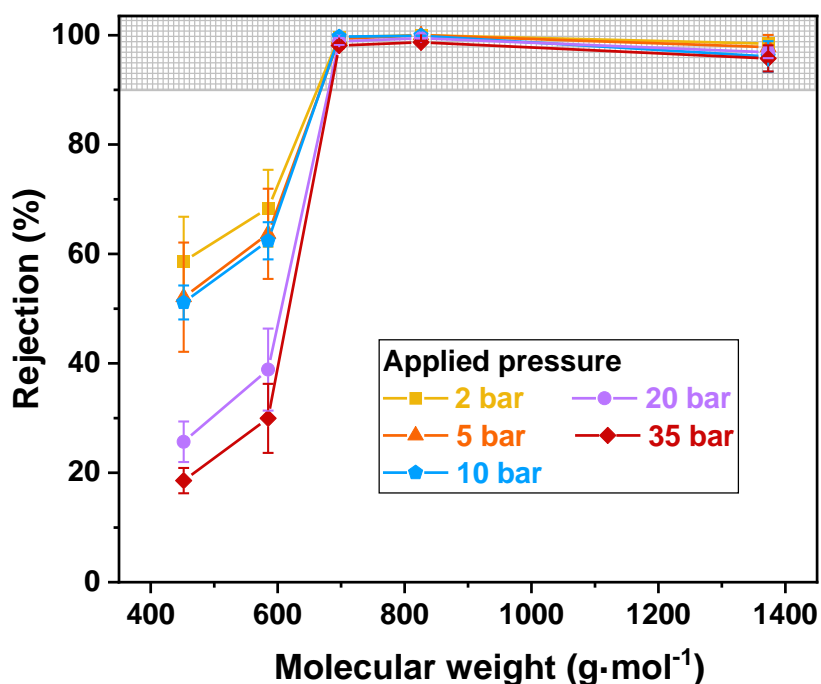


**Figure 3.36** Dye rejections of a CC3-PAN membrane under a range of applied pressures. All error bars depict the standard deviations (SD) of the data points obtained from at least three independent membranes.

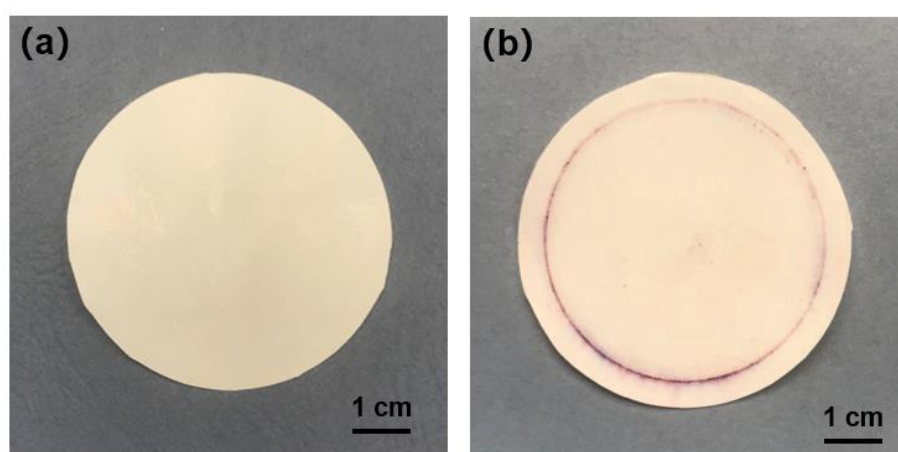


**Figure 3.37** Photographs of CC3-PAN-24H-0.8% membrane. (a) As-prepared CC3-PAN-24H-0.8%, and (b) CC3-PAN-24H-0.8% after a series of dye filtration tests using a commercial bench-scale dead-end stirred-cell filtration unit (Sterlitech<sup>®</sup> HP4750 stirred cell) that was kept under 10 bar nitrogen atmosphere. The diameter of the filtration dish was 4.7 cm and a stirrer bar agitation speed of 400 rpm was used during the measurements.

Importantly, CC3-PAN remained colourless and relatively clean during the membrane measurements (photographs of the as-prepared membrane and the same one after a series of dye filtration experiments showing in **Figure 3.37**), indicating that the membrane did not appear to adsorb the larger dyes.

To confirm that dye adsorption did not contribute to the selectivity performance of CC3-PAN, mass balance calculations were used to measure the dye concentration in the retentate during the separations. After permeating 48 mL of congo red (CR) feed, the absorption intensity of CR in the retentate increased from 1.24 to 2.53, while its absorption intensity in the permeate was only 0.02. In combination, these values are consistent with ~100% of the dye being rejected (**Table 3.4** and **Figure 3.38**).

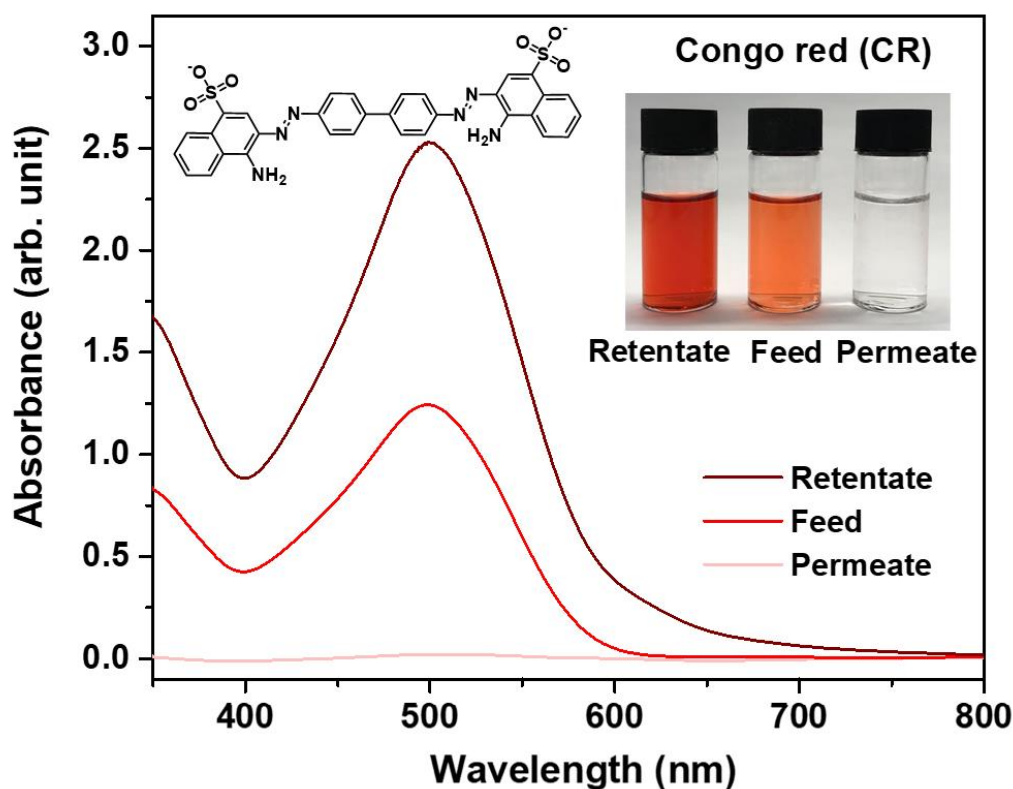


**Figure 3.38** UV-vis absorption spectra of congo red (CR) in water before (feed) and after (permeate and retentate) selectivity tests performed with CC3-PAN. Inserts show photographs of the feed, permeate, and retentate solutions, and the molecular structure of CR. Dye rejection was calculated using the intensity of the maximum absorption peak in the permeate and the feed and Eq. 3 in the Methods section. Mass balance calculations were performed using the maximum absorption peaks values of the feed, permeate, and retentate with Eq. 2.4 in the Methods section of Chapter 2. Copyright © 2022, Springer Nature and Ai He, etc.

For comparison, we also immersed crystals of **CC3 $\alpha$**  (100 mg) and a cutout section of **CC3-PAN** with a diameter of 4.7 cm directly in separate water solutions (100 mL) that contained 20 ppm BB concentrations to determine if the dye was adsorbed by these samples over one week. From these adsorption experiments shown in **Figure 3.39**, we found that **CC3 $\alpha$**  crystals and a **CC3-PAN** segment did not absorb BB from water. These results all indicate that the dyes were rejected by the membrane rather than being adsorbed.

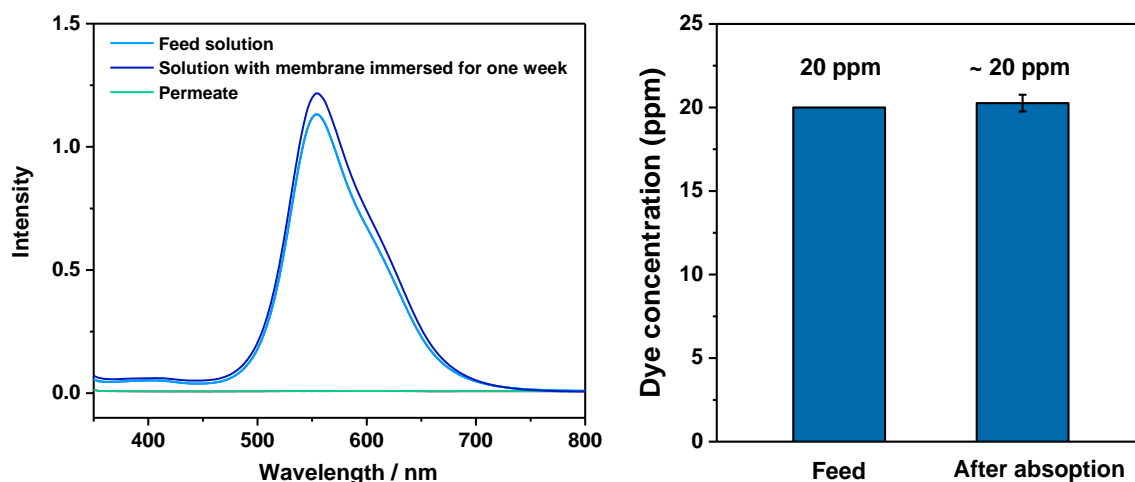


**Figure 3.39** Dye absorption test. UV absorption spectra and the concentration of BB feed solution and the solution with a cutout section of **CC3-PAN** with a diameter of 4.7 cm immersed for one week, measured by UV absorption data and calculated by running five samples with known concentration as the standard line. The dye concentration remained at ~ 20 ppm after the absorption test was run continually for one week, showing there was no obvious absorption on the membrane surface. The error bar depicts the standard deviations of the data from at least three independent membranes.

#### 3.4.4 Effects of Reaction Solvents

**CC3** films synthesised at the interface with different organic solvents were carried out to investigate how reaction solvent affected the structure and crystallinity of the **CC3** films. When fabricated using interfacial crystallisation in other solvents, the **PAN** membrane was fixed and acted as a support for the **CC3** film layers, where two cage precursors were allowed to react at the interface of two immiscible solvents. The amine monomer was always dissolved in the aqueous phase, whereas the aldehyde was dissolved in dichloromethane, mesitylene, or ethyl acetate solution.



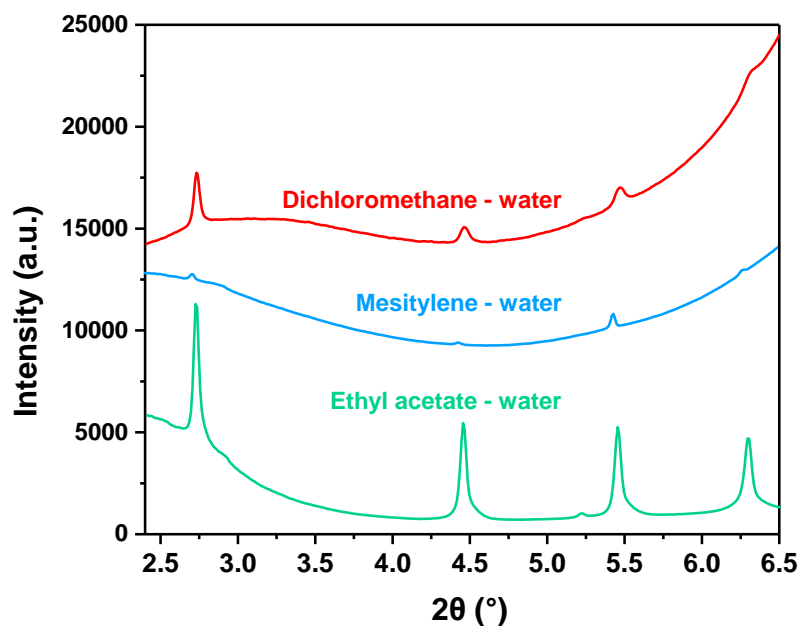


**Figure 3.40** Out-of-plane GIXRD characterisation of **CC3-PAN-24H-0.8%** samples that were synthesised using the organic solvents, dichloromethane, mesitylene, ethyl acetate to dissolve TFB. The amine monomer was dissolved in the water phase. Film synthesis conditions, reagent concentration: TFB 0.8 wt.% in DCM, mesitylene, or ethyl acetate (30 mL), CHDA 0.8 wt.% in water (32 mL); reaction conditions: 24 hours at room temperature; dish diameter: 7.4 cm. The GIXRD patterns indicate that **CC3-PAN-24H-0.8%** fabricated between water and ethyl acetate had the highest crystallinity, while the comparable reflection positions indicate that the **CC3** films had the same **CC3 $\alpha$**  structure.

As shown in **Figure 3.40**, the obtained diffraction patterns indicate that the **CC3** film fabricated from water and ethyl acetate has a higher crystallinity, while the **CC3** film membrane obtained from mesitylene and water had the lowest crystallinity. These films do, however, have the same polymorphic form as **CC3 $\alpha$** , and have shown very similar MWCO during the dye rejection studies.

### 3.4.5 Effects of Membrane Activation

We believe the cage membrane could complete its crystalline rearrangement in solvent and form the most stable state within a period of time. Therefore, we have activated these membranes using different treatments. The as-prepared **CC3-PAN** membranes were soaked in water (without drying) at room temperature for 1 day, 3 days, and 7 days, to generate

membranes referred to hereafter as **CC3-PAN**, **CC3-PAN-3**, **CC3-PAN-7**, respectively, while the as-prepared membrane is abbreviated as **CC3-PAN-0**.

The native water permeance of **CC3-PAN-0** was  $6.1 \text{ L}\cdot\text{m}^{-2}\cdot\text{h}^{-1}\cdot\text{bar}^{-1}$ , but it improved to  $43.0 \text{ L}\cdot\text{m}^{-2}\cdot\text{h}^{-1}\cdot\text{bar}^{-1}$  for **CC3-PAN**,  $60.2 \text{ L}\cdot\text{m}^{-2}\cdot\text{h}^{-1}\cdot\text{bar}^{-1}$  for **CC3-PAN-3**, and  $145.7 \text{ L}\cdot\text{m}^{-2}\cdot\text{h}^{-1}\cdot\text{bar}^{-1}$  for **CC3-PAN-7**, as shown in **Figure 3.41**. Increased MeOH permeances were observed in methanol after soaking the membrane for longer durations in water beforehand and were determined to be  $15.1 \text{ L}\cdot\text{m}^{-2}\cdot\text{h}^{-1}\cdot\text{bar}^{-1}$  for **CC3-PAN-0**,  $85.1 \text{ L}\cdot\text{m}^{-2}\cdot\text{h}^{-1}\cdot\text{bar}^{-1}$  for **CC3-PAN**,  $159.0 \text{ L}\cdot\text{m}^{-2}\cdot\text{h}^{-1}\cdot\text{bar}^{-1}$  for **CC3-PAN-3**, and  $324.8 \text{ L}\cdot\text{m}^{-2}\cdot\text{h}^{-1}\cdot\text{bar}^{-1}$  for **CC3-PAN-7**. We proposed that soaking in water enables cage crystals to further complete the self-correction and self-regulation from their metastable form, which activates the membranes and thus endows higher guest permeance.

Despite the significant improvements in solvent permeance after pre-treatment in water, the dye rejection performance **CC3-PAN-0**, **CC3-PAN**, **CC3-PAN-3**, **CC3-PAN-7** were comparable. As shown in **Figure 3.42**, these treated membranes were found to have comparable MWCO of  $\sim 600 \text{ g}\cdot\text{mol}^{-1}$  under the same measurement conditions.

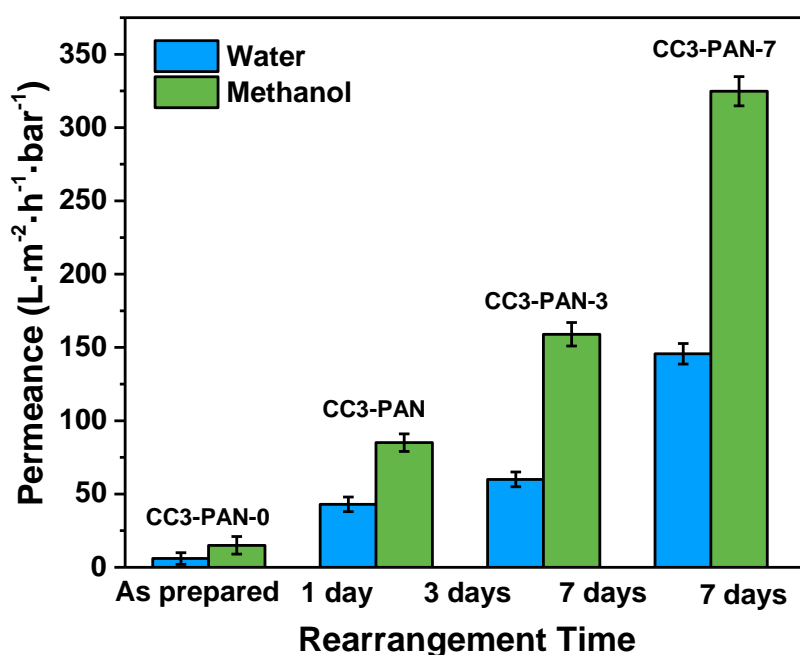


**Figure 3.41** Water and MeOH permeance of the as-prepared membrane (**CC3-PAN-0**) and the water treated **CC3-PAN**, **CC3-PAN-3**, and **CC3-PAN-7** membranes. Error bars depict the standard deviations (SD) of the data from at least three independent membranes, and were calculated by Eq. 3 in the Methods section.

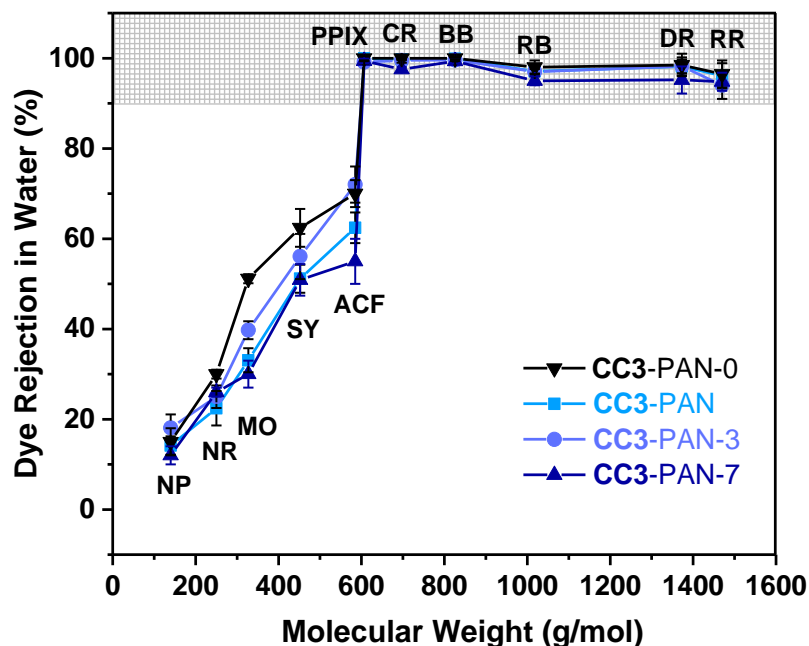


**Figure 3.42** MWCO curves for dyes for as-synthesised CC3-PAN-0, CC3-PAN, CC3-PAN-3, CC3-PAN-7 in water. Error bars depict the standard deviations (SD) of the data from at least three independent membranes, and were calculated by Eq. 3 in the Methods section.

### 3.4.6 Longer Duration Studies

Longer duration studies have been carried using 20 ppm rose bengal in water feedstock after continuous collection of the permeate every 0.5 h for at least 20 hours. The data in **Figure 3.43** demonstrated a consistent dye rejection (99.7 % for RB) and water permeance ( $\sim 43.0 \text{ L}\cdot\text{m}^{-2}\cdot\text{h}^{-1}\cdot\text{bar}^{-1}$ ) over one day, showing good mechanical robustness of the CC3-PAN membrane.

Long-term operation for solvent permeation was performed on CC3-PAN and CC3-PAN-7 membrane using a cross-flow rig under a continual feedstock supply, with a flow rate of  $25 \text{ L}\cdot\text{h}^{-1}$  which was provided by the liquid pump. The cell input flow was introduced tangentially to create proper mixing close to the membrane surface to minimise concentration polarisation. The result is shown in **Figure 3.44**, and this proved that the high flux remained intact on both membranes after 48 hours with little attenuation over this period.

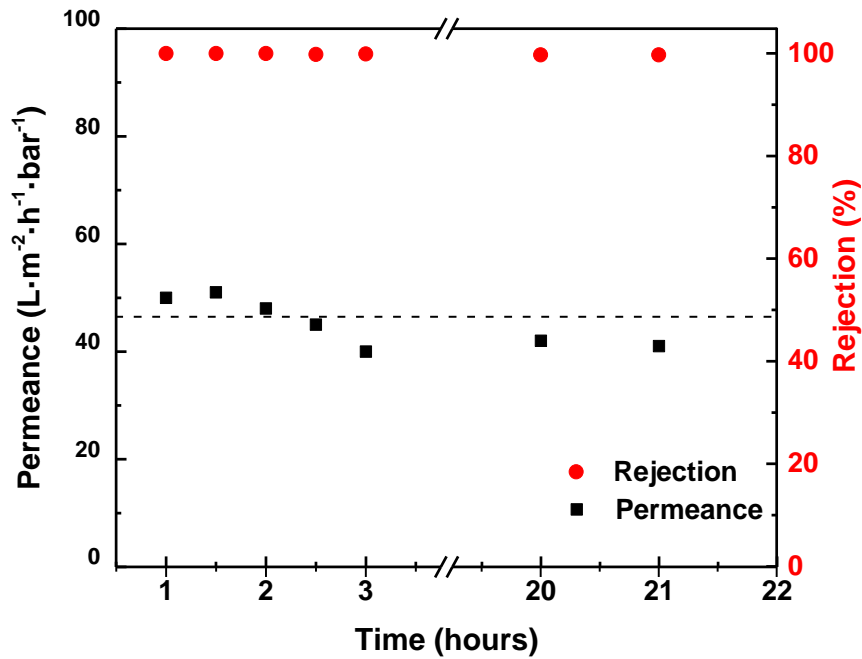


**Figure 3.43** Membrane selectivity and stability of CC3-PAN in water. The plot shows water permeance and dye rejection of RB from a 20 ppm feedstock for the CC3-PAN membrane over ~ 20 hours in a 50 mL transparent Merck Millipore Amicon<sup>®</sup> dead-end stirred cell which is connected to an 800 mL Merck Millipore Amicon<sup>®</sup> RC800 reservoir. The upstream nitrogen pressure was kept at 1 bar during the measurement, with a stirrer agitation speed of 400 rpm.

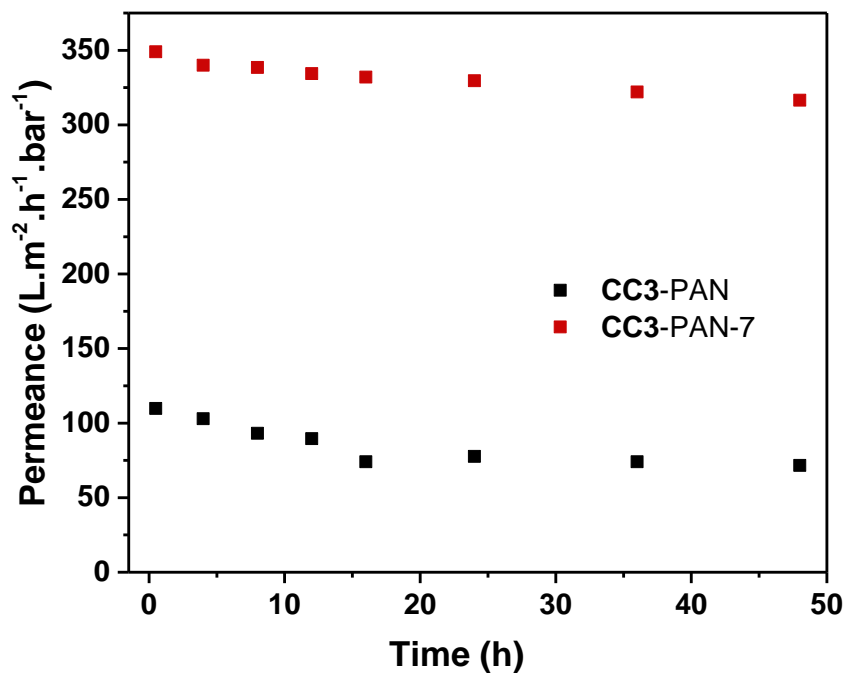


**Figure 3.44** Methanol permeance for CC3-PAN and CC3-PAN-7 over 50 hours using a cross-flow rig kept under a 10 bar nitrogen pressure.

Furthermore, as the membrane performance studies were performed while magnetically stirring the feedstock solutions at 400 rpm, all membranes have exhibited good tear resistance. These measurements indicated that the **CC3**-PAN has excellent solvent resistance and long-term stability. The internal structures are stable, owing to the crystalline structures with highly ordered window-to-window packing and well-defined channels.

### 3.5 Studies for Amorphous Cage Membranes

Interestingly, these POCs have guest selective microporous structures if they can be processed into specific polymorphic forms. For instance, crystalline **CC3** packs window-to-window and forms interconnected 3D diamondoid channels<sup>1</sup>, while the amorphous **CC3** has a random packing of the cage molecules<sup>5</sup>. Therefore, we are also interested in templating the packing arrangements of POCs in the porous membranes to modulate selective guest permeation.

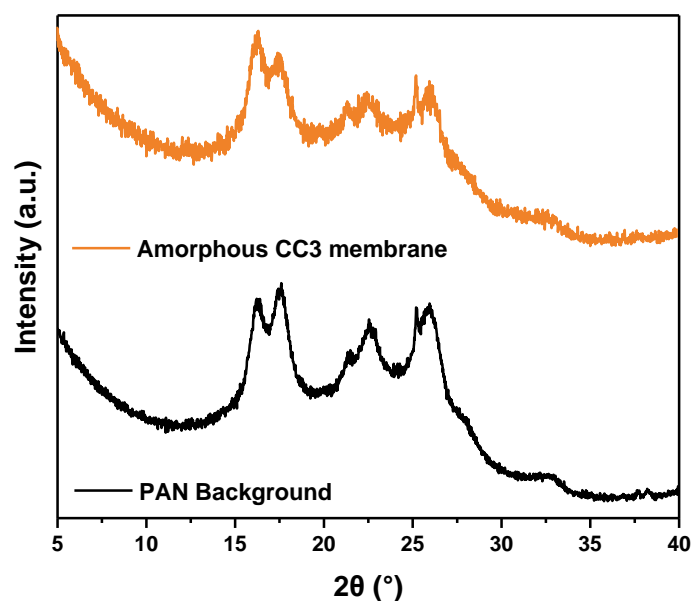


**Figure 3.45** PXRD pattern of blank PAN membrane (black) and amorphous **CC3** membrane (orange). PXRD patterns were collected in transmission mode with Cu-K $\alpha$  radiation over the  $2\theta$  range of 5-40° using a step size of 0.013°. Data collection times, crystalline **CC3a** reference: amorphous **CC3** membrane: 60 minutes.

**CC3** membranes with different polymorphic forms were, therefore, prepared by spin-coating onto the PAN support from **CC3** chloroform solution (see detailed experiments in **Chapter 2**). As discussed in **Section 3.3**, these obtained membranes are amorphous based on the Raman spectra. Furthermore, they did not show any PXRD signals out of the PAN background, as is

shown in **Figure 3.45**. Since the evaporation speed of the solvent is very quick during the coating process, it is reasonable to obtain the amorphous **CC3** coatings.

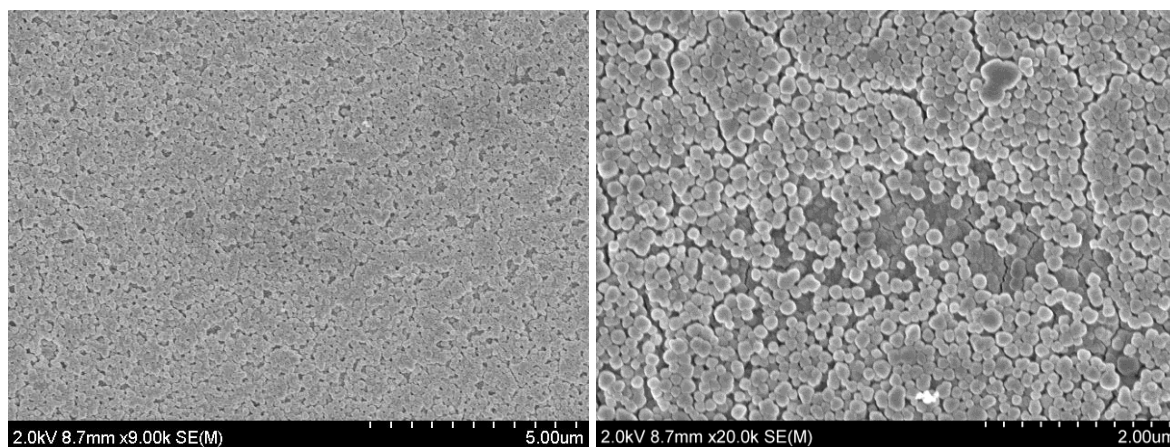


**Figure 3.46** SEM images with different resolutions showing the surface morphology of an amorphous **CC3** membrane on a PAN support, made by spin-coating method.

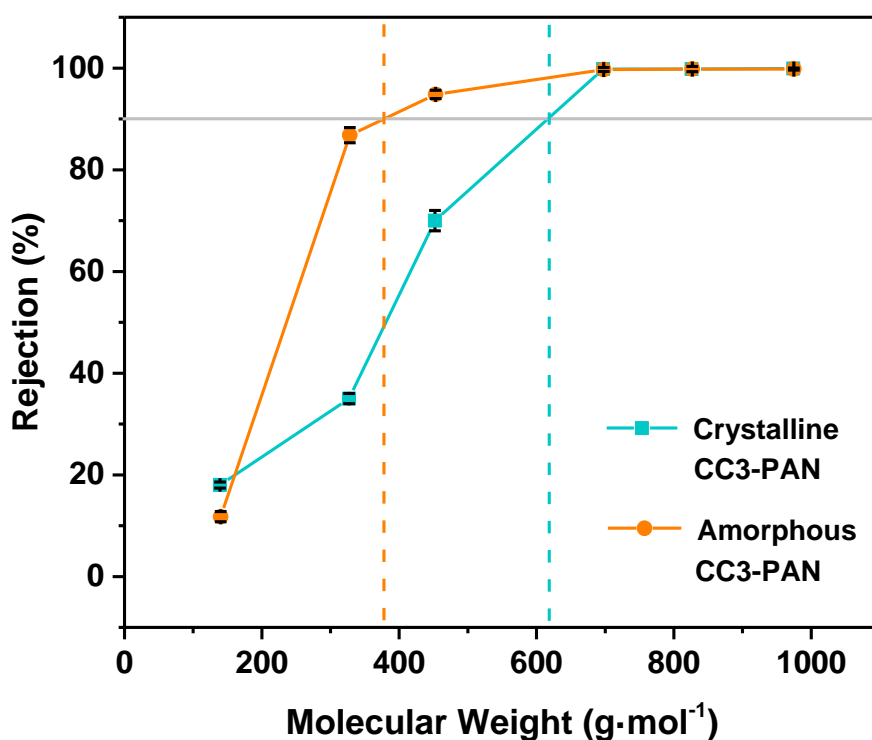


**Figure 3.47** Molecular weight cut-off (MWCO) curves for crystalline and amorphous cage films on PAN support (**CC3-PAN**). Six dye molecules were used in 20 ppm water solution during the selectivity experiments, including Rose Bengal (974 g/mol), Brilliant Blue (827 g/mol), Congo Red (697 g/mol), Sunset Yellow (452 g/mol), Methyl orange (327 g/mol), and 4-nitrophenol (139 g/mol). The MWCO is defined by 90% rejection.

The surface morphology of the materials was studied by SEM. As is shown in **Figure 3.46**, the surface is not as continuous in the amorphous membrane as the crystalline **CC3**-PAN; instead, spherical nanoparticles were observed on top of the membrane support. As the spin-coated **CC3** membranes were proved to be amorphous, no octahedral crystals can be found. The coatings appeared to consist of multiple layers, which was affected by the speed and time during the spin-coating process.

The MWCO curves for both crystalline and amorphous cage films have been calculated using six dye molecules. Both films showed good rejection ( $\sim 99\%$ ) for Rose Bengal, Brilliant Blue, and Congo Red, and no rejection for 4-nitrophenol ( $\sim 15\%$ ). Interestingly, the crystalline and amorphous cage films exhibit an obvious shift on MWCO, which is  $\sim 600$  g/mol for crystalline cage film and 400 g/mol for amorphous cage film (**Figure 3.47**). The **CC3** molecule has a window size ranging from 5.6 – 6.7 Å, and when it packs window-to-window and forms its  $\alpha$ -phase crystalline structure, the narrowest point in the pore channels is 5.3 Å<sup>11</sup>. However, the rigid cage bodies are flexible during guest diffusion, which could breathe by more than 2 Å to a diameter of 7.4 Å<sup>11</sup>. By comparing the molecule sizes of these six dyes (Table S1) with flexible cage window size, it is reasonable to assume that the larger dyes like Rose Bengal (10.6 Å), Brilliant Blue (10.1 Å), and Congo Red (7.7 Å) couldn't permeate the cage channels, while the smaller dye molecules, such as Sunset Yellow (7.0 Å), Methyl Orange (4.5 Å) and 4-Nitrophenol (4.3 Å) were able to pass through the cage membrane. During the dye rejection tests with the amorphous cage film the MWCO curve shifted  $\sim 200$  g/mol. The amorphous membrane has a random and less dense packing of the cage molecules<sup>5</sup>. We believe this random packing of cage molecules creates a disconnected diffusion pathway for the dyes (**Figure 3.48**). As a result, Sunset Yellow and Methyl Orange are unable to permeate through the amorphous cage membrane. Therefore, we have managed to modulate the membrane pore channels via different packing arrangements of porous organic cages, thus achieving selective guest permeation through the thin films.

As discussed before, the crystalline cage membrane (**CC3**-PAN) showed excellent permeance toward non-polar solvents and protic/aprotic organic solvents thanks to the highly ordered channels in the film. By contrast, when these experiments were performed using the amorphous cage membrane, we observed very low permeance of these aforementioned solvents, which is 0.6 L·m<sup>-2</sup>·h<sup>-1</sup>·bar<sup>-1</sup> for ethanol, 2.1 L·m<sup>-2</sup>·h<sup>-1</sup>·bar<sup>-1</sup> for water, 4.0 L·m<sup>-2</sup>·h<sup>-1</sup>·bar<sup>-1</sup> for acetonitrile, 5.0 L·m<sup>-2</sup>·h<sup>-1</sup>·bar<sup>-1</sup> for acetone, and no permeance for hexane, heptane and toluene was observed. A plot was calculated by pure solvent permeances versus their combined solvent



properties (viscosity  $\eta$ , molar diameter  $d_m$ , and solubility parameter  $\delta_d$ ) and is shown in **Figure 3.49**, where  $R^2$  is the coefficient of determination for the function and the value is 0.9526.

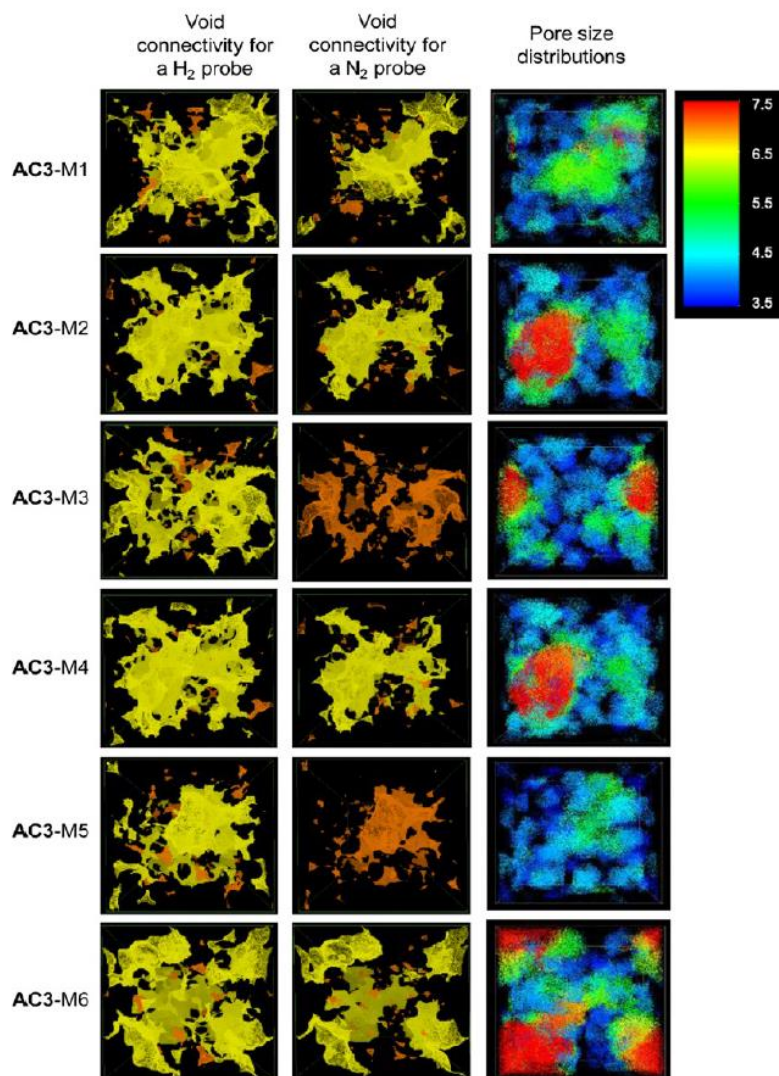


**Figure 3.48** Visualization of void connectivity for the amorphous CC3 models. Interconnected and unconnected voids are colored yellow and orange, respectively, both for a H<sub>2</sub> radius of 1.42 Å (left column) and a N<sub>2</sub> radius of 1.82 Å (center column). The color map of pore sizes in different structural models, ranging from diameter of 3.5 to 7.5 Å is shown on the right. Reprinted with permission from reference<sup>5</sup>. Copyright 2013, American Chemical Society.



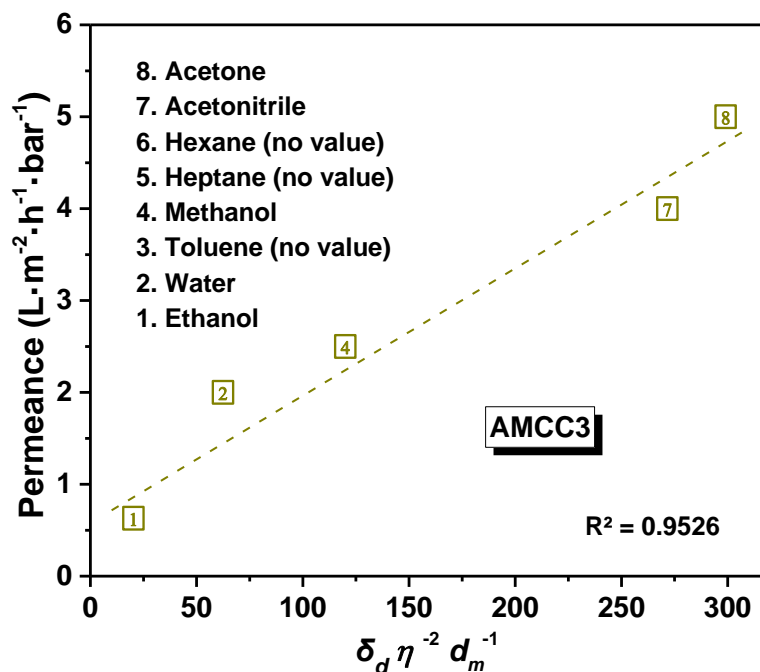


**Figure 3.49** Plots showing pure solvent permeances versus their combined solvent properties (viscosity, molar diameter, and solubility parameter) for amorphous CC3 membrane (AMCC3). The cell was kept at room temperature under 10 bar upstream pressure in a nitrogen atmosphere, with 400 rpm magnetic stirring.

It is also reported that the amorphous membranes suffer from ageing during long-term use<sup>38</sup>. The solvent permeance dropped to zero on the amorphous CC3 membrane after 24 hours of continuous permeation, which is due to the ageing of the membrane, and the interconnected pore structure might have been destroyed during the long time and high pressure (10 bar). As is shown in **Figure 3.50** and discussed before, by contrast, the CC3-PAN membrane during the long-term operation experiments over 24 hours has been proven to remain in high permeance values with little attenuation, indicating good solvent residence and shape-persistence of the crystalline film.

We attribute the low permeance and the poor performance in long-term operation and high-pressure condition to the disordered packing in the amorphous membrane, as is shown in **Figure 3.51(b)**. The CC3 molecules pack randomly rather than pack window-to-window, and the shape of the molecules could be flexible or even collapse, especially with the interaction of other solvents or external forces (e.g., pressure). This is caused by the flexible imine bonds in the CC3 molecules without the ordered packing, which could act as a support frame. By comparison, the excellent solvent permeance and long-term solvent resistance confirmed the

crystalline films show highly ordered window-to-window packing with well-defined and interconnected channels (Figure 3.51(a)), and the internal structures are chemically stable.

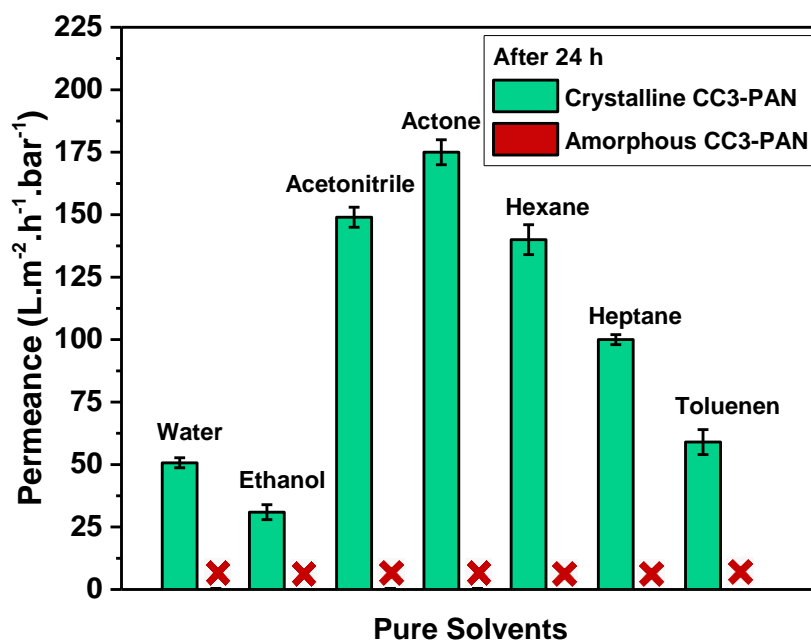


**Figure 3.50** Pure solvent permeances for the crystalline and amorphous cage films on PAN support after 24 hours. The cell was kept at room temperature (25 °C) under 10 bar upstream pressure in a nitrogen atmosphere, with 400 rpm magnetic stirring.

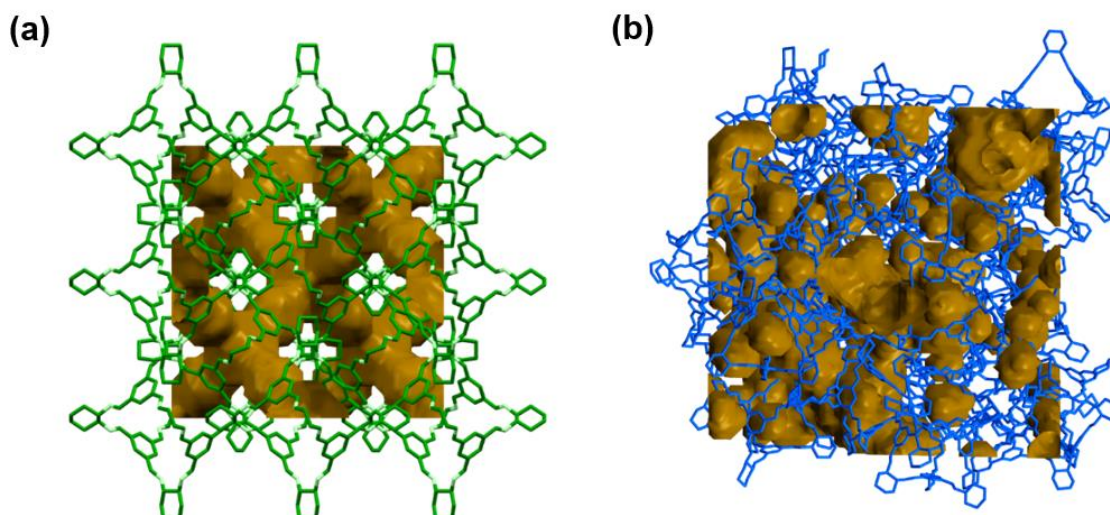


**Figure 3.51** (a) Crystalline structure and (b) amorphous packing of cage CC3 molecules, with the voids shown in yellow colour probed by N<sub>2</sub> molecules (kinetic diameter of 1.82 Å).

## 3.6 Characterisation and Performance for Other Cage Membranes

### 3.6.1 Cage Membranes Made with Co-crystals

Apart from the crystalline CC3 films fabricated by interfacial method, highly porous crystalline solids can be produced by mixing different organic cage modules that self-assemble by means of chiral recognition. For example, mixing solutions of CC3-S and CC3-R (5 mg/mL) leads to rapid precipitation of racemic octahedral nanocrystals. As a result, well-defined, porous (CC3-S, CC3-R) co-crystals are formed, thereby translating intermolecular heterochiral interactions into nanoscale morphology control<sup>66</sup>. These porous nanocrystals would show particular applications, for example, in size-based molecular separations.

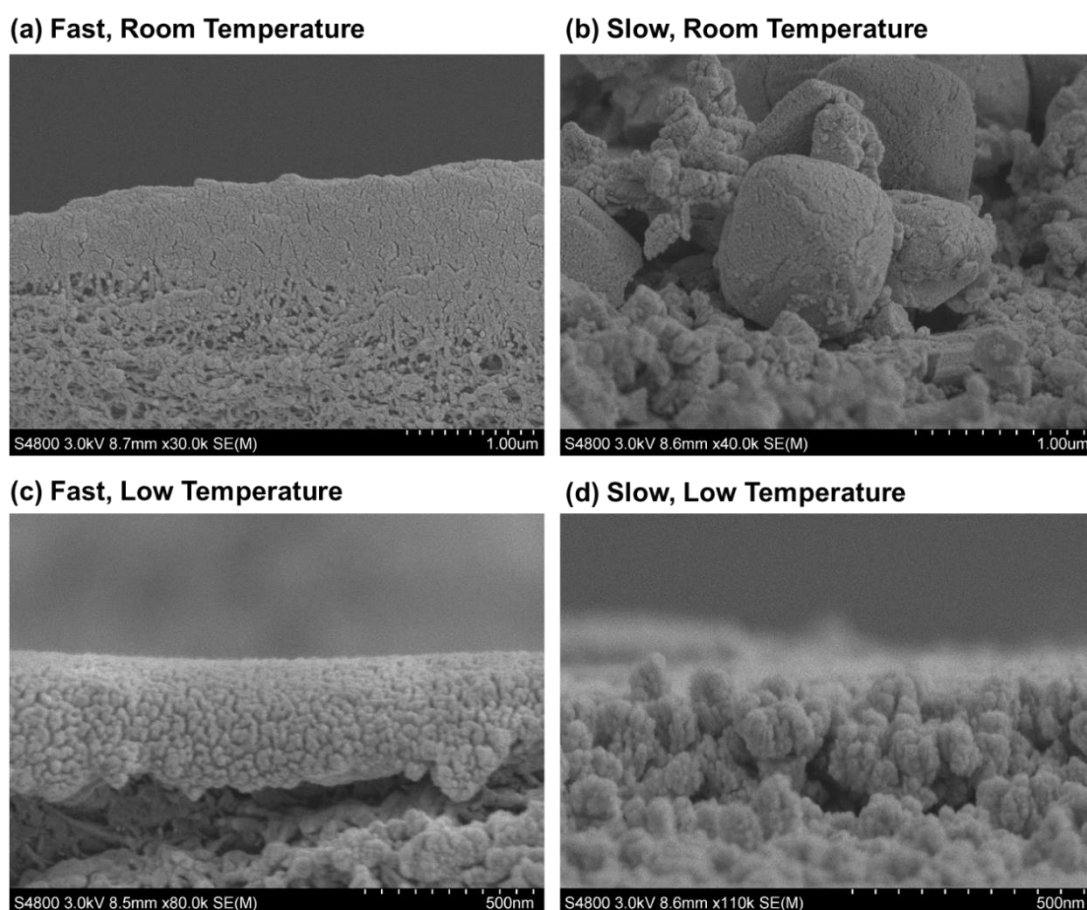


**Figure 3.52** SEM images showing spin-coated CC3R/CC3S nanoparticles on PAN support, with four different synthesis conditions of CC3R/CC3S nanoparticles: (a) fast addition, at room temperature, (b) slow addition, at room temperature, (c) fast addition, at low temperature (dry ice/acetone bath), (d) slow addition, at low temperature (dry ice/acetone bath). CC3R or CC3S was dissolved in DCM to make it 1.5 mg/mL solution. Fast addition: add CC3R solution into

*CC3S solution immediately; slow addition: CC3R solution was slowly and carefully added into CC3S solution using a 1 mL syringe with a speed rate of 1 mL/min.*

Therefore, we have tried to spin coat **CC3** film using the **CC3R/CC3S** self-assembled nanoparticles, and the influences of the synthesis conditions have been investigated. The **CC3R/CC3S** self-assembled nanoparticles have been synthesised by addition of the solution with dissolved **CC3R** or **CC3S** to another, via different solution addition rates and under different temperatures. The nanocrystals have been formed in the solution, and the dispersion was used for spin-coating on PAN support. SEM was applied to study the morphology of the obtained **CC3R/S-PAN** membrane, and the images are shown in **Figure 3.52**. Uniform coatings can be seen on the porous PAN support for the samples with a fast addition rate ((a) and (c)), and the shape of these nanoparticles are round. By contrast, clear octahedrons can be observed with slow addition rate ((b) and (d)), where large octahedrons with a diameter of ~1  $\mu\text{m}$  can be found on the membrane with nanoparticles made at room temperature, while the low temperature leads to smaller nanocrystal sizes of a diameter between 200 – 300 nm.

As a result, it can be concluded that the addition rate of the **CC3R/S** solution would affect the shape of the nanocrystals - slow addition makes the crystals to be more octahedral, and fast addition would result in round particles; temperature, on the other hand, would affect the size of the nanocrystals formed in solution – smaller particles would be formed under low temperature.

### **3.6.2 Surface Morphology Studies of Cage Coatings Made by Other Methods**

Meanwhile, **CC3** membranes fabricated using other approaches have been compared here as well. We have first studied the surface morphology by SEM to investigate whether the membrane was successfully formed and whether the surface is uniform and continuous.

**CC3** membranes have been fabricated by casting, where the **CC3** molecules were fully dissolved in DCM (0.5 wt. %) and allowed to evaporate on top of a porous substrate such as PAN or AAO membrane. Different conditions of the casting process resulted in different morphology of the obtained membranes, as shown in **Figure 3.53**. When the **CC3** DCM solution was kept in open air and allowed to slowly evaporate (with lid or without lid) for 72 hours, large octahedral crystals were found discretely distributed on the membrane surface, with a diameter of 20-50  $\mu\text{m}$  when evaporated without lid, i.e., quicker evaporation rate (**Figure**

3.53 (a)), and a diameter of 0.5-1  $\mu\text{m}$  with the lid on (Figure 3.53 (b)). As the PAN support nucleated large crystal growth, these crystals were discrete and did not form a continuous coating on the substrate.

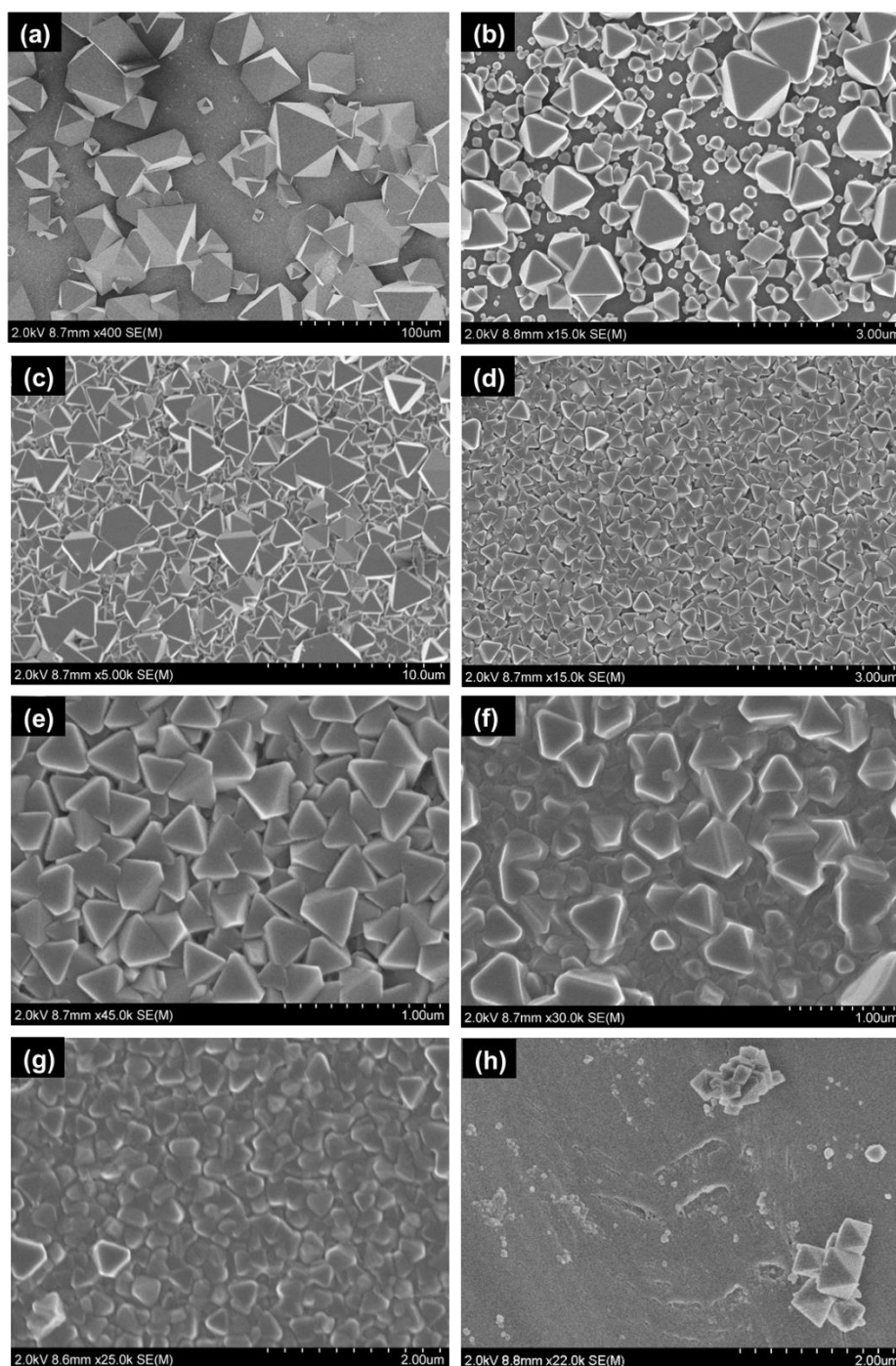


**Figure 3.53** SEM images showing the surface morphology of CC3 membranes fabricated by casting method. Film synthesis conditions, reagent concentration: CC3 0.5 wt.% in DCM (30 mL), dish diameter: 7.4 cm. Detailed conditions are shown in Figure 3.54.

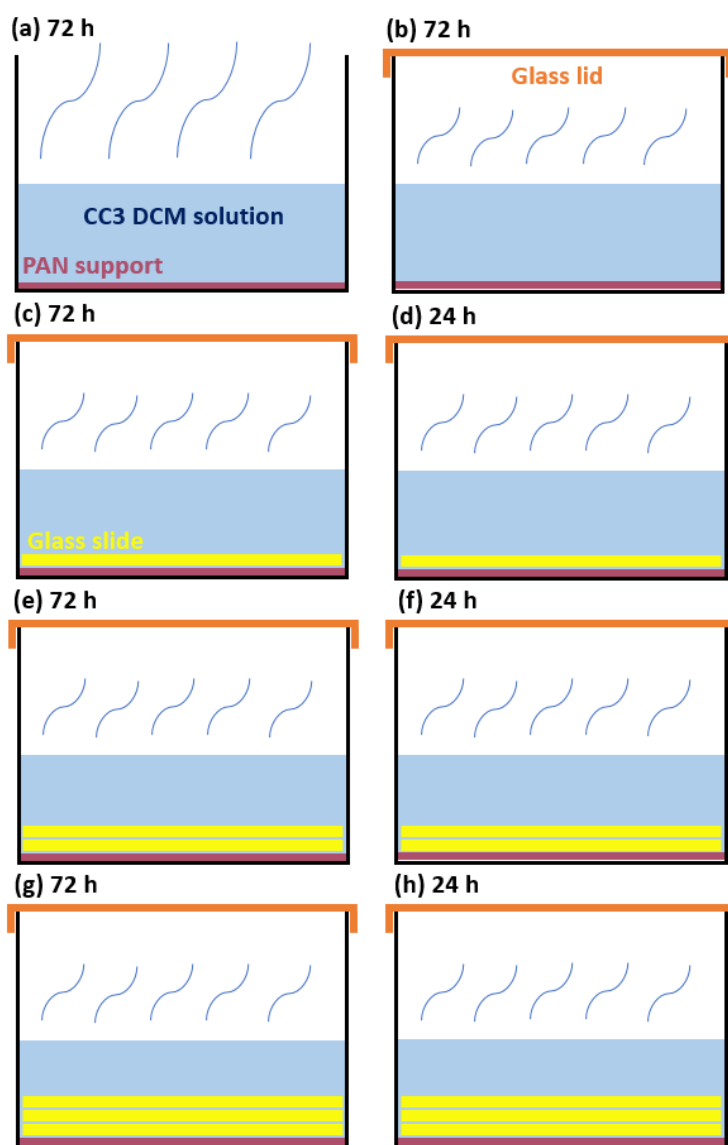


**Figure 3.54** Illustration diagram of different casting conditions of 5 wt. % CC3 DCM solutions on porous PAN support: (a) Casting solution in the open air, 72 hours; (b) casting solution with a glass lid on, 72 hours; casting solution with a lid on, one piece of a glass slide on top of the PAN support, (c) 72 hours, (d) 24 hours; casting solution with a lid on, two pieces of a glass slide on top of the PAN support, (e) 72 hours, (f) 24 hours; casting solution with a lid on, three pieces of a glass slide on top of the PAN support, (g) 72 hours, (h) 24 hours. Reagent concentration: CC3 0.5 wt.% in DCM (30 mL), dish diameter: 7.4 cm.

To make the CC3 film more continuous rather than discrete particles on top of the support, efforts were made to make the crystals smaller. A piece of a glass slide (or multiple pieces of glass slides) was put on top of the PAN membrane in order to restrict the formation of the CC3 crystals, as is shown in **Figure 3.54**. When the CC3 nanocrystals started to grow, they were kept in a thin layer of liquid between the glass slide and porous PAN substrate. Using more

pieces of glass slides meant that a thinner layer of liquid solution was created at the interface. The SEM images of the CC3-PAN membranes obtained using these different conditions are shown in **Figure 3.53** (c) - (h). It can be observed that octahedral crystals are packed in a denser manner on the surface, and the size of these crystals are smaller. The thinner the liquid layer between the glass slide and porous PAN substrate, the denser coatings formed. Besides, a shorter evaporation time resulted in a more continuous layer on the substrate.

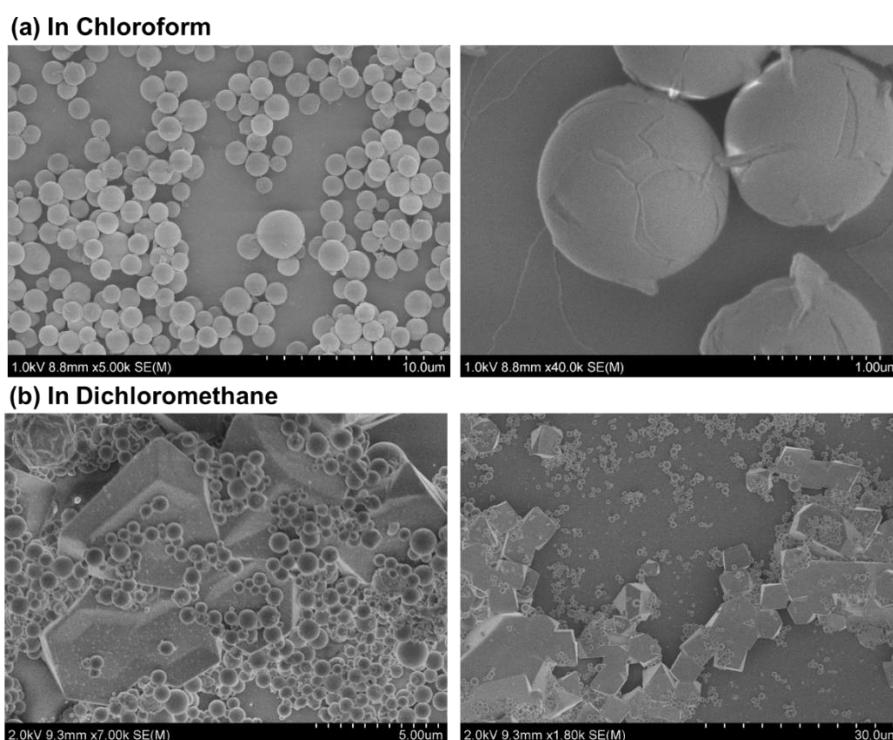


**Figure 3.55** SEM images with different resolutions showing the surface morphology of CC3 membranes synthesized in the single-phase: (a) in chloroform, (b) in dichloromethane. Film synthesis conditions, reagent concentration: TFB 0.8 wt.% and CHDA 0.8 wt.% in 30 mL chloroform or DCM; reaction conditions: 24 hours at room temperature.

As the previous CC3-PAN was obtained at the interface of two liquid phases (water and DCM), we investigated the membrane synthesis in the single-phase as well. As is shown in **Figure 3.55**, large spherical particles can be seen on the surface with a diameter of  $\sim 1 \mu\text{m}$  when synthesized by the starting reagents in chloroform. A thin skin layer can be observed on the surface of these particles. A mixture of hexagonal crystals, octahedral crystals and spherical particles can be found on the membrane synthesized by in DCM. This is because a quicker reaction happens in the single-phase once the two reagents meet, and faster evaporation of the solvent leads to less continuous coatings. As chloroform evaporates faster than DCM, the spherical particles form while the solvent evaporates, rather than hexagon or octahedron shaped



crystals. As a result, no continuous **CC3** coating or film formed in both conditions. This further proved the advantage of our novel interfacial synthesis method for a continuous, defect-free and crystalline film on the substrate.

### 3.6.3 Surface Morphology and Dye Rejection of Cage Membranes Made by Other Methods

We have fabricated the **CC3** membranes using an interfacial method under 10 bar pressure in a dead-end cell. The set-up and conditions were the same as the interfacial method mentioned before, but 10 bar pressure was applied during the reaction. The SEM images of the obtained **CC3** membranes are listed in **Figure 3.56**. The surface morphology is very different from **CC3**-PAN, where the continuous film with some wrinkles can be observed on the surface. These wrinkles might be caused by the pressure while the reaction goes on.

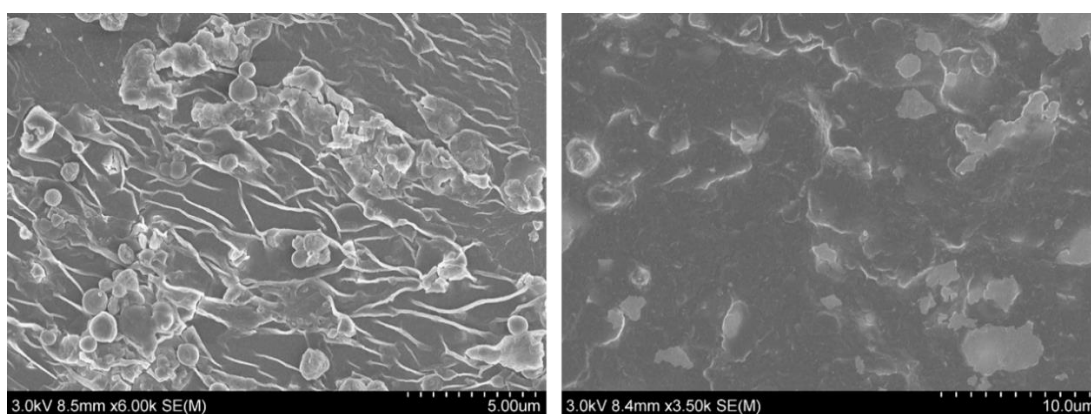


**Figure 3.56** SEM images with different resolutions showing the surface morphology of **CC3** membranes made by high pressure method (**CC3**-PAN-HP).

Unlike the MWCO of  $\sim 600 \text{ g}\cdot\text{mol}^{-1}$  for **CC3**-PAN, it was found that **CC3**-PAN-HP has a smaller MWCO ( $\sim 250 \text{ g}\cdot\text{mol}^{-1}$ ) (**Figure 3.58**), indicating a more rigid and ordered packing of the **CC3**. For **CC3** crystals, the diffusion diameter ( $D_f$ ) exists in the lattices, and the cage cavity diameter ( $D_i$ ) itself can be the separation envelope (**Figure 3.57**) if there are crystal defects/dislocations *etc.* The cage membrane consists of small cage crystals, however the membrane itself is not a single crystal. We believe the grain boundaries inside the cage membrane create a larger diffusion pathways ( $D_i$ ) for the guests rather than the extrinsic voids of a cage crystal ( $D_f$ ). The treatment with high pressure may have caused the pore structure change of the **CC3** lattices and resulted in narrower pores. Also, there is a possibility that the grain boundaries were reduced with the effects of high-pressure treatment, which may cause a shift of MWCO.



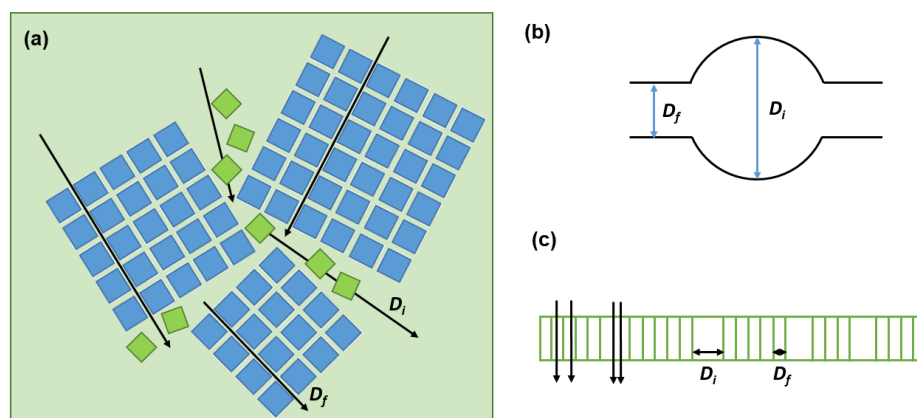


**Figure 3.57** Illustration of the diffusion diameter ( $D_f$ ) and cage cavity diameter ( $D_i$ ) in the cage membrane: (a) the possible permeance pathways in the membrane; (b) the schematic diagram for the cage pores; (c) the schematic diagram of a membrane consists of two different diameters.

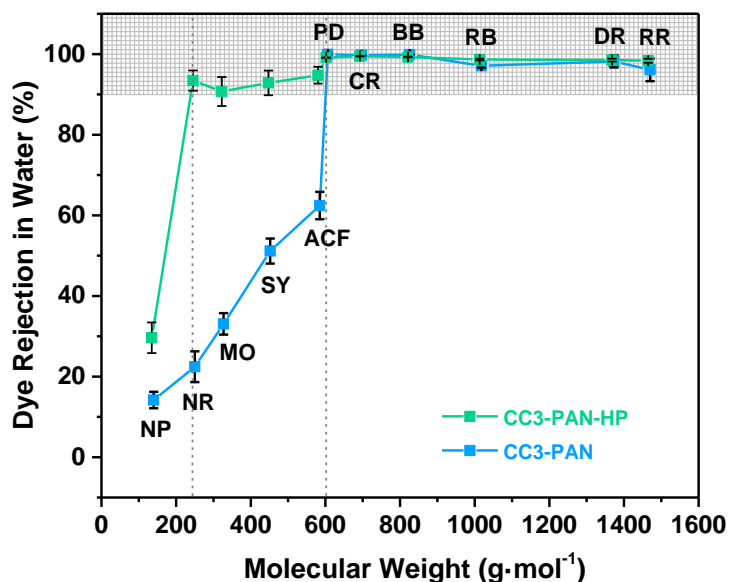


**Figure 3.58** Molecular weight cut-off curve of different dyes in water for cage membranes synthesized under high pressure (CC3-PAN-HP) compared with CC3-PAN. RR, Reactive Red 120; DR, Direct Red 80; RB, Rose Bengal; CR, Congo Red; PD, Protoporphyrin IX disodium; ACF, Acid Fuchsin; SY, Sunset Yellow; MO, Methyl Orange; NR, Neutral Red; NP, 4-Nitrophenol, 20 ppm.

To broaden the solvent that can be used for the **CC3** membrane synthesis, sonochemistry was utilised instead. Instead of using DCM or chloroform, the PAN membrane was placed in water with TFB and CHDA under ultra-sonic (550W Branson Sonifier SFX550 cell disrupter with O.D. 3 mm microtip) for 30 minutes. The SEM images of the resulting membrane are shown

in **Figure 3.59**, which is very different from the cage membranes we made previously. It exhibits a continuous, homogeneous surface with a very dense coating, and multiple layers can be seen on the surface.

The dye rejection experiments of the sonochemistry **CC3** membranes have exhibited a similar MWCO of  $\sim 600 \text{ g}\cdot\text{mol}^{-1}$  (**Figure 3.60**), indicating the obtained membranes may have a similar pore size with **CC3-PAN**. In this case, we have successfully broadened the synthesis solvent from DCM and chloroform to water, a cheaper, safer and more common solvent in our daily life and industry. Moreover, the 24 hours reaction time can be dramatically reduced to 0.5 hours due to the high efficiency of the ultra-sonic acceleration.

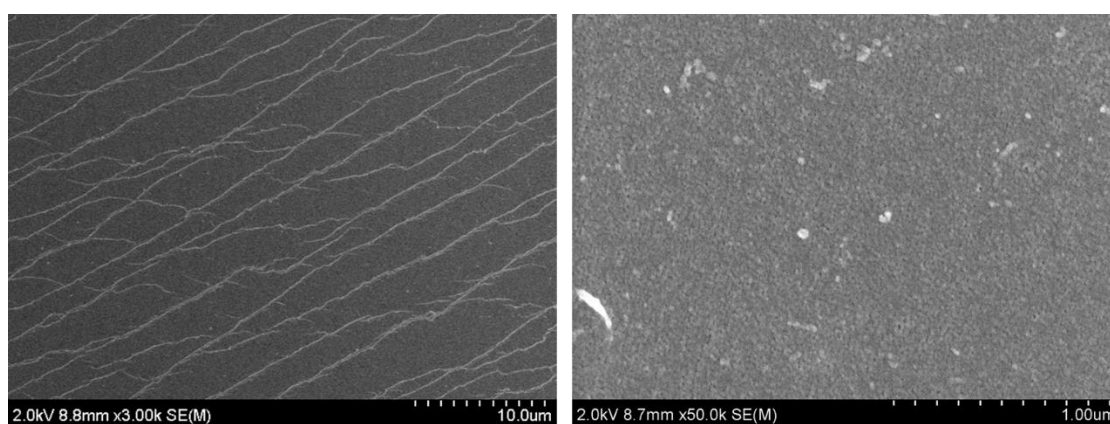


**Figure 3.59** SEM images with different resolutions showing the surface morphology of **CC3** membranes synthesized by sonochemistry.

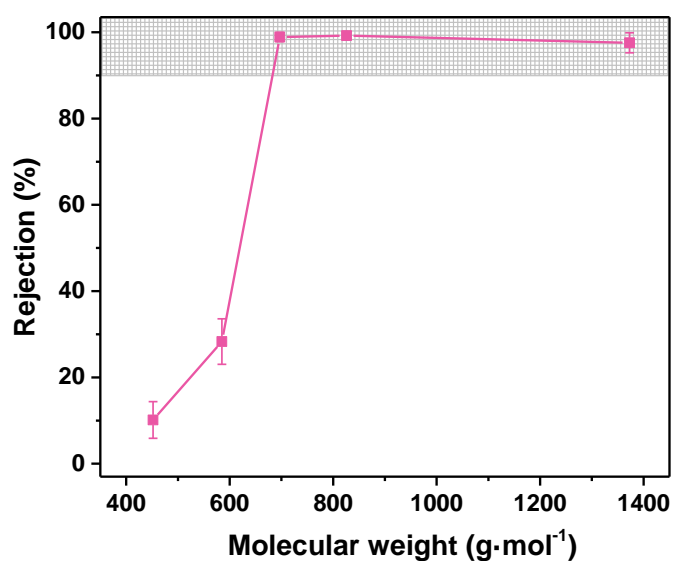


**Figure 3.60** Molecular weight cut-off curve of different dyes in water for **CC3** membranes synthesized via sonochemistry.

### 3.6.4 Discussions on Scalability

Scalability is another concern that may restrict the potential application of these cage membranes. Although porous organic cages are a relatively new class of material, they are synthesisable at scale for real-life application. For example, a spin-out company at Liverpool (CageCapture Ltd, <https://cagecapture.com>) commercialises **CC3** and analogues for air purification applications on the kilogram scale. Porous organic cages are also solution-processable and may be more compatible with specific manufacturing processes than insoluble porous solids. We have established a flow synthesis technology to produce crystalline **CC3** continuous in a flow in our lab<sup>67</sup>, and it is possible if we apply a hollow fiber in the system and we may get the crystalline **CC3** coated hollow fibre with a quite large scale.

The amorphous cage membranes made by spin-coating can be made faster, but they offer very low permeance. While crystalline membranes could have better properties, we know that scalability is a broad challenge in this area. However, the solubility of porous organic cages means they might be processed using electrospray coating or continuous dip coating / casting<sup>68</sup>, or possibly even new techniques such as 3D printing<sup>69</sup>. Hence, there is broad scope for crystalline porous organic cages membrane to be scalable. This is not a trivial challenge—at this point, this performance results from interfacial crystallisation, which might be hard to scale—but we are optimistic that a solution to this might be found in practical.

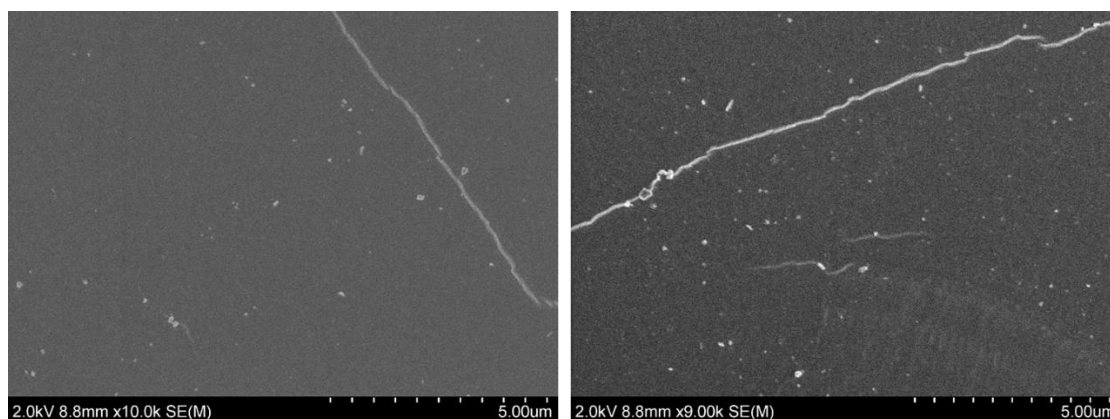


**Figure 3.61** SEM images with different resolutions showing the surface morphology of **CC3** membranes made by *in-situ* method.

Moreover, we have studied cage membrane fabrication by the *in-situ* method (see section 2.5.3 in **Chapter 2**), which has been used on a large scale in industry<sup>70</sup>. The surface morphology (**Figure 3.61**) shows a very thin layer that is continuous and uniform. No large particles can be seen on the surface. The dye rejection data shown in **Figure 3.62** confirmed that the obtained

**CC3** membrane is continuous and defect-free, acting well as a separation membrane for dyes. This means the **CC3** membranes could be fabricated in-situ on a large scale, and they have potential applications in many fields.

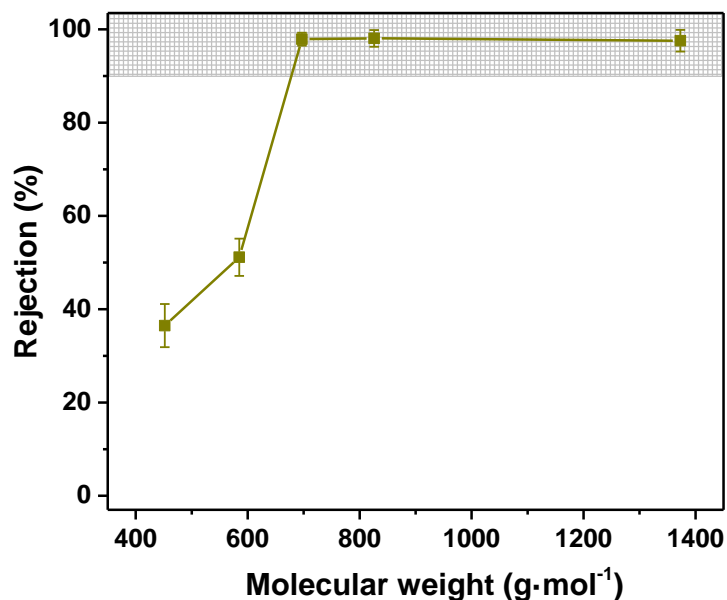


**Figure 3.62** *Molecular weight cut-off curve of different dyes in water for **CC3** membranes synthesized via in-situ method.*

### 3.7 Conclusions

POC membranes have been fabricated via several methods to overcome the challenges of the processability of POC crystallites as thin films. Importantly, a novel synthetic strategy to fabricate crystalline POC membranes has been developed using a simple aqueous–organic interfacial technique. The interfacial approach enables the directly in-situ formation of thin films consisting of **CC3** molecules under mild conditions. The resulting POC membrane is continuous, defect-free, and has high solvent permeances for a range of organic solvents while also showing excellent dye rejection performances. To the best of our knowledge, this is the first time an interfacial reaction process has been used to prepare continuous crystalline POC membranes that have been used in molecular separations, bringing a breakthrough in discrete porous materials applications.

We attribute the high solvent permeance of **CC3**-PAN to highly ordered pore channels in POC crystals positioned throughout the membrane structure. The mechanism of the **CC3** film

formation has been studied and can be described in four stages during the process. Effects of crystallinity, reaction solvents, membrane activation, pressure and long duration have been investigated. Notably, it has been observed that there is a shift of the MWCO for these porous organic membranes if processed into different structures (crystalline and random packing). For example, amorphous **CC3** membranes fabricated via spin-coating have shown a MWCO of  $\sim 400 \text{ g} \cdot \text{mol}^{-1}$ , which indicates we have successfully modulated the pore structures of these membrane materials.

Moreover, cage membranes made with **CC3** molecules or co-crystals, using different methods including casting, in-situ synthesis, sonochemistry, have been studied. These approaches enable a faster synthesis process (e.g., 30 min) with more mild conditions (e.g., in water), which might make these membranes more scalable in the future. The scalability of the **CC3** membranes can be achieved practically due to their solution processable properties (i.e., the solubility of POCs). Therefore, it is anticipated that the synthesis technique and unique templating method demonstrated herein for the fabrication of defect-free, free-standing POC membranes would broaden the realm of the practical application of these macrocyclic materials.

### 3.8 Chapter Acknowledgements

In this chapter, I would like to thank Prof. Andrew I. Cooper, Dr. Marc A. Little, Prof. Andrew G. Livingston, Dr. Zhiwei Jiang and Dr. Michael E. Briggs for their supervision and suggestions on my work. I acknowledge the discussion and efforts of this project from all the authors of the paper ‘A Smart, Responsive Crystalline Porous Organic Cage Membrane with Switchable Pore Apertures for Graded Molecular Sieving’ which will be soon published in *Nature Materials*: Marc A. Little, Andrew I. Cooper, Zhiwei Jiang, Andrew G. Livingston, Yue Wu, Michael E. Briggs, Hadeel Hussain, and Jonathan Rawle.

For funding, I acknowledge the Engineering and Physical Sciences Research Council (EPSRC) (EP/N004884/1), the Leverhulme Trust via the Leverhulme Research Centre for Functional Materials Design, the China Scholarship Council for a studentship and the Royal Society of Chemistry for a Researcher Mobility Grant (M19-2442). Zhiwei synthesised the membrane support and conducted the AFM measurements. Briggs helped with the cage synthesis. Hadeel Hussain and Jonathan Rawle designed and set up the in-situ GIXRD system and helped with these measurements. Marc and Yue helped with the GIXRD measurements and processed the

X-ray data. Andrew provided facility support and insights into advanced membrane science. I also acknowledge Miss Hongmei Chen for assistance during the I07 measurements, Mr. Rob Clowes for instrument support and setting up the filtration cell, and Mr. Haofan Yang and Dr. Tom Mitra for discussions on SEM images. I would like to thank Dr. Keith Arnold for obtaining the FIB-SEM images. Thank all the authors for their valuable discussion of the data and commented on the manuscript submitted to Nature Materials.

### 3.9 References

1. Tozawa, T. *et al.* Porous organic cages. *Nat. Mater.* **8**, 973–978 (2009).
2. Hasell, T. & Cooper, A. I. Porous organic cages: soluble, modular and molecular pores. *Nat. Rev. Mater.* **1**, 16053 (2016).
3. Zhang, G. & Mastalerz, M. Organic cage compounds – from shape-persistency to function. *Chem. Soc. Rev.* **43**, 1934–1947 (2014).
4. Mastalerz, M. Porous Shape-Persistent Organic Cage Compounds of Different Size, Geometry, and Function. *Acc. Chem. Res.* **51**, 2411–2422 (2018).
5. Jiang, S. *et al.* Molecular dynamics simulations of gas selectivity in amorphous porous molecular solids. *J. Am. Chem. Soc.* **135**, 17818–17830 (2013).
6. Giri, N. *et al.* Liquids with permanent porosity. *Nature* **527**, 216 (2015).
7. Sturluson, A., Huynh, M. T., York, A. H. P. & Simon, C. M. Eigencages: learning a latent space of porous cage molecules. *ACS Cent. Sci.* **4**, 1663–1676 (2018).
8. Jelfs, K. E. & Cooper, A. I. Molecular simulations to understand and to design porous organic molecules. *Curr. Opin. Solid State Mater. Sci.* **17**, 19–30 (2013).
9. Little, M. A. & Cooper, A. I. The chemistry of porous organic molecular materials. *Adv. Funct. Mater.* 1909842 (2020) doi:10.1002/adfm.201909842.
10. Chen, L. *et al.* Separation of rare gases and chiral molecules by selective binding in porous organic cages. *Nat Mater* **13**, 954–960 (2014).
11. Mitra, T. *et al.* Molecular shape sorting using molecular organic cages. *Nat. Chem.* **5**, 276–281 (2013).

12. Hasell, T. *et al.* Porous organic cages for sulfur hexafluoride separation. *J. Am. Chem. Soc.* **138**, 1653–1659 (2016).
13. Liu, M. *et al.* Barely porous organic cages for hydrogen isotope separation. *Science* **366**, 613–620 (2019).
14. Nunes, S. P. & Peinemann, K.-V. *Membrane technology: in the chemical industry*. (John Wiley & Sons, 2006).
15. Kim, D., Salazar, O. R. & Nunes, S. P. Membrane manufacture for peptide separation. *Green Chem.* **18**, 5151–5159 (2016).
16. Marchetti, P., Jimenez Solomon, M. F., Szekely, G. & Livingston, A. G. Molecular separation with organic solvent nanofiltration: A critical review. *Chemical Reviews* vol. 114 10735–10806 (2014).
17. Elimelech, M. & Phillip, W. A. The future of seawater desalination: energy, technology, and the environment. *Science* **333**, 712–717 (2011).
18. Shannon, M. A. *et al.* Science and technology for water purification in the coming decades. *Nature* vol. 452 301–310 (2008).
19. Wang, Y., Zhu, J., Huang, H. & Cho, H. H. Carbon nanotube composite membranes for microfiltration of pharmaceuticals and personal care products: Capabilities and potential mechanisms. *J. Memb. Sci.* **479**, 165–174 (2015).
20. Sholl, D. S. & Lively, R. P. Seven chemical separations to change the world. *Nat. News* **532**, 435 (2016).
21. Elimelech, M. & Phillip, W. A. The future of seawater desalination: Energy, technology, and the environment. *Science* vol. 333 712–717 (2011).
22. Park, H. B., Kamcev, J., Robeson, L. M., Elimelech, M. & Freeman, B. D. Maximizing the right stuff: The trade-off between membrane permeability and selectivity. *Science* vol. 356 1138–1148 (2017).
23. Koros, W. J. & Zhang, C. Materials for next-generation molecularly selective synthetic membranes. *Nat. Mater.* **16**, 289–297 (2017).
24. Kabay, N., Arda, M., Trochimczuk, A. & Streat, M. Removal of chromate by solvent impregnated resins (SIRs) stabilized by coating and chemical crosslinking. I. Batch-

- mode sorption studies. *React. Funct. Polym.* **59**, 9–14 (2004).
25. Jiang, Z., Karan, S. & Livingston, A. G. Water transport through ultrathin polyamide nanofilms used for reverse osmosis. *Adv. Mater.* **30**, 1705973 (2018).
  26. Cundy, C. S. & Cox, P. A. The hydrothermal synthesis of zeolites: Precursors, intermediates and reaction mechanism. *Microporous Mesoporous Mater.* **82**, 1–78 (2005).
  27. Thomas, A. Functional materials: from hard to soft porous frameworks. *Angew. Chemie Int. Ed.* **49**, 8328–8344 (2010).
  28. Furukawa, H., Cordova, K. E., O’Keeffe, M. & Yaghi, O. M. The chemistry and applications of metal-organic frameworks. *Science* **341**, 1230444 (2013).
  29. Côté, A. P. *et al.* Porous, crystalline, covalent organic frameworks. *Science* **310**, 1166–1170 (2005).
  30. Lin, R.-B. *et al.* Multifunctional porous hydrogen-bonded organic framework materials. *Chem. Soc. Rev.* **48**, 1362–1389 (2019).
  31. Dey, K. *et al.* Selective molecular separation by interfacially crystallized covalent organic framework thin films. *J. Am. Chem. Soc.* **139**, 13083–13091 (2017).
  32. Matsumoto, M. *et al.* Lewis-acid-catalyzed interfacial polymerization of covalent organic framework films. *Chem* **4**, 308–317 (2018).
  33. Corcos, A. R. *et al.* Reducing the pore size of covalent organic frameworks in thin-film composite membranes enhances solute rejection. *ACS Mater. Lett.* **1**, 440–446 (2019).
  34. Zhang, C., Wu, B.-H., Ma, M.-Q., Wang, Z. & Xu, Z.-K. Ultrathin metal/covalent-organic framework membranes towards ultimate separation. *Chem. Soc. Rev.* **48**, 3811–3841 (2019).
  35. Wang, Z., Zhang, S., Chen, Y., Zhang, Z. & Ma, S. Covalent organic frameworks for separation applications. *Chem. Soc. Rev.* **49**, 708–735 (2020).
  36. Venna, S. R. & Carreon, M. A. Metal organic framework membranes for carbon dioxide separation. *Chem. Eng. Sci.* **124**, 3–19 (2015).
  37. Fenton, J. L., Burke, D. W., Qian, D., Cruz, M. O. de la & Dichtel, W. R. Polycrystalline covalent organic framework films act as adsorbents, not membranes. *J. Am. Chem. Soc.*



- 143**, 1466–1473 (2021).
38. Song, Q. *et al.* Porous organic cage thin films and molecular-sieving membranes. *Adv. Mater.* **28**, 2629–2637 (2016).
  39. Brutschy, M., Schneider, M. W., Mastalerz, M. & Waldvogel, S. R. Porous organic cage compounds as highly potent affinity materials for sensing by quartz crystal microbalances. *Adv. Mater.* **24**, 6049–6052 (2012).
  40. Hasell, T., Zhang, H. & Cooper, A. I. Solution-processable molecular cage micropores for hierarchically porous materials. *Adv. Mater.* **24**, 5732–5737 (2012).
  41. Bushell, A. F. *et al.* Nanoporous organic polymer/cage composite membranes. *Angew. Chemie Int. Ed.* **52**, 1253–1256 (2013).
  42. Zhu, G., O’Nolan, D. & Lively, R. P. Molecularly mixed composite membranes: challenges and opportunities. *Chem. – A Eur. J.* **26**, 3464–3473 (2020).
  43. Alexandre, P.-E. *et al.* A Robust Porous Quinoline Cage: Transformation of a [4+6] Salicylimine Cage by Povarov Cyclization. *Angew. Chemie Int. Ed.* **59**, 19675–19679 (2020).
  44. Mastalerz, M., Schneider, M. W., Oppel, I. M. & Presly, O. A Salicylbisimine Cage Compound with High Surface Area and Selective CO<sub>2</sub>/CH<sub>4</sub> Adsorption. *Angew. Chemie Int. Ed.* **50**, 1046–1051 (2011).
  45. Elbert, S. M. *et al.* Shape-Persistent Tetrahedral [4+6] Boronic Ester Cages with Different Degrees of Fluoride Substitution. *Chem. – A Eur. J.* **24**, 11438–11443 (2018).
  46. Avellaneda, A. *et al.* Kinetically Controlled Porosity in a Robust Organic Cage Material. *Angew. Chemie Int. Ed.* **52**, 3746–3749 (2013).
  47. Ding, H. *et al.* Targeted synthesis of a large triazine-based [4+6] organic molecular cage: Structure, porosity and gas separation. *Chem. Commun.* **51**, 1976–1979 (2015).
  48. Hasell, T., Chong, S. Y., Jelfs, K. E., Adams, D. J. & Cooper, A. I. Porous organic cage nanocrystals by solution mixing. *J. Am. Chem. Soc.* **134**, 588–598 (2012).
  49. Focher, B., Naggi, A., Torri, G., Cosani, A. & Terbojevich, M. Structural differences between chitin polymorphs and their precipitates from solutions—evidence from CP-MAS <sup>13</sup>C-NMR, FT-IR and FT-Raman spectroscopy. *Carbohydr. Polym.* **17**, 97–102

- (1992).
50. Gillet, P., Le Cléac'h, A. & Madon, M. High-temperature raman spectroscopy of SiO<sub>2</sub> and GeO<sub>2</sub> Polymorphs: Anharmonicity and thermodynamic properties at high-temperatures. *J. Geophys. Res. Solid Earth* **95**, 21635–21655 (1990).
  51. Phillippi, C. M. & Mazdiyasi, K. S. Infrared and Raman spectra of zirconia polymorphs. *J. Am. Ceram. Soc.* **54**, 254–258 (1971).
  52. Pierce, J. Colour in textile effluents-the origins of the problem. *J. Soc. Dye. Colour.* **110**, 131–133 (2008).
  53. Laing, I. G. The impact of effluent regulations on the dyeing industry. *Rev. Prog. Color. Relat. Top.* **21**, 56–71 (2008).
  54. de Lima, R. O. A. *et al.* Mutagenic and carcinogenic potential of a textile azo dye processing plant effluent that impacts a drinking water source. *Mutat. Res. Toxicol. Environ. Mutagen.* **626**, 53–60 (2007).
  55. De Aragão Umbuzeiro, G. *et al.* The contribution of azo dyes to the mutagenic activity of the Cristais River. *Chemosphere* **60**, 55–64 (2005).
  56. Mazzo, T. M., Saczk, A. A., Umbuzeiro, G. A. & Zanoni, M. V. B. Analysis of aromatic amines in surface waters receiving wastewater from a textile industry by liquid chromatographic with electrochemical detection. *Anal. Lett.* **39**, 2671–2685 (2006).
  57. Robinson, T., McMullan, G., Marchant, R. & Nigam, P. Remediation of dyes in textile effluent: a critical review on current treatment technologies with a proposed alternative. *Bioresour. Technol.* **77**, 247–255 (2001).
  58. David R. Lide. CRC handbook of chemistry and physics: A ready-reference of chemical and physical data, 85th edition. *J. Am. Chem. Soc.* **127**, 4542–4542 (2005).
  59. C. M. Hansen. Hansen solubility parameters: A user's handbook, Second edition. *CRC Press, Boca Raton, FL* (2007).
  60. J. A. Riddick, W. B. Bunger & T. L. Bunger. Organic solvents, Third edition. *J. Pharm. Sci.* **60**, 1112 (1971).
  61. B. E. Poling, J. M. Prausnitz, J. P. O. Properties of gases and liquids, Fifth edition. *McGraw-Hill Education, London* (2001).
  62. Van Der Bruggen, B., Schaep, J., Wilms, D. & Vandecasteele, C. Influence of molecular

- size, polarity and charge on the retention of organic molecules by nanofiltration. *J. Memb. Sci.* **156**, 29–41 (1999).
63. Korson, L., Drost-Hansen, W. & Millero, F. J. Viscosity of water at various temperatures. *J. Phys. Chem.* **73**, 34–39 (1969).
  64. Buekenhoudt, A. *et al.* Unravelling the solvent flux behaviour of ceramic nanofiltration and ultrafiltration membranes. *J. Memb. Sci.* **439**, 36–47 (2013).
  65. Aminabhavi, T. M., Patil, V. B., Aralaguppi, M. L. & Phayde, H. T. S. Density, viscosity, and refractive index of the binary mixtures of cyclohexane with hexane, heptane, octane, nonane, and decane at (298.15, 303.15, and 308.15) K. *J. Chem. Eng. Data* **41**, 521–525 (1996).
  66. Jones, J. T. A. *et al.* Modular and predictable assembly of porous organic molecular crystals. *Nature* **474**, 367 (2011).
  67. Briggs, M. *et al.* Dynamic flow synthesis of porous organic cages. *Chem. Commun.* **51**, 17390–17393 (2015).
  68. Carta, M. *et al.* An Efficient Polymer Molecular Sieve for Membrane Gas Separations. *Science* **339**, 303–307 (2013).
  69. Chowdhury, M. R., Steffes, J., Huey, B. D. & McCutcheon, J. R. 3D printed polyamide membranes for desalination. *Science* **361**, 682–686 (2018).
  70. Lianchao, L., Baoguo, W., Huimin, T., Tianlu, C. & Jiping, X. A novel nanofiltration membrane prepared with PAMAM and TMC by in situ interfacial polymerization on PEK-C ultrafiltration membrane. *J. Memb. Sci.* **269**, 84–93 (2006).

# Chapter 4

## **A Smart, Responsive Crystalline Porous Organic Cage Membrane with Switchable Pore Apertures for Graded Molecular Sieving**

Some of the contents in this chapter are taken from the paper:

“A Smart and Responsive Crystalline Porous Organic Cage Membrane with Switchable Pore Apertures for Graded Molecular Sieving”, *Nature Materials* **21**, 463–470 (2022)

[Ai He](#), Zhiwei Jiang, Yue Wu, Hadeel Hussain, Jonathan Rawle, Michael E. Briggs, Marc A. Little, Andrew G. Livingston\*, Andrew I. Cooper\*

## 4.1 Background and Introduction

Many practically important molecular separations involve ternary systems or more complex mixtures—in general, the separation of multiple hydrocarbon fractions from crude oil by distillation<sup>1</sup>, pervaporation or organic solvent reverse osmosis<sup>2,3</sup>, sieving out by-products from reactions or the removal of numerous impurities from a pharmaceutical product by chromatography using solvent gradients<sup>4</sup>, for example in the liquid phase peptide synthesis of pharmaceuticals<sup>5</sup>. One of the practical examples is the purification of fatty acids<sup>6,7</sup>, such as the recovery of omega-3 polyunsaturated fatty acids from fish oil by nanofiltration<sup>8</sup>.

To achieve equivalent separations from complex mixtures using membranes, cascades of membranes with graded molecular weight cut-offs have been developed<sup>1</sup>, using phase inversion (polymeric membranes)<sup>9</sup> or sol-gel processing (ceramic membranes)<sup>10</sup> by manipulating the receipt of dope solution or fabrication conditions to produce multiple membranes with a variety of pore sizes. This places membranes at a disadvantage for ternary and higher separations—whereas a single distillation or chromatography column can produce multiple fractions with differing compositions. Separating more than binary solute systems using a membrane cascade requires multiple pumped recycle streams and complex fluid controls<sup>11</sup>. While solvent gradients are used with significant effect in chromatography to modulate solid-liquid interactions, there are as yet no reports of membranes that respond to solvent gradients by changing their solute selectivity.

The guest selectively can be controlled and altered if the membrane material itself has switchable porosity. Herein porous organic cages (POCs) exhibit two advantages: they are solution-processable, and their solid-state structures are defined by non-covalent intermolecular interactions. Consequently, POC structures can be controlled using a range of post-synthesis crystal design strategies<sup>12</sup>. Thus they can novelly offer the possibility of introducing tunable porosity or even smart, switchable porosity.

A unique property of POCs is that their bulk materials properties can be altered by directing the discrete, solution-processable components to pack in different polymorphic forms<sup>13</sup>. Furthermore, because POC crystals are modular, structure transformations have been used to switch their crystal packings and alter their solid state functions<sup>14,15</sup>. For example, the non-covalent solid-state structures of POCs crystal can be switched using chemical stimuli to alter their bulk porosity<sup>14,15</sup>.

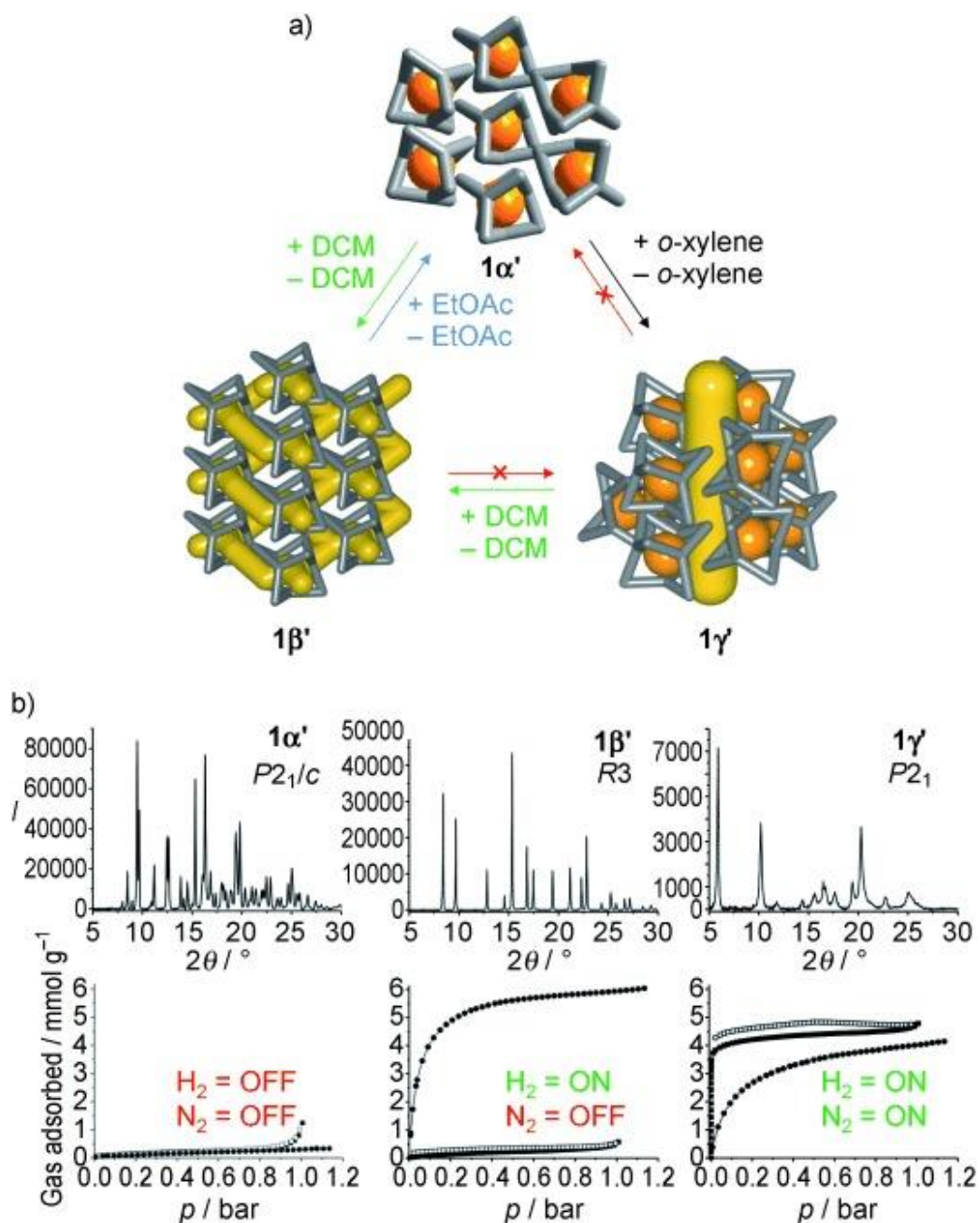


**Figure 4.1** Example of CCI switching its packing in DCM and *o*-xylene, which changes its sorption properties. (a) Scheme of solid-state “on–off” porosity switching. (b) Powder XRD patterns and gas sorption for the bulk materials after guest removal. Reprinted from *Angew. Chemie Int. Ed.* 2011, **50**, 749–753<sup>15</sup>. Copyright 2011, with permission from *Angewandte Chemie International Edition*.

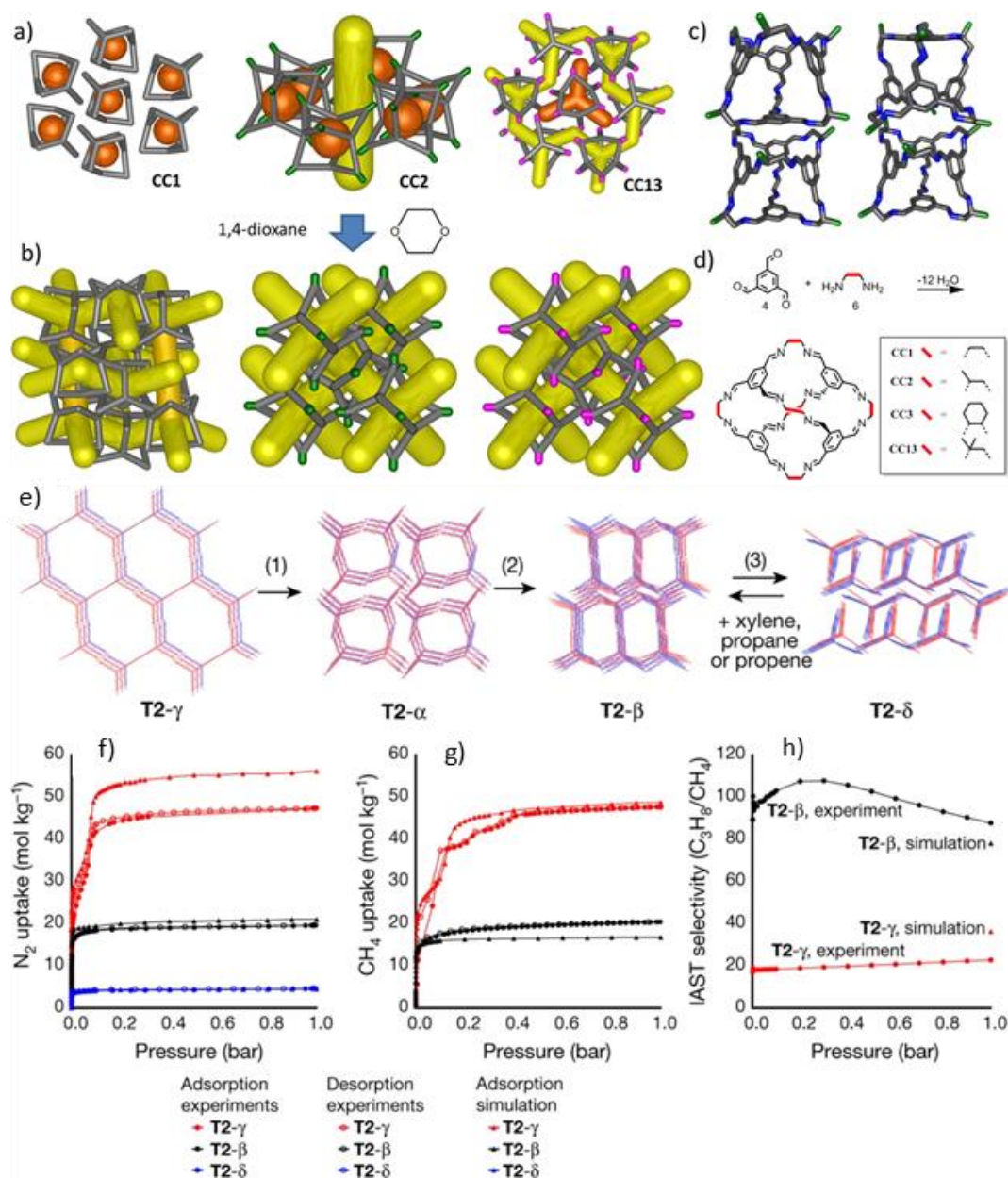


**Figure 4.2** Polymorph transformation of **CCI**, **CC2**, **CC13** examples (a)-(d), and **T2** example (e)-(h). (a)-(d) Schematic low-energy crystal packings for **CCI**, **CC2**, and **CC13**, and crystallisation in the presence of 1,4-dioxane causes 3-dimensional diamondoid pore structure of **CC3**. Reprinted from *J. Am. Chem. Soc.* 2014, 136, 1438–1448<sup>16</sup>. Copyright 2014, with permission from the American Chemical Society. (e)-(h) Overlays of predicted (red) and experimental (blue) structures for **T2-γ**, **T2-α**, **T2-β** and **T2-δ**, their gas adsorption isotherms and pressure-dependent selectivity. Reprinted from *Nature* 2017, 543, 657–664<sup>17</sup>. Copyright 2017, with permission from Springer Nature.

Meanwhile, the [4+6] imine POC, **CC1**, was crystallised from ethyl acetate and found to switch its packing in dichloromethane (DCM) and ortho-xylene, which then changed its sorption



properties<sup>15</sup>. As exposure of its nonporous phase, **CC1** $\alpha'$ , to different trigger molecules directs the structure into one of two porous forms, **CC1** $\beta'$  and **CC1** $\gamma'$ , this was used to on-off cycle its porosity to H<sub>2</sub> (**Figure 4.1**). A followed-up study showed that tetrahedral **CC1**, **CC2** and **CC13** molecules show 2-dimensional layered pore structure with formally disconnected voids, and could transfer to 3-dimensional interpenetrating pore network in the presence of 1,4-dioxane<sup>16</sup>. In this case, a large increase in porosity has been achieved by a simply solvent-directed control over crystal packing rather than by increasing the size of the cage modules themselves (**Figure 4.2**).

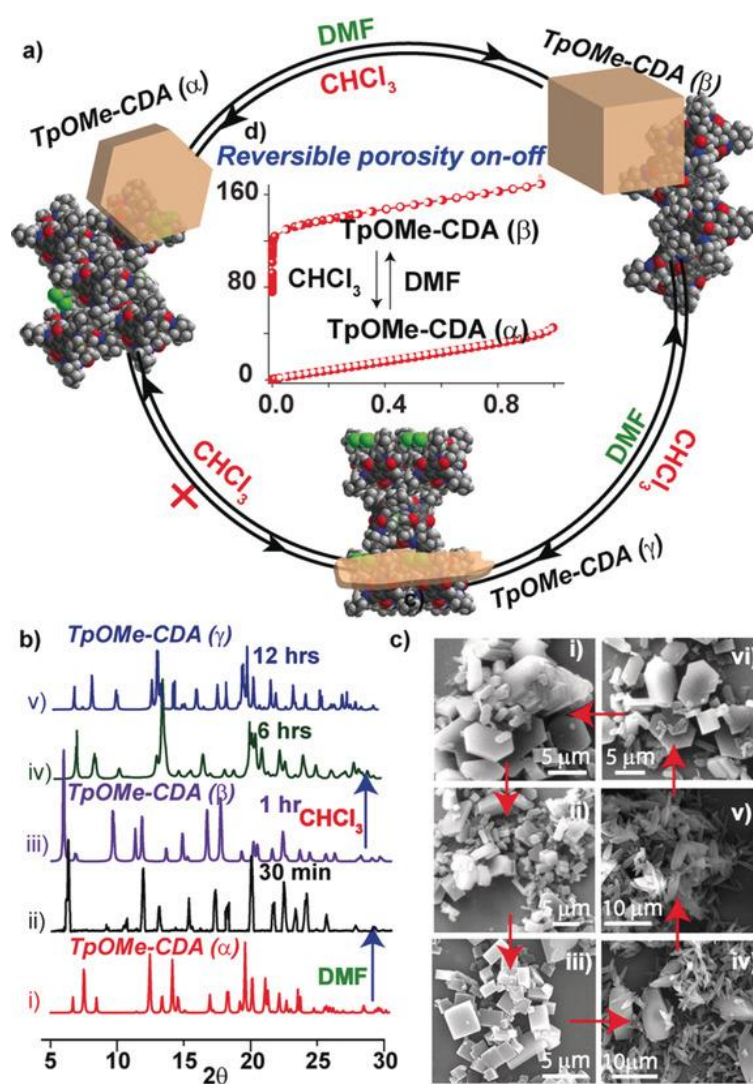


**Figure 4.3** Representation of the reversible conversion and morphological diversity in the **TpOMe-CDA** polymorphs. (a) Morphological conversion is represented in a reversible cyclic manner. (b) The PXRD profiles and (c) FESEM images of **TpOMe-CDA** polymorphs. Reprinted from *Angew. Chemie Int. Ed.* 2019, **58**, 4243–4247<sup>14</sup>. Copyright 2019, with permission from *Angewandte Chemie International Edition*.



Benzimidazolone **T2** has been reported to keep its hexagonal **T2- $\gamma$**  phase while crystallised from dimethyl sulfoxide/acetone, and this polymorph transforms back to a solvate of **T2- $\beta$**  upon exposure to xylene, propane or propene, and thus presents a different porosity to  $N_2$  and  $CH_4$  (**Figure 4.2**)<sup>17</sup>. Another [4+6] imine-linked cage (**TpOMe-CDA**, synthesised by 2,4,6-trimethoxy-1,3,5-triformyl benzene (**TpOMe**) and 1,2-diaminocyclohexane (**CDA**)) retains its structure to the thermodynamically stable polymorph, **TpOMe-CDA ( $\alpha$ )** phase, in many organic solvents (acetone, methanol, tetrahydrofuran, 1,4-dioxane, and ethyl acetate), but exhibits reversible porosity on-off for  $N_2$  uptake with the polymorphic conversion to **TpOMe-CDA ( $\beta$ )** phase by *N,N*-dimethylformamide and **TpOMe-CDA ( $\gamma$ )** phase by chloroform (**Figure 4.3**)<sup>14</sup>.

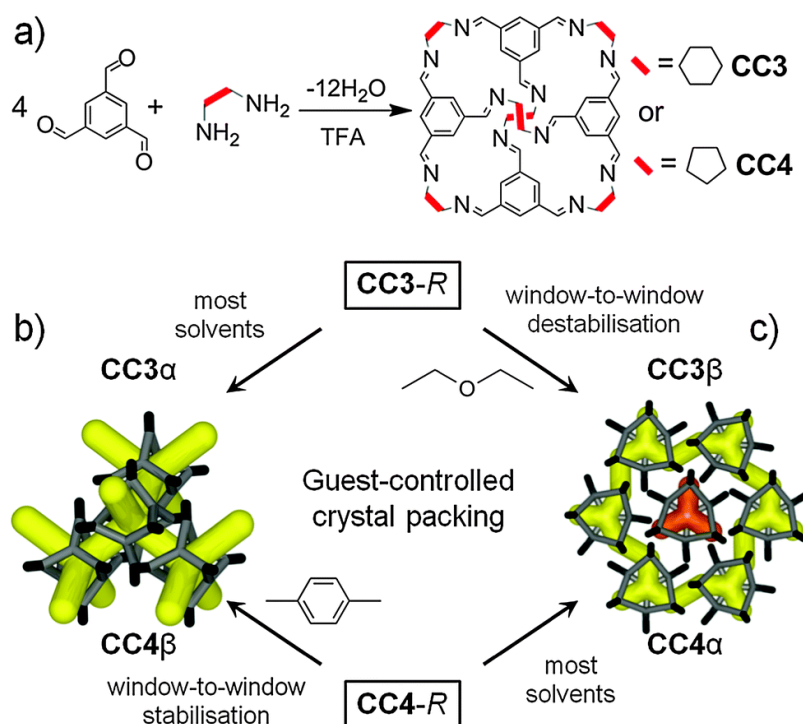


**Figure 4.4** (a) Synthesis of organic cage molecules **CC3** and **CC4**. Scheme showing interchangeable crystal packings for cages **CC3** and **CC4**; (b) 3-D diamondoid pore channels; and (c) 2-D layered pore structure with formally disconnected voids. Orange = disconnected voids; yellow = interconnected pores. Reprinted from *Chem. Commun.*, 2014, **50**, 9465-9468<sup>18</sup>. Copyright 2014, with permission from the Royal Society of Chemistry.

As such, POCs are intriguing and relatively unexplored candidates for producing new types of membrane material with tunable porosity, or even new types of membranes with switchable, ‘on/off’ porosity. However, for polymorphic switching of POCs to be associated with changes in bulk sorption properties, access to highly crystalline forms with defined pore structures have been required.

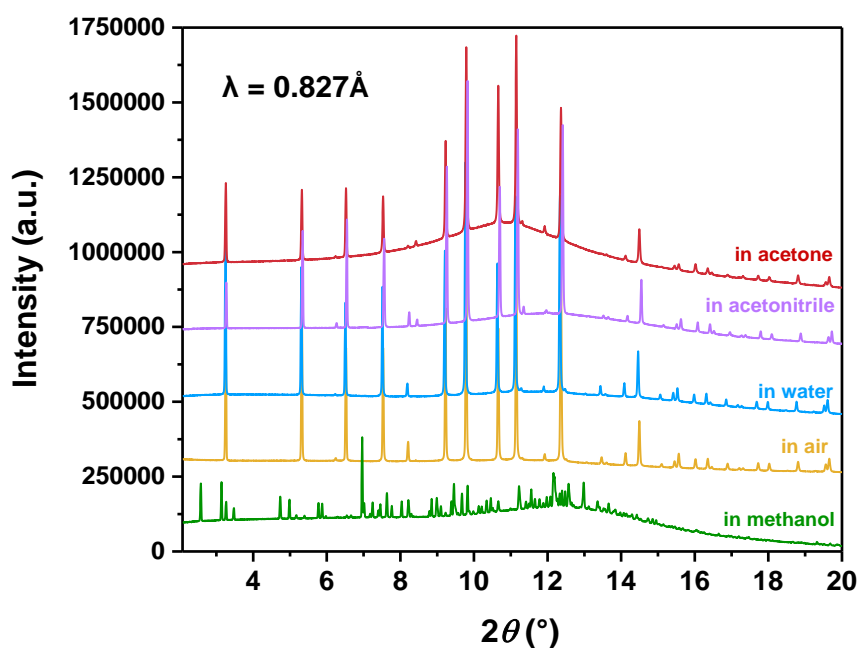
Previous studies have shown that certain POCs can be switched between more than one polymorph to modify the porosity in the materials<sup>14,15</sup>. The solid-state structure of **CC3** has been directed into different polymorphs by crystallisation from specific solvents<sup>18</sup>. For example, as is shown in **Figure 4.4**, **CC3** prefers to pack in a window-to-window arrangement in most solvents, which generates an interconnected diamondoid pore network. This thermodynamic polymorph, **CC3 $\alpha$** , has an apparent Brunauer-Emmett-Teller (BET) surface area ( $S_{\text{ABET}}$ ) of  $\sim 410 \text{ m}^2 \cdot \text{g}^{-1}$  in the crystalline state. These **CC3 $\alpha$**  crystal packing modes can be interchanged by using specific co-solvents, such as diethyl ether, to direct the crystal packing. In this **CC3 $\beta$**  phase, the cage windows pack in a relatively inefficient manner, forming extrinsic cavities into which the methyl termini of the diethyl ether solvent molecules are directed, where **these** extrinsic lattice sites can accommodate additional gas molecules. Therefore, with apparent  $S_{\text{ABET}}$  of  $555 \text{ m}^2 \cdot \text{g}^{-1}$ , the gas uptake ( $\text{N}_2$ ,  $\text{H}_2$ ,  $\text{CO}_2$ ) and porosity for **CC3 $\beta$**  is higher than for **CC3 $\alpha$**  due to its lower density ( $0.922 \text{ g} \cdot \text{cm}^{-3}$  for **CC3 $\beta$**  vs.  $0.973 \text{ g} \cdot \text{cm}^{-3}$  for **CC3 $\alpha$** ). But until now, the solid-state transformation of **CC3** crystals was not explored.

In this chapter, highly crystalline, close-packed and defect-free films of a robust imine POC, **CC3**, have been studied on their tunable porosity / switchable porosity. We were motivated to investigate whether a solvent stimulus could be used to switch the solid-state structure of the **CC3 $\alpha$**  membrane, thus changing the pore aperture and affecting its separation behaviour.

The results presented in this Chapter demonstrate that exposure of the non-covalent crystal packing of **CC3** in methanol (MeOH) induces a rapid phase transformation from **CC3 $\alpha$**  to a different crystalline phase, **CC3 $\gamma'$** , which consists of less densely packed POCs. This transformation systematically increases the effective pore aperture of the resulting membrane, **CC3 $\gamma'$ -PAN**, which allows the permeation of larger organic dyes that were found to have been rejected in water. The difference in selectivity is not a simple swelling effect, but rather a phase transition that can be understood at the atomistic level. Furthermore, this switchable porosity is reversible, and, surprisingly, it does not compromise the continuity of the membrane. Importantly, understanding the dynamic transformation between two solvents enables the manipulation of the pore aperture in a single **CC3-PAN** membrane. Such technology allows us to separate three organic dyes with different sizes continuously from a ternary system via a graded molecular sieving experiment using one single, ‘smart’ membrane.

## 4.2 Solid-state Structural Transformation Study on Cage Membranes

(a)



(b)

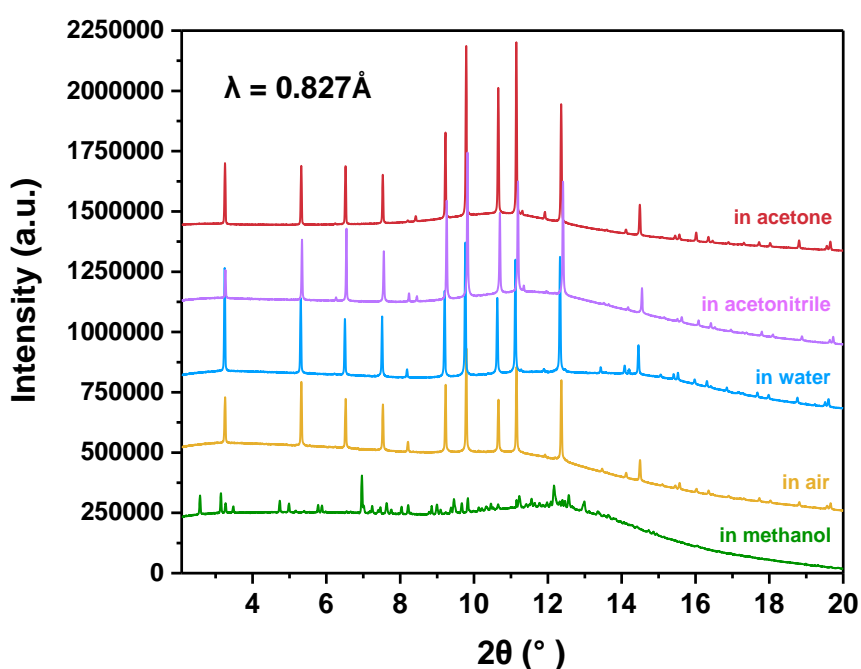


**Figure 4.5** PXRD patterns recorded on (a) bulk grown powders of as-synthesised CC3 $\alpha$  crystals loaded into glass capillaries and then suspended in organic solvents; (b) CC3 $\alpha$  film that was scraped of a glass substrate loaded in glass capillaries and then dispersed in organic solvents. TFB 0.8 wt.% in DCM (30 mL), CHDA 0.8 wt.% in water (32 mL); reaction conditions: 24 hours at room temperature; dish diameter: 7.4 cm. Wavelength:  $\lambda = 0.827 \text{ \AA}$ .

To determine if the solvents could direct **CC3** to pack in different ways in the cage membrane, we have screened the polymorphic forms of **CC3** in other solvents. We started with air-dried **CC3** (i.e., desolvated), and a series of GIXRD patterns were then recorded after submerging the material in various organic solvents, including acetonitrile, acetone, and methanol.

As shown in **Figure 4.5**, both bulk grown powders of as-synthesised **CC3 $\alpha$**  crystals and **CC3 $\alpha$**  film that was scraped of a glass substrate have been measured. These experiments revealed that **CC3** submerged in water, acetone, and acetonitrile had the same structure as the air-dried material. Interestingly, we found that **CC3** transformed into a new structure when submerged in methanol, confirmed by its different GIXRD pattern.

To investigate whether this phase transformation occurred to the pre-fabricated membrane, we set up a series of *in-situ* GIXRD measurements by covering the membrane surface with a thin layer of solvent (water, methanol, acetone, and acetonitrile) during the GIXRD scans (see **Chapter 2** for experimental details). In the GIXRD patterns shown in **Figure 4.6**, we observed that solvating the composite **CC3-PAN** membrane in water, acetone, and acetonitrile caused small shifts of the diffraction peak positions to lower angle positions due to solvent swelling, without significant structural changes to the **CC3 $\alpha$**  phase. However, the **CC3-PAN** membrane exhibited a different structure in methanol, and the structural transformation is consistent with that of the bulk material phase transformation in methanol.

By indexing the GIXRD pattern shown in **Figure 4.7**, we confirmed this was a MeOH-solvated **CC3** phase, referred to hereafter as **CC3 $\gamma'$** , that was isolated previously by crystallising **CC3** from dichloromethane and MeOH<sup>19</sup>.

The **CC3 $\gamma'$**  structure has monoclinic *C2* crystal symmetry and its crystal packing is markedly different from **CC3 $\alpha$** . In its thermodynamically most stable polymorph, **CC3 $\alpha$** <sup>20</sup>, the cage packs in a window-to-window arrangement to generate an interconnected diamondoid pore network (**Figure 4.8 h and i**). By contrast, in the **CC3 $\gamma'$**  phase, hexagonally arranged **CC3** molecules extend this window-to-window pairing, thus generating a 2D honeycomb, solvent-filled virtual pore network running through the intrinsic cage voids (**Figure 4.8 a-c**).

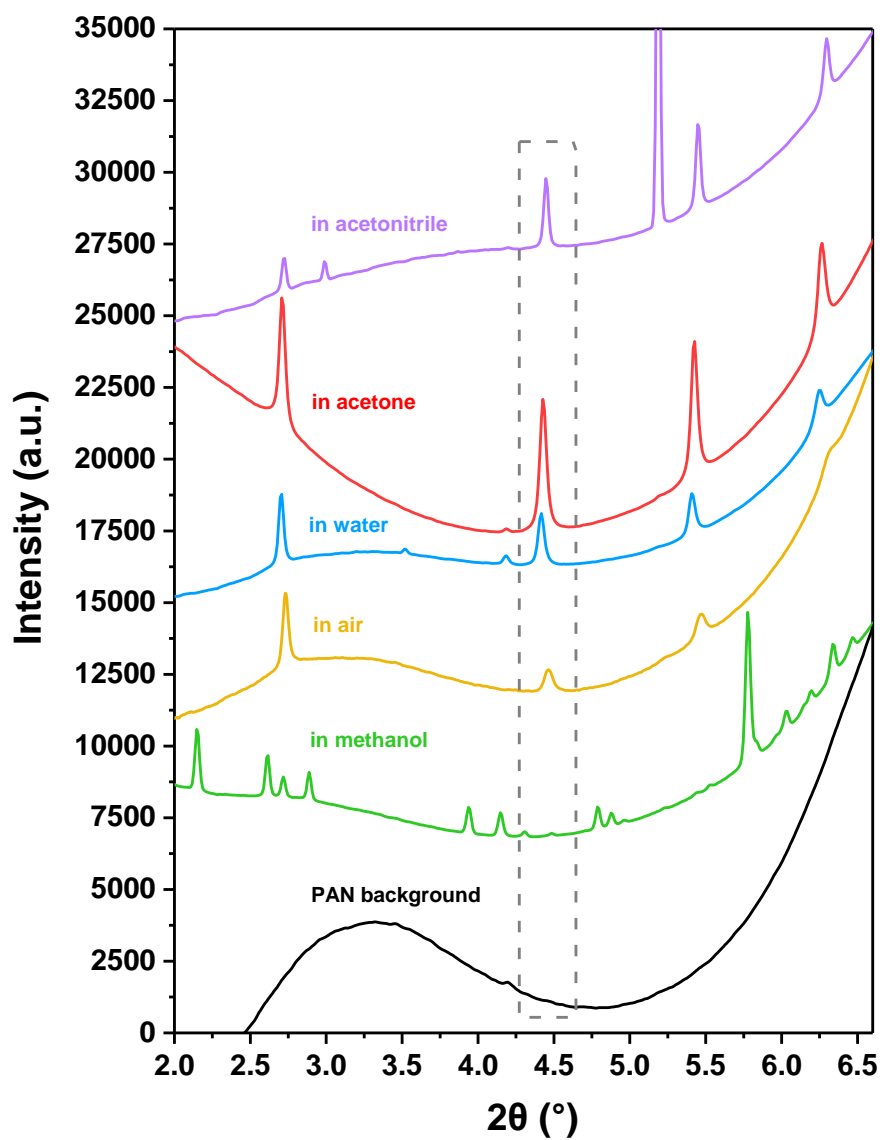
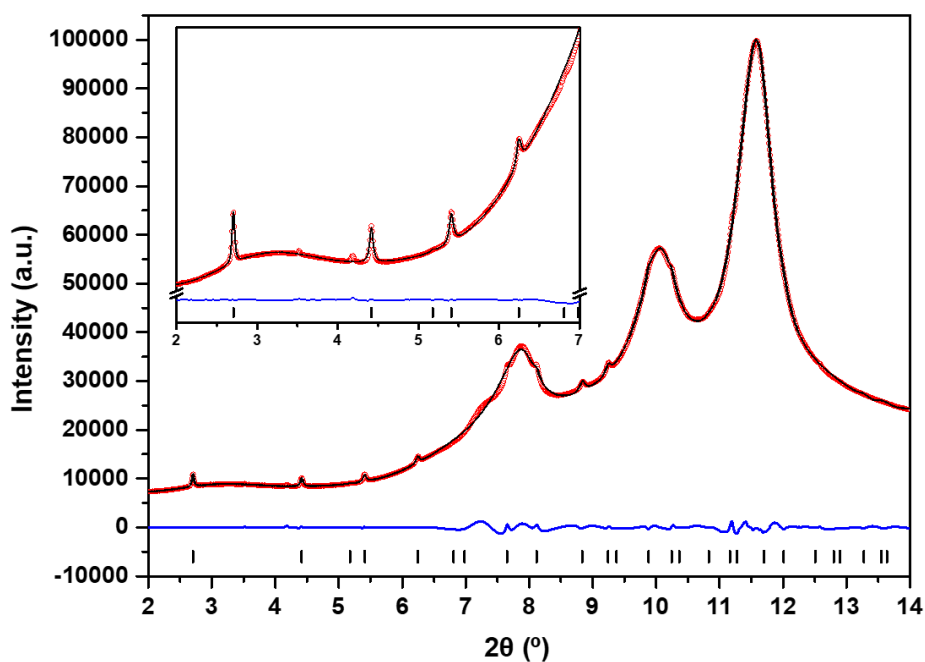


**Figure 4.6** Out-of-plane GIXRD diffraction patterns ( $\lambda = 0.689 \text{ \AA}$ ) that were recorded after coating the surface of CC3 $\alpha$ -PAN-24H-0.8% with different organic solvents. The solvent layer was covered with Mylar film during the measurements.

(a)



(b)

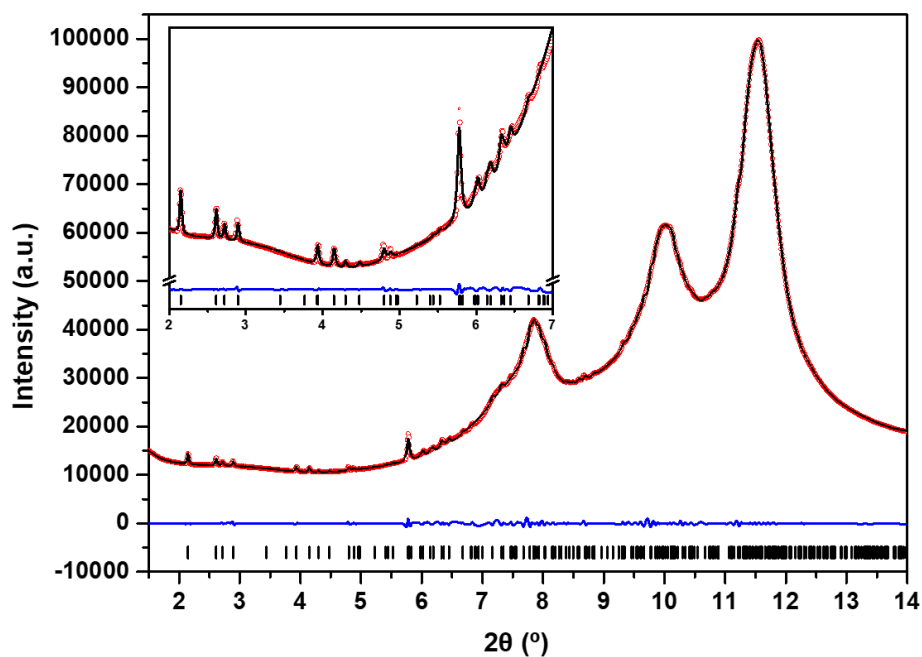


**Figure 4.7** Pawley refinements for out-of-plane GIXRD patterns ( $\lambda = 0.689 \text{ \AA}$ ) of (a)  $\text{CC3}\alpha$ -PAN-24H-0.8% in water ( $R_p = 0.73\%$ ,  $R_{wp} = 1.09\%$ ,  $F4_132$ ,  $a = 25.285 \text{ \AA}$ ,  $V = 16166.4 \text{ \AA}^3$ ), and (b)  $\text{CC3}\gamma'$ -PAN-24H-0.8% in MeOH ( $R_p = 0.47\%$ ,  $R_{wp} = 0.92\%$ ,  $C2$ ,  $a = 27.377 \text{ \AA}$ ,  $b = 20.096 \text{ \AA}$ ,  $c = 21.936 \text{ \AA}$ ,  $\beta = 123.1^\circ$ ,  $V = 10108.4 \text{ \AA}^3$ ). Red circles: experimental PXRD pattern, black line: fitting pattern, blue curve: difference between experimental and refinement, black bars: reflection positions. Copyright © 2022, Springer Nature and Ai He, etc.

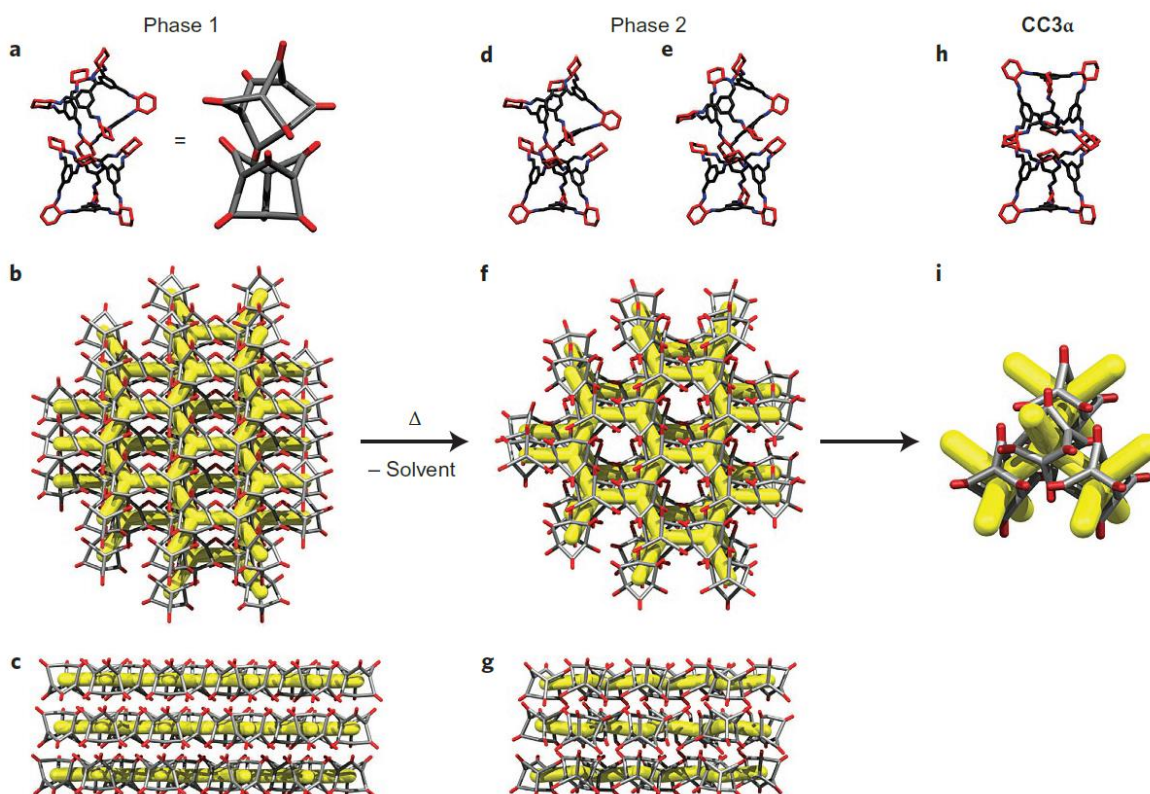


**Figure 4.8** A metastable solvate phase of a porous cage, phase 1 ( $CC3\gamma'$ ), has virtual 2D pores but this transforms over time to a denser phase,  $CC3\alpha$ , with 3D pores. **a**, Representation of the single-crystal structure for  $CC3 \cdot (MeOH)_{12.5} \cdot (H_2O)_3$  (phase 1) showing a window-to-window cage pairing arrangement. **b,c**, Hexagonally arranged  $CC3$  molecules generate a 2D honeycomb, solvent-filled virtual pore network (yellow), shown in here in the perspective views [101] (**b**) and [010] (**c**). **d,e**, Single-crystal structure after heating to remove the solvent to generate  $(CC3)_2$  (phase 2) showing cage-window pairings from crystallographically independent pore networks. **f,g**, 2D honeycomb pore network in the perspective views [001] (**f**) and [010] (**g**). **h,i**, Phase 2 is metastable and transforms easily to the thermodynamic solvent-free polymorph  $CC3\alpha$ , with a 3D pore network. Reprinted from *Nat. Chem.* 2015, 7, 153–159. Copyright 2015, with permission from Springer Nature.

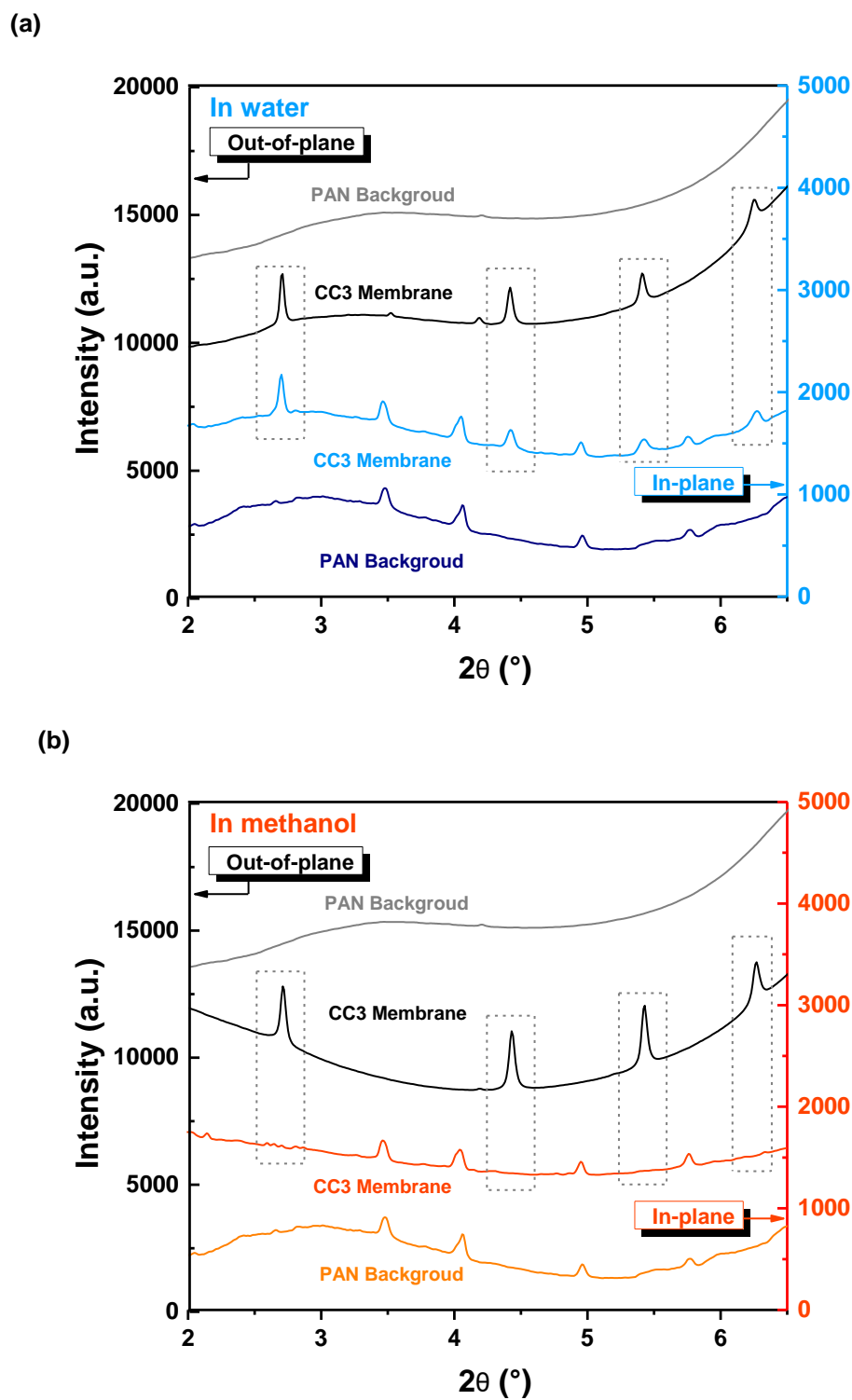


**Figure 4.9** Crystallographic characterisation of cage membranes. The diffraction data collected from beamline I07: (a) out-of-plane and in-plane diffraction data of the blank polymer background and the CC3 membrane in water; (b) out-of-plane diffraction data of the blank polymer background and the CC3 membrane in methanol. Film synthesis condition: concentration: trimethylbenzene (TFB) 0.8 wt. %, (1R,2R)-1,2-cyclohexanediamine (CHDA) 0.8 wt. %; reaction time: 24 h; at room temperature.



Both in-plane and out-of-plane diffractions were recorded during the GIXRD measurements. With a relatively strong background signal from the polyacrylonitrile substrate (peaks correspond to the polyacrylonitrile material<sup>21</sup>), extra peaks were observed and correspond to the crystalline **CC3** membranes. As is shown in **Figure 4.9**, the reflection positions are the same in both in-plane and out-of-plane diffraction while the membrane is immersed in water, indicating that the **CC3** molecules packing in **CC3 $\alpha$**  phase have no preferred orientation; the diffraction patterns for membrane in methanol exhibits reflections for **CC3 $\gamma'$**  phase only in the out-of-plane data, showing no extra peaks from in-plane data.

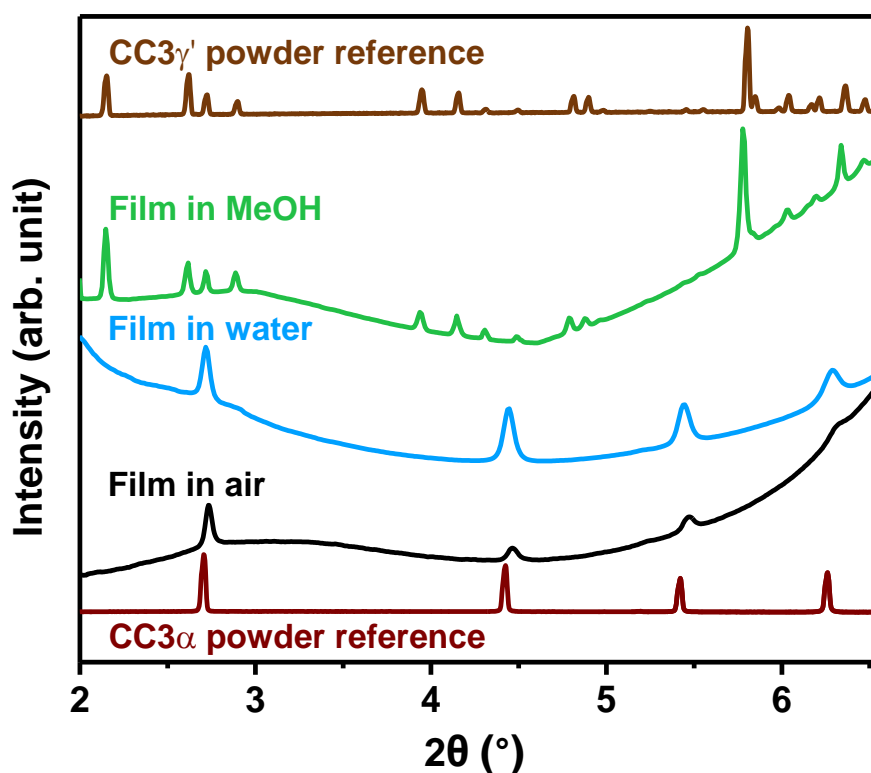


**Figure 4.10** X-ray diffraction characterisation of **CC3-PAN** membranes. GIXRD patterns confirm the structure of **CC3 $\alpha$ -PAN** in air and water, and **CC3 $\gamma'$ -PAN** in MeOH. Experimental PXRD patterns of **CC3 $\alpha$**  and **CC3 $\gamma'$**  powders are included as references.

We have further compared the solid-state switching of the **CC3-PAN** membrane in water and in methanol. As is shown in **Figure 4.10**, we found that both air-dried and water-solvated membranes exhibited the same diffraction patterns as the reference peaks of **CC3 $\alpha$**  powders measured by PXRD, which is referred to hereafter as **CC3 $\alpha$ -PAN**. By contrast, the crystalline **CC3 $\alpha$**  film on the substrate transformed into **CC3 $\gamma'$**  phase when submerged in MeOH, and this is referred to hereafter as **CC3 $\gamma'$ -PAN**, respectively.

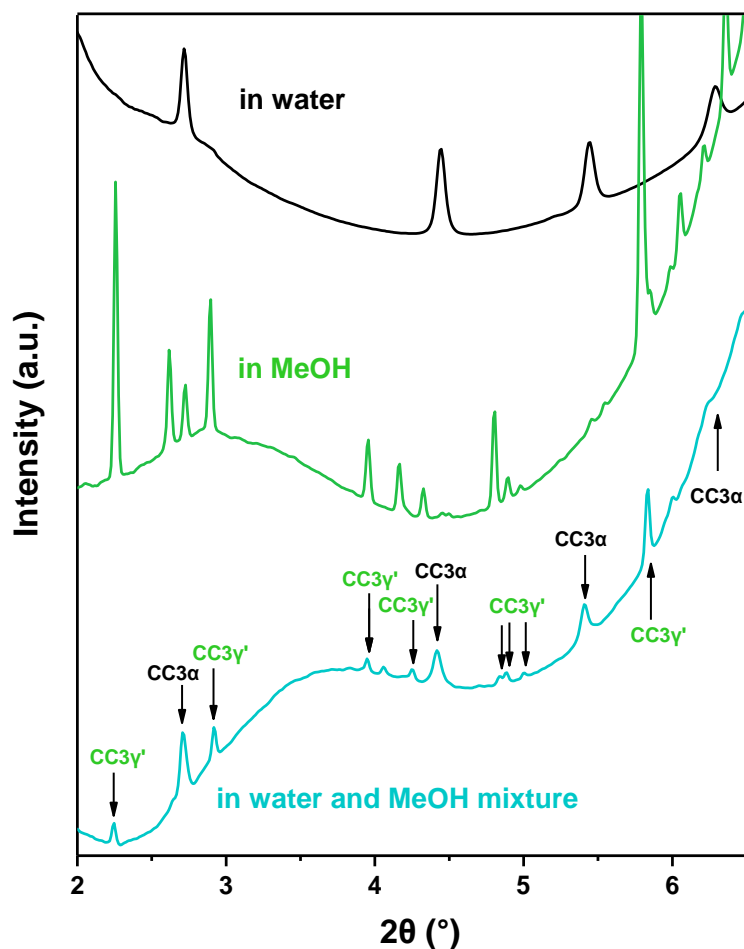


**Figure 4.11** GIXRD characterisation of  $CC3$ -PAN,  $CC3\alpha$ -PAN coated in a layer of water (black),  $CC3\gamma'$ -PAN coated in a layer of MeOH (green),  $CC3\alpha$ -PAN that was immersed in water and then also covered in a MeOH solvent layer (cyan) with the diffraction peaks assigned to  $CC3\alpha$ -PAN and  $CC3\gamma'$ -PAN included in the resulting GIXRD pattern.

To investigate the structural transformation between  $CC3\alpha$ -PAN and  $CC3\gamma'$ -PAN, we performed a series of *in-situ* GIXRD measurements while dosing the membrane surface with solvent vapour and after coating the membrane surface in a thin solvent layer (see **Chapter 2** for full experimental details). As is shown in **Figure 4.11**,  $CC3\gamma'$ -PAN formed when immersed in MeOH and then transformed back into  $CC3\alpha$ -PAN after being submerged in water, with clear evidence of both phases found (marked for each diffraction peak) when the membrane was immersed in a mixture of water and MeOH, or if a small amount of MeOH remained in the sample. **Figure 4.12** indicates that  $CC3\gamma'$ -PAN formed in MeOH gradually transformed

back into  $CC3\alpha$ -PAN while the MeOH vapour evaporated from the membrane at room temperature. By slowly removing the methanol from the environment, the phase transition has been completed, which has been shown as the desolvated  $CC3\alpha$  phase.

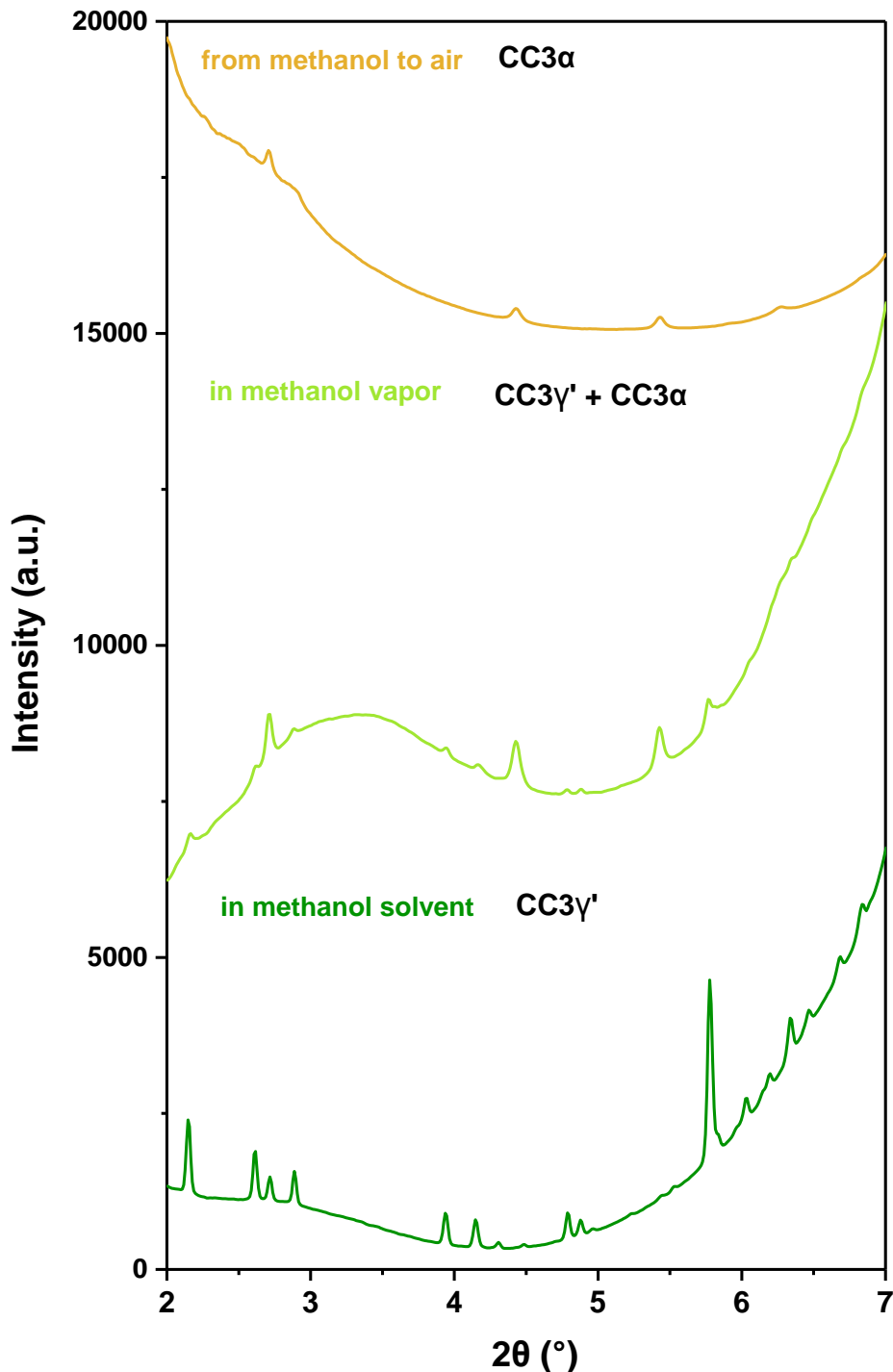


**Figure 4.12** GIXRD characterisation of  $CC3$  membranes,  $CC3\gamma'$ -PAN coated in layer of MeOH solvent (dark green), after exposing  $CC3\alpha$ -PAN to MeOH vapour for 30 minutes, after drying  $CC3\gamma'$ -PAN in air for 30 minutes (orange).

This has been further confirmed by desolvating the **CC3** crystals using variable temperature high-resolution PXRD measurement, where a bulk powdered sample of the **CC3** $\gamma'$  suspended in MeOH in a capillary was gradationally heated (**Figure 4.13**) and powders that were isolated by scraping the **CC3** film from a **CC3**-PAN membrane (**Figure 4.14**). After heating the powdered MeOH solvated **CC3** $\gamma'$  sample to 85–95 °C, it cleanly transformed into **CC3** $\alpha$ , replicating the transformation we observed between **CC3** $\gamma'$ -PAN and **CC3** $\alpha$ -PAN that we attributed to desolvation.

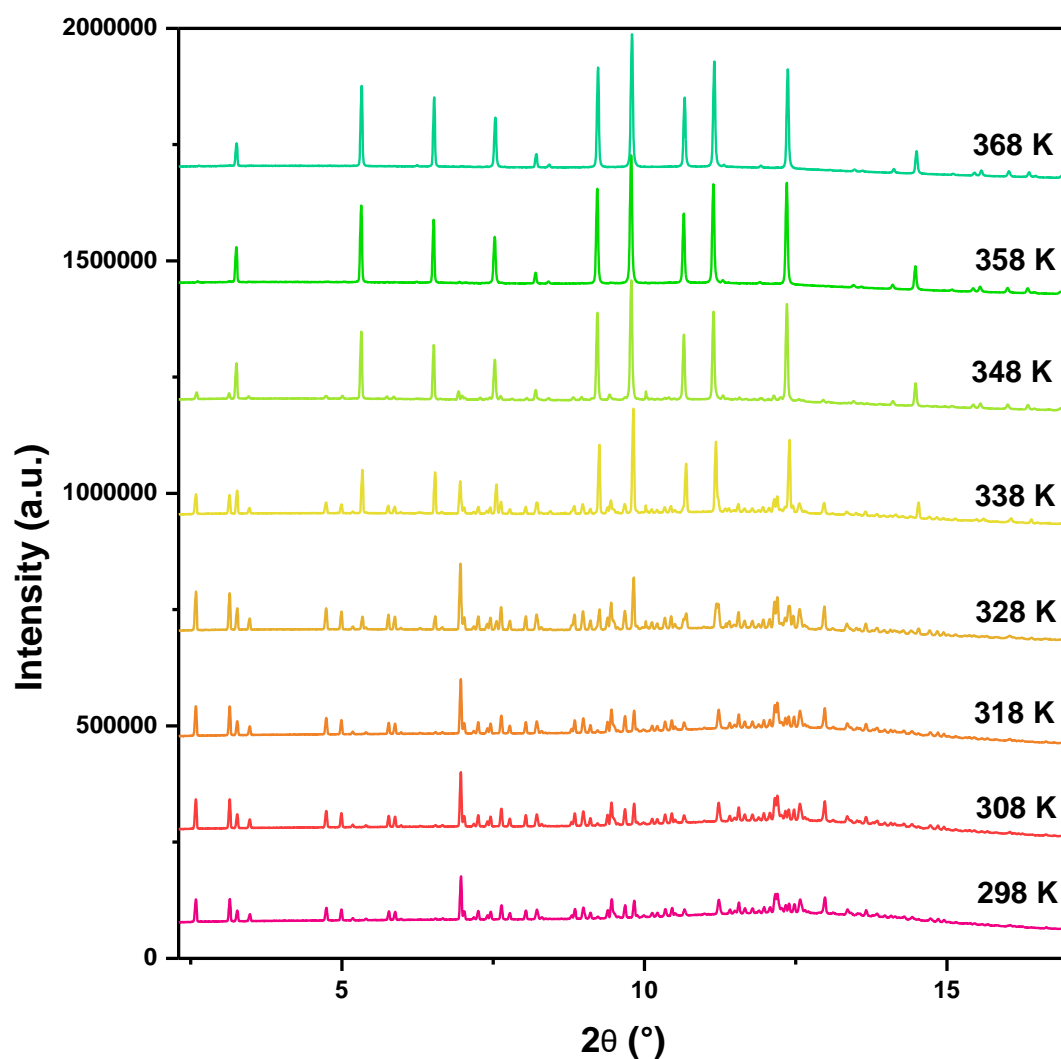


**Figure 4.13** Crystallographic characterisation of bulk crystalline **CC3** solid reference at various temperatures. The diffraction data collected from beamline III.

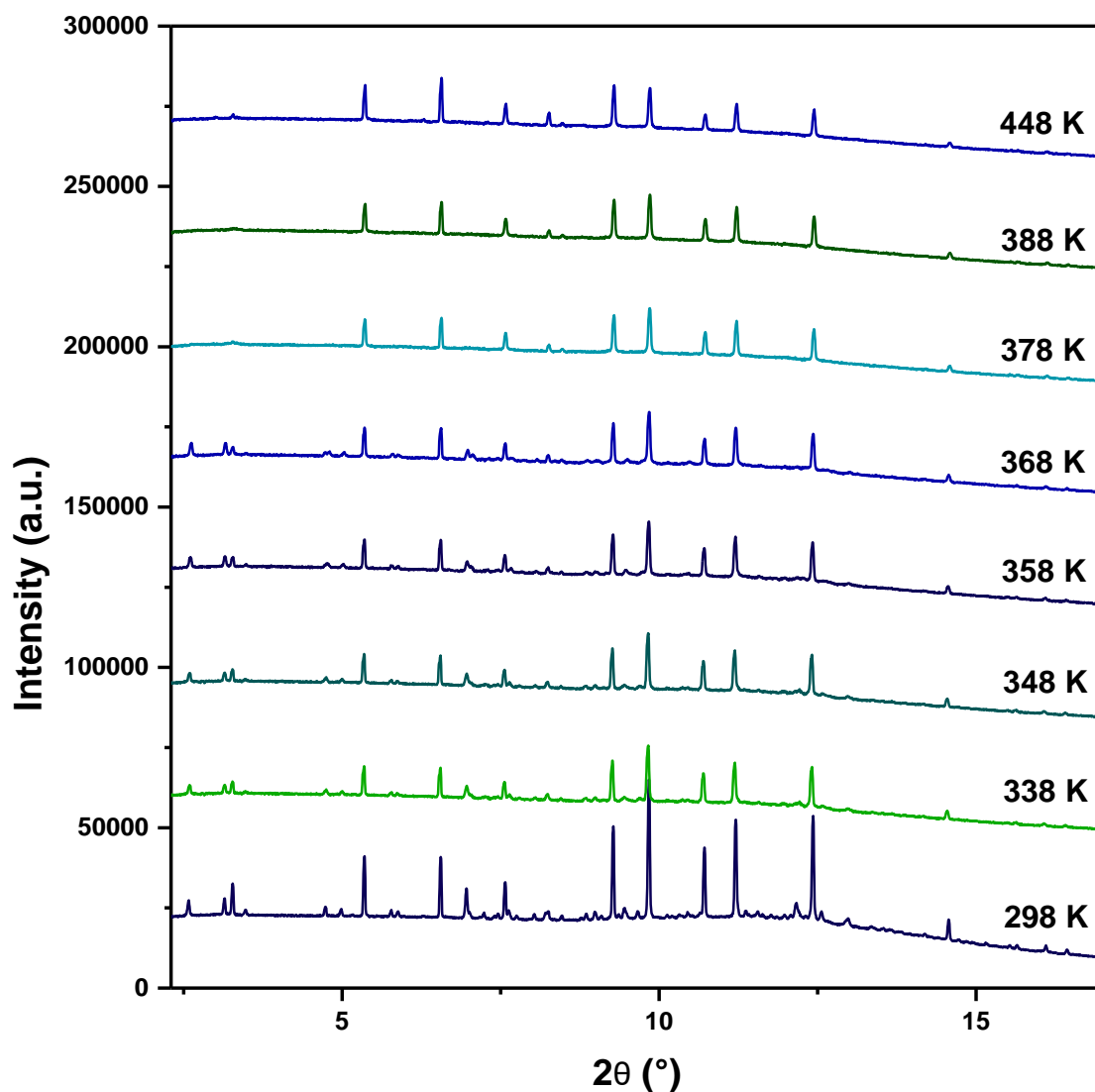
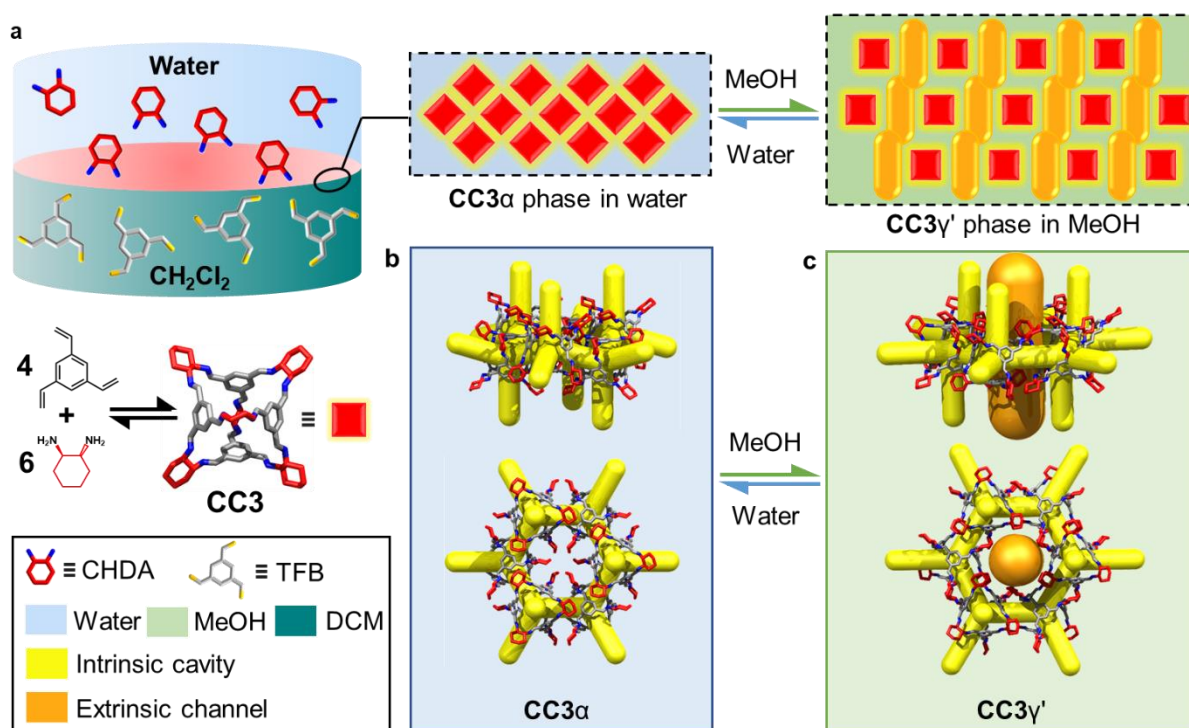


**Figure 4.14** Crystallographic characterisation of cage membranes at various temperatures. The diffraction data collected from beamline I11 on the powders collected from CC3 membranes. Film synthesis condition: concentration: trifmlylbenzene (TFB) 0.8 wt. %, (1R,2R)-1,2-cyclohexanediamine (CHDA) 0.8 wt. %; reaction time: 24 h; at room temperature.

It is essential to prove the structural transformation is reversible for the membrane with methanol and with water, and this enables us to study further whether the pore apertures and separation behaviour of the membrane has been affected.

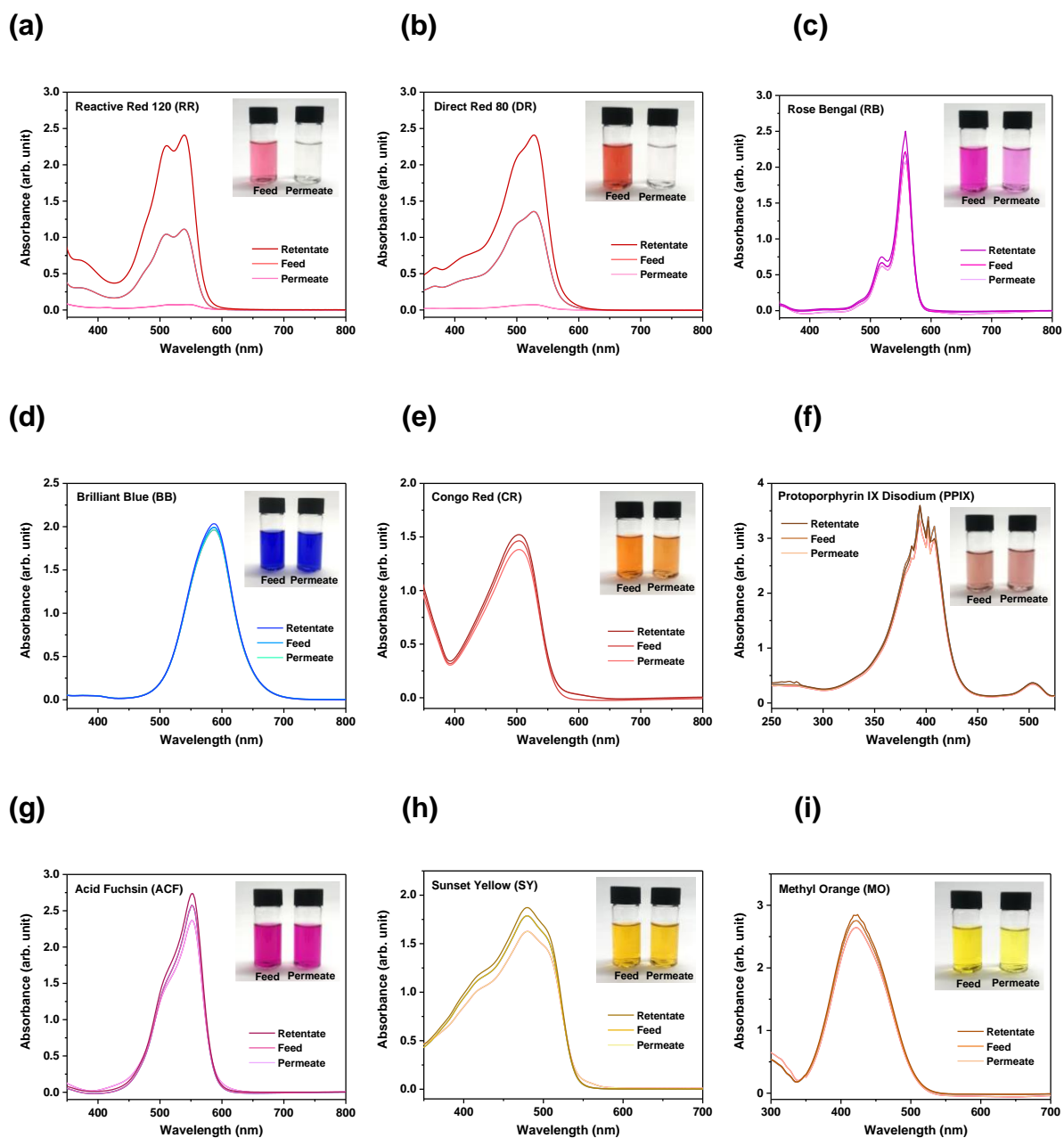
### 4.3 Switchable Pore Aperture with Dye Rejection Study

Continuous crystalline **CC3** films were produced at a water-dichloromethane interface via interfacial condensation reaction and crystallisation process, and the **CC3** composite membrane is designed to exhibit switchable structures in water and in MeOH, based on the evidence of its structural transformation between **CC3 $\alpha$**  and **CC3 $\gamma'$** , as is shown in **Figure 4.15**. In the **CC3 $\alpha$**  phase in water, the cage packs in a window-to-window arrangement to generate an interconnected diamondoid pore network (yellow channels in **Figure 4.15 b**). By contrast, in the **CC3 $\gamma'$**  phase, while in MeOH, the **CC3** molecules are packed in a less dense arrangement, thus providing large extrinsic pores between hexagonally arranged **CC3** molecules (orange channels in **Figure 4.15 c**).



**Figure 4.15** Synthesis of a crystalline **CC3** film and its crystal structures. (a), Scheme showing the interfacial synthesis method used to fabricate crystalline **CC3** films, which were subsequently adhered to polyacrylonitrile (PAN) support. These crystalline cage films can cycle between two different forms, **CC3 $\alpha$ -PAN** and **CC3 $\gamma'$ -PAN**, by cycling the solvent between water and MeOH. CHDA = 1R,2R-cyclohexanediamine; TFB = 1,3,5-triformylbenzene;  $\text{CH}_2\text{Cl}_2$  = dichloromethane. (b), **CC3 $\alpha$**  structure with its 3D pore network shown in yellow. (c), The **CC3 $\gamma'$**  structure, formed by soaking in MeOH, has additional extrinsic solvent-filled channels, shown here in orange, that opens up additional porosity in the membrane in response to the MeOH solvent.

Therefore, the reversible transition between  $CC3\alpha$ -PAN and  $CC3\gamma$ '-PAN is believed to create different diffusion pathways through the membrane structure. To investigate the effect of this structural transformation on permeance and dye rejection, we prepared  $CC3$ -PAN samples and tested the membrane performance.



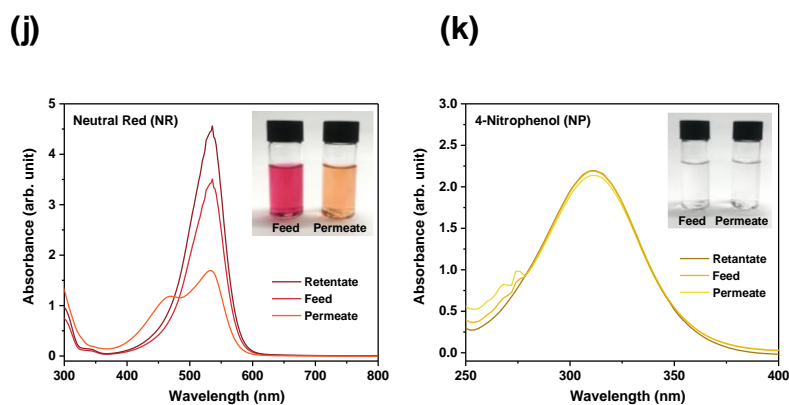


**Figure 4.16** UV absorption spectra of dyes in methanol before and after selectivity tests performed with CC3 $\gamma$ -PAN. Inserts show photographs of the feed and the permeate. Note, NR is a pH indicator, changing from red to yellow between pH 6.8 and 8.0; as the NR permeate was orange in colour the dye concentration was calculated using both yellow and red peaks in the UV absorption spectrum. Copyright © 2022, Springer Nature and Ai He, etc.

**Table 4.1** Dye rejection measurement data for CC3-PAN determined using MeOH feedstocks.

Solvent	Dye	Sample Collected	Volume (mL)	Wavelength <sup>[a]</sup> (nm)	Absorption	Rejection (%)	Ref. Figure
MeOH	RR	Feed	100	540	1.11	92.78 ± 3.10	Figure 4.16 (a)
		Permeate	52	538	0.07		
		Retentate	48	538	2.41		
MeOH	DR	Feed	100	526	1.36	93.02 ± 2.54	Figure 4.16 (b)
		Permeate	52	528	0.07		
		Retentate	48	528	2.42		
MeOH	RB	Feed	100	558	2.21	2.52 ± 2.05	Figure 4.16 (c)
		Permeate	57	558	2.08		
		Retentate	43	558	2.50		
MeOH	BB	Feed	100	588	1.98	0.76 ± 0.26	Figure 4.16 (d)
		Permeate	51	588	1.96		
		Retentate	49	587	2.03		
MeOH	CR	Feed	100	502	1.46		



		Permeate	46	502	1.38	$3.70 \pm 2.47$	Figure 4.16 (e)
		Retentate	54	504	1.52		
MeOH	PPIX	Feed	120	394	3.51	$5.96 \pm 3.41$	Figure 4.16 (f)
		Permeate	55	394	3.33		
		Retentate	65	394	3.60		
MeOH	ACF	Feed	100	552	2.57	$5.21 \pm 3.02$	Figure 4.16 (g)
		Permeate	58	552	2.37		
		Retentate	42	553	2.73		
MeOH	SY	Feed	100	481	1.79	$3.24 \pm 2.63$	Figure 4.16 (h)
		Permeate	59	480	1.63		
		Retentate	41	480	1.87		
MeOH	MO	Feed	100	422	2.76	$4.05 \pm 2.95$	Figure 4.16 (i)
		Permeate	52	422	2.64		
		Retentate	48	424	2.85		
MeOH	NR	Feed	100	534	3.51	$4.82 \pm 3.28$	Figure 4.16 (j)
		Permeate <sup>[b]</sup>	46	536	1.69		
				466	1.18		
		Retentate	54	536	4.56		
MeOH	NP	Feed	100	311	2.14	$2.77 \pm 2.05$	Figure 4.16 (k)
		Permeate	55	312	2.13		
		Retentate	45	310	2.14		

<sup>[a]</sup> Wavelength of maximum absorbance. <sup>[b]</sup> Wavelength of maximum absorbance of the peak at the red colour absorbance (520 nm) and orange colour absorbance (455 nm). As NR is a pH indicator changing from red to yellow between pH 6.8 and 8.0, the dye concentration was calculated using the absorbance of both yellow and red peaks.

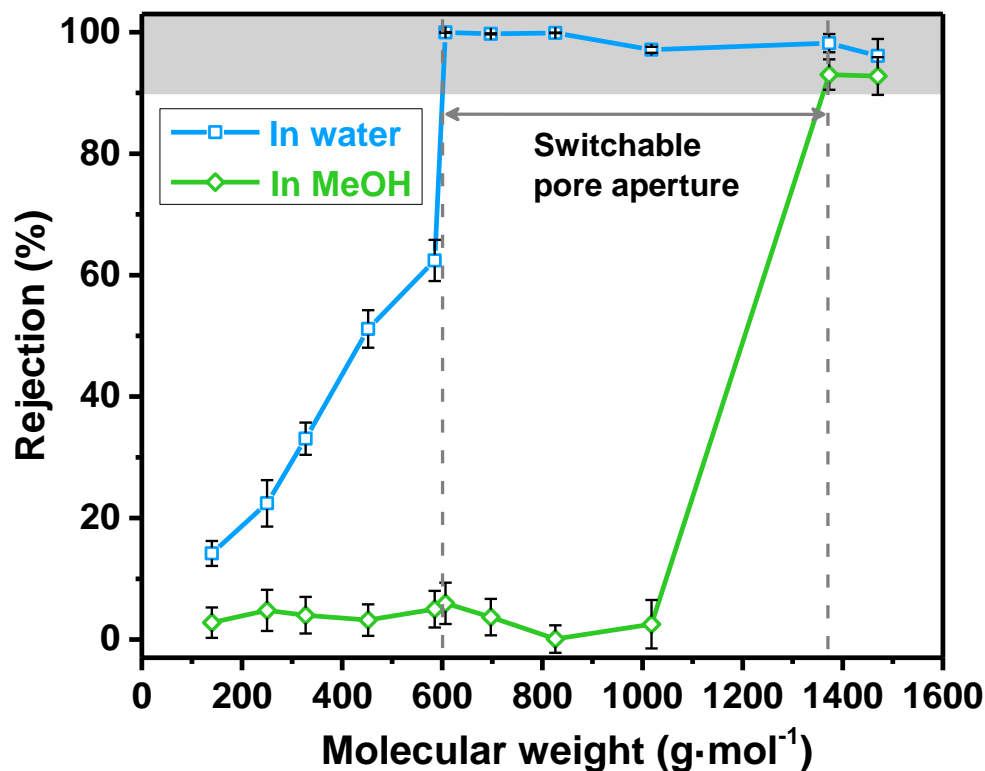
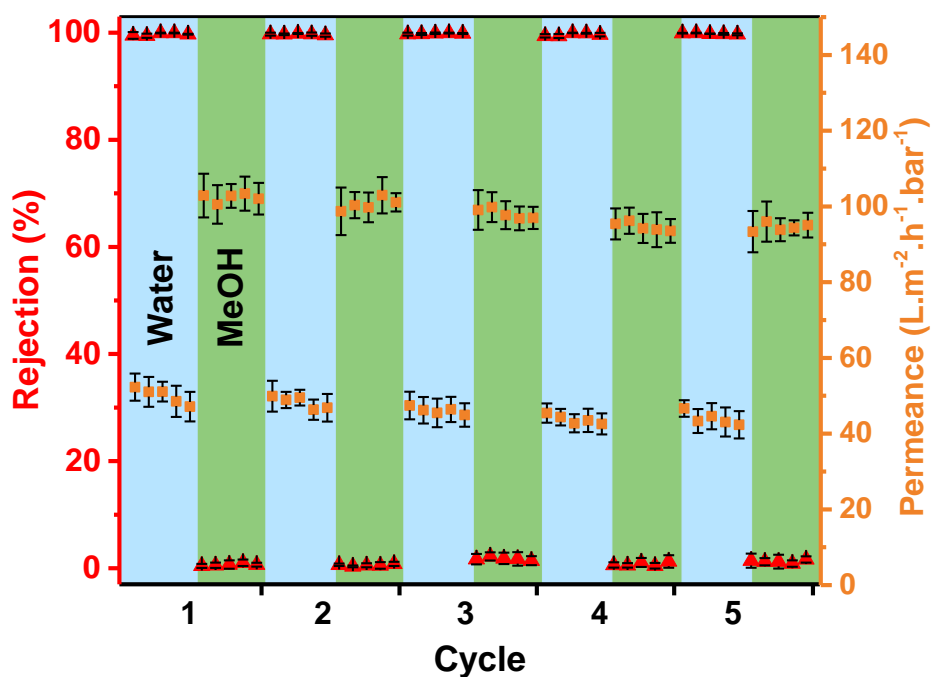


**Figure 4.17** MWCO curve for  $CC3\alpha$ -PAN in water and  $CC3\gamma'$ -PAN in MeOH containing 20 ppm dye solutes. The MWCO was determined by interpolating from the plot of rejection against the molecular weight of the dyes and corresponds to the molecular weight for which rejection reaches 90%. All error bars depict the SD of the data points obtained from at least three independent membranes. Copyright © 2022, Springer Nature and Ai He, etc.

Instead of water, which has been studied for the cage membrane performance exhaustively in **Chapter 3**, we herein used MeOH to dissolve the dyes and filtered these solutions through the  $CC3$ -PAN membrane under the same conditions. The outcome of the dye rejection experiments is shown in detail in **Figure 4.16** and **Table 4.1**, where we can see that only the two larger dyes RR (92.8%) and DR (93.0%) were rejected from the MeOH feedstocks, while the other dyes we tested could pass through the  $CC3\gamma'$ -PAN membrane.

Interestingly, the MWCO shifted from 600  $g\cdot mol^{-1}$  in water to 1400  $g\cdot mol^{-1}$  in MeOH for the same membrane (**Figure 4.17**). We attribute this dramatic change in MWCO to the phase transformation to  $CC3\gamma'$ -PAN in MeOH, which exhibited a less dense packing form with large extrinsic pores between hexagonally arranged  $CC3$  molecules (**Figure 4.15**).

(a)



(b)

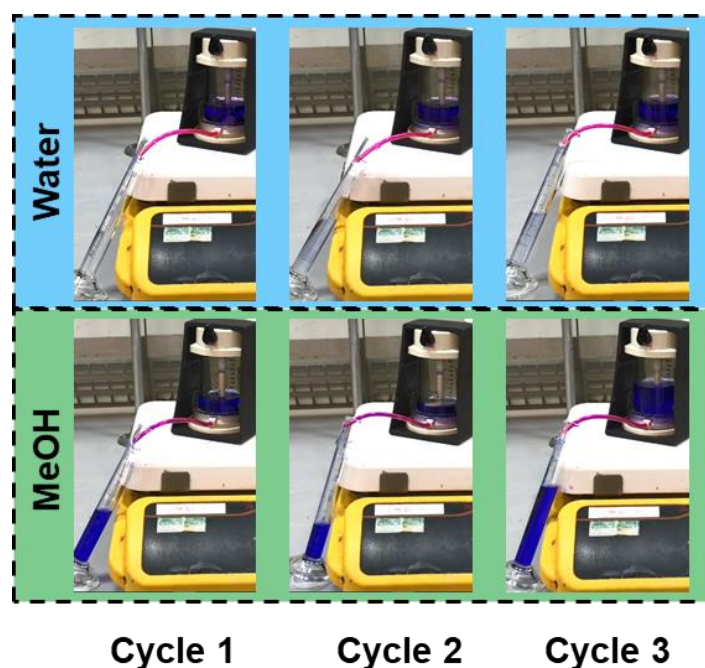


**Figure 4.18** (a) Reversible dye rejection of brilliant blue (BB) and solvent permeance of the CC3-PAN membrane observed upon switching the feedstock solvent between water and MeOH. All error bars denote the standard deviations (SD) for measurements from at least three independent membranes. (b) Photographs of a CC3-PAN in a filtration dead-end cell captured from a continuous real-time video at different filtration times; BB is rejected in water by CC3 $\alpha$ -PAN while CC3 $\gamma'$ -PAN does not reject BB in MeOH.

**Table 4.2** *Reversible dye rejection data for CC3-PAN, recorded while switching the feedstock between 20 ppm BB dissolved in water and MeOH feedstocks.*

Cycle	Solvent	Dye	Sample Collected	Volume (mL)	Wavelength (nm)	Absorption	Rejection (%)
1	Water	BB	Feed	110	552	1.3823	
			Permeate 1	11	551	0.0018	99.87
			Permeate 2	13	551	0.0006	99.96
			Permeate 3	14	551	0.0018	99.87
			Permeate 4	12	551	0.0021	99.85
			Permeate 5	9	551	0.0028	99.80
			Retentate	51	551	2.2893	
1	MeOH	BB	Feed	110	587	1.6239	
			Permeate 1	9	587	1.6090	0.92
			Permeate 2	15	587	1.6041	1.22
			Permeate 3	10	587	1.595	1.78
			Permeate 4	11	587	1.5935	1.87
			Permeate 5	10	587	1.6077	1.00
			Retentate	55	587	1.7284	
2	Water	BB	Feed	100	551	1.2468	
			Permeate 1	6	551	0.0023	99.83
			Permeate 2	11	551	0.0025	99.82
			Permeate 3	8	551	0.0023	99.83
			Permeate 4	10	551	0.0017	99.88
			Permeate 5	12	551	0.0023	99.83
			Retentate	53	552	2.7621	
2	MeOH	BB	Feed	100	587	1.6959	
			Permeate 1	12	587	1.6811	0.87
			Permeate 2	10	587	1.6922	0.22
			Permeate 3	18	587	1.6827	0.78
			Permeate 4	6	586	1.6723	1.39

			Permeate 5	7	586	1.6906	0.31
			Retentate	47	587	1.7140	
			Feed	100	552	1.3208	
			Permeate 1	17	552	0.0018	99.86
			Permeate 2	15	552	0.0020	99.85
3	Water	BB	Permeate 3	11	551	0.0037	99.72
			Permeate 4	7	551	0.0021	99.84
			Permeate 5	8	551	0.0025	99.81
			Retentate	42	551	3.1182	
			Feed	100	587	1.6648	
			Permeate 1	12	587	1.6410	1.43
			Permeate 2	21	586	1.6134	3.09
3	MeOH	BB	Permeate 3	9	587	1.6263	2.31
			Permeate 4	11	587	1.6275	2.24
			Permeate 5	6	587	1.6475	1.04
			Retentate	41	587	1.6976	
			Feed	100	552	1.3546	
			Permeate 1	10	551	0.0023	99.83
			Permeate 2	8	551	0.0018	99.87
4	Water	BB	Permeate 3	7	551	0.0018	99.87
			Permeate 4	8	551	0.0024	99.82
			Permeate 5	11	551	0.0020	99.85
			Retentate	56	552	2.4845	
			Feed	100	587	1.6761	
			Permeate 1	15	586	1.6555	1.23
			Permeate 2	17	587	1.6587	1.04
4	MeOH	BB	Permeate 3	10	587	1.6416	2.06
			Permeate 4	8	587	1.6733	0.17
			Permeate 5	6	587	1.6598	0.97

			Retentate	44	587	1.6664	
			Feed	100	550	1.3024	
			Permeate 1	10	551	0.0001	99.99
			Permeate 2	15	551	0.0001	99.99
5	Water	BB	Permeate 3	14	551	0.0035	99.73
			Permeate 4	7	551	0.0051	99.61
			Permeate 5	11	551	0.0014	99.89
			Retentate	43	551	2.8876	
			Feed	100	587	1.6548	
			Permeate 1	21	586	1.6753	3.20
			Permeate 2	7	586	1.6584	2.00
5	MeOH	BB	Permeate 3	6	587	1.6885	2.99
			Permeate 4	10	587	1.6823	1.23
			Permeate 5	11	587	1.6548	1.59
			Retentate	45	587	1.7529	
			Feed	100	552	1.3620	
			Permeate 1	12	551	0.0022	99.84
			Permeate 2	13	552	0.0019	99.86
6	Water	BB	Permeate 3	11	551	0.0020	99.85
			Permeate 4	8	551	0.0044	99.68
			Permeate 5	9	551	0.0034	99.75
			Retentate	47	551	2.5413	

**Table 4.3** Reversible dye rejection data for three CC3-PAN samples, recorded while switching the feedstock between 20 ppm BB dissolved in water and MeOH feedstocks. The details of membrane sample I are shown in **Table 4.2**.

Cycle	Solvent	Rejection for BB (%)			Average Value (%)	Standard Deviation (%)
		Sample I	Sample II	Sample III		
1	Water	99.87	98.61	100.00	99.49	0.50
		99.96	98.99	99.35	99.43	0.40
		99.87	99.99	99.99	99.95	0.06
		99.85	99.99	99.98	99.94	0.07
		99.80	99.73	99.61	99.71	0.08
	MeOH	0.92	0.39	0.01	0.44	0.37
		1.22	0.02	0.41	0.55	0.50
		1.78	0.31	0.00	0.70	0.77
		1.87	0.54	0.68	1.03	0.60
		0.99	0.17	0.84	0.67	0.36
2	Water	99.83	99.35	99.99	99.72	0.27
		99.82	99.49	99.77	99.69	0.15
		99.83	99.77	99.99	99.86	0.09
		99.88	99.32	99.99	99.73	0.29
		99.83	99.12	99.71	99.55	0.31
	MeOH	0.87	0.32	0.71	0.63	0.23
		0.22	0.24	0.56	0.34	0.16
		0.78	0.87	0.01	0.55	0.39
		1.39	0.08	0.08	0.51	0.62
		0.31	0.85	1.25	0.80	0.38
3	Water	99.86	99.36	99.99	99.74	0.27
		99.85	99.50	99.92	99.76	0.18
		99.72	99.97	99.99	99.89	0.12

		99.84	99.99	99.96	99.93	0.07
		99.81	99.77	99.97	99.85	0.08
		1.43	2.99	0.64	1.69	0.98
		3.09	2.33	1.20	2.21	0.77
	MeOH	2.31	0.38	2.83	1.84	1.05
		2.24	0.01	2.97	1.74	1.26
		1.04	0.64	2.58	1.42	0.84
		99.83	99.32	99.08	99.41	0.31
		99.87	98.97	99.28	99.37	0.38
	Water	99.87	99.99	99.98	99.95	0.05
		99.82	99.91	99.99	99.91	0.07
		99.85	99.90	99.16	99.64	0.34
4		1.23	0.02	0.58	0.61	0.49
		1.04	0.01	0.53	0.53	0.42
	MeOH	2.06	0.02	1.18	1.08	0.84
		0.17	0.01	1.20	0.46	0.53
		0.97	0.01	2.83	1.27	1.17
		99.99	99.84	99.91	99.91	0.06
		99.99	99.86	99.99	99.95	0.06
	Water	99.73	99.85	99.83	99.80	0.05
		99.61	99.99	99.68	99.76	0.16
		99.89	99.75	99.45	99.70	0.18
5		3.20	0.05	0.98	1.41	1.32
		2.00	0.35	1.32	1.22	0.68
	MeOH	2.99	0.01	0.69	1.23	1.28
		1.23	0.01	1.34	0.86	0.60
		1.59	0.96	2.37	1.64	0.58



**Table 4.4** Solvent permeance data for three CC3-PAN samples, recorded while switching the feedstock between 20 ppm BB dissolved in water and MeOH feedstocks.

Cycle	Solvent	Permeance (L.m <sup>-2</sup> .h <sup>-1</sup> .bar <sup>-1</sup> )			Average Value (L.m <sup>-2</sup> .h <sup>-1</sup> .bar <sup>-1</sup> )	Standard Deviation (L.m <sup>-2</sup> .h <sup>-1</sup> .bar <sup>-1</sup> )
		Sample I	Sample II	Sample III		
1	Water	49.36	50.16	57.32	52.28	3.58
		45.60	52.55	54.94	51.03	3.96
		47.77	51.35	54.14	51.09	2.61
		42.87	50.16	52.55	48.53	4.12
		43.50	45.38	52.55	47.14	3.90
	MeOH	100.19	110.87	97.55	102.87	5.76
		106.62	100.89	94.16	100.56	5.09
		102.74	106.67	98.96	102.79	3.15
		102.63	109.23	98.27	103.38	4.51
		107.70	100.63	97.77	102.03	4.17
2	Water	55.32	48.88	45.51	49.90	4.07
		50.16	50.64	45.88	48.89	2.14
		47.38	52.32	48.77	49.49	2.08
		43.50	49.91	45.60	46.34	2.67
		42.99	51.74	45.79	46.84	3.65
	MeOH	95.54	93.15	107.48	98.72	6.27
		95.54	103.56	101.91	100.34	3.46
		98.72	104.97	95.54	99.74	3.92
		101.51	109.43	97.93	102.95	4.80
		100.70	104.20	98.31	101.07	2.42
3	Water	51.94	47.32	42.99	47.42	3.65
		51.14	43.95	43.44	46.18	3.52
		50.74	42.04	43.69	45.49	3.77
		50.95	43.22	44.99	46.39	3.31

		47.77	40.62	46.38	44.93	3.09
		95.54	106.45	95.21	99.07	5.22
		95.54	105.09	98.82	99.82	3.96
	MeOH	93.95	102.71	96.43	97.69	3.69
		97.76	100.16	92.61	96.84	3.15
		99.50	98.57	92.85	96.97	2.94
		45.38	42.35	48.60	45.44	2.55
		43.22	47.43	42.44	44.36	2.19
	Water	39.44	43.72	45.03	42.73	2.39
		41.22	41.44	47.83	43.50	3.07
		38.83	45.43	43.44	42.57	2.77
4		95.54	90.32	100.32	95.39	4.08
		92.36	95.54	100.76	96.22	3.46
	MeOH	88.85	95.99	97.77	94.20	3.85
		91.23	90.03	100.32	93.86	4.59
		90.63	92.05	97.93	93.54	3.16
		43.60	47.77	48.57	46.65	2.18
		40.83	41.40	47.77	43.33	3.15
	Water	40.03	45.38	48.38	44.60	3.45
		38.44	42.99	47.80	43.08	3.82
		38.22	41.80	46.99	42.34	3.60
5		90.00	88.99	101.02	93.34	5.45
		98.60	88.60	100.76	95.99	5.30
	MeOH	95.99	89.57	95.99	93.85	3.03
		97.18	92.76	93.12	94.35	2.00
		98.94	90.99	95.26	95.06	3.25

To perform switchable molecular separations while cycling between **CC3 $\alpha$ -PAN** and **CC3 $\gamma$ '-PAN**, a single membrane was used interchangeably with water and MeOH feedstocks containing the BB dye for five consecutive cycles (**Table 4.3**, **Table 4.4**, and **Table 4.5**). As is

shown in **Figure 4.18**, we found that both water and MeOH permeances remained high after cycling between **CC3 $\alpha$ -PAN** and **CC3 $\gamma$ '-PAN** ( $\sim 45 \text{ L}\cdot\text{m}^{-2}\cdot\text{h}^{-1}\cdot\text{bar}^{-1}$  for water and  $\sim 100 \text{ L}\cdot\text{m}^{-2}\cdot\text{h}^{-1}\cdot\text{bar}^{-1}$  for MeOH). More importantly, the rejection of BB switches between  $\sim 100\%$  in water to  $\sim 0\%$  in MeOH in each cycle; that is, the membrane can be switched 'on' and 'off' using a solvent. This switchable membrane performance results from the reversible transition between **CC3 $\alpha$ -PAN** and **CC3 $\gamma$ '-PAN**, which appears to be complete within the one minute that it takes to switch the feedstock (**Figure 4.19**), and creates alternative diffusion pathways through the membrane structure.

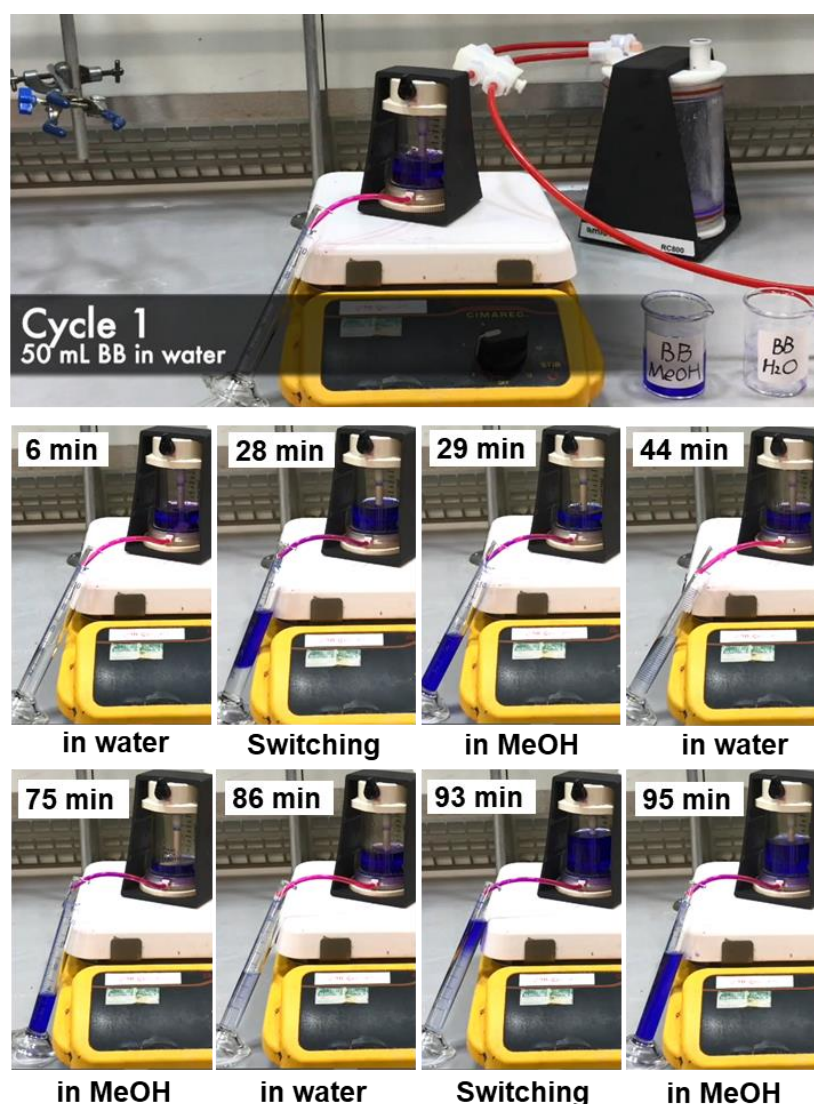


**Figure 4.19** Set-up for the reversible day rejection experiments and photographs of a **CC3-PAN** in a filtration dead-end cell captured from a continuous real-time video at different filtration times, clearly showing the switching occurred instantly between the two solvents.

Crucially, to confirm that **CC3** could be cycled between **CC3 $\alpha$ -PAN** and **CC3 $\gamma'$ -PAN**, we performed a series of *in situ* GIXRD measurements on solvated **CC3** films while performing two consecutive cycles. We found that the composite membrane transformed cleanly between **CC3 $\alpha$ -PAN** and **CC3 $\gamma'$ -PAN** when the solvent was switched between water and MeOH and back again (**Figure 4.20**). It is essential to prove the structural transformation is reversible between methanol and water, where the structural transformation behaviour corresponds to the reversible dye rejection experiments. We attributed this switching phenomenon solely to the phase transformation of **CC3** films with the *in situ* GIXRD evidence rather than swelling of the membranes, which is discussed further in the next section.

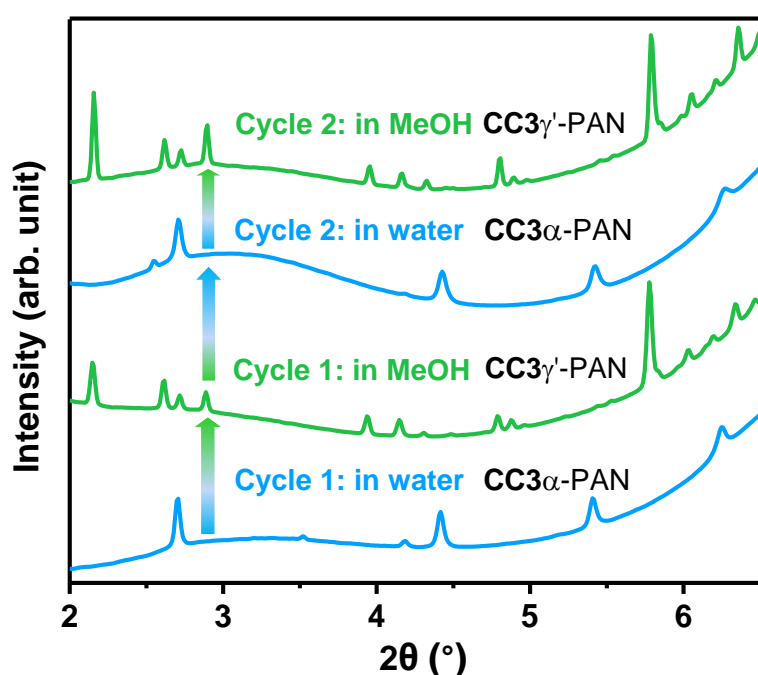


**Figure 4.20** *In situ* GIXRD patterns showing the reversible phase transition of the cage membranes between **CC3 $\alpha$ -PAN** and **CC3 $\gamma'$ -PAN**, switched by cycling 100 mL solvent between water and MeOH. Copyright © 2022, Springer Nature and Ai He, etc.

#### 4.4 Investigations on Effects of Crystallinity and Solvation

We further investigated how crystallinity influences the switchable pore aperture by measuring dye rejection of **CC3-PAN** membranes that had lower crystallinity, i.e., **CC3** films fabricated using lower concentrations or shorter reaction times on the PAN support.

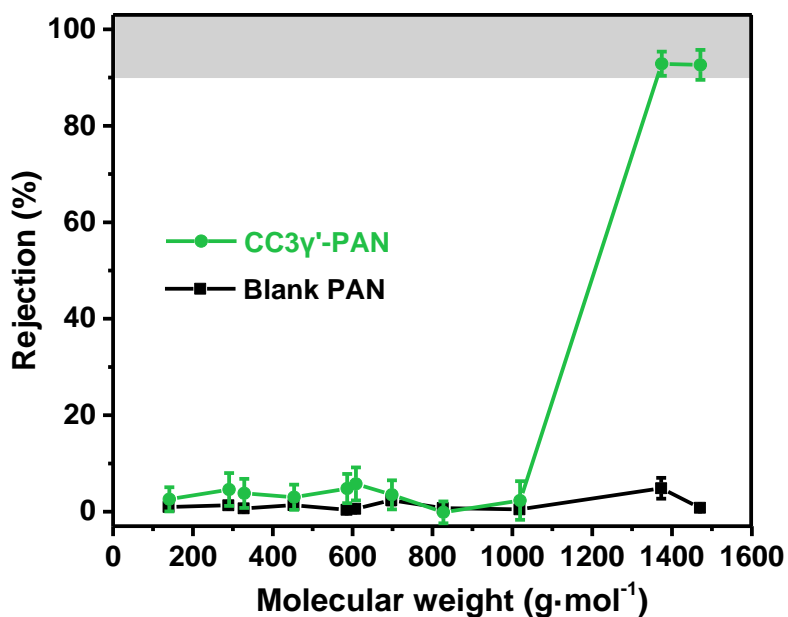


**Figure 4.21** Dye rejection versus molecular weight cut-off curve for CC3γ'-PAN and blank PAN membrane in MeOH containing 20 ppm dye solutes. The upstream nitrogen pressure was kept at 10 bar during the measurement and the stirrer agitation speed was 400 rpm. The error bars denote the standard deviations for measurements from at least three independent membranes.

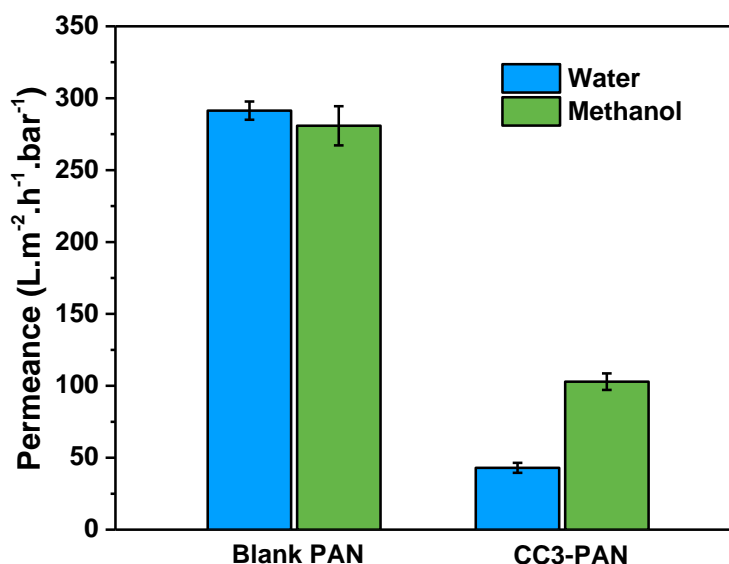


**Figure 4.22** Water and MeOH permeance of a blank PAN membrane and the CC3-PAN membranes. The permeance values were measured under the same conditions with the upstream nitrogen pressure kept at 10 bar during the measurement, and the stirrer agitation speed was set at 400 rpm. The error bars denote the standard deviations for measurements from at least three independent membranes.

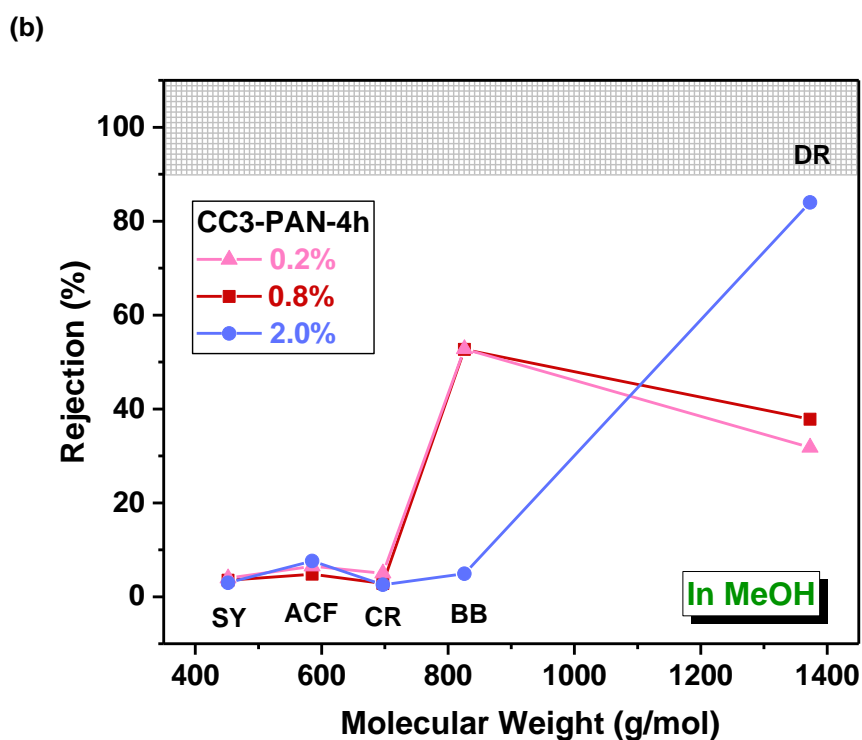
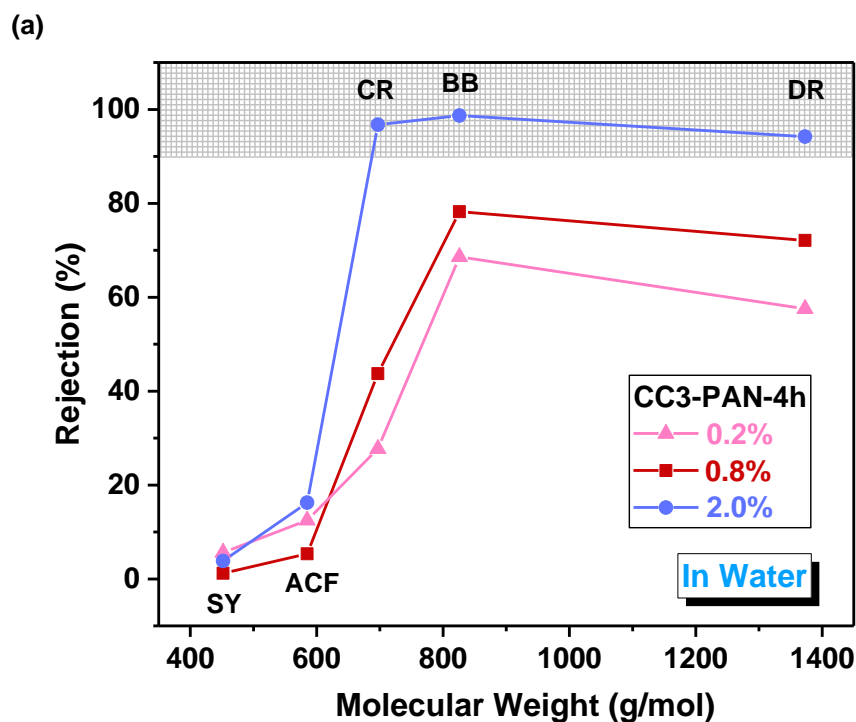


**Figure 4.23** Dye rejection measurements for CC3-PAN-4H-Y% membranes fabricated using different reagent concentrations: 0.2, 0.8, and 2.0 wt.%. The dead-end cell was kept under a 10 bar nitrogen atmosphere, and the stirrer bar agitation speed was 400 rpm. Generic CC3 film synthesis conditions, reagent concentration: TFB 0.2, 0.8, or 2.0 wt.% in DCM (30 mL), CHDA 0.2, 0.8, or 2.0 wt.% in water (32 mL); reaction conditions: 4 hours at room temperature; dish diameter: 7.4 cm. Dye concentration: 20 ppm.

Firstly, we conducted the dye rejection measurements on the blank PAN as blank control data, shown in **Figure 4.21**, comparing with  $\text{CC3}\gamma'$ -PAN. Unlike the  $\text{CC3}\gamma'$ -PAN showing a MWCO of  $1400 \text{ g}\cdot\text{mol}^{-1}$ , none of these dyes in MeOH was rejected on a blank PAN sample. Water and MeOH permeances of a blank PAN membrane and the  $\text{CC3}$ -PAN membrane are shown in **Figure 4.22**. The blank PAN exhibited similar permeance of water and MeOH, while the  $\text{CC3}$ -PAN had a 2.5 times higher permeance value of MeOH than that of water.

For these samples fabricated with different reagent concentrations, as is shown in **Figure 4.23**,  $\text{CC3}$ -PAN-4hr-0.8% rejected 78.2% of brilliant blue (BB) from water compared to 52.7% from MeOH. In contrast, the less crystalline  $\text{CC3}$ -PAN-4hr-0.2% had a less distinct BB rejection performance of 68.6% from water and 52.8% from MeOH.

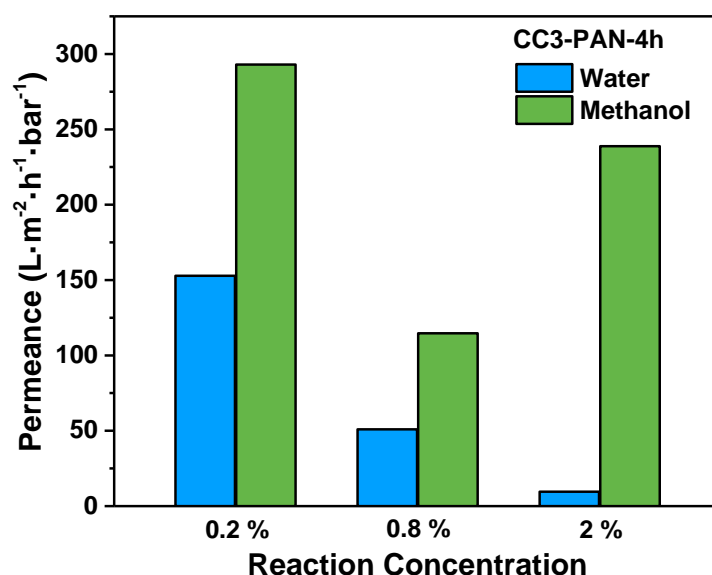


**Figure 4.24** Water and MeOH permeance rates for  $\text{CC3}$ -PAN-4H-Y% membranes fabricated using different reagent concentrations: 0.2, 0.8, and 2.0 wt.%. The dead-end cell was kept under a 10 bar nitrogen atmosphere and the stirrer bar agitation speed was 400 rpm. Generic film synthesis conditions, reagent concentration: TFB 0.2, 0.8, or 2.0 wt.% in DCM (30 mL), CHDA 0.2, 0.8, or 2.0 wt.% in water (32 mL); reaction conditions: 4 hours at room temperature; dish diameter: 7.4 cm.

As for the permeance for water and MeOH (**Figure 4.24**), the  $\text{CC3}$ -PAN-4H-2.0% had 20 times higher MeOH permeance ( $238.9 \text{ L}\cdot\text{m}^{-2}\cdot\text{h}^{-1}\cdot\text{bar}^{-1}$ ) compared to water permeance ( $9.6 \text{ L}\cdot\text{m}^{-2}\cdot\text{h}^{-1}\cdot\text{bar}^{-1}$ ). The lower water permeance value compared to  $\text{CC3}$ -PAN-4H-0.8% and  $\text{CC3}$ -PAN-4H-0.2% is attributed to its higher dye rejection performance, but the MeOH permeance was higher than  $\text{CC3}$ -PAN-4H-0.8% ( $114.6 \text{ L}\cdot\text{m}^{-2}\cdot\text{h}^{-1}\cdot\text{bar}^{-1}$ ), indicating that the higher

crystallinity created a more ordered pore structure in the membranes. By contrast, **CC3-PAN-4H-0.2%** with a lower crystallinity exhibited a MeOH permeance ( $293.0 \text{ L}\cdot\text{m}^{-2}\cdot\text{h}^{-1}\cdot\text{bar}^{-1}$ ) that was twice the water permeance ( $152.9 \text{ L}\cdot\text{m}^{-2}\cdot\text{h}^{-1}\cdot\text{bar}^{-1}$ ), which we attribute to the combined solvent properties (viscosity  $\eta$ , molar diameter  $d_m$ , and solubility parameter  $\delta_d$ ) rather than the structural transformation in the two solvents. These rejection and permeance data reveals that the high crystallinity in the **CC3** membrane is essential for regulating its separation performance after switching its pore aperture using a solvent stimulus.

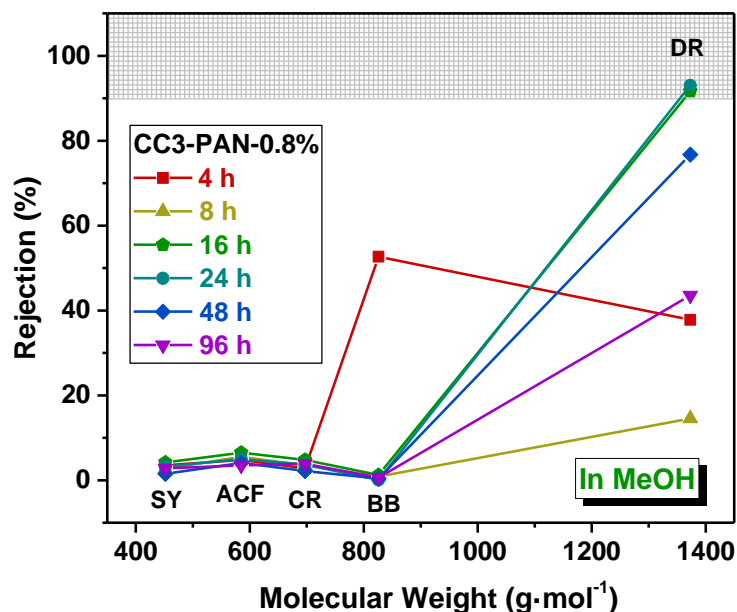


**Figure 4.25** Dye rejection measurements for **CC3 $\alpha$ -PAN-Xhr-0.8%** membranes fabricated using reaction times that ranged between 4–96 hours in MeOH. Reaction times of 4 hours were not long enough to form a defect-free **CC3** film and its dye rejection performance was poor. While cracks appeared in the membrane fabricated after 96 hours that contributed to its lower rejection performance. The dead-end cell was kept under a 10 bar nitrogen atmosphere and the stirrer bar agitation speed was 400 rpm. Dye concentration: 20 ppm.

We also studied the membrane performance using the **CC3-PAN** membranes fabricated at different times, which are defined to be at different formation stages based on the discussion in **Chapter 3**. As is shown in **Figure 4.25**, the amorphous oligomeric membranes produced in **Stage 1** (**CC3-PAN-4H-0.8%**) exhibited a similar rejection of DR (52.7%) and BB (37.8%) in MeOH, which indicated **CC3-PAN-4H-0.8%** failed to form a defect-free membrane for separation. All of the rest **CC3-PAN-0.8%** samples showed no rejection for BB ( $\sim 0.5\%$ ), but the rejection for the larger dye, DR, increased along with the reaction time – 14.5%, 91.6%, and 93.0% for **CC3-PAN-8H-0.8%**, **CC3-PAN-16H-0.8%**, and **CC3-PAN-24H-0.8%** in **Stage**



2 and **Stage 3**, respectively. As the crystallinity of the membranes increased, the more completed phase transition occurred in the solvent. Afterwards, while the highly crystalline membranes formed with prolonged reaction time in **Stage 4**, the physical defects and cracks on the membrane surface reduced the rejection of DR to 76.7 % (**CC3-PAN-48H-0.8%**) and 43.5% (**CC3-PAN-96H-0.8%**).

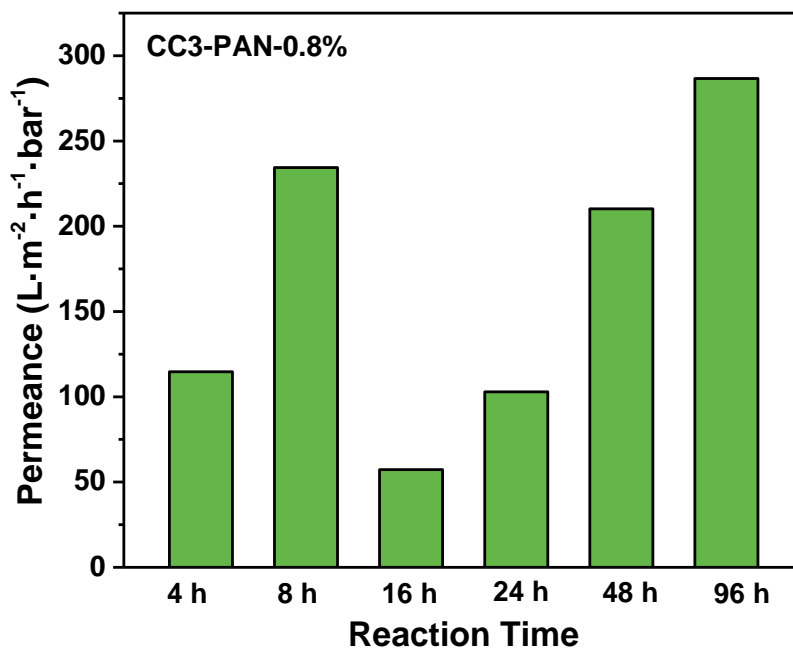


**Figure 4.26** MeOH permeance rates for **CC3a-PAN-XH-0.8%** membranes fabricated using reaction times that ranged between 4–96 hours. The dead-end stirred cell was kept under a 10 bar nitrogen atmosphere and the stirrer bar agitation speed was 400 rpm. Generic film synthesis conditions, reagent concentration: TFB 0.8 wt.% in DCM (30 mL), CHDA 0.8 wt.% in water (32 mL); reaction conditions: room temperature; dish diameter: 7.4 cm.

The MeOH permeance increased proportionally in line with the increased reaction time, as is shown in **Figure 4.26**, which is 57.3, 102.9, and 210.2 L·m<sup>-2</sup>·h<sup>-1</sup>·bar<sup>-1</sup> for 16, 24, and 48 hours. The permeance value for the highly crystalline **CC3-PAN-4H-0.8%** was the highest one (286.6 L·m<sup>-2</sup>·h<sup>-1</sup>·bar<sup>-1</sup>), however, it failed to achieve comparable separation performances. The amorphous oligomeric **CC3-PAN-4H-0.8%** showed a relatively higher rejection for DR and BB than **CC3-PAN-8H-0.8%**, so it is reasonable that **CC3-PAN-4H-0.8%** exhibited lower solvent permeance than the latter.

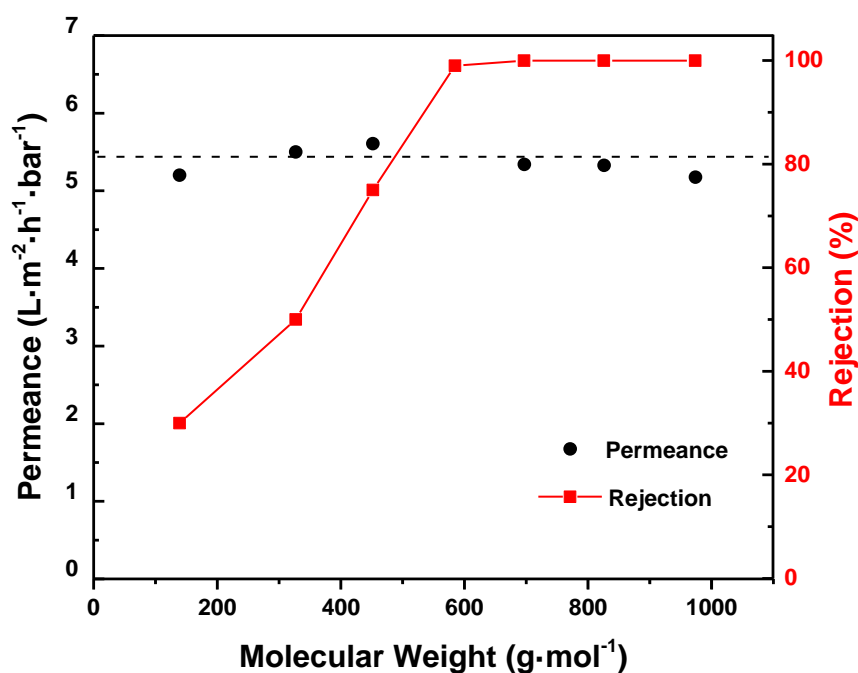


**Figure 4.27** MWCO curve and water permeance for the reference Synder<sup>®</sup> NDX nanofiltration membrane that exhibits a MWCO cut-off between 500 and 700 g·mol<sup>-1</sup>.

Moreover, we used an amorphous polymer membrane, commercial Synder<sup>®</sup> NDX nanofiltration membrane as a reference to determine the effects of solvation on the effective size of the dyes, and to confirm the importance of the crystallinity on the structural transformation. As is shown in **Figure 4.27**, the Synder<sup>®</sup> NDX nanofiltration membrane exhibited a comparable MWCO (500–700 g·mol<sup>-1</sup>) to our CC3-PAN (~600 g·mol<sup>-1</sup>) in water, with a low water permeance (5.5 L·m<sup>-2</sup>·h<sup>-1</sup>·bar<sup>-1</sup>), which is attributed to the amorphous polymeric structure in the membrane.

Unlike the CC3-PAN with a dramatic MWCO shift from 1400 g·mol<sup>-1</sup> to 600 g·mol<sup>-1</sup>, Synder<sup>®</sup> NDX exhibited similar rejection behaviour in both water (99.9%), MeOH (97.0%) and acetonitrile (99.9%), as is shown in **Figure 4.28**. Note, the Synder<sup>®</sup> NDX nanofiltration membrane was not resistant to acetone, and the membrane fragmented in acetone, causing it to fail to reject BB in acetone. CC3-PAN membrane, by contrast, exhibited good rejection in water (99.8%), acetonitrile (98.0%) and acetone (95.2%), and no rejection in methanol, because the same phase, CC3 $\alpha$ , was present in these solvents (**Figure 4.5** and **Figure 4.6**), this confirmed the phase transition occurs in these unique crystalline membranes.

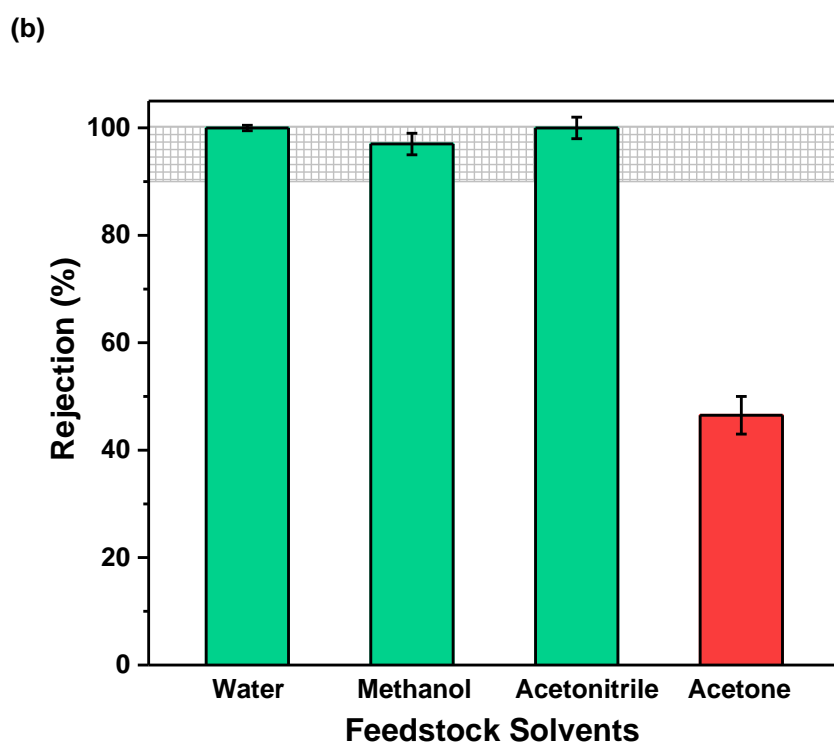
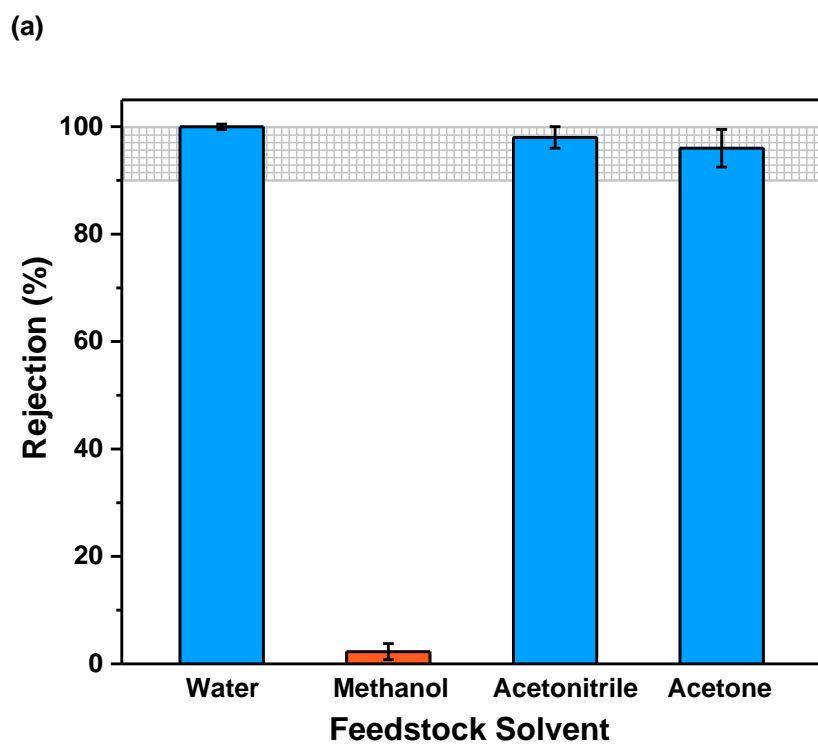


**Figure 4.28** Dye rejection of BB dye in different solvents using, (a) *CC3 $\alpha$ -PAN*; (b) the *Synder<sup>®</sup> NDX* membrane as the reference. Note, the low dye rejection of BB in acetone using *Synder<sup>®</sup> NDX* indicates that this membrane is not resistant to degradation in acetone. All the error bars depict the standard deviations of the data from at least three independent membranes.

To further validate that the switching phenomenon is solely linked to the phase transformation of the CC3 films, rather than swelling of the membranes, we carried out the nanofiltration experiments using CC3-PAN membranes soaked in acetone. As is shown in **Figure 4.29**, the CC3-PAN membrane was found to exhibit a very comparable MWCO in acetone to that observed in water. This indicated that the separation is a size-based effect rather than differences between dye ionisation. Hence, the permeance and selectivity of the CC3 membrane is switched by transforming the modular and non-covalent packing of CC3 between CC3 $\alpha$ -PAN and CC3 $\gamma$ '-PAN using a solvent stimulus.

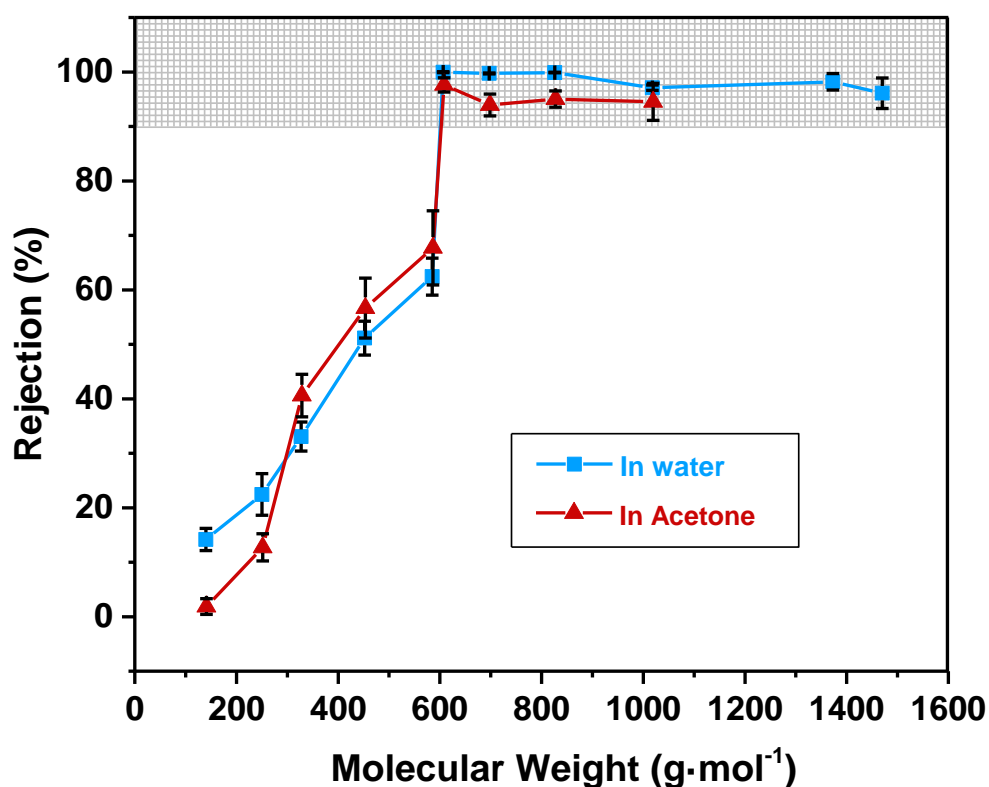


**Figure 4.29** Molecular weight cut-off (MWCO) curve for CC3 $\alpha$ -PAN determined using organic dyes dissolved in water or acetone. MWCO cut-off curves were obtained plotting dye rejection versus the molecular weight of the dyes. The molecular weight corresponding to a rejection of 90% is the MWCO. Dye feedstock concentration: 20 ppm. Note, DR and RR are insoluble in acetone and their dye rejection performance could not be measured. SY and CR have a maximum solubility of 5 ppm in acetone, thus 5 ppm CR in acetone dye solution was used instead of 20 ppm solution. All the error bars depict the standard deviations of the data from at least three independent membranes. Copyright © 2022, Springer Nature and Ai He, etc.

Remarkably, the acetone permeance of **CC3 $\alpha$ -PAN** reached  $177 \text{ L}\cdot\text{m}^{-2}\cdot\text{h}^{-1}\cdot\text{bar}^{-1}$  with a MWCO of  $\sim 600 \text{ g}\cdot\text{mol}^{-1}$ , which is well above the upper bound performance (that describes the competitive trade-off between permeance and MWCO) for nanofiltration membranes reported in the literature (**Figure 4.30**), including metal-organic framework (MOF), macrocycle (MC), nanoparticles (NPs), graphene oxide (GO), polymer membranes, and commercially available membranes. **Figure 4.31** shows acetone permeance versus MWCO values for other nanofiltration membranes in comparison to **CC3 $\alpha$ -PAN**, with a higher resolution showing the citation number of each point; detailed information for the membranes reported in the literature or are commercially available, and citations for the relevant studies are shown in **Table 4.5**.

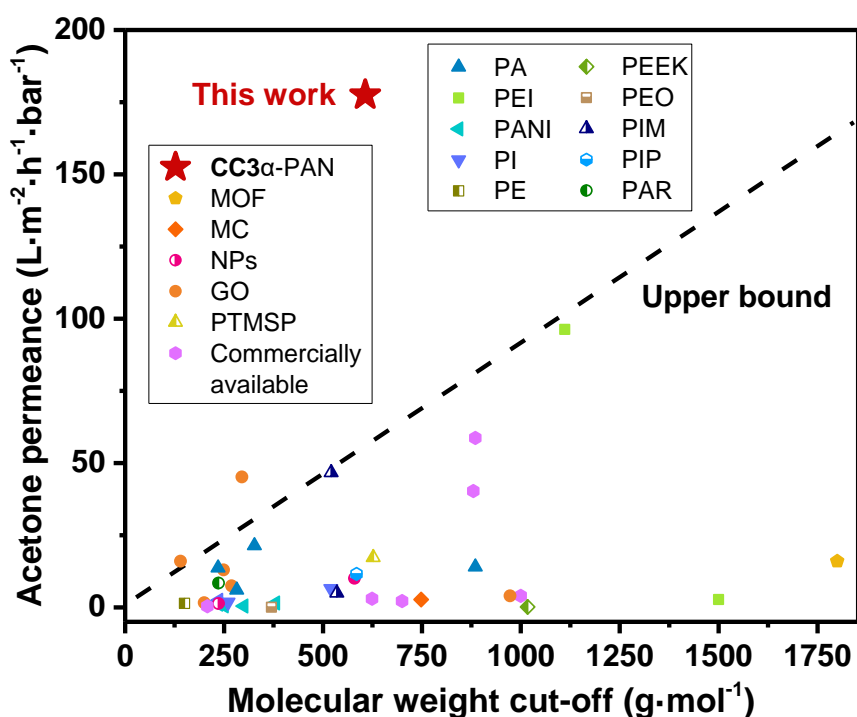
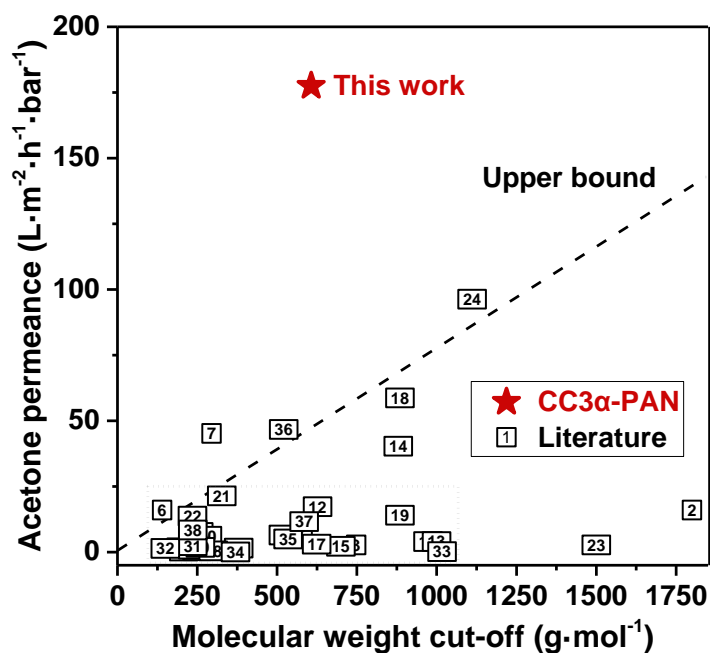


**Figure 4.30** Acetone permeance versus MWCO of generally solutes in acetone for nanofiltration membranes reported in the literature and **CC3 $\alpha$ -PAN**. MOF, metal-organic framework; MC, macrocycle; NPs, nanoparticles; GO, graphene oxide; PTMSP, poly[1-(trimethylsilyl)-1-propyne]; PA, polyamide; PEI, polyethyleneimine; PANI, polyaniline; PI, polyimide; PE, polyethylene; PEEK, Poly(ether ether ketone); PEO, poly(ethylene oxide); PIM, polymers of intrinsic microporosity; PIP, piperazine; PAR, polyacrylate (see **Table 4.5** for further details). Copyright © 2022, Springer Nature and Ai He, etc.

(a)



(b)

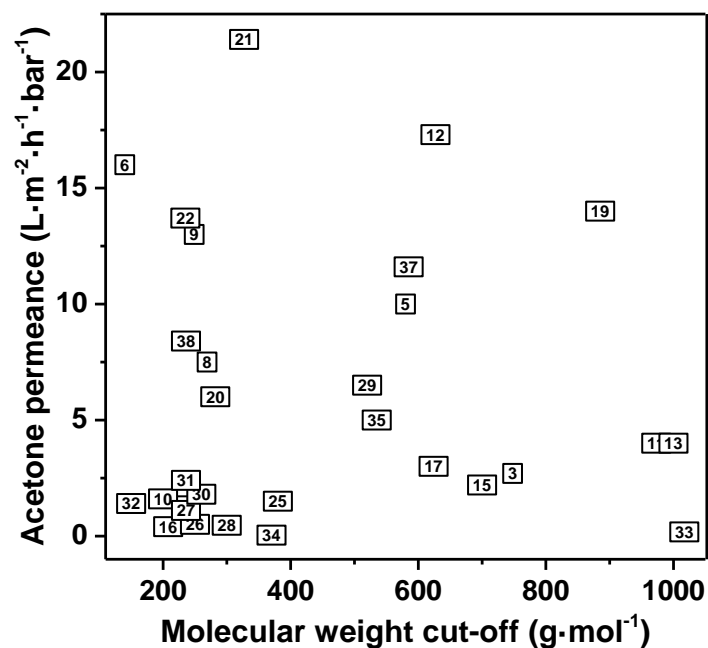


**Figure 4.31** (a) Acetone permeance versus MWCO values for nanofiltration membranes reported in the literature in comparison to CC3 $\alpha$ -PAN. The upper bound has been added to highlight the trade-off between permeance and rejection, where rejection performance negatively correlates with molecular weight cut-off. The area with dash square is shown in higher resolution in (b). Further information about the membranes shown in the plot is included in **Table 4.5**. Copyright © 2022, Springer Nature and Ai He, etc.

**Table 4.5** Detailed information about the acetone permeance and MWCO values in acetone for the membranes reported in the literature or are commercially available. The permeance values with different units have been transferred to ( $L \cdot m^{-2} \cdot h^{-1} \cdot bar^{-1}$ ) for comparison. All the membranes cited here were tested in acetone. POC, porous organic cage; MOF, metal-organic framework; MC, macrocycle; NPs, nanoparticles; GO, graphene oxide; PTMSP, poly[1-(trimethylsilyl)-1-propyne]; PA, polyamide; PEI, polyethyleneimine; PANI, polyaniline; PI, polyimide; PE, polyethylene; PEEK, Poly(ether ether ketone); PEO, poly(ethylene oxide); PIM, polymers of intrinsic microporosity; PIP, piperazine; PAR, polyacrylate.

No.	MW CO ( $g \cdot mol^{-1}$ )	P ( $L \cdot m^{-2} \cdot h^{-1} \cdot bar^{-1}$ )	Solvent	Solute	Process configuration	Membrane type	Membrane Material	Year	Reference
This work	607	177.5	Acetone	Protoporphyrin IX disodium	Dead-end cell	POC	cages on polyacrylonitrile ultrafiltration membrane	2020	-
2	1800	16.0	Acetone	Polystyrene	Cross-flow	MOF	HKUST-1 / P84	2014	22
3	748	2.7	Acetone	Clarithromycin	Cross-flow	MC	$\beta$ -cyclodextrin film composite (TFC)	2019	23
4	236	1.3	Acetone	Methylstyrene dimer	Cross-flow	NPs	P[N-isopropylacrylamide-2-(hydroxy)ethyl methacrylate] nanoparticles /crosslinked P84	2013	24
5	580	10.0	Acetone	Styrene oligomers	Cross-flow	NPs	Grignard grafted TiO <sub>2</sub> /alumina	2014	25
6	140	16.0	Acetone	Oligostyrene	Cross-flow	GO	Covalently cross-linked polybenzimidazole/graphene	2018	26

							oxide membranes		
7	295	45.2	Acetone	Oligostyrene	Cross-flow	GO	Non-crosslinked polybenzimidazole/graphene oxide membranes	2018	26
8	269	7.5	Acetone	Methyl red	Dead-end cell	GO	Graphene oxide hollow fibre membranes with a porous poly(methyl methacrylate) sacrificial layer	2015	27
9	249	13.0	Acetone	Chrysoidine G	Dead-end cell	GO	Highly laminated graphene oxide membranes	2017	28
10	200	1.6	Acetone	Polyethylene glycol	Dead-end cell	GO	Polyethyleneimine-graphene oxide layer on dopamine coated polyacrylonitrile ultrafiltration membrane	2015	29
11	973	4.0	Acetone	Rose bengal	Dead-end cell	GO	Graphene oxide-layered hollow fibers	2020	30
12	627	17.3	Acetone	Remazol brilliant blue R	Cross-flow	PTMSP	Poly[1-(trimethylsilyl)-1-propyne] (PTMSP) / poly(acrylonitrile) (PAN)	2009	31
13	1000	4.0	Acetone	Soybean oil	Dead-end cell	Commercial	SolSep-NF030306	2011	32
14	880	40.3	Acetone	Erythro sine B	Cross-flow	Commercial	SolSep-169	2006	33



15	700	2.2	Acetone	Bromothymol blue	Cross-flow	Commercial	MPF-50	2006	33
16	208	0.4	Acetone	Eusolex	Cross-flow	Commercial	HITK-T1	2006	33
17	624	3.0	Acetone	Bromothymol blue	Cross-flow	Commercial	FSTi-128	2006	33
18	885	58.7	Acetone	Triglycerides	Dead-end cell	Commercial	SolSep-NF010206	2018	34
19	885	14.0	Acetone	Triglycerides	Dead-end cell and cross-flow	PA	[Poly(amide-ether) copolymer] top layer membrane	1999	35
20	282	6.0	Acetone	Oleic acid	Cross-flow	PA	Polyamide (PA)/PAN	2002	36
21	327	21.4	Acetone	Methyl orange	Dead-end cell	PA	m-Xylylenediamine (m-XDA) - trimesoyl chloride (TMC) membranes	2020	37
22	235	13.7	Acetone	Styrene dimer	Cross-flow	PA	Plant-based monomer TFC membranes	2021	38
23	1500	2.7	Acetone	Polyethylene glycol	Dead-end cell	PEI	Polyethylenimine	2015	29
24	1111	96.3	Acetone	Acid yellow 79	Dead-end cell	PEI	Polydopamine-polyethylenimine on polyacrylonitrile ultrafiltration membrane	2018	39
25	380	1.5	Acetone	Oligostyrene	Hollow fibre	PANI	Polyaniline hollow fibres	2008	40

					testing module					
26	250	0.5	Acetone	Oligostyrene	Spiral-wound module	PANI	Polyaniline spiral-wound module	2010	41	
27	236	1.1	Acetone	Oligostyrene	Dead-end cell and cross-flow	PANI	Cross-linked Polyaniline (PANI)	2009	42	
28	300	0.46	Acetone	Poly(propylene glycols)	Dead-end cell and cross-flow	PANI	PANI-poly(2-acrylamido-2-methyl-1-propanesulfonic acid) (PAMPSA) membranes	2019	43	
29	520	6.5	Acetone	Oligostyrene	Cross-flow	PI	P84 (PI)	2014	44	
30	260	1.8	Acetone	Oligostyrene	Cross-flow	PI	Crosslinked polyamide-imide (Torlon®)	2013	45	
31	236	2.4	Acetone	Methylstyrene dimer	Dead-end cell	PI	Polyamide (PA)/crosslinked P84 PI	2012	46	
32	150	1.4	Acetone	Triethylene glycol	Dead-end cell	PE	Teflon AF2400/polyethylene (PE) membranes	2020	47	
33	1017	0.18	Acetone	Rose bengal	Dead-end cell	PEEK	Poly(ether ether ketone) (PEEK) membranes crosslinked with diamines	2013	48	
34	370	0.04	Acetone	Ethylene glycol oligomers	Dead-end cell	PEO	[polystyrene-block-poly(ethylene oxide)/homopolymer]/alumina	2010	49	

35	535	5.0	Acetone	Hexaphenylbenzene	Dead-end cell	PIM	[polymers of intrinsic microporosity (PIM-1)/polyethyleneimine(PEI)]/PAN	2012	50
36	521	46.7	Acetone	Mometasone furoate	Molecular simulation	PIM	Functional PIM-1 membranes	2019	51
37	585	11.6	Acetone	Acid fuchsin	Cross-flow	PIP	Polyamide-based polyamide/piperazine (PEI/PIP) polyimide hollow fibre membranes	2020	52
38	236	8.4	Acetone	Methylstyrene dimer	Dead-end cell and cross-flow	PAR	Polyarylate (PAR)/PI nanofilm	2016	53

#### 4.5 Grade Sieving and Other Applications

A series of BB feedstocks in water and MeOH solvent mixtures were used to determine the dynamic transformation between **CC3 $\alpha$ -PAN** and **CC3 $\gamma$ '-PAN** and its effect on the selective permeance of BB.

Interestingly, the BB rejection rate verse water content can be formulated by fitting a logical curve, which reveals that critical transition between **CC3 $\alpha$ -PAN** and **CC3 $\gamma$ '-PAN** occurs at a water concentration of around 61.7% (**Figure 4.32**), after which a good rejection of BB was achieved. The critical transition point is found very close to the rate golden ratio (61.8%). The fitting curve has been concluded to **Eq.4.1**, with the following parameters:  $k = -16.117 \pm 0.9688$ ,  $p = 4.58e-08$ ;  $a = 0.617 \pm 0.004$ ,  $p = 2e-16$ ; residual standard error: 0.0219. Conversely, the percentage of water or methanol content (x) can be detected by testing the rejection of BB (y) in the mixture by using this equation. Understanding this dynamic transformation enables the manipulation of the pore aperture in a single **CC3-PAN** membrane by simply adjusting the

water concentration in a water-MeOH mixture, without any activation processes<sup>54</sup> or the use of multiple membranes<sup>55</sup>.

$$y = \frac{1}{1 + e^{-16.1168 \cdot (x - 0.6174)}} \quad (\text{Eq.4.1})$$

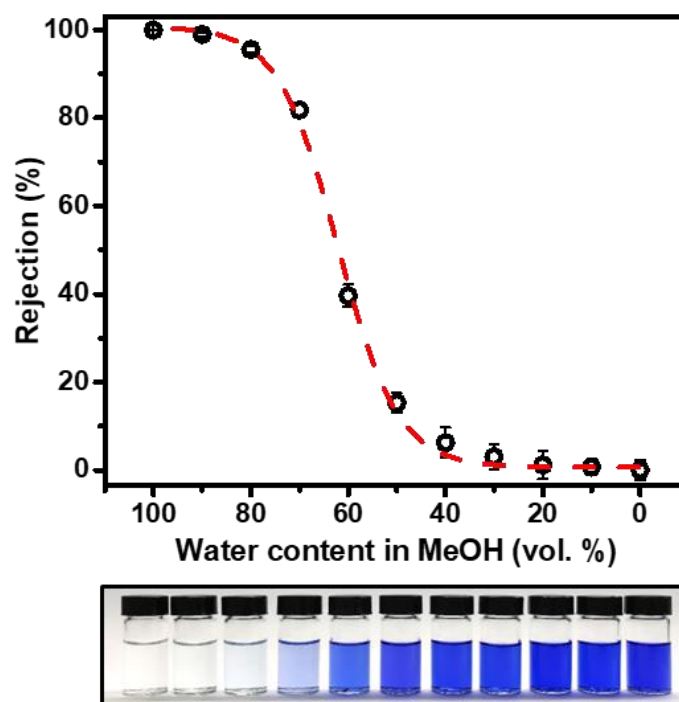


**Figure 4.32** *BB rejection in mixtures of water and MeOH (vol/vol) for CC3-PAN. All error bars depict the SD of the data points obtained from at least three independent membranes. The red dash line was fitted as the logistic function ( $y = 1/(1 + \exp(-16.1 * (x - 0.617)))$ ), see **Chapter 2** for fitting method). Below is the photograph of each permeate of BB in water and MeOH mixture with the water content ranging from 0–100 vol.%.*

To demonstrate the potential advantage of this technology, we performed a graded sieving experiment to separate molecules from a ternary mixture using a single membrane. As is shown in **Figure 4.33**, as the cage membrane switches to a different structure in two solvents, the smallest molecule (yellow) could permeate the membrane pores in both water and methanol, while the largest molecule (red) cannot get through in either solvent. Initially, we started with a MeOH feedstock (100 mL) that contained 20 ppm of the three dyes, 4-nitrophenol (NP) (yellow,  $139 \text{ g}\cdot\text{mol}^{-1}$ ), BB (blue,  $826 \text{ g}\cdot\text{mol}^{-1}$ ), and direct red 80 (DR) (red,  $1373 \text{ g}\cdot\text{mol}^{-1}$ ), starting with the membrane  $\text{CC3}\gamma'$ -PAN. After flowing the MeOH feedstock through  $\text{CC3}\gamma'$ -PAN, DP was rejected, while NP and BB were found in the permeate. After rinsing the membrane with water, we then undertook the separation of NP and BB in the MeOH filtrate.

This was achieved by adding water (90% vol/vol, 90 mL) to 10 mL of the MeOH filtrate (10 mL) and repeating the separation processes, whereupon the membrane switches to CC3 $\alpha$ '-PAN. Analysis of the permeate revealed that BB was rejected (98.2%) by CC3 $\alpha$ '-PAN, leaving only NP in the permeate (Table 4.6). Hence, the three dye molecules with different molecular weights have been separated using a single membrane by this graded sieving approach.

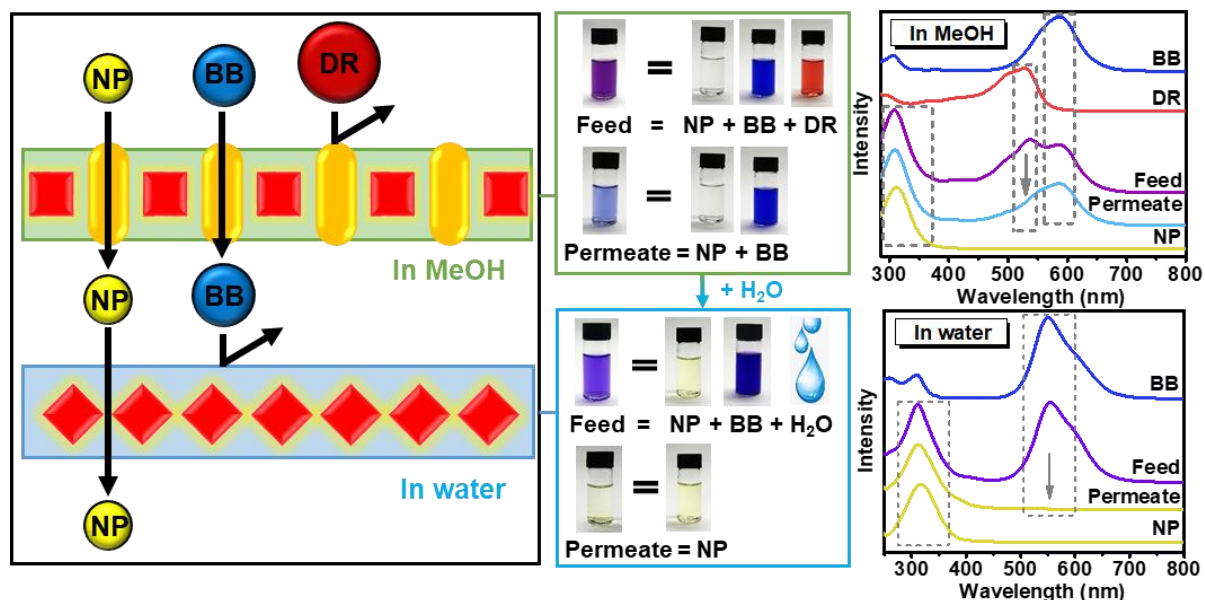


**Figure 4.33** Graded sieving using a single switchable membrane. Scheme showing the different pore apertures in the CC3-PAN membrane when in MeOH (green) and in water (blue); the photographs show feed and permeate dye solutions, along with the relevant UV absorption spectra. The CC3 $\gamma$ '-PAN removes DR selectively from the NP/BP/DR mixture; after that, switching to the CC3 $\alpha$ -PAN phase by contact with water allows BB to be separated from NP, all using a single membrane. Note that NP is colourless in MeOH but yellow-coloured in water; for better visual presentation, the feed and permeate (in water) were first concentrated by a factor of 10 for these photographs and UV spectra were recorded.

**Table 4.6** Dye rejection measurement data for CC3-PAN in water and methanol mixture of as-collected solution and concentrated solution. Hypothetically, assuming the dye rejection was 0%, the dye concentration would be 2 ppm in the as-collected permeate and 20 ppm in the concentrated permeate.

Solvent	Sample Collected	Volume (mL)	Dye	Wavelength (nm)	Absorption	Rejection (%)
---------	------------------	-------------	-----	-----------------	------------	---------------

	As-collected Feed	100	NP	310	0.064	N.A.
			BB	548	0.055	
Water/MeOH (90/10 vol/vol)	Permeate	50	NP	314	0.060	6.25 ± 3.50
			BB	548	0.001	98.18 ± 0.52
	Retentate	50	NP	312	0.066	N.A.
			BB	550	0.098	
	Concentrated Feed	100	NP	314	0.575	N.A.
			BB	554	0.592	
Water/MeOH (90/10 vol/vol)	Permeate	50	NP	314	0.486	15.40 ± 1.84
			BB	552	0.033	98.20 ± 0.75
	Retentate	50	NP	312	0.588	N.A.
			BB	554	0.965	

Continuous ternary molecular separation has been investigated in this three-molecule system as well. Alternatively, a water feedstock containing a mixture of the three dyes (NP, BB, DR) was filtered through the **CC3**-PAN membrane (**Figure 4.34**). Since **CC3**-PAN adopts its **CC3 $\alpha$** -PAN structure in water, the narrower pore aperture only allowed the smallest molecule, NP, to diffuse through the membrane, while the larger molecules, BB and DR were rejected and retained in the cell. Excess water was added into the cell to flush the residual NP from the retentate, and this process was repeated until the NP concentration in the permeate was below 1%. Subsequently, 90 vol.% of MeOH was added into the water retentate to generate a feedstock that transformed the membrane structure to **CC3 $\gamma'$** -PAN with the larger pore aperture. BB could then diffuse through the membrane alone, while DR was retained in the cell. Finally, excess MeOH was used for flushing any residue BB from the cell to leave only DR in the retentate, where it could be collected in pure form (see **Chapter 2** for full experimental details). As a result, by introducing a solvent gradient, a single membrane with a switchable pore aperture enables a ternary separation in a continuous process.

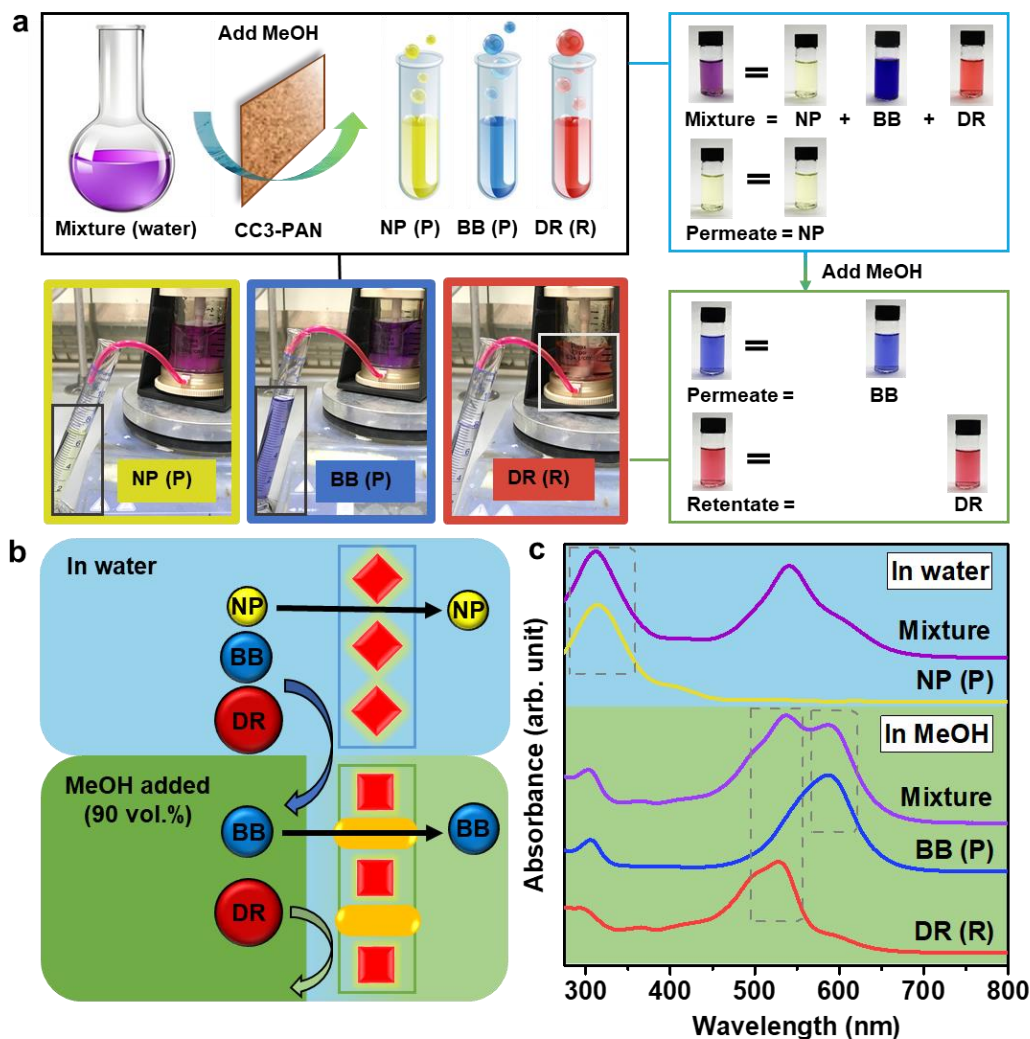


**Figure 4.34** Continuous ternary molecular separation using a single switchable membrane. (a) Scheme showing ternary molecular separation of three dyes direct red 80 (DR), BB, and 4-nitrophenol (NP) using one single membrane (CC3-PAN), and photographs showing the separation experiment in a filtration dead-end cell, the nascent mixture feedstock, the permeate (P) collected in the first and second step, and the retentate (R) collected in the second step. (b), Scheme showing ternary molecular separation process of three dyes using one single membrane in a continuous process: Step 1, CC3 $\alpha$ -PAN in water only allows permeation of NP, leaving BB and DR in the retentate. Step 2, 90 vol.% MeOH was added into the retentate to transform the membrane structure to CC3 $\gamma$ '-PAN that only allows permeation of BB, leaving DR in the retentate. Liquid flushing was carried out between the steps to enrich the dyes in the retentate. (c), UV-vis absorption spectra of the mixture containing three molecules in water, permeate from water, mixture and permeate from 90 vol.% of MeOH in water, and the remaining retentate. Note, the maximum absorbance wavelength for BB is 551 nm in water and 587 nm in MeOH; BB also shows absorbance at 305 nm in MeOH while NP shows its maximum absorbance at 312 nm in the same solvent.

**Table 4.7** Continuous dye rejection measurement data for CC3-PAN in water and methanol/water mixture (90/10 vol/vol) while methanol was added to the retentate solution in Step 2 of ternary molecular separation process.

Solvent	Sample Collected	Volume (mL)	Dye	Wavelength (nm)	Absorption	Concentration (%)	Outcome
Water	Feed	100	NP	310	3.414	33.333	
			BB	551	1.428	33.333	
			DR	540	1.638	33.333	
	Permeate	50	NP	310	3.278	<b>98.083 ± 1.272</b>	
			BB	551	0.010	0.794 ± 0.215	
			DR	540	0.018	1.122 ± 0.324	
MeOH/ Water (90/10 vol/vol)	Feed (Retentate)	100	NP	313	0.284	0.982 ± 0.086	
			BB	588	0.733	50.587 ± 1.357	
			DR	535	0.824	49.576 ± 1.024	
	Permeate	50	NP	313	0.208	0.001 ± 0.001	
				305	0.249		
			BB	535	0.424	<b>99.560 ± 0.282</b>	
				588	0.730		
			DR	530	0.395	0.439 ± 0.282	
	Retentate	50	NP	312	0.201	0.001 ± 0.001	
			BB	588	0.140	0.440 ± 0.282	
			DR	530	0.701	<b>99.559 ± 0.282</b>	

Continuous ternary molecular separation has been investigated in this three-molecule system as well. Alternatively, a water feedstock containing a mixture of the three dyes (NP, BB, DR) was filtered through the CC3-PAN membrane (**Figure 4.34**, see **Chapter 2** for full experimental details). Since CC3-PAN adopts its CC3 $\alpha$ -PAN structure in water, the narrower pore aperture only allowed the smallest molecule, NP, to diffuse through the membrane, while the larger molecules, BB and DR were rejected and retained in the cell. NP was thus collected from the permeate. Excess water was added into the cell to flush the residual NP from the



retentate, and this process was repeated until the NP concentration in the permeate was below 1%. Subsequently, 90 vol.% of MeOH was added into the water retentate to generate a feedstock that transformed the membrane structure to **CC3 $\gamma$ '**-PAN with the larger pore aperture. BB could then diffuse through the membrane alone, while DR was retained in the cell. Finally, excess MeOH was used for flushing any residue BB from the cell to leave only DR in the retentate, where it could be collected in pure form (**Table 4.7**). As a result, by introducing a solvent gradient, a single membrane with a switchable pore aperture enables a ternary separation in a continuous process.

These technologies also enable the cage membranes to be considered as stimuli-responsive membranes, which can be utilised in a wide range of applications, such as drug delivery<sup>56</sup>, biosensors<sup>57</sup>, and fermentation<sup>58</sup>. Moreover, as the switchable behaviour was repeatable for five consecutive cycles without any loss in permeance or rejection performance, it makes these cage membranes highly attractive for anti-fouling or self-cleaning membranes<sup>59</sup> that could be regenerated after simply being "flushed" with a different solvent, in this case, MeOH.

## 4.6 Conclusion and Outlook

A novel synthetic strategy has been developed to fabricate a smart and responsive crystalline POC membrane with switchable pore apertures, using the combination of aqueous–organic interfacial reaction and crystallisation process. The POC membranes, in this case, **CC3**-PAN, have achieved high permeances for a range of organic solvents—in some cases, such as for acetone, exceeding the upper performance bound—while also showing excellent separation performances. We attribute the high solvent permeance of **CC3**-PAN to highly ordered pore channels in POC crystals positioned throughout the membrane structure.

Solid-state structural transformation of **CC3** has been observed and studied using several solvents. In situ GIXRD measurements in water and methanol have determined two different molecule packing forms in the same cage membrane. When the cage molecules are arranged in **CC3 $\alpha$**  phase, they pack in a window-to-window arrangement to generate an interconnected diamondoid pore network. By comparison, in **CC3 $\gamma$ '** phase, the **CC3** molecules are packed in a less dense arrangement, thus providing large extrinsic pores between hexagonally arranged **CC3** molecules. The reversible transition between **CC3 $\alpha$** -PAN and **CC3 $\gamma$ '**-PAN, therefore, can create different diffusion pathways through the membrane structure.

We have demonstrated the highly ordered crystalline structure of these POC membranes, with a switchable phase transition between two unique crystalline forms, **CC3 $\alpha$ -PAN** and **CC3 $\gamma$ '-PAN**. Dye rejection experiments showed that only the two larger dyes had been rejected from the MeOH feedstocks with its **CC3 $\gamma$ '** phase, while most of the dyes could get through the cage membrane. As a result, the MWC0 shifted from 600 g·mol<sup>-1</sup> in water to 1400 g·mol<sup>-1</sup> in MeOH for the same membrane. We attributed this switching phenomenon solely to phase transformation between the two solvents, where alternative diffusion pathways were created through the membrane structure. The single cage membrane was also tested interchangeably with water and MeOH dye feedstocks for five consecutive cycles, and the reversible selectivity of the dye proved that the membrane can be switched 'on' and 'off' using a solvent.

Effects of crystallinity and solvation have been investigated using the cage membranes with lower crystallinity. The rejection and permeance data indicates the high crystallinity in the **CC3** membrane is essential for regulating its separation performance after switching its pore aperture using a solvent stimulus, whilst the amorphous membrane didn't show this unique switching property. Nanofiltration experiments in acetone confirmed the molecular separation is a size-based effect rather than differences between dye ionisation.

The dynamic transformation has been studied using water and methanol solvent mixtures with different concentrations, and the critical transition between **CC3 $\alpha$ -PAN** and **CC3 $\gamma$ '-PAN** was found to occur at a water concentration of 61.7%. To demonstrate the functional advantage that this creates, we performed a graded sieving experiment and a continuous ternary separation process to separate a mixture of three organic dye molecules with a single, smart membrane by introducing a solvent gradient. This allows the collection of three molecules separately from a ternary mixture and creates a membrane-based parallel to the widespread and highly effective use of solvent gradients in chromatography<sup>60</sup>. More generally, these POC membranes with switchable pore apertures and stimuli-responsive properties could lead to new applications in triggered drug delivery<sup>56</sup>, biosensors<sup>57</sup>, or fermentation/fractionation processes<sup>58</sup>.

However, challenges still remain for these exciting porous materials to be employed in membrane fields. For example, the mechanisms for mass transfer in the pores of these membranes are still not clear enough, and the large-scale industrial applications still need to be enhanced. While the current synthesis process makes it challenging to implement these POC membranes in commercial processes, it is conceivable that a more scalable production method might be developed in the future; for example, by exploiting the solution processability of these

molecular cages. Future efforts will focus on using computational methods, such as crystal structure prediction (CSP), to design POC crystals with specific properties that can be designed from first principles. We believe this research is valuable for the development of novel membrane materials using POC families.

## 4.7 Chapter Acknowledgments

In this Chapter, I would like to thank Prof. Andrew I. Cooper, Dr. Marc A. Little, Prof. Andrew G. Livingston, Dr. Zhiwei Jiang and Dr. Michael E. Briggs for their supervision and suggestions on my work. I acknowledge the discussion and efforts of this project from all the authors of the paper ‘A Smart, Responsive Crystalline Porous Organic Cage Membrane with Switchable Pore Apertures for Graded Molecular Sieving’ which will be soon published in *Nature Materials*: Marc A. Little, Andrew I. Cooper, Zhiwei Jiang, Andrew G. Livingston, Yue Wu, Michael E. Briggs, Hadeel Hussain, and Jonathan Rawle.

For funding, I acknowledge the Engineering and Physical Sciences Research Council (EPSRC) (EP/N004884/1), the Leverhulme Trust via the Leverhulme Research Centre for Functional Materials Design, the China Scholarship Council for a studentship and the Royal Society of Chemistry for a Researcher Mobility Grant (M19-2442).

I acknowledge Diamond Light Source for access to beamlines I07 (SI24359) and I11 (CY23666) that contributed to the results presented here, and thank Dr. Hadeel Hussain, and Dr. Jonathan Rawle as they discussed, designed, and set up the in-situ GIXRD system and helped in the measurements. I acknowledge Dr. Marc A. Little and Dr. Zhiwei Jiang for the design of the switching of the membrane and crystallographic characterisations, and thank Dr. Marc A. Little and Dr. Yue Wu for the help for measurements, and processing and refining the diffraction data. I would like to thank Prof. Andrew G. Livingston for facility support and insights into advanced membrane science. I also would like to thank Miss Hongmei Chen for assistance during the I07 measurements, Dr. Peng Cui and Miss Hui Gao for assistance during the I11 measurements, Mr. Yan Li for fitting the logical curve, and Mr. Rob Clowes for instrument support and setting up the filtration cell and the high-pressure filtration experiments.

## 4.8 References

1. Thompson, K. A. *et al.* N-Aryl-linked spirocyclic polymers for membrane separations of complex hydrocarbon mixtures. *Science* **369**, 310–315 (2020).
2. Suganuma, S. & Katada, N. Innovation of catalytic technology for upgrading of crude oil in petroleum refinery. *Fuel Process. Technol.* **208**, 106518 (2020).
3. Jang, H.-Y. *et al.* Torlon® hollow fiber membranes for organic solvent reverse osmosis separation of complex aromatic hydrocarbon mixtures. *AIChE J.* **65**, e16757 (2019).
4. Yeo, J. *et al.* Liquid Phase Peptide Synthesis via One-Pot Nanostar Sieving (PEPSTAR). *Angew. Chemie Int. Ed.* **60**, 7786–7795 (2021).
5. Takahashi, D., Inomata, T. & Fukui, T. AJIPHASE®: A Highly Efficient Synthetic Method for One-Pot Peptide Elongation in the Solution Phase by an Fmoc Strategy. *Angew. Chemie Int. Ed.* **129**, 7911–7915 (2017).
6. Lv, E., Ding, S., Lu, J., Yi, W. & Ding, J. Separation and purification of fatty acids by membrane technology: a critical review. *Int. J. Chem. React. Eng.* **18**, (2020).
7. Gilmer, C. M., Zvokel, C., Vick, A. & Bowden, N. B. Separation of saturated fatty acids and fatty acid methyl esters with epoxy nanofiltration membranes. *RSC Adv.* **7**, 55626–55632 (2017).
8. Ghasemian, S., Sahari, M. A., Barzegar, M. & Gavlighi, H. A. Concentration of Omega-3 polyunsaturated fatty acids by polymeric membrane. *Int. J. Food Sci. Technol.* **50**, 2411–2418 (2015).
9. Da Silva Bural, J., Peeva, L., Marchetti, P. & Livingston, A. Controlling molecular weight cut-off of PEEK nanofiltration membranes using a drying method. *J. Memb. Sci.* **493**, 524–538 (2015).
10. Lu, Y., Chen, T., Chen, X., Qiu, M. & Fan, Y. Fabrication of TiO<sub>2</sub>-doped ZrO<sub>2</sub> nanofiltration membranes by using a modified colloidal sol-gel process and its application in simulative radioactive effluent. *J. Memb. Sci.* **514**, 476–486 (2016).
11. Siew, W. E., Livingston, A. G., Ates, C. & Merschaert, A. Molecular separation with an organic solvent nanofiltration cascade—augmenting membrane selectivity with process engineering. *Chem. Eng. Sci.* **90**, 299–310 (2013).

12. Little, M. A. & Cooper, A. I. The chemistry of porous organic molecular materials. *Adv. Funct. Mater.* 1909842 (2020) doi:10.1002/adfm.201909842.
13. Hasell, T. & Cooper, A. I. Porous organic cages: soluble, modular and molecular pores. *Nat. Rev. Mater.* **1**, 16053 (2016).
14. Bera, S. *et al.* Porosity switching in polymorphic porous organic cages with exceptional chemical stability. *Angew. Chemie - Int. Ed.* **58**, 4243–4247 (2019).
15. Jones, J. T. A. *et al.* On-off porosity switching in a molecular organic solid. *Angew. Chemie Int. Ed.* **50**, 749–753 (2011).
16. Hasell, T. *et al.* Controlling the crystallization of porous organic cages: Molecular analogs of isorecticular frameworks using shape-specific directing solvents. *J. Am. Chem. Soc.* **136**, 1438–1448 (2014).
17. Pulido, A. *et al.* Functional materials discovery using energy-structure-function maps. *Nature* **543**, 657–664 (2017).
18. Little, M. A., Chong, S. Y., Schmidtman, M., Hasell, T. & Cooper, A. I. Guest control of structure in porous organic cages. *Chem. Commun.* **50**, 9465–8 (2014).
19. Little, M. A. *et al.* Trapping virtual pores by crystal retro-engineering. *Nat. Chem.* **7**, 153–159 (2015).
20. Jones, J. T. A. *et al.* Modular and predictable assembly of porous organic molecular crystals. *Nature* **474**, 367 (2011).
21. Zhang, Z., Zhang, L., Wang, S., Chen, W. & Lei, Y. A convenient route to polyacrylonitrile/silver nanoparticle composite by simultaneous polymerization–reduction approach. *Polymer (Guildf)*. **42**, 8315–8318 (2001).
22. Campbell, J., Székely, G., Davies, R. P., Braddock, D. C. & Livingston, A. G. Fabrication of hybrid polymer/metal organic framework membranes: Mixed matrix membranes versus in situ growth. *J. Mater. Chem. A* **2**, 9260–9271 (2014).
23. Xu, S. J., Shen, Q., Xu, Z. L. & Dong, Z. Q. Novel designed TFC membrane based on host-guest interaction for organic solvent nanofiltration (OSN). *J. Memb. Sci.* **588**, 117227 (2019).
24. Siddique, H. *et al.* Membranes for organic solvent nanofiltration based on preassembled

- nanoparticles. *Ind. Eng. Chem. Res.* **52**, 1109–1121 (2013).
25. Rezaei Hosseinabadi, S. *et al.* Organic solvent nanofiltration with Grignard functionalised ceramic nanofiltration membranes. *J. Memb. Sci.* **454**, 496–504 (2014).
  26. Fei, F., Cseri, L., Szekely, G. & Blanford, C. F. Robust covalently cross-linked polybenzimidazole/graphene oxide membranes for high-flux organic solvent nanofiltration. *ACS Appl. Mater. Interfaces* **10**, 16140–16147 (2018).
  27. Chong, J. Y., Aba, N. F. D., Wang, B., Mattevi, C. & Li, K. UV-enhanced sacrificial layer stabilised graphene oxide hollow fibre membranes for nanofiltration. *Sci. Rep.* **5**, 1–11 (2015).
  28. Yang, Q. *et al.* Ultrathin graphene-based membrane with precise molecular sieving and ultrafast solvent permeation. *Nat. Mater.* **16**, 1198–1202 (2017).
  29. Ding, R. *et al.* Graphene oxide-embedded nanocomposite membrane for solvent resistant nanofiltration with enhanced rejection ability. *Chem. Eng. Sci.* **138**, 227–238 (2015).
  30. Mahalingam, D. K. *et al.* Spray-coated graphene oxide hollow fibers for nanofiltration. *J. Memb. Sci.* **606**, 118006 (2020).
  31. Volkov, A. V. *et al.* High permeable PTMSP/PAN composite membranes for solvent nanofiltration. *J. Memb. Sci.* **333**, 88–93 (2009).
  32. Darvishmanesh, S., Robberecht, T., Luis, P., Degrè, J. & Van Der Bruggen, B. Performance of nanofiltration membranes for solvent purification in the oil industry. *J. Am. Oil Chem. Soc.* **88**, 1255–1261 (2011).
  33. Geens, J., Boussu, K., Vandecasteele, C. & Van der Bruggen, B. Modelling of solute transport in non-aqueous nanofiltration. *J. Memb. Sci.* **281**, 139–148 (2006).
  34. Nur Fitrah Awang Ismail, D. & Faisal Ghazali, N. Separation of fatty acids from palm oil using organic solvent nanofiltration. *Malaysian J. Anal. Sci.* **22**, 561–569 (2018).
  35. Zwijnenberg, H. J., Krosse, A. M., Ebert, K., Peinemann, K. V. & Cuperus, F. P. Acetone-stable nanofiltration membranes in deacidifying vegetable oil. *JAOCs, J. Am. Oil Chem. Soc.* **76**, 83–87 (1999).
  36. Kim, I.-C., Jegal, J. & Lee, K.-H. Effect of aqueous and organic solutions on the

- performance of polyamide thin-film-composite nanofiltration membranes. *J. Polym. Sci. Part B Polym. Phys.* **40**, 2151–2163 (2002).
37. Li, Y., Li, S., Zhu, J., Volodine, A. & Van der Bruggen, B. Controllable synthesis of a chemically stable molecular sieving nanofilm for highly efficient organic solvent nanofiltration. *Chem. Sci.* **11**, 4263–4271 (2020).
  38. Park, S.-H. *et al.* Hydrophobic thin film composite nanofiltration membranes derived solely from sustainable sources. *Green Chem.* (2021) doi:10.1039/d0gc03226c.
  39. Wu, X. *et al.* Adsorption-assisted interfacial polymerization toward ultrathin active layers for ultrafast organic permeation. *ACS Appl. Mater. Interfaces* **10**, 10445–10453 (2018).
  40. Loh, X. X. *et al.* Polyaniline hollow fibres for organic solvent nanofiltration. *Chem. Commun.* 6324–6326 (2008) doi:10.1039/b815632h.
  41. Sairam, M. *et al.* Spiral-wound polyaniline membrane modules for organic solvent nanofiltration (OSN). *J. Memb. Sci.* **349**, 123–129 (2010).
  42. Loh, X. X. *et al.* Crosslinked integrally skinned asymmetric polyaniline membranes for use in organic solvents. *J. Memb. Sci.* **326**, 635–642 (2009).
  43. Sarihan, A. *et al.* Exploiting the electrical conductivity of poly-acid doped polyaniline membranes with enhanced durability for organic solvent nanofiltration. *J. Memb. Sci.* **579**, 11–21 (2019).
  44. Siddique, H., Bhole, Y., Peeva, L. G. & Livingston, A. G. Pore preserving crosslinkers for polyimide OSN membranes. *J. Memb. Sci.* **465**, 138–150 (2014).
  45. Dutczak, S. M., Cuperus, F. P., Wessling, M. & Stamatialis, D. F. New crosslinking method of polyamide-imide membranes for potential application in harsh polar aprotic solvents. *Sep. Purif. Technol.* **102**, 142–146 (2013).
  46. Jimenez Solomon, M. F., Bhole, Y. & Livingston, A. G. High flux membranes for organic solvent nanofiltration (OSN)-Interfacial polymerization with solvent activation. *J. Memb. Sci.* **423–424**, 371–382 (2012).
  47. Shi, G. M. & Chung, T. S. Teflon AF2400/polyethylene membranes for organic solvent nanofiltration (OSN). *J. Memb. Sci.* **602**, 117972 (2020).

48. Hendrix, K., Van Eynde, M., Koeckelberghs, G. & Vankelecom, I. F. J. Crosslinking of modified poly(ether ether ketone) membranes for use in solvent resistant nanofiltration. *J. Memb. Sci.* **447**, 212–221 (2013).
49. Li, X. *et al.* Ordered nanoporous membranes based on diblock copolymers with high chemical stability and tunable separation properties. *J. Mater. Chem.* **20**, 4333–4339 (2010).
50. Fritsch, D., Merten, P., Heinrich, K., Lazar, M. & Piske, M. High performance organic solvent nanofiltration membranes: Development and thorough testing of thin film composite membranes made of polymers of intrinsic microporosity (PIMs). *J. Memb. Sci.* **401–402**, 222–231 (2012).
51. Xu, Q. & Jiang, J. Effects of functionalization on the nanofiltration performance of PIM-1: Molecular simulation investigation. *J. Memb. Sci.* **591**, 117357 (2019).
52. Goh, K. S. *et al.* Thin-film composite hollow fibre membrane for low pressure organic solvent nanofiltration. *J. Memb. Sci.* **597**, 117760 (2020).
53. Jimenez-Solomon, M. F., Song, Q., Jelfs, K. E., Munoz-Ibanez, M. & Livingston, A. G. Polymer nanofilms with enhanced microporosity by interfacial polymerization. *Nat. Mater.* **15**, 760–767 (2016).
54. Karan, S., Jiang, Z. & Livingston, A. G. Sub-10 nm polyamide nanofilms with ultrafast solvent transport for molecular separation. *Science* **348**, 1347–1351 (2015).
55. Dey, K. *et al.* Selective molecular separation by interfacially crystallized covalent organic framework thin films. *J. Am. Chem. Soc.* **139**, 13083–13091 (2017).
56. Loftsson, T., Vogensen, S. B., Brewster, M. E. & Konráosdóttir, F. Effects of cyclodextrins on drug delivery through biological membranes. *Journal of Pharmaceutical Sciences* vol. 96 2532–2546 (2007).
57. Kohli, P., Wirtz, M. & Martin, C. R. Nanotube membrane based biosensors. *Electroanalysis* **16**, 9–18 (2004).
58. O'Brien, D. J. & Craig, J. C. Ethanol production in a continuous fermentation/membrane pervaporation system. *Appl. Microbiol. Biotechnol.* **44**, 699–704 (1996).
59. Ragesh, P., Anand Ganesh, V., Nair, S. V. & Nair, A. S. A review on 'self-cleaning and



- multifunctional materials'. *Journal of Materials Chemistry A* vol. 2 14773–14797 (2014).
60. Aumann, L. & Morbidelli, M. A continuous multicolumn countercurrent solvent gradient purification (MCSGP) process. *Biotechnol. Bioeng.* **98**, 1043–1055 (2007).

# Chapter 5

## **Ultrathin Crosslinked Porous Organic Cage Nanofilm Composite Membranes for Tuneable Molecular Sieving**

The project included in this Chapter is still undergoing, and the manuscript ‘Ultrathin Polyamide Nanofilms Incorporating Porous Organic Cages for Tuneable Molecular Sieving’ will be submitted when finished.

## 5.1 Background and Introduction

As an energy-efficient technology, membrane separations has been successfully applied in seawater desalination, wastewater treatment, carbon capture, *etc*<sup>1</sup>. However, as the current membrane technologies cannot satisfy the increasing demands of wastewater or seawater treatment, new-generation membrane materials are required. Such as those with desirable selectivity, high permeability, and good stability since they can significantly accelerate the practical applications of membrane separation technology<sup>2</sup>. In particular, membranes for molecular separation with precisely controlled geometries are required in many important areas, including gas separation<sup>3</sup> and nanofiltration (NF)<sup>4</sup>. In recent years, molecular sieving materials have attracted much interest for precise and tuneable membrane separation<sup>5-9</sup>.

Among these novel sieving materials, porous organic cages (POCs) are distinct for NF applications for the reasons that they have well-defined pore structures, adjustable pore sizes, good processability, and water stability<sup>10</sup>. A critical advantage of POCs is that these porous materials could be finely modified or functionalised, and the functionalised products are processable into a membrane. Therefore, the design and fabrication of membranes with precise and tunable molecular sieving properties can be achieved.

Synthetic control over pore size and pore connectivity of the POCs can be pre-designed or pre-modified, practically, by selecting or alerting the precursors through the synthesis pathway. Li et al.<sup>11</sup> have reported a synthesis strategy to control the self-assembly pathway as well as product yields of POCs, by using two different triformyl precursors via imine condensation. A rigid, planar precursor favours the formation of prisms, whilst the more twisted one favours tetrahedron (**Figure 5.1(a)**). As a comparison, a more flexible precursor adopting both relatively planar and twisted conformations has produced both prisms and tetrahedrons in high yields. The Cooper group<sup>12</sup> has prepared two pillared co-crystals from ditopic linkers and tetrahedral nodes via molecular reticular synthesis by opting for a series of linear tetraaldehyde precursors in a targeted way. Supramolecular nanotubes, consisting of tubular covalent cages, TCC1, TCC2 and TCC3, have been obtained with both 1D porous nanotubes and 3D diamondoid pillared porous networks. This strategy of positioning organic molecules in a controllable manner in the solid state contributes to the opportunities for the pre-synthesis of new functions in multiple fields.

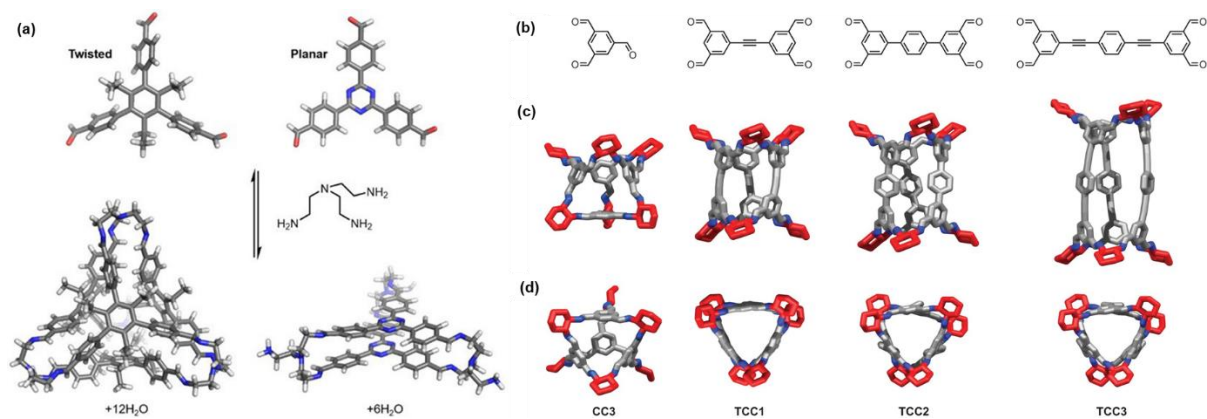


**Figure 5.1** (a) Precursor control over the self-assembly of organic cages via imine condensation. Reprinted from reference<sup>11</sup> with permission. (b) to (d) shows the chiral TCCs as linear ditopic building blocks. (b) Linear tetraaldehyde precursors for the TCC series plus the TFB precursor for CC3 (left). Side view (c) and view through the cage windows (d) of the tetrahedral CC3 and the trigonal prismatic cage family, TCC1–TCC3. Reprinted from reference<sup>12</sup> with permission.

Though POCs are solution-processable, some of POCs show limited solubility. Examples of the modification of their solubility have been reported by using a ‘dynamic covalent scrambling’ approach. Lee *et al.*<sup>13</sup> studied the equilibration of an alkyne metathesis cage (**Figure 5.2(a)**), and dynamic scrambling was applied to demonstrate the ‘kinetic trapping’ observed in the reaction route. Under the alkyne metathesis condition, the pre-formed cages showed no scrambled distribution, and the self-sorted parent cages remained intact (**Figure 5.2(b)**, **aaaa** and **bbbb**). By contrast, there were five cage species (**Figure 5.2(c)**, **aaaa**, **aaab**, **aabb**, **abbb**, and **bbbb**) with mixed functionality observed in the scrambled systems when using alkyne metathesis precursors with different alkyl functionality. They have thus provided an appealing strategy to modify the POC materials as their dynamic covalent chemistry allows the tailoring of their properties for specific functions.

The Cooper group<sup>14</sup> confirmed that the dynamic covalent scrambling method could be used to increase the solubility and porosity of cage mixtures. The co-reaction of the two vicinal diamines with different ratios generated a ‘scrambled’ distribution of POCs with varying functionalities on the periphery (**Figure 5.2(d)**,  $\text{CC1}^n\text{CC3}^{6-n}$ ), which enables us to tune the guest selectivity of the scrambled cage for a range of guest molecules. Inspired by this, two solution-processable dissymmetric racemic analogues of the chiral POC, **CC3**, was then synthesised by the same group<sup>15</sup>. They have been characterised as a racemate pair of the R,R,R,S,S,S and S,S,S,R,R,R-diastereomers (**CC3-RS** and **CC3-SR**) with high porosity, and

were proved an order of magnitude more soluble in solvent, making them excellent candidates for incorporating into a membrane for separation applications.

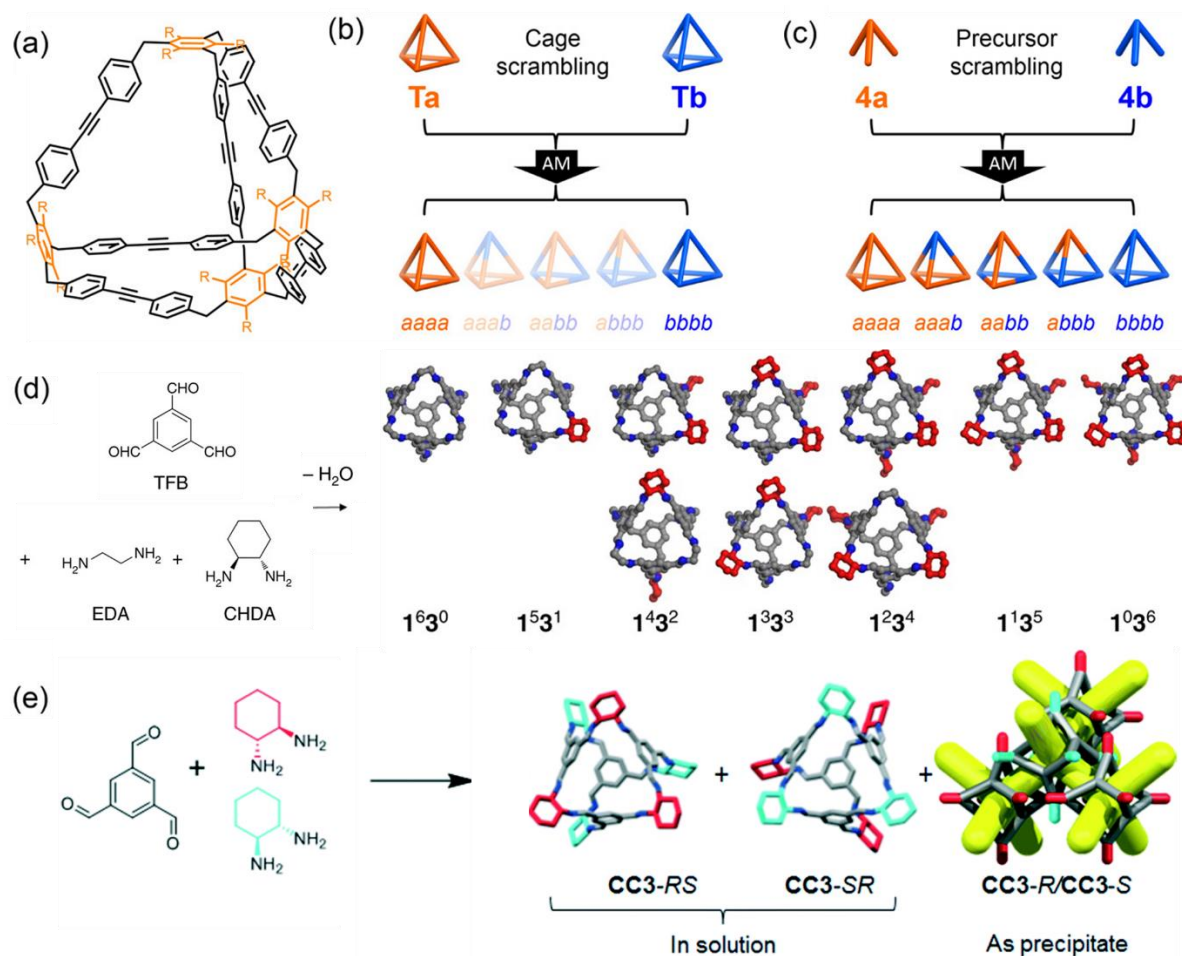


**Figure 5.2** (a) The alkyne POCs reported by Lee *et al.* and the mixtures synthesised when scrambled reactions, using either the pre-formed cages (b) or precursors (c), were attempted. Reprinted from reference<sup>13</sup> with permission. (d) The direct co-reaction of two different diamines leads to 'scrambled' POC mixtures with a distribution of molecular shape. Reprinted from reference<sup>14</sup> with permission. (e) TFB and rac-CHDA react to form CC3-RS and CC3-SR, which are soluble and remain in solution, as well as CC3-R and CC3-S, which immediately co-crystallise to form the racemate, CC3-R/CC3-S, as a white precipitate. Reprinted from reference<sup>15</sup> with permission.

Differing from the previous strategies to control the chemical functionalities of targeted POCs by pre-synthesis route (pre-synthesis functionalisation) or during the synthesis process (inter-synthesis functionalisation), another commonly used method for material altering is post-synthesis functionalisation, where the material is synthesised first and then subjected to

functionalisation under controlled conditions<sup>16</sup>. Frequently, an anchoring point in the material backbone is utilised as a reactive site for controlling the exact position of the introduced chemical group. Post-synthesis functionalisation has been the favoured approach, as evidenced by its widespread application<sup>16</sup>.

The Cooper group<sup>17</sup> has demonstrated a series of new imine POCs, **CC16**, **CC17**, **CC18** and **CC19**, with a range of chemical functionalities on the cage periphery. They used different functionalised diamine precursors, and this led to cage compounds of different sizes and porosities, including one cage with the reactive sites for further post-synthetic modification. Twelve symmetrically peripheral hydroxyl groups in the **CC17** molecule allowed it to be amenable to further functionalisation, for example, modifying the properties such as solubility or melting point.

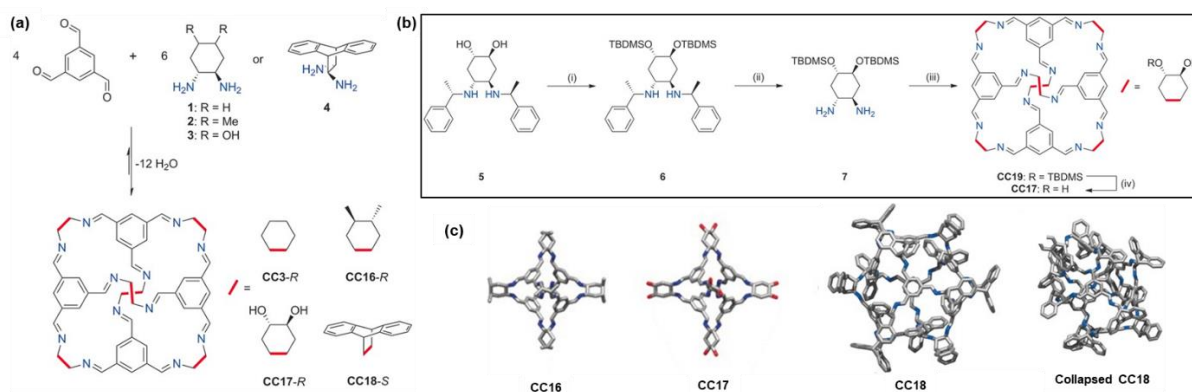


**Figure 5.3** (a) Reaction Scheme for the synthesis of cages **CC16** and **CC17**. The [4+6] isomer of **CC18** was not isolated; instead, a larger [8+12] cage was formed. (b) Reaction Scheme for the synthesis of a periphery-functionalised POC, **CC17**. (c) Molecular structures of **CC16**, **CC17**, **CC18**, and collapsed **CC18**. Reprinted from reference<sup>17</sup> with permission.

Meanwhile, the same group<sup>18</sup> reported the synthesis of dodecaamide cages from organic imine cage **CC1** via reduction to an amine cage, **RCC1**. This simple, one-step amidation reaction (**Figure 5.4**(a)) has produced a range of 12-arm organic building blocks (the molecular structure of one of these is shown in **Figure 5.4**(b)) for supramolecular chemistry via the derivatisation of **RCC1**. As an example of the post-synthetic modification, large, rigid, microporous 12-arm dendrimers have been prepared. This also enables the preparation of other framework materials such as MOFs or COFs comprising POC with intrinsic porosity as linkers. For example, a cage-MOF complex was prepared between **RCC1** and zinc nitrate (**Figure 5.4**(c) and (d)), where **RCC1** was used as a porous organic linker.

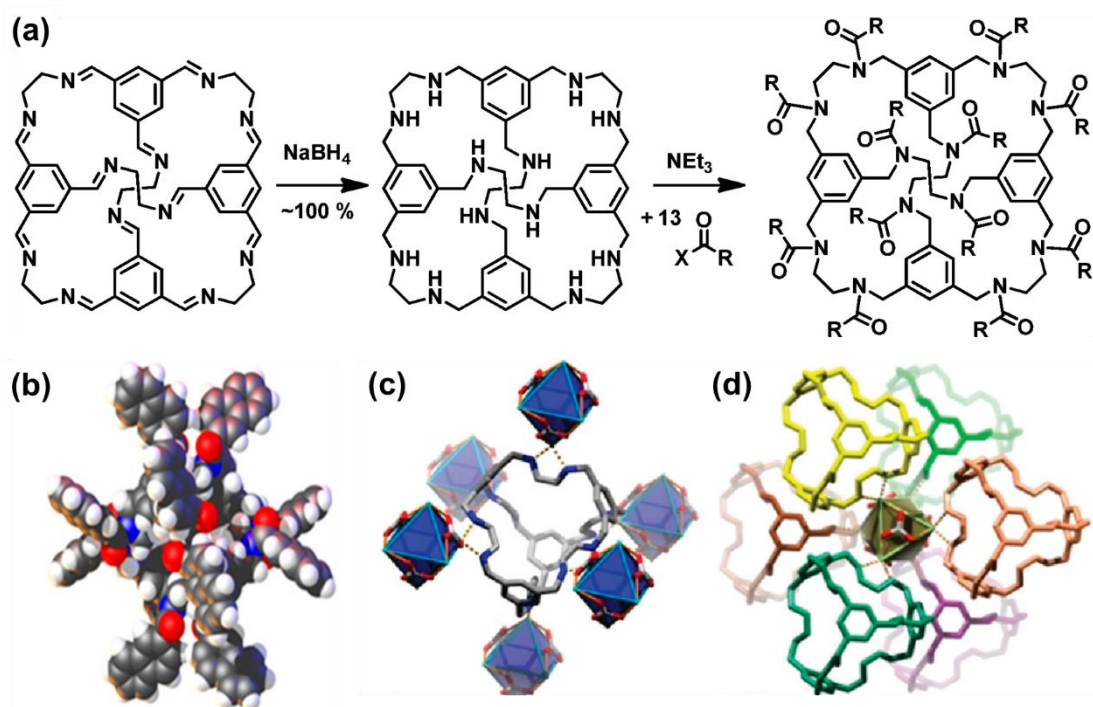


**Figure 5.4** (a) Synthesis of dodecaamide cages from organic imine cage *CCI* via reduction to an amine cage, *RCCI*. (b) Molecular structure of a dodecaamide cage. Reprinted from reference<sup>18</sup> with permission. (c) A single *RCCI* cage is linked to six octahedral ( $Zn_6(\mu_3-CO_3)_4$ )<sup>4+</sup> clusters in the MOF, nitrogen shown in blue, oxygen in red, carbon in gray. (d) Each zinc cluster is linked to six *RCCI* molecules. Reprinted from reference<sup>19</sup> with permission.

Since then, imine cage molecules were reduced to amines for post-synthesis functionalisation, as well as for improving their chemical stability. However, this introduces molecular flexibility and leads to poor or even none permanent solid-state porosity. Cooper group<sup>20</sup> has reported a post-synthesis strategy to achieve shape persistence in amine cages by tying the cage vertices with carbonyls such as formaldehyde or acetone. The synthesis route and the reaction are shown in **Figure 5.5**, where one acetone molecule can be reacted with the diamine in one *RCC3* molecule. In contrast, six formaldehyde molecules can be reacted to the six diamine sites. As a result, these tied cages showed enhanced porosity and unprecedented chemical stability toward acidic or basic conditions.

As the POC can be pre-modified or post-functionalised by other chemicals and gain additional chemical structure with modified properties, it is reasonable the structure of these membranes consisting of POCs can be tuned. In **Chapter 4**, a crystalline membrane consisting of pure POCs (*CC3*) has been prepared and studied, and the membrane was found to show switchable pore apertures by a solvent stimulus. The switchable pore structures have resulted from the



change of the external environment rather than the intrinsic pore size. On the other hand, it is believed that the POC based membranes can be tuned if the chemical functionalities or the structures of the POC itself could be altered.

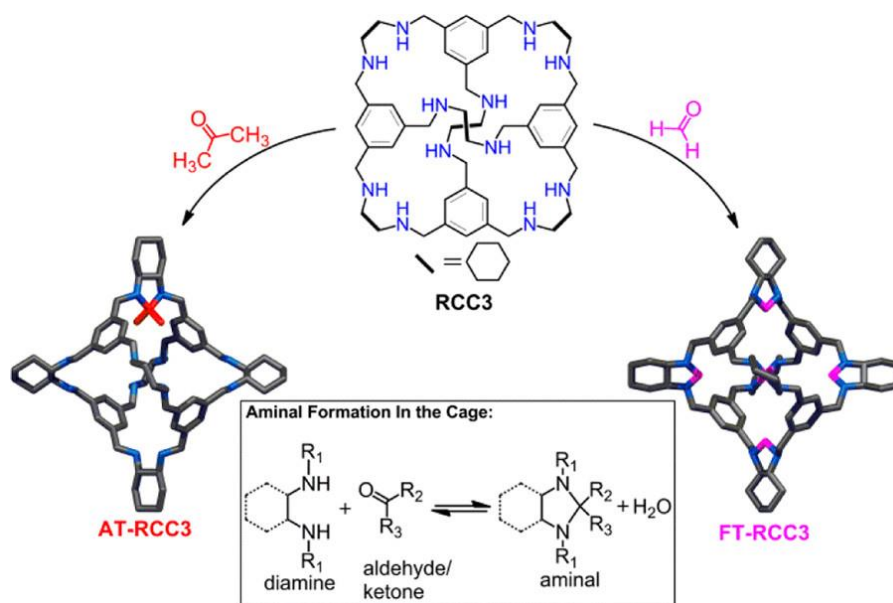


**Figure 5.5** Synthesis of “tied” porous cages by acetone and formaldehyde. Reprinted from reference<sup>20</sup> with permission.

Herein, the POC based membranes showing tuneable molecular sieving properties have been fabricated and post-modified in this Chapter. Both pre-synthesis functionalisation and post-synthesis functionalisation approaches have been utilised to enable the membrane with tuneable separation ability.

To introduce a similar pore network with different pore channels into the membrane, a series of reduced imine POCs were used as precursors for the synthesis of the membrane material. Taking RCC1 as an example reagent, a novel synthesis via interfacial polymerisation (IP) method to fabricate target membranes has been proposed in **Figure 5.6**. Three aminic cages, RCC1, RCC2 and RCC3, synthesised by reducing imine containing cages (CC1, CC2 and CC3), have been utilised as a reactive monomer for IP with reactive linkers. These RCC molecules have a similar tetrahedral structure but with different linkages to the cage windows.

With the fast interface reaction of trimesoyl chloride (TMC) in the organic phase and POCs in the aqueous phase, continuous thin film has been formed at the interface in a short time with the desirable cage-shape windows. The obtained ultrathin nanofilm (10~50 nm) retains the interconnected, sub-1 nm pore channels with a narrow size distribution, as well as robust



crosslinked and well-defined structures. All these characteristics endow the nanofilms with enhanced solution permeability and good selectivity, thus making them attractive materials in water treatment for NF and RO applications, including the filtration of NaCl or MgSO<sub>4</sub> aqueous solution and the removal of heavy metal ions from wastewater such as Cd<sup>2+</sup> and Hg<sup>2+</sup>. Importantly, the obtained membranes with **RCC1**, **RCC2** and **RCC3** showed different permeance and rejection values due to the variety of the structures on the nanofilms, indicating that the membranes can be tuned for adjustable and precise molecular sieving.

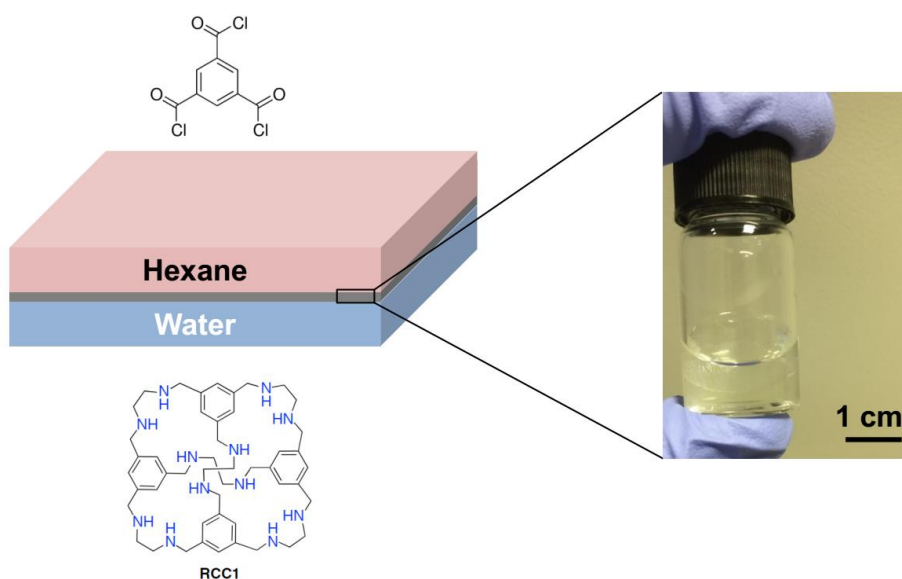


**Figure 5.6** Schematic of the interfacial polymerisation process at a free aqueous–organic interface with **RCC1** and TMC, and an image of the actual object at the interface in a glass vessel.

Moreover, these POC based crosslinked membranes can be further post-functionalised since they retain the basic structure and chemical skeleton of a single POC molecule. In this Chapter, a novel post-synthetic functionalisation method inspired by the previous work has been demonstrated by using formaldehyde as the post-treatment linker.

## 5.2 Fabrication of Nanofilm Composite Membranes

Since the reduced cage molecules show a better solubility in an aqueous solution, water was used for dissolving the cages, and the interface was obtained by layering organic liquid on the water phase. As is shown in **Figure 5.7**, polyamide nanofilm was fabricated by the condensation polymerisation of trimesoyl chloride (TMC) in hexane and reduced cage

monomers dissolved in water, including RCC1, RCC2 and RCC3. TMC, which can form three amide groups, was used as a crosslinker for the interfacial polymerisation for its rapid reaction rate. Instead of a 3D network formed in one homogenous phase, ultra-thin film was formed at the liquid-liquid interface by the restriction of two immiscible solvents.

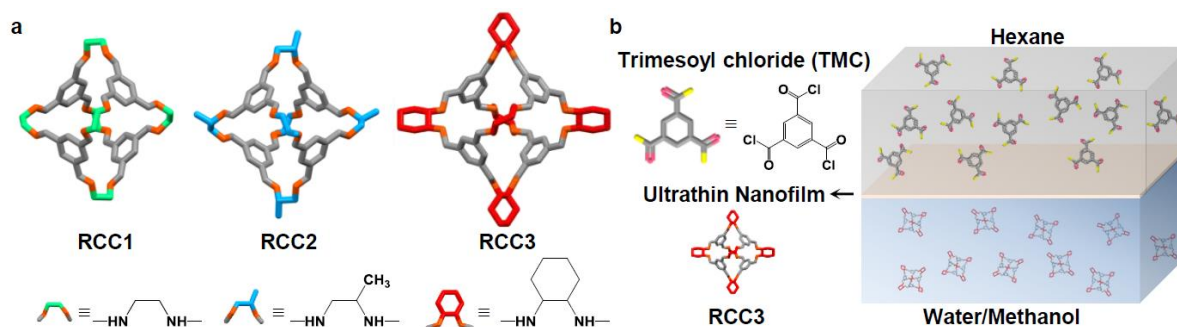


**Figure 5.7** Fabrication of ultrathin polyamide nanofilms incorporating porous organic cages. (a) Schematic demonstrating the molecular structure of various reduced crystalline cages (RCC) comprising flexible amine bonds and tuneable alkane linkages. (b) Fabrication of ultrathin polyamide nanofilm at a free interface between a water/methanol solution containing RCC molecules and a hexane solution containing trimesoyl chloride (TMC).

As a result, the interfacial reaction was rapid in seconds to minutes, with free-standing, continuous film formed rapidly at the interface (**Figure 5.8** (a) and (b)). They were then able to be collected on different substrates. Cage nanofilms deposited on anodised aluminum (AAO) or silicon wafer have been used to characterise their morphology and thickness, and the films on the PAN support membrane (cage nanofilm composite membrane) have been applied for separation tests. Remarkably, a large-scale composite membrane (more than 9 cm in diameter, **Figure 5.8** (c)) was obtained using this novel interfacial synthesis approach.

All RCC molecules we used in the reaction are alike with a tetrahedral structure (**Figure 5.7**(a)). The only difference is the linkage varying from C-C (RCC1) to C-C connecting with an extra methyl (RCC2) to C6 cyclic (RCC3), and the structure and the performance of the obtained nanofilms will be studied. Other reduced cages, such as RCC5, have less or even no solubility in water, although they can have larger windows that may contribute to a different pore structure. They have been synthesised and used for nanofilm fabrication, but no successful examples have been obtained yet.

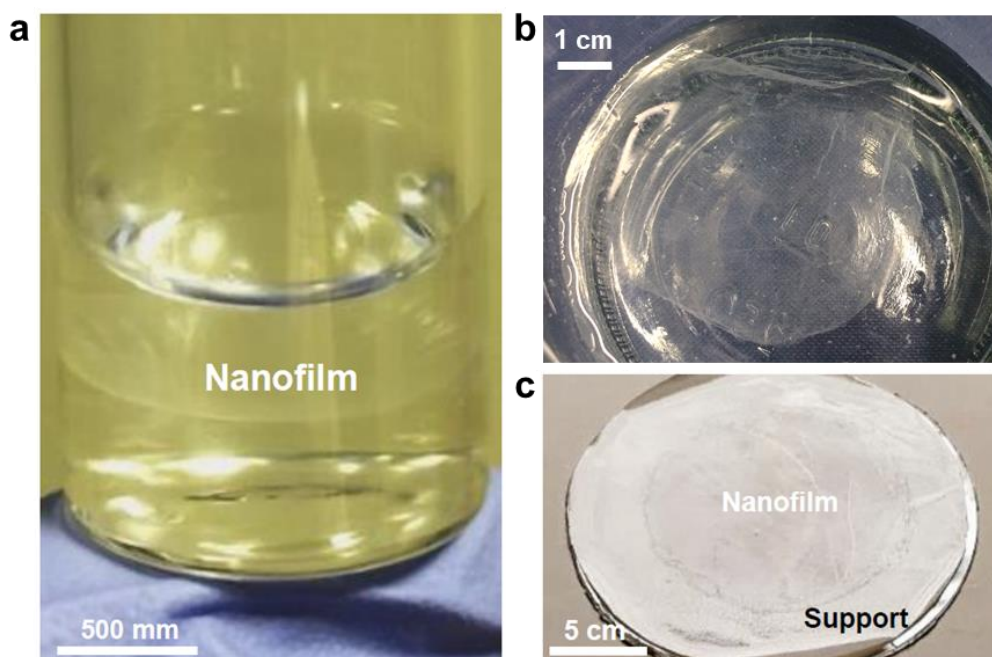


**Figure 5.8** *Photographic image of an ultrathin nanofilm fabricated from reduced amine cages (RCC) and trimesoyl chloride (TMC) in large scale and that on the PAN support membranes. (a) Side view of a RCC nanofilm at a free interface in the beaker. (b) Top view of a RCC nanofilm at a free interface in the beaker. (c) Photographic image of a composite membrane comprising a nanofilm transferred from the free interface onto a polyacrylonitrile (PAN) support.*

### 5.3 Surface Characterisation and Morphology Study

The surface morphologies of these nanofilms have been investigated by SEM and AFM, using a series of nanofilms deposited on different substrates, including AAO, silicon wafers and PAN support membranes.

The RCC1 nanofilm was first to be observed on AAO support under SEM (**Figure 5.9**), which exhibits continuous and homogenous surface morphology. The crosslinked cage nanofilm is thin and uniform, and no visible defects were found on the surface. From its cross-sectional images, the nanofilm was appeared to be very thin, which was down to a few nanometres.

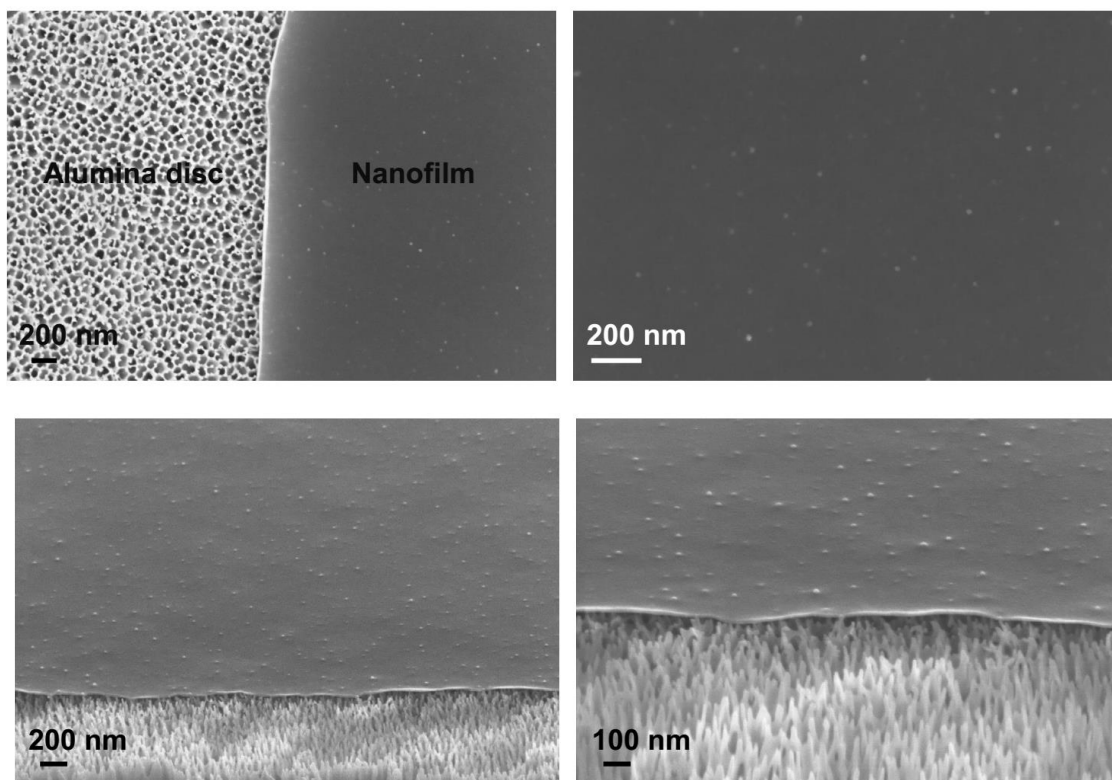


**Figure 5.9** SEM images for a composite membrane comprising the nanofilm made from 0.1 wt.% RCC1 and 0.1 wt.% TMC (RCC1 nanofilm) at a free interface and then transferred onto an alumina support, showing its surface morphology and cross-sectional structures.

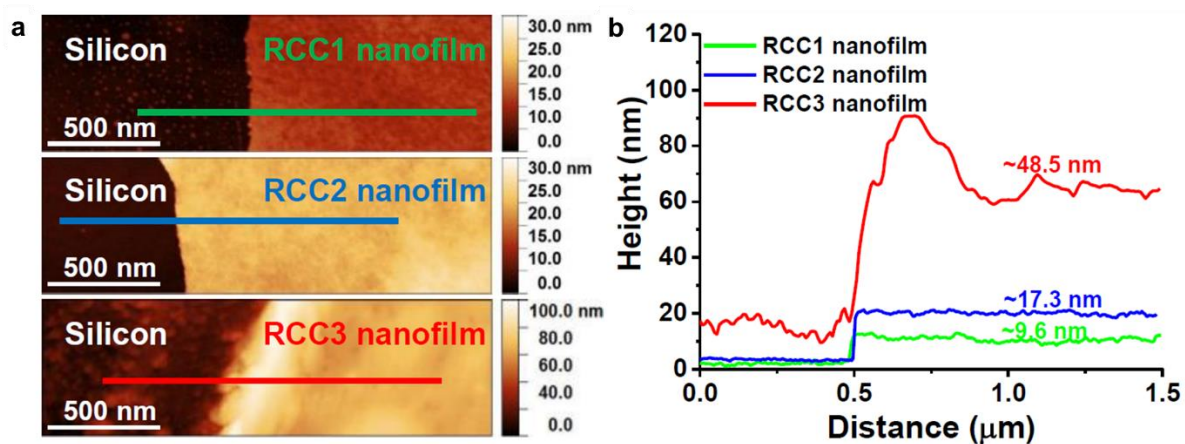


**Figure 5.10** (a) Atomic force microscopy (AFM) height image of the nanofilms made from RCC1, RCC2, and RCC3 reacting with TMC and then transferred on silicon wafers. (b) Height profile of the lines scanned in (a).

The thicknesses of the nanofilms were then precisely detected by atomic force microscopy (AFM) on silicon wafers. As is shown in **Figure 5.10**, the RCC3 nanofilm exhibited a much thicker thickness of ~50 nm, whilst the RCC1 nanofilm has a thickness ~10 nm, and the RCC2

one is ~20 nm thick. The difference in the thickness of these nanofilms indicated that the structure of the film would be different due to the different linkages on the nascent cage monomers. With the thickness in tens of nanometres which contributes to the high permeance, and no visible defects contributing to high rejection, the ultra-thin and crosslinked nanofilms were expected to be promising in the molecular separation area.

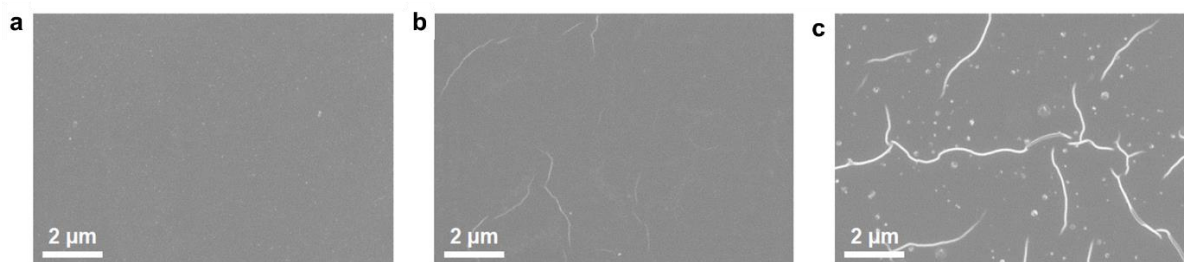


**Figure 5.11** SEM surface images of the nanofilms made from **a**, RCC1, **b**, RCC2, and **c**, RCC3 reacting with TMC and then transferred on PAN supports.

To study the difference of the cage nanofilm composite membrane structure, the surface morphology of RCC1 transferred onto PAN support was further compared with RCC2 and RCC3 films on the same supports. As is shown in **Figure 5.11**, instead of the smooth surface morphology for RCC1 nanofilm, a surface with a few more strips was observed for RCC2 film, and more stripes/wrinkles and some uneven spots were found on the crumpled RCC3 film. Interestingly, the morphology of the RCC3 nanofilm looked like the formation of the Turing pattern, which usually consists of stripes or spots<sup>21</sup>. One recent example of polyamide membranes with nanoscale Turing structures was reported by Zhang et al.<sup>21</sup> in 2018. In the study, they have fabricated polyamide membranes using the interfacial polymerisation method, where the reactions occur at the interface between oil and water layers. The addition of polyvinyl alcohol to the aqueous phase reduced the diffusion of the monomer, and this generated the membranes with Turing patterns like bumps, voids, and islands, which were proved to show better performance for water desalination.

Other characterisations, including element analysis, Brunauer-Emmett-Teller (BET) surface area analysis, thermogravimetric analysis (TGA), FT-IR and Raman, were utilised further to study the nanofilm at the Imperial College London, and the measurements are still in process.



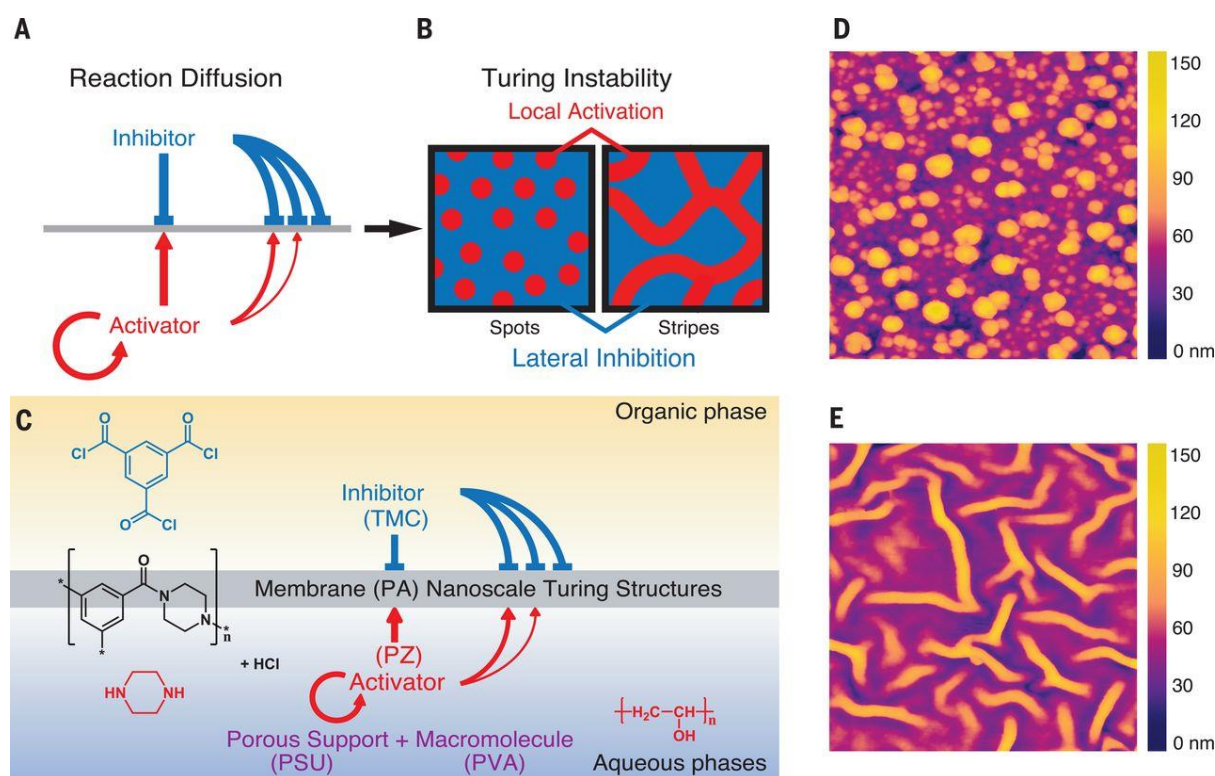


**Figure 5.12** Turing-type structures in interfacial polymerisation. (a) Schematic diagram of activator-inhibitor interaction in a reaction-diffusion process. (b) Spatial representation of local activation and lateral inhibition. In two dimensions, Turing structures generally consist of spots or stripes. (c) Schematic illustration of interfacial polymerisation Turing system. (d and e) AFM topography images of the Turing-type PA membranes. Bright yellow and orange regions correspond to the formed solid-state nanoscale Turing structures. Reprinted from reference<sup>21</sup> with permission.

## 5.4 Post-functionalisation of the Nanofilm

In the previous reports<sup>18–20</sup>, imine cage molecules that were reduced to amines were processed using various post-synthesis functionalisation strategies. For example, the diamines in the RCC1 were utilised for synthesising 12-arm dendrimers<sup>18</sup>, or used as the organic linkers for cage-MOFs<sup>19</sup>. It was found that the diamines in RCC3 can be reacted with small carbonyl molecules<sup>20</sup>. One of the suitable “tie” molecules on the cage vertices was formaldehyde because it is the smallest carbonyl molecule and it is highly reactive. As is shown in **Figure 5.5**, one of the six diamine vertices on each RCC3 cage was able to be reacted with acetone to afford a new molecule, acetone tied RCC3, by forming a 5-member imidazolidine (aminal)

ring;. In contrast, all the six diamine sites were occupied by formaldehyde immediately, giving a formaldehyde tied **RCC3** product after washing with methanol and drying.

Gas adsorption analysis for desolvated acetone tied **RCC3** showed a very low amount of  $N_2$  (1.11 mmol/g) and  $H_2$  (1.29 mmol/g) adsorption at 77 K and 1 bar (**Figure 5.13(a)**), with a BET surface area of only  $67\text{ m}^2/\text{g}$ . This resulted from its crystal structure where disconnected voids were found because the dimethyl groups blocked two of the four windows on each acetone tied **RCC3** molecule. This cage material showed a surprising high  $CO_2$  uptake at ambient temperature (**Figure 5.13(b)**), and the ideal gas selectivity for  $CO_2/N_2$  was calculated as  $57^{20}$ .

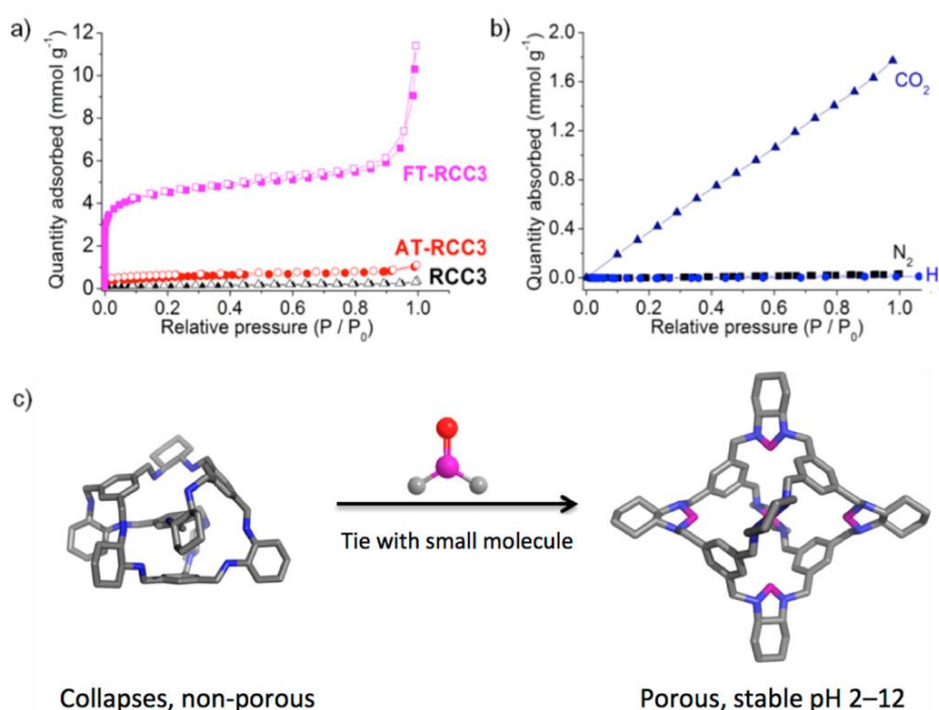


**Figure 5.13** (a)  $N_2$  adsorption/desorption isotherms at 77 K showing a substantial increase in porosity for FT-RCC3 vs AT-RCC3 and RCC3. Solid symbols, adsorption; open symbols, desorption. (b)  $CO_2$  (navy triangles),  $N_2$  (black squares), and  $H_2$  (blue circles) adsorption isotherms for AT-RCC3 at 298 K. (c) Scheme showing the non-porous RCC3 has been tied up by formaldehyde to be porous RCC3. Reprinted from reference<sup>20</sup> with permission.

Unlike acetone tied **RCC3**, there was no indication of any loss of crystallinity for formaldehyde tied **RCC3** after either desolvation or after gas adsorption. Therefore, it was observed that formaldehyde tied **RCC3** adsorbed 11.2 mmol/g at 77 K and 1.0 bar with an apparent BET surface area of  $377\text{ m}^2/\text{g}$ , 4.3 mmol/g of  $H_2$  at 77 K and 1.0 bar, and 1.42 mmol/g of  $CO_2$  at 298 K and 1 bar (**Figure 5.13(a)**). The BET surface area was slightly lower than the  $409\text{ m}^2/\text{g}$

measured for the parent imine cage, **CC3**<sup>22</sup>, but compared to the non-porous **RCC3**, it showed a shape-persistent structure comprising a permanent void. Also, the formaldehyde tied **RCC3** has exhibited excellent stability toward water and also to both acids and bases (**Figure 5.13(c)**).

Therefore, the nanofilms were further post-functionalised by using formaldehyde as the post-treatment linker. This could happen because there are unreacted diamines remaining in the crosslinked cage networks. There are twelve amine sites in total in one cage molecule, and ideally, they should have all been reacted with the crosslinker TMC with three amide groups due to their high reactivity and rapid reaction rate. However, the size of the TMC provided steric hindrance while reacting with the closely packed cage molecules, causing fewer TMC molecules could be anchored on the amine sites. Therefore, the remained diamines became available for post-functionalisation. Theoretically, **RCC3** nanofilms appeared to have more unreacted amines and, thus, are more reactive with formaldehyde, as the steric hindrance of the crosslinker in **RCC3** is larger than **RCC2** and **RCC1**. Herein we applied **RCC3** nanofilm as the model sample to study its post-functionalisation. As is shown in **Figure 5.14**, the adjacent unreacted amines in the **RCC3** nanofilm were reacted and thus 'tied' by formaldehyde, leading to a reduced cavity size of the nanofilm. The formaldehyde tied **RCC3** nanofilm is referred to hereafter as **FT-RCC3**.

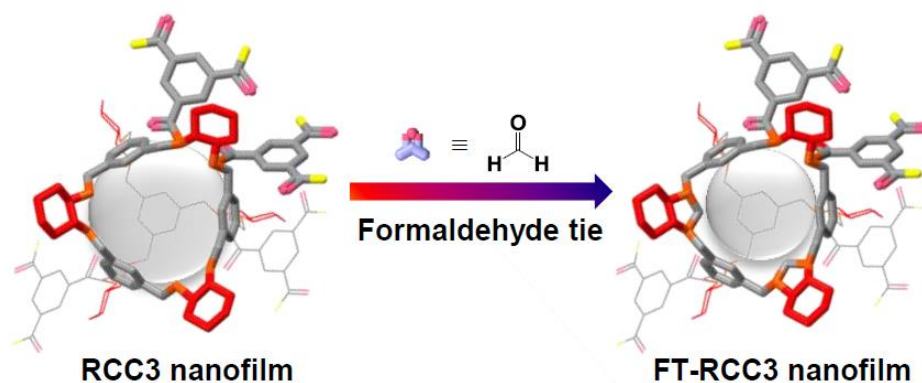


**Figure 5.14** Formation of formaldehyde tied **RCC3** (**FT-RCC3**) nanofilm by soaking **RCC3** nanofilm in formaldehyde solution overnight, wherein adjacent unreacted amines of **RCC3** nanofilms were tied up to reduce the cavity size.



## 5.5 Structure and Composition Study of the Nanofilm

To study the structure and composition of the nanofilms before and after the post-functionalisation, GIXRD and XPS measurements were carried out on the composite membranes or the free-standing nanofilms.

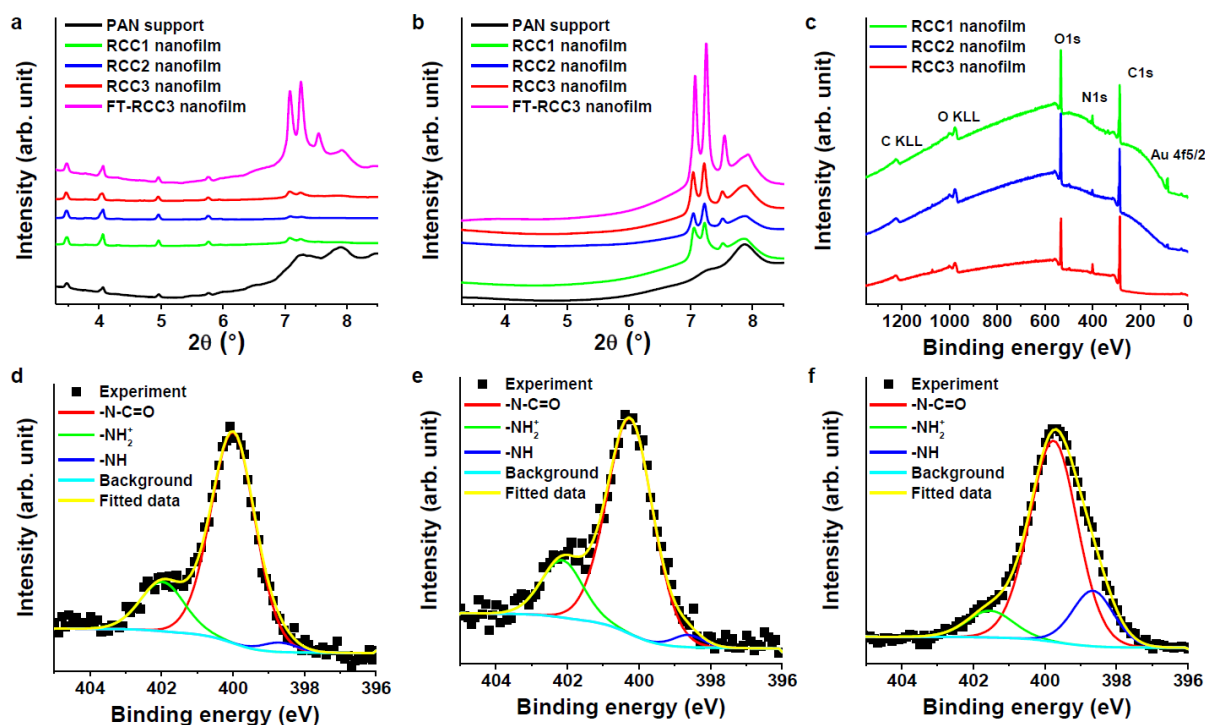


**Figure 5.15** Characterisation of composite membranes comprising nanofilms incorporating porous organic cages. Grazing incidence X-ray diffraction (GIXRD) diffraction pattern of **a**, in plane and **b**, out of plane to the nanofilm surface on polyacrylonitrile (PAN) support. **c**, X-ray photoelectron spectroscopy (XPS) survey spectra of free standing RCC1, RCC2, and RCC3 nanofilms on gold coated silicon wafers. XPS N1s narrow scan of **d**, RCC1 nanofilm, **e**, RCC2 nanofilm, and **f**, RCC3 nanofilm.

The GIXRD was performed on the nanofilm composite membranes. The in-plane diffraction is parallel to the film surface, and the data is shown in **Figure 5.15(a)**. Basically, RCC1, RCC2, and RCC3 did not show any distinctive diffraction pattern apart from the PAN background, meaning no straight and periodic pores throughout the film. After tie-up, a distinctive diffraction pattern was pronounced on FT-RCC3 nanofilm, indicating stiff bonding after tie-up creates periodic pores. For the out-of-plane diffraction, which is perpendicular to film surface, all nanofilms showed a distinctive diffraction pattern than PAN background (**Figure 5.15(b)**), meaning one layer is stacked on another in an orientated manner, or in other words,

the interspace is periodic. The GIXRD data, however, needs to be further confirmed for the nanofilms on other substrates with a cleaner background, rather than PAN support which has a strong and complex background signal, so that the influence from the background would be minimised.

XPS has been performed for the nanofilms on gold-coated silicon wafers. As is shown in **Figure 5.15(c)**, the decrease of the gold (Au) peak was found for the **RCC1** to **RCC2** to **RCC3** nanofilms, indicating thicker film formation. This corresponds to the thickness data confirmed by AFM. Moreover, XPS narrow scans for N1s have been carried out on these nanofilms, to investigate the composition of the functional groups on the films. As interpreted from **Figure 5.15(d)** to (f), the percentage of crosslinked amines is the least for **RCC3** nanofilm, indicating the potential adjacent amine available for formaldehyde tie-up. This is reasonable because the **RCC3** molecules are larger with the cyclohexyl linkages (**Figure 5.7(a)**), which contributed to more hindrance and less interaction while reacting with the crosslinker TMC. To further confirm the percentage of free amines converted to the tied up amines, XPS of FT-**RCC3** has been done at Imperial College London, and the data is currently being processed.

## 5.6 Membrane Performance for Separation

To check whether a defect-free membrane was obtained, **RCC1** nanofilm composite membrane has been used to study the membrane performance, which was prepared using 0.2 wt.% **RCC1** reagent reacted with 0.2 wt.% TMC. During the performance tests, the composite membrane was proved to be robust to withstand 20 bar, showing the strength of the nanofilm. The permeance of different solvents was calculated in **Figure 5.16(a)**. The nanofilm appeared hydrophilic, exhibiting high water permeance ( $3.85 \text{ L}\cdot\text{m}^{-2}\cdot\text{h}^{-1}\cdot\text{bar}^{-1}$ ) and low toluene permeance ( $0.442 \text{ L}\cdot\text{m}^{-2}\cdot\text{h}^{-1}\cdot\text{bar}^{-1}$ ).

Negatively charged dyes with various molecular weights ranging from 1000 to 300 Da were diluted in water as the feed for dead-end filtration. As shown in **Figure 5.17(a)**, the permeance is around  $3.6 \text{ L}\cdot\text{m}^{-2}\cdot\text{h}^{-1}\cdot\text{bar}^{-1}$ , and all show excellent rejections around 98 % for dyes with a molecular weight larger than 300 Da. After the filtration of the nanofilm, the permeate solution has become colourless compared with the feed solution with strong yellow colour (**Figure 5.17(b)**). The dye filtration experiment confirmed that the **RCC1** nanofilm composite membrane is defect-free and behaves well for separation.

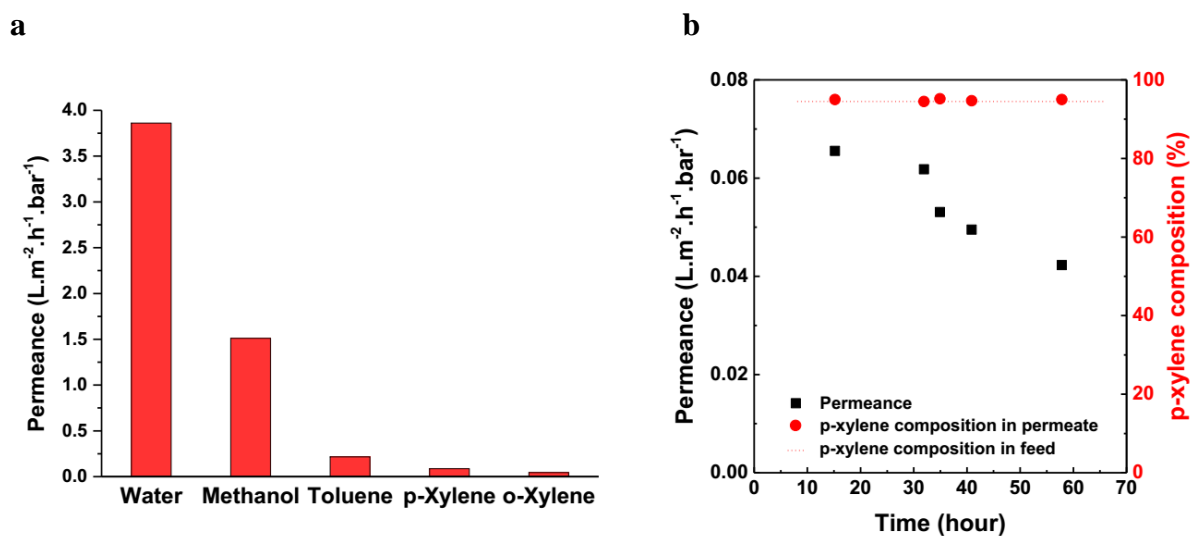


**Figure 5.16** (a) Different solvent permeance and (b) xylene separation by RCCI nanofilms.

To investigate the possibility to achieve one of the most challenging applications in membrane field, p-xylene and o-xylene separation<sup>23</sup>, for the nanofilm, a feed of p-xylene (95 vol.%) and o-xylene (5 vol.%) was tested in dead-end filtration. The permeance of p-xylene ( $0.086 L \cdot m^{-2} \cdot h^{-1} \cdot bar^{-1}$ , **Figure 5.16(b)**) was found to be twice of o-xylene ( $0.043 L \cdot m^{-2} \cdot h^{-1} \cdot bar^{-1}$ ), however no separation of p-xylene over o-xylene was seen after 60 hours filtration.

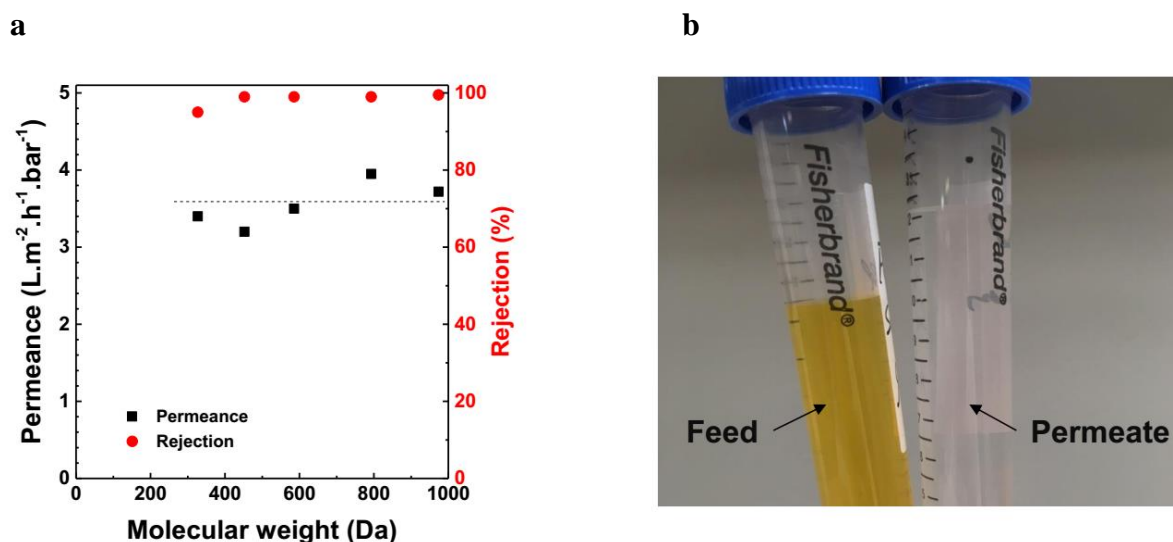


**Figure 5.17** (a) Water permeance and dye rejection of the RCCI nanofilms; (b) digital photographs of the the feed solution and permeate solution after the filtration by cage nanofilm.

To explore the possibility of the NF membranes for water purification or desalination,  $\text{MgSO}_4$  in water solution ( $1\text{g}\cdot\text{L}^{-1}$ ) was used as feed for dead-end filtration. During a three-hour running process, the water permeance is around  $3\text{ L}\cdot\text{m}^{-2}\cdot\text{h}^{-1}\cdot\text{bar}^{-1}$ , the salt rejection is around 90% (**Figure 5.17**), exhibiting good NF performance for common ions in aqueous conditions. It should be noted that the rejection could be further improved in a cross-flow environment for mitigating concentration polarisation and allowing membranes to reach a steady state. Other multivalent ions have been used for filtration tests, and monovalent ions were applied to investigate the desalination performance of the nanofilm at Imperial College London. However, the measurements are still ongoing, and the results are not discussed in this thesis.

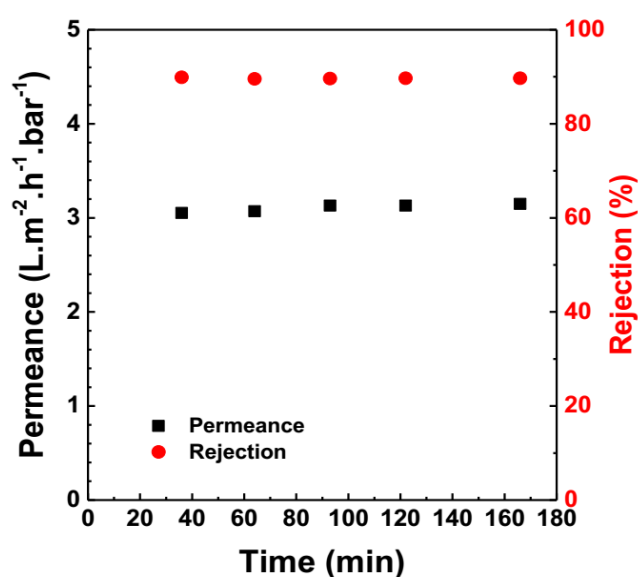


**Figure 5.18** Permeance of water and rejection of  $\text{MgSO}_4$  for the RCC1 nanofilm in the duration of 3 h.

The RCC1 nanofilm has shown comparable water permeance to other traditional NF membranes<sup>24</sup> ( $2\text{--}3\text{ L m}^{-2}\text{ h}^{-1}\text{ bar}^{-1}$ ) with a similar rejection, but the value is not attractive. To further improve the permeance of the membranes, the concentration was adjusted to 0.1 wt.% of reduced cage monomers with 0.1 wt.% TMC, and a series of RCC1, RCC2, and RCC3 nanofilms were fabricated for the membrane performance. The permeances of various pure solvents, including water, ethanol, methanol, acetonitrile, acetone, hexane, toluene, and heptane, have been measured and shown in **Figure 5.19(a)**. RCC2 and RCC3 membranes showed nearly twice higher water permeance than that of RCC1 composite membrane, whilst RCC3 exhibited a few times higher permeance for all the organic solvents than RCC1 and RCC2.

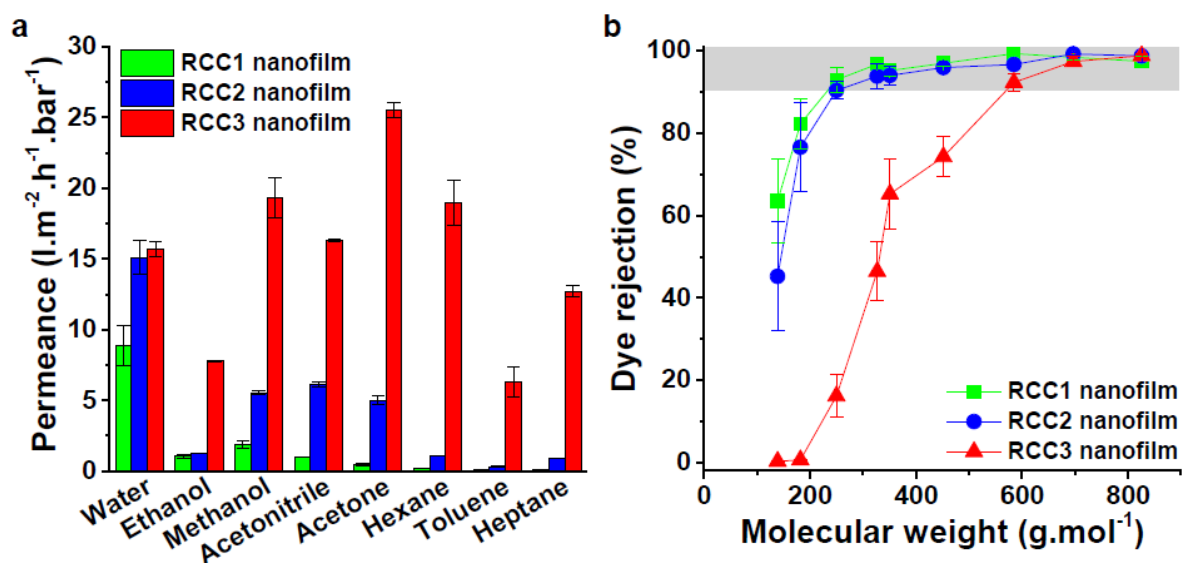


**Figure 5.19** (a) Permeance of pure solvents for nanofilms made from RCC1, RCC2, and RCC3 at 0.1 wt.% reacted with 0.1 wt.% TMC and then transferred on PAN supports. (b) Dye rejections for RCC1, RCC2, and RCC3 membranes in a.

MWCO curves have been concluded from the dye rejection measurements, and a dramatic shift of MWCO has been observed. As is shown in **Figure 5.19(b)**, both RCC1 and RCC2 nanofilms showed a similar MWCO of  $\sim 250 \text{ g}\cdot\text{mol}^{-1}$  (the rejection of Trolox dye with  $250 \text{ g}\cdot\text{mol}^{-1}$  molecular weight is 90%), whilst RCC3 nanofilm had a larger cutoff of  $\sim 600 \text{ g}\cdot\text{mol}^{-1}$  with the rejection for acid fusion dye ( $585 \text{ g}\cdot\text{mol}^{-1}$ ) is  $\sim 92\%$ . RCC3 nanofilms exhibited a very distinct guest sieving property, although they all consisted of similar cage units with tetrahedral structures (**Figure 5.7(a)**), indicating that larger pores were formed in RCC3 nanofilm. The shift of the MWCO also matches the XPS data and the permeance values. This could have resulted from a larger steric hindrance of RCC3 than the other cage molecules, and thus less available amines in RCC3 were reacted with TMC.

Furthermore, membranes with lower concentration have been fabricated on RCC3 nanofilms, using 0.05 wt.% and 0.02 wt.% of the reagents RCC3 and TMC, compared to 0.1 wt.% of these, referred to hereafter as RCC3-0.05, RCC3-0.02, and RCC3-0.1. The dye filtration data of these membranes is shown in **Figure 5.20**. Three different nanofilms all showed a very similar MWCO of  $585 \text{ g}\cdot\text{mol}^{-1}$  for the dye molecules, where the UV-vis spectra and photos of acid fuchsin dye for feed, permeate, and retentate solutions have been shown in **Figure 5.20(b)**. However, the lowest permeance of RCC3-0.02 nanofilm is unusual, as the thickness of RCC3-0.02 should be the thinnest among all, leading to the highest permeance. Generally, the permeance of a membrane depends on the porosity, operating pressure, pore diameter and

thickness of the selective membrane<sup>24</sup>; with other conditions are the same, the thinner selective layer is, the higher permeance the membrane has. A possible reason for the unusual permeance value for RCC3 nanofilm could be a lower crosslinking degree of RCC3-0.02 nanofilm from a lower concentration of RCC3. This results in the compaction of the membrane due to the collapse of a loosely crosslinked nanofilm.

On the other hand, more free amine residue would be available in RCC3-0.02 nanofilm. This creates a potential to make a tighter membrane by fabricating FT-RCC3-0.02 nanofilm wherein more amines are tied up to further reduce the cavity size in contrast to FT-RCC3-0.1 shown in **Figure 5.21**. The thickness of these nanofilms made at different concentrations has been measured at Imperial College London. However, the measurements are still ongoing, and the results are not yet discussed in this thesis.

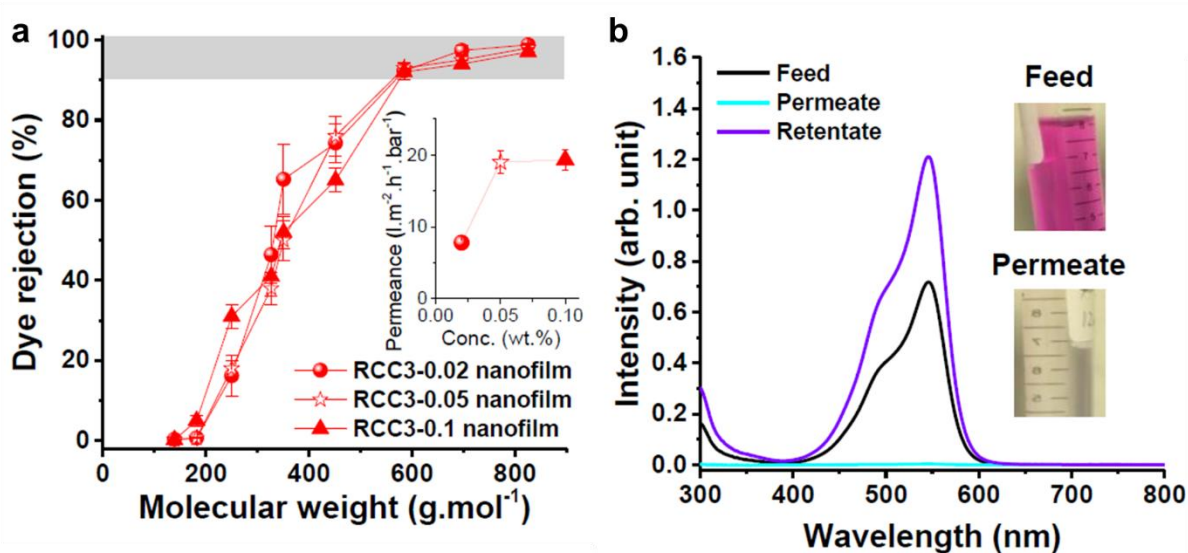


**Figure 5.20** (a) Dye rejections of nanofilms made from 0.02 wt.%, 0.05 wt.%, and 0.1 wt.% RCC3 reacted with 0.1 wt.% TMC and transferred onto PAN supports. Inset shows the methanol permeance of these nanofilms. (b) Ultraviolet visible (UV-vis) spectra of acid fuchsin dye for feed, permeate, and retentate solutions. The inset shows the feed and permeate solutions.

To investigate the influence on the membrane performance by post-functionalisation, FT-RCC3 nanofilms have been used for dye filtration experiments. As is shown in **Figure 5.21**, the FT-RCC3 nanofilm showed slighter lower permeance for methanol, and the dye rejection data exhibited a shift of MWCO, which is 585 g.mol<sup>-1</sup> for RCC3 and a tighter MWCO of 452 g.mol<sup>-1</sup> for FT-RCC3. The result indicated narrower pores were formed in FT-RCC3 nanofilm after tied with the formaldehyde molecules. Therefore, the pore structure of the nanofilm

composite membrane has been successfully tuned by post-functionalisation such as formaldehyde tie-up strategy.

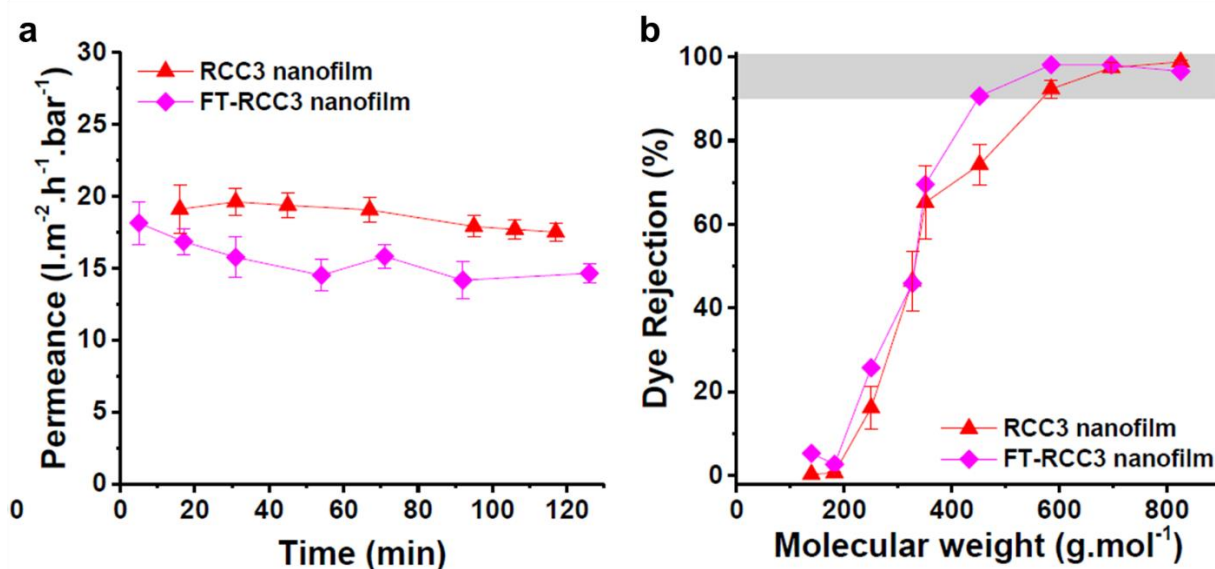


**Figure 5.21** (a) Methanol permeance over time for RCC3 nanofilm and formaldehyde tied RCC3 nanofilm (FT-RCC3). (b) Dye rejections for RCC3 and FT-RCC3 nanofilms.

## 5.7 Conclusions and Future Work

In this Chapter, thin-film composite membranes comprising a cage nanofilm separating layer have been fabricated at a free aqueous–organic interface. Transfer of these ultrathin nanofilms onto porous supports provided fast water transport through the resulting nanofilm composite membranes. The RCC1 nanofilm was continuous and robust, with an ultrathin thickness of about 10 nm. Supported by the crosslinker, the reduced cages are supposed not to collapse in solid state and are equipped with excellent pore channels for separation. With the defect-free and hydrophilic nanofilm, the composite membranes have shown high rejection of dyes as well as salt ions.

In addition, a series of nanofilms made from RCC1, RCC2 and RCC3 exhibited distinctive performance by altering the molecule type. The surface morphology and composition of the nanofilms have been investigated to link their permeance and rejection performance to the membrane structures. RCC1 and RCC2 nanofilms had a similar MWCO of  $\sim 250 \text{ g}\cdot\text{mol}^{-1}$ , while RCC3 nanofilm showed a shift of its cutoff to  $\sim 600 \text{ g}\cdot\text{mol}^{-1}$ . The RCC3 nanofilm has been used for post-functionalisation where the unreacted amines were tied up by formaldehyde.

Tunable sieving effect was found in the FT-RCC3 nanofilm that the MWCO shifted from  $\sim 600 \text{ g}\cdot\text{mol}^{-1}$  to  $\sim 450 \text{ g}\cdot\text{mol}^{-1}$  after the tie-up procedure.

Hence, the cage nanofilm composite membranes showing adjustable molecule separation properties have been successfully designed and fabricated by altering the monomeric cage molecule type in the interfacial synthesis pathway and a tie-up post-functionalisation strategy. This makes these materials exciting candidates for different applications in many important fields, such as wastewater treatment<sup>25,26</sup>, water purification<sup>27,28</sup>, heavy metals removal<sup>29,30</sup>, formaldehyde removal<sup>31–33</sup>, and chiral separation<sup>34,35</sup>.

The accurate pore structures of these nanofilms, however, have not been well studied. The computation modelling and simulation are further needed for DFT pore size estimation. The degree of crosslinking in the nanofilms needs to be studied by relevant characterisations such as XPS. Further investigation on the functionality of the nanofilms is still required, for example, by using other POCs with different pore sizes or structures such as RCC5, RCC17 and TCC1. Nevertheless, the systemic study of these novel membranes would contribute to a comprehensive understanding of the functional membranes with tuneable molecular sieving ability and bring insights to the design of the next-generation membrane materials.

## 5.8 Acknowledgements

In this Chapter, I would like to thank Prof. Andrew I. Cooper, Prof. Andrew G. Livingston, Dr. Zhiwei Jiang and Dr. Marc A. Little, for their supervision and suggestions on my work. I acknowledge the discussion and efforts of this project from all the authors of the manuscript ‘Ultrathin Polyamide Nanofilms Incorporating Porous Organic Cages for Tuneable Molecular Sieving’, which is currently in preparation for the submission: Zhiwei Jiang, Chen Yang, Ming Liu, Michael E. Briggs, Marc A. Little, Andrew I. Cooper, and Andrew G. Livingston.

For funding, I acknowledge the Engineering and Physical Sciences Research Council (EPSRC) (EP/N004884/1), the Leverhulme Trust via the Leverhulme Research Centre for Functional Materials Design, the China Scholarship Council for a studentship and the Royal Society of Chemistry for a Researcher Mobility Grant (M19-2442). I would like to thank the Cooper group for additional funding to support my visit and study at Imperial College London in 2019.

Some of the experiments and discussions in this project have been carried out in the Livingston group at Imperial College London. I acknowledge Dr Zhiwei Jiang for the collaboration and



discussion on this project, especially for exploring the optimised conditions for the successful membrane fabrication. The cage membranes were prepared at Imperial College, and the SEM, AFM, XPS and the membrane performance were measured by Dr Zhiwei Jiang. I would like to thank Mr. Chen Yang for the assistant of membrane preparation and dye filtration, Miss Siyao Li for the help with the experiment set-ups when I was in Imperial College, and Dr Tianying Liu for setting up the cross-flow rig. I acknowledge Diamond Light Source for access to beamlines I07 (SI24359) that contributed to the results presented here and thank Dr. Hadeel Hussain, and Dr. Jonathan Rawle as they discussed, designed, and set up the GIXRD system and helped in the measurements. I also thank Prof. Andrew G. Livingston for facility support and insights into advanced membrane science, Prof. Andrew I. Cooper and Dr. Marc A. Little for the scientific support from material aspects.

## 5.9 References

1. Koros, W. J. & Zhang, C. Materials for next-generation molecularly selective synthetic membranes. *Nat. Mater.* **16**, 289–297 (2017).
2. Park, H. B., Kamcev, J., Robeson, L. M., Elimelech, M. & Freeman, B. D. Maximizing the right stuff: The trade-off between membrane permeability and selectivity. *Science* **356**, (2017).
3. Arabi Shamsabadi, A. *et al.* Next generation polymers of intrinsic microporosity with tunable moieties for ultrahigh permeation and precise molecular CO<sub>2</sub> separation. *Prog. Energy Combust. Sci.* **84**, 100903 (2021).
4. Zhao, Y. *et al.* Differentiating Solutes with Precise Nanofiltration for Next Generation Environmental Separations: A Review. *Environ. Sci. Technol.* **55**, 1359–1376 (2021).
5. Gin, D. L. & Noble, R. D. Designing the Next Generation of Chemical Separation Membranes. *Science* **332**, 674–676 (2011).
6. Liu, G. *et al.* Graphene oxide for high-efficiency separation membranes: Role of electrostatic interactions. *Carbon N. Y.* **110**, 56–61 (2016).
7. Liu, G. *et al.* Mixed matrix formulations with MOF molecular sieving for key energy-intensive separations. *Nat. Mater.* **17**, 283–289 (2018).
8. Zhang, X. *et al.* In-situ grown covalent organic framework nanosheets on graphene for membrane-based dye/salt separation. *J. Memb. Sci.* **581**, 321–330 (2019).

9. Li, P. *et al.* A Rod-Packing Microporous Hydrogen-Bonded Organic Framework for Highly Selective Separation of C<sub>2</sub>H<sub>2</sub>/CO<sub>2</sub> at Room Temperature. *Angew. Chemie Int. Ed.* **54**, 574–577 (2015).
10. Tozawa, T. *et al.* Porous organic cages. *Nat. Mater.* **8**, 973–978 (2009).
11. Jiao, T., Wu, G., Chen, L., Wang, C. Y. & Li, H. Precursor Control over the Self-Assembly of Organic Cages via Imine Condensation. *J. Org. Chem.* **83**, 12404–12410 (2018).
12. Slater, A. G. *et al.* Reticular synthesis of porous molecular 1D nanotubes and 3D networks. *Nat. Chem.* **9**, 17–25 (2017).
13. Lee, S., Yang, A., Money Penny, T. P. & Moore, J. S. Kinetically Trapped Tetrahedral Cages via Alkyne Metathesis. *J. Am. Chem. Soc.* **138**, 2182–2185 (2016).
14. Jiang, S. *et al.* Porous organic molecular solids by dynamic covalent scrambling. *Nat. Commun.* **2**, 1–7 (2011).
15. Slater, A. G., Little, M. A., Briggs, M. E., Jelfs, K. E. & Cooper, A. I. A solution-processable dissymmetric porous organic cage. *Mol. Syst. Des. Eng.* **3**, 223–227 (2018).
16. Canossa, S., Wuttke, S., Canossa, S. & Wuttke, S. Functionalization Chemistry of Porous Materials. *Adv. Funct. Mater.* **30**, 2003875 (2020).
17. Reiss, P. S. *et al.* Periphery-Functionalized Porous Organic Cages. *Chem. – A Eur. J.* **22**, 16547–16553 (2016).
18. Culshaw, J. L. *et al.* Dodecaamide cages: Organic 12-arm building blocks for supramolecular chemistry. *J. Am. Chem. Soc.* **135**, 10007–10010 (2013).
19. Swamy, S. I. *et al.* A metal-organic framework with a covalently prefabricated porous organic linker. *J. Am. Chem. Soc.* **132**, 12773–12775 (2010).
20. Liu, M. *et al.* Acid- and base-stable porous organic cages: Shape persistence and pH stability via post-synthetic ‘tying’ of a flexible amine cage. *J. Am. Chem. Soc.* **136**, 7583–7586 (2014).
21. Tan, Z., Chen, S., Peng, X., Zhang, L. & Gao, C. Polyamide membranes with nanoscale Turing structures for water purification. *Science* **360**, 518–521 (2018).
22. Hasell, T., Chong, S. Y., Jelfs, K. E., Adams, D. J. & Cooper, A. I. Porous organic cage nanocrystals by solution mixing. *J. Am. Chem. Soc.* **134**, 588–598 (2012).

23. Yang, Y., Bai, P. & Guo, X. Separation of Xylene Isomers: A Review of Recent Advances in Materials. *Ind. Eng. Chem. Res.* **56**, 14725–14753 (2017).
24. Cheng, X. Q. *et al.* Towards sustainable ultrafast molecular-separation membranes: From conventional polymers to emerging materials. *Prog. Mater. Sci.* **92**, 258–283 (2018).
25. Sonune, A. & Ghate, R. Developments in wastewater treatment methods. *Desalination* **167**, 55–63 (2004).
26. Ezugbe, E. O. & Rathilal, S. Membrane Technologies in Wastewater Treatment: A Review. *Membr. 2020, Vol. 10, Page 89* **10**, 89 (2020).
27. Savage, N. & Diallo, M. S. Nanomaterials and Water Purification: Opportunities and Challenges. *J. Nanoparticle Res. 2005 74* **7**, 331–342 (2005).
28. Geise, G. M. *et al.* Water purification by membranes: The role of polymer science. *J. Polym. Sci. Part B Polym. Phys.* **48**, 1685–1718 (2010).
29. Qdais, H. A. & Moussa, H. Removal of heavy metals from wastewater by membrane processes: a comparative study. *Desalination* **164**, 105–110 (2004).
30. Li, Z., Yu, J. W. & Neretnieks, I. Electroremediation: Removal of Heavy Metals from Soils by Using Cation Selective Membrane. *Environ. Sci. Technol.* **32**, 394–397 (1998).
31. Tan, M. X., Sum, Y. N., Ying, J. Y. & Zhang, Y. A mesoporous poly-melamine-formaldehyde polymer as a solid sorbent for toxic metal removal. *Energy Environ. Sci.* **6**, 3254–3259 (2013).
32. Talaiekhosani, A., Salari, M., Talaei, M. R., Bagheri, M. & Eskandari, Z. Formaldehyde removal from wastewater and air by using UV, ferrate(VI) and UV/ferrate(VI). *J. Environ. Manage.* **184**, 204–209 (2016).
33. Zvulunov, Y., Ben-Barak-Zelas, Z., Fishman, A. & Radian, A. A self-regenerating clay-polymer-bacteria composite for formaldehyde removal from water. *Chem. Eng. J.* **374**, 1275–1285 (2019).
34. Xie, R., Chu, L. Y. & Deng, J. G. Membranes and membrane processes for chiral resolution. *Chem. Soc. Rev.* **37**, 1243–1263 (2008).
35. Afonso, C. A. M. & Crespo, J. G. Recent Advances in Chiral Resolution through Membrane-Based Approaches. *Angew. Chemie Int. Ed.* **43**, 5293–5295 (2004).

# **Chapter 6**

## **Conclusions and Outlook**

This thesis has reviewed state-of-art molecular sieving membrane materials and systemically studied POC based membranes for liquid-phase separation applications. The POC membranes were fabricated using different strategies, and the obtained membranes were characterised to study their structures and separation performance.

Firstly, POC-based membranes were fabricated using several methods to overcome the challenges of processing highly crystalline POC thin films, including spin-coating, casting, in-situ synthesis, sonochemistry. These approaches exhibited a fast synthesis process (*e.g.*, 30 min) with mild conditions (*e.g.*, in water). Surface morphology and dye rejection have been studied on these membranes. It has been observed that there is a shift of the MWCO for these porous organic membranes if processed into different structures (crystalline and random packing). For example, amorphous **CC3** membranes fabricated via spin-coating have shown a MWCO of  $\sim 400 \text{ g}\cdot\text{mol}^{-1}$  compared to the crystalline **CC3** membranes with a MWCO of  $\sim 600 \text{ g}\cdot\text{mol}^{-1}$ , which indicates the pore structures of these membrane materials have successfully been modulated by altering the polymorphs of the POCs.

In **Chapter 3**, a novel synthetic strategy to fabricate crystalline POC membranes has been developed using a simple aqueous–organic interfacial technique. The interfacial approach enables the directly in-situ formation of thin films consisting of **CC3** molecules under mild conditions. The resulting POC composite membrane, **CC3-PAN**, was continuous, defect-free, and showed high solvent permeances for a range of organic solvents—in some cases, such as for acetone, exceeding the upper performance bound—while also demonstrating excellent dye rejection performances. To the best of our knowledge, this is the first time an interfacial reaction process has been used to prepare continuous crystalline POC membranes that have been used in molecular separations, bringing a breakthrough in discrete porous materials applications.

We attribute the high solvent permeance of **CC3-PAN** to highly ordered pore channels in POC crystals positioned throughout the membrane structure. The mechanism of the **CC3** film formation has been studied, which can be described in four stages during the process. Effects of crystallinity, reaction solvents, membrane activation, pressure and long duration have been investigated in detail.

Interestingly, these highly ordered crystalline POC membranes exhibited a switchable phase transition between two unique crystalline forms, **CC3 $\alpha$ -PAN** and **CC3 $\gamma'$ -PAN**. In **Chapter 4**, solid-state structural transformation of **CC3** has been observed and studied using several

solvents. In situ GIXRD measurements in water and methanol have determined two different molecule packing forms in the same cage membrane. When the cage molecules are arranged in the  $CC3\alpha$  phase, they pack in a window-to-window arrangement to generate an interconnected diamondoid pore network. By comparison, in the  $CC3\gamma'$  phase, the  $CC3$  molecules are packed in a less dense arrangement, thus providing large extrinsic pores between hexagonally arranged  $CC3$  molecules. The reversible transition between  $CC3\alpha$ -PAN and  $CC3\gamma'$ -PAN, therefore, can create different diffusion pathways through the membrane structure.

Dye rejection experiments showed that only the two larger dyes had been rejected from the MeOH feedstocks with its  $CC3\gamma'$  phase, while most of the dyes could get through the cage membrane. As a result, the MWCO shifted from  $600\text{ g}\cdot\text{mol}^{-1}$  in water to  $1400\text{ g}\cdot\text{mol}^{-1}$  in MeOH for the same membrane. We attributed this switching phenomenon solely to phase transformation between the two solvents, where alternative diffusion pathways were created through the membrane structure. This was confirmed by nanofiltration experiments in acetone. The single cage membrane was also tested interchangeably with water and MeOH dye feedstocks for five consecutive cycles, and the reversible selectivity of the dye proved that the membrane can be switched 'on' and 'off' using a solvent.

Effects of crystallinity and solvation have been investigated using cage membranes with lower crystallinity. The rejection and permeance data indicates the high crystallinity in the  $CC3$  membrane is essential for regulating its separation performance after switching its pore aperture using a solvent stimulus, whilst the amorphous membrane didn't show this unique switching property. Meanwhile, the dynamic transformation has been studied using water and methanol solvent mixtures with different concentrations, and the critical transition between  $CC3\alpha$ -PAN and  $CC3\gamma'$ -PAN was found to occur at a water concentration of 61.7%.

To demonstrate the functional advantage of the structural transformation, we performed a graded sieving experiment and a continuous ternary separation process to separate a mixture of three organic dye molecules with a single, smart membrane by introducing a solvent gradient. This allows the collection of three molecules separately from a ternary mixture and creates a membrane-based parallel to the widespread and highly effective use of solvent gradients in chromatography<sup>1</sup>. POC membranes with switchable pore apertures could also lead to new applications in triggered drug delivery<sup>2</sup>, biosensors<sup>3</sup>, or fermentation/fractionation processes<sup>4</sup>.

Moreover, in **Chapter 5**, a series of thin-film composite membranes comprising a cage nanofilm separating layer have been fabricated at a free aqueous–organic interface, using the

reduced amine cages, **RCC1**, **RCC2** and **RCC3**. Transfer of these ultrathin nanofilms onto porous supports provided fast water transport through the resulting nanofilm composite membranes. The nanofilms were continuous and robust with an ultrathin thickness. Supported by the crosslinker, the reduced cages are supposed not to collapse in solid state and are equipped with excellent pore channels for separation. With a defect-free and hydrophilic nanofilm layer, the composite membranes have shown high rejection of dyes as well as salt ions.

By altering the molecule type during the synthesis, **RCC1**, **RCC2**, and **RCC3** nanofilms exhibited distinctive performance, where **RCC1** and **RCC2** nanofilms had a similar MWCO of  $\sim 250 \text{ g}\cdot\text{mol}^{-1}$ , while **RCC3** nanofilm showed a shift of its cutoff to  $\sim 600 \text{ g}\cdot\text{mol}^{-1}$ . The surface morphology and composition of these nanofilms have been studied to link their different permeance and rejection performance to the varied membrane structures.

The **RCC3** nanofilm has been used for post-functionalisation where the unreacted amines were tied up by formaldehyde. A tunable sieving effect was found in the FT-**RCC3** nanofilm that the MWCO shifted from  $\sim 600 \text{ g}\cdot\text{mol}^{-1}$  to  $\sim 450 \text{ g}\cdot\text{mol}^{-1}$  after the tie-up procedure. This indicates that the cage nanofilm composite membranes showing adjustable molecular separation properties have been successfully designed and fabricated by altering the monomeric cage molecule type in the interfacial synthesis pathway or a tie-up post-functionalisation strategy. This makes these materials exciting candidates for different applications in many important fields, such as wastewater treatment<sup>5</sup>, water purification<sup>6</sup>, heavy metals removal<sup>7</sup>, formaldehyde removal<sup>8</sup>, and chiral separation<sup>9</sup>.

To summarise, several types of POC base membranes have been successfully prepared, including amorphous POC membranes, smart and responsive crystalline POC membranes with switchable pore apertures, and cross-linked POC nanofilm composite membranes with tuneable separation property. It is anticipated that these synthesis techniques and unique templating methods demonstrated herein for the fabrication of defect-free, tuneable POC based membranes would broaden the realm of the practical application of these novel macrocyclic materials.

However, challenges still remain for these exciting porous materials to be employed in membrane fields. For example, the mechanisms for mass transfer in the pores of these membranes are still not clear enough, and the degree of membrane cross-linking has not been determined. Further investigation of these novel membranes would contribute to a comprehensive understanding of the functional membranes with tuneable molecular sieving ability and bring insights to the design of the next-generation membrane materials.

Among the extended POC family, only several cages, including **CC3**, **RCC1**, **RCC2**, and **RCC3**, have been used and studied for the membrane formation in this thesis. Other suitable cage molecules with different structures or functional groups may be selected to fabricate the target membranes with desired performance. While only liquid-phase separation has been discussed in this thesis, potential applications for these POC membranes can be further explored, for gas separation<sup>10</sup>, hydrogen isotope separation<sup>11</sup>, or xylene separation<sup>12</sup>, or chiral molecular recognition<sup>13</sup>.

In addition, the scalability of the POC membranes, as an important factor in large-scale industrial applications, can be achieved practically due to their solution processable properties (i.e., the solubility of POCs), but haven't been compressively studied in this work. Trials to enhance the scalability, such as in-situ growth of the POC membranes or flow synthesis method, would be valuable and beneficial to make POCs more attractive candidates in both academe and industry.

While the current synthesis process makes it challenging to implement these POC membranes in commercial processes, it is conceivable that a more scalable production method might be developed in the future; for example, by exploiting the solution processability of these molecular cages. Future efforts will focus on using computational methods, such as crystal structure prediction (CSP)<sup>14</sup>, to design POC crystals with specific properties that can be designed from first principles. We believe this research is valuable for the development of novel membrane materials using POC families.



## References

1. Aumann, L. & Morbidelli, M. A continuous multicolumn countercurrent solvent gradient purification (MCSGP) process. *Biotechnol. Bioeng.* **98**, 1043–1055 (2007).
2. Loftsson, T., Vogensen, S. B., Brewster, M. E. & Konráosdóttir, F. Effects of cyclodextrins on drug delivery through biological membranes. *Journal of Pharmaceutical Sciences* vol. 96 2532–2546 (2007).
3. Kohli, P., Wirtz, M. & Martin, C. R. Nanotube membrane based biosensors. *Electroanalysis* **16**, 9–18 (2004).
4. O'Brien, D. J. & Craig, J. C. Ethanol production in a continuous fermentation/membrane pervaporation system. *Appl. Microbiol. Biotechnol.* **44**, 699–704 (1996).
5. Ezugbe, E. O. & Rathilal, S. Membrane Technologies in Wastewater Treatment: A Review. *Membr. 2020, Vol. 10, Page 89* **10**, 89 (2020).
6. Geise, G. M. *et al.* Water purification by membranes: The role of polymer science. *J. Polym. Sci. Part B Polym. Phys.* **48**, 1685–1718 (2010).
7. Qdais, H. A. & Moussa, H. Removal of heavy metals from wastewater by membrane processes: a comparative study. *Desalination* **164**, 105–110 (2004).
8. Talaiekhosani, A., Salari, M., Talaei, M. R., Bagheri, M. & Eskandari, Z. Formaldehyde removal from wastewater and air by using UV, ferrate(VI) and UV/ferrate(VI). *J. Environ. Manage.* **184**, 204–209 (2016).
9. Afonso, C. A. M. & Crespo, J. G. Recent Advances in Chiral Resolution through Membrane-Based Approaches. *Angew. Chemie Int. Ed.* **43**, 5293–5295 (2004).
10. Song, Q. *et al.* Porous organic cage thin films and molecular-sieving membranes. *Adv. Mater.* **28**, 2629–2637 (2016).
11. Liu, M. *et al.* Barely porous organic cages for hydrogen isotope separation. *Science* **366**, 613–620 (2019).
12. Mitra, T. *et al.* Molecular shape sorting using molecular organic cages. *Nat. Chem.* **5**, 276 (2013).
13. Xie, S. M. *et al.* A chiral porous organic cage for molecular recognition using gas chromatography. *Anal. Chim. Acta* **903**, 156–163 (2016).

14. Slater, A. G. *et al.* Computationally-Guided Synthetic Control over Pore Size in Isostructural Porous Organic Cages. *ACS Cent. Sci.* **3**, 734–742 (2017).